

# Permeation Barrier for Lightweight Liquid Hydrogen Tanks



Dissertation zur Erlangung des Doktorgrades  
der Mathematisch-Naturwissenschaftlichen Fakultät  
der Universität Augsburg

vorgelegt von

**Daniel Schultheiß**

16. April 2007

---

**OPUS Augsburg**

der Online-Publikationsserver der Universität Augsburg

Erstgutachter: Prof. Dr. Siegfried R. Horn  
Zweitgutachter: Prof. Dr. Ferdinand Haider

Tag der mündlichen Prüfung: 06. Juni 2007

# Contents

Table of Contents	i
Notation	iii
<b>1 Introduction</b>	<b>1</b>
<b>2 Permeation in Metals and Polymers</b>	<b>7</b>
2.1 Structure of Metals and Polymers . . . . .	7
2.2 Fundamental Equations . . . . .	9
2.3 Sorption . . . . .	10
2.3.1 Modes of Sorption . . . . .	10
2.3.2 Sorption in Metals . . . . .	12
2.3.3 Sorption in Polymers . . . . .	13
2.3.4 General Sorption Equation . . . . .	14
2.4 Diffusion . . . . .	14
2.4.1 Phenomenological Description . . . . .	14
2.4.2 Atomistic Description . . . . .	16
2.4.3 Solution of Fick's Laws . . . . .	18
2.4.4 Grain Boundary Diffusion . . . . .	19
2.5 Permeation . . . . .	22
2.5.1 Phenomenological Description . . . . .	22
2.5.2 Experimental Determination of $P$ and $D$ . . . . .	23
2.5.3 Serial and Parallel Permeation . . . . .	26
2.5.4 Permeation through Substrates with Defective Liners . . . . .	28
2.5.5 Comparison of Hydrogen and Helium Permeation . . . . .	30
2.6 Simulation of Permeation . . . . .	31
<b>3 Preselection of Feasible Liner Materials and Production Processes</b>	<b>39</b>
3.1 Literature Review of LH <sub>2</sub> Tank Liners . . . . .	39
3.2 Literature Review of Hydrogen Permeabilities . . . . .	41
3.3 Outgassing and Literature Review of Outgassing Rates . . . . .	42
3.4 Vacuum Stability and Material Preselection . . . . .	44
3.5 Literature Review and Preselection of Liner Production Processes . . . . .	46

<b>4</b>	<b>Materials</b>	<b>51</b>
4.1	Substrates . . . . .	51
4.2	Liners . . . . .	53
4.3	Specimens . . . . .	60
<b>5</b>	<b>Measurement of Permeation</b>	<b>61</b>
5.1	Room Temperature Permeation Measurement Apparatus . . . . .	61
5.1.1	Test Set-up . . . . .	61
5.1.2	Test Procedure . . . . .	63
5.1.3	Calibration . . . . .	65
5.2	Cryogenic Permeation Measurement Apparatus . . . . .	67
5.3	Evaluation and Error Estimation . . . . .	71
<b>6</b>	<b>Results and Discussion</b>	<b>73</b>
6.1	Initial Permeation Tests . . . . .	73
6.1.1	Reliability of the Measurement Apparatuses . . . . .	73
6.1.2	Comparison of Hydrogen and Helium Permeation . . . . .	76
6.1.3	Influence of the Feed Pressure . . . . .	80
6.1.4	Influence of Thermal Cycling . . . . .	81
6.2	Results of the Permeation Measurements . . . . .	82
6.2.1	CFRP Substrates . . . . .	82
6.2.2	Metal Sheets and Foils . . . . .	83
6.2.3	Metal-plated CFRP . . . . .	85
6.2.4	Miscellaneous Coatings on CFRP . . . . .	89
6.3	Simulation of Transient Permeation . . . . .	90
6.3.1	Simulation of Grain Boundary Diffusion . . . . .	90
6.3.2	Simulation of Two-layer Permeation . . . . .	91
6.3.3	Simulation of Permeation through Substrates with Defective Liner . . . . .	95
6.4	Discussion . . . . .	97
6.4.1	Permeation through CFRP . . . . .	97
6.4.2	Permeation through Metal-plated CFRP . . . . .	98
6.4.3	Evaluation of the Barrier Function of the Liners . . . . .	103
<b>7</b>	<b>Conclusions</b>	<b>105</b>
<b>A</b>	<b>Literature Survey of H<sub>2</sub> Permeabilities</b>	<b>111</b>
<b>B</b>	<b>Literature Survey of Outgassing Rates</b>	<b>123</b>
<b>C</b>	<b>List of Materials</b>	<b>129</b>
<b>D</b>	<b>Measured Data</b>	<b>133</b>
	<b>Bibliography</b>	<b>137</b>

## Notation

## List of frequently used symbols

$a$	lattice constant	$P_0$	pre-exponential factor of $P$
$b$	width	$Q$	gas flow
$d$	diameter of the sealing ring	$Q_G$	outgassing rate
$j$	normalized flux	$Q_L$	leak rate
$l$	thickness	$Q_P$	permeation gas flow
$m$	mass	$Q_T$	throughput
$n$	pressure exponent (sorption)	$R$	universal gas constant (mostly
$p$	pressure (general)		in the form of $RT$ )
$p_f, p_p$	pressure at feed/permeate side	$R$	defect separation distance
$p_s$	vapor saturation pressure	$S$	solubility, Henry's constant
$q_G$	area specific outgassing rate	$S_0$	pre-exponential factor of $S$
$r$	defect radius	$S_S$	solubility, Sievert's constant
$s$	pumping speed	$T$	temperature
$s_{\text{eff}}$	effective pumping speed	$T_{\text{mc}}$	$T$ of the measuring chamber
$t$	time	$T_g$	glass transition temperature
$x$	coordinate	$V$	volume
$A$	area	$\iota$	barrier constant
$C$	concentration	$\mu$	chemical potential
$C_f, C_p$	$C$ at the feed/permeate side	$\mu^0$	standard chemical potential at
$D$	diffusivity		standard conditions
$D_0$	pre-exponential factor of $D$	$\nu_f$	fractional free volume
$E_a$	activation energy (general)	$\tau$	dimensionless time
$E_D, E_P, E_S$	activation energy of $D, P, S$		
$J$	flux	Subscripts	
$J_{\text{ss}}$	steady-state flux	G	grain
$M$	molar mass	B	grain boundary
$N$	number of particle in mol	s	substrate
$P$	permeability	l	liner

## List of Abbreviations and Acronyms

bcc	body-centered cubic	SEM	scanning electron microscopy
cAu	chemical gold	UHV	ultra high vacuum
cCu	chemical copper		
cNiP	chemical nickel phosphor	ECTFE	ethylen/chlortrifluorethylen
fcc	face-centered cubic	HDPE	high density polyethylene
hcp	hexagonal close-packed	Inconel	austenitic nickel-based alloy
		Kovar	nickel-cobalt ferrous alloy
CFRP	carbon fiber reinforced plastic	LDPE	low density polyethylene
CPMA	cryogenic permeation measurement apparatus	Monel	nickel copper iron alloy
		Mylar	see PETP
DLC	diamond-like carbon	PA	polyamide
EDX	energy dispersive x-ray	PBO	polyphenylene oxide
FDM	finite difference method	PC	polycarbonate
LH <sub>2</sub>	liquid hydrogen	PE	polyethylene
LHe	liquid helium	PETP	Polyethylenterephthalat
LN <sub>2</sub>	liquid nitrogen	PI	polyimide
M01, ...	material system number	PP	polypropylene
PVD	physical vapor deposition	PTFE	polytetrafluoroethylene
QMS	quadrupole mass spectrometer	PU	polyurethane
RT	room temperature	PVC	polyvinyl chloride
RTPMA	room temperature permeation measurement apparatus	SS	stainless steel
		Teflon	see PTFE
S01, ...	specimen number	VdC	vinylidenchloride

## Abbreviation List of Company Names

C01	BMW Group
C02	Oerlikon Space AG
C03	Institut für Verbundwerkstoffe GmbH
C04	AIMT Holding GmbH
C05	Lüberg Elektronik GmbH & Co. Rothfischer KG
C06	Aluminal Oberflächentechnik GmbH & Co. KG
C07	Leistner GmbH
C08	OMT – Oberflächen- und Materialtechnologie GmbH
C09	Universität Augsburg, Institut für Physik
C10	MT Aerospace AG
C11	Magna Steyr Space Technology
C12	Linde AG
C13	Alfa Aesar GmbH & Co. KG
C14	Roth GmbH

# Chapter 1

## Introduction

Conventional fossil energy sources like coal, oil and natural gas are only time-limited available [1–11]. Additionally, the emission of carbon dioxide owing to the combustion of fossil energy sources is made responsible for the increasing greenhouse effect and therefore for the global warming [12–15]. Hydrogen ( $H_2$ ) is an alternative energy carrier that does not contain carbon. Its usage as a fuel in automobiles is the subject of recent research and development. Thereby, the storage of  $H_2$  on board is an essential issue. One technical solution is the storage of liquefied hydrogen (20 K, 1 – 6 bar) in vacuum insulated tank vessels. Liquid hydrogen ( $LH_2$ ) tanks made of carbon fiber reinforced plastics (CFRP) are of special interest because they enable lightweight structures. However, the permeation of hydrogen through CFRP, a potential source of deteriorating the vacuum, is still a challenge to be solved.

### Automotive $LH_2$ Tank and its Vacuum Insulation

The minimization of arbitrary heat fluxes into the liquid hydrogen is one of the key issues when developing a  $LH_2$  tank. Heat transfer leads to an evaporation and hence to a loss of hydrogen. Vacuum insulations, as employed in thermo flasks, provide the most efficient protection.

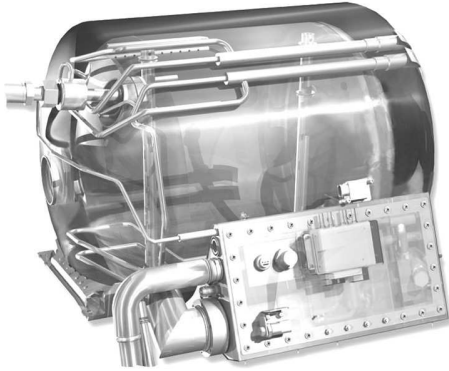
Figure 1.1 illustrates the  $LH_2$  tank of the BMW *Hydrogen 7*. Concerning the storage function, the main parts of the system are the inner and the outer tank vessel, and the in-between superinsulation. Further parts are explained within the figure. The superinsulation consists of an evacuated space in combination with multi-layer foils, see figure 1.2. The vacuum between the inner and the outer tank vessel enables a reduction of the convection and thermal conduction. The multi-layer foils are added to reduce the radiation. Compared to other insulation methods, the superinsulation is advantageous because of its very low thermal conductivity<sup>1</sup>.

Figure 1.3 emphasizes the importance of high vacuum within the superinsulation. The thermal conductivity of the superinsulation is plotted as a function of the vacuum pressure. Exceeding  $10^{-3}$  mbar, the thermal conductivity increases rapidly. At 0.3 mbar, the insulation is deteriorated by factor 200.

The main factors that can deteriorate the insulating vacuum are schematically shown in figure 1.4. These five factors can be categorized into three processes: gas permeation,

---

<sup>1</sup>The thermal conductivity of the superinsulation is approximately  $3 \cdot 10^{-5}$  W/m K. For comparison, the thermal conductivity of polystyrene (Styrofoam) is between  $3 \cdot 10^{-3}$  W/m K at very low temperatures and 1.5 W/m K at room temperature [16].



**Figure 1.1:** X-ray view of the  $\text{LH}_2$  tank of the *Hydrogen 7*. The tank consists of an inner and an outer tank, enclosing an insulating vacuum. The inner tank contains the stored hydrogen as well as filling and extraction pipes, an evaporator and a level gauge. The inner tank is suspended from the outer tank at the polar caps. The auxiliary box outside the tank hosts, among other things, valves and a heat exchanger. Source: Magna Steyr.

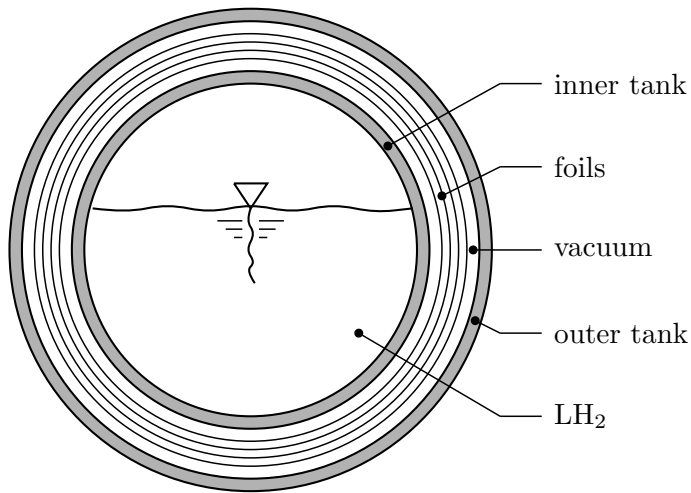


**Figure 1.2:** Schematic section of a  $\text{LH}_2$  tank. The inner tank stores the liquid hydrogen. It is surrounded by the superinsulation consisting of vacuum and multi-layer foils. The inner tank and the insulation are hosted by the outer tank. Suspensions, pipes, valves, etc. are not drawn.

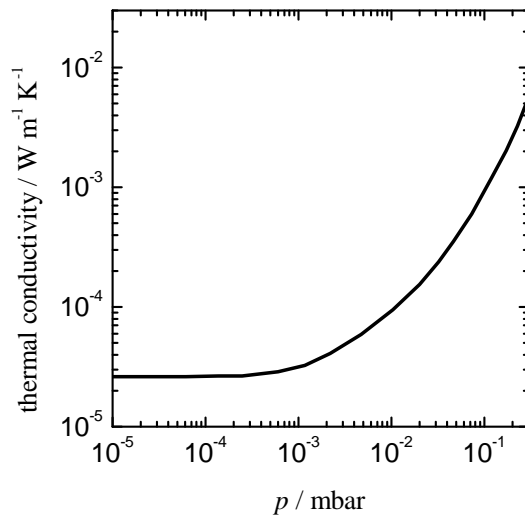


**Figure 1.3:** Thermal conductivity of the superinsulation as a function of the vacuum pressure. The conductivity increases strongly for pressures greater than  $10^{-3}$  mbar. From [17].



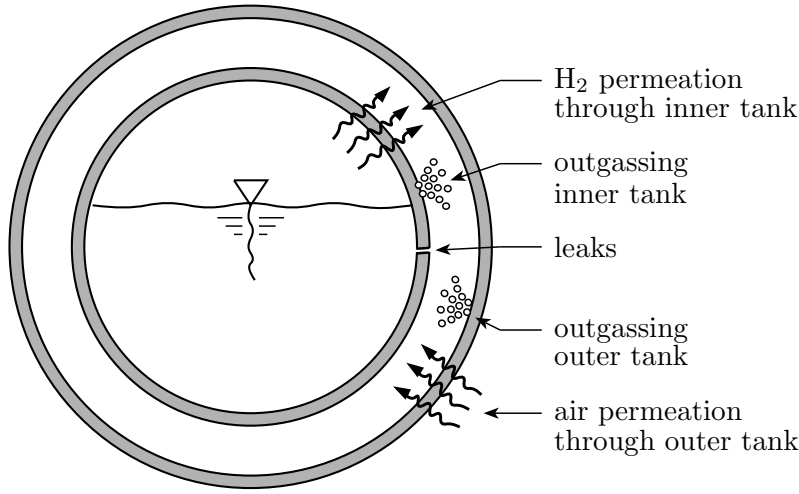


**Figure 1.4:** Main factors that deteriorate the vacuum of the superinsulation. Influences of suspensions, pipes, valves, etc. are not considered here.

outgassing and leakage. While definitions and detailed explanations of permeation and outgassing are given in chapter 2 and 3, leakage is not further investigated.

### Automotive Lightweight LH<sub>2</sub> Tank

The state-of-the-art LH<sub>2</sub> tank as described above is cylindrically shaped and made of stainless steel (SS). Its mass without auxiliary system parts is approximately 100 kg, for 10 kg stored LH<sub>2</sub> [18]. The automotive industry would benefit from an optimized shape and a reduced weight of the tank. One objective of the European project *StorHy* (Hydrogen Storage Systems for Automotive Application) is to present such a tank. More specific, the tank mass for a storage capacity of 10 kg LH<sub>2</sub> shall be reduced from 100 kg to 30 kg. The chosen tank design is depicted in figure 1.5. Although it reminds to the cylindrical shape, this storage system contains all necessary elements to realize a form-adapted design.

CFRP meets the demands of the new design and the weight reduction. Compared to stainless steel, the weight-specific stiffness and strength of CFRP can be several times higher [19; 20]. Besides their advantageous mechanical properties, the design of CFRPs can be optimized to fulfill specific requirements like anisotropic loads — as existing in a LH<sub>2</sub> vessel. On the other hand, CFRP is highly permeable to hydrogen and shows high outgassing rates. Hence, a liner is required, that means a permeation and outgassing barrier to protect the vacuum.

### Objective and Outline

The objective of this thesis is the development of an adequate protection (liner) against H<sub>2</sub> permeation through the inner vessel of a CFRP liquid hydrogen tank. The liner shall additionally prevent the outgassing of the CFRP. Considering outgassing, a liner at the outside of the inner tank is mandatory. To prevent permeation, the liner can be either applied at one of both surfaces or inside the tank shell. The liners investigated in this work are only applied at the surface facing the vacuum, i. e. at the outside of the inner tank.

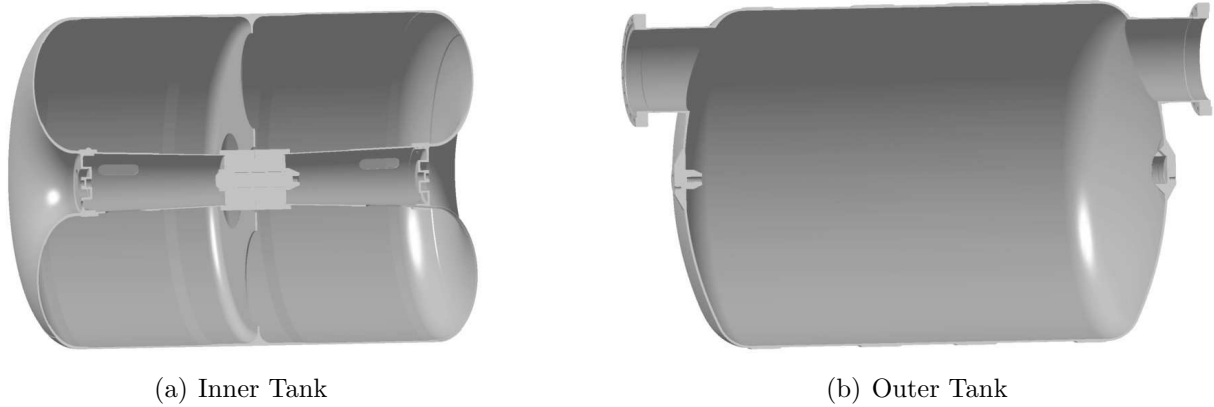


**Figure 1.5:** Design of the chosen lightweight  $\text{LH}_2$  tank concept. The inner tank contains a tension sheet to suppress buckling of the cylindrical part as well as a tension bar to carry axial loads and enable flat polar caps. Though both elements would not be required for a cylindrical tank, they are mandatory for a free-form tank with concave-convex shapes. Hence, this inner tank includes all parts to demonstrate the feasibility of a form-adapted design. The outer tank follows the shape of the inner tank. A transformation to a form-adapted design can be realized by adding stiffeners. Source: BMW Group Research and Technology.

The more specific objective of this work is to preselect and subsequently test suitable liner materials and the according production processes. Thereby, the main emphasis is laid on the evaluation of these liner materials and –production processes regarding their permeation performance.

Following this introductory chapter, chapter 2 gives an introduction to permeation through metals and polymers. Since it is important for understanding the different permeation processes, first the structure of metals and polymers is explained. After presenting equations to describe gases and their transport, the two subprocesses of permeation, sorption and diffusion, are described. There, the modes of sorption, the differences between sorption in metals and polymers, the atomistic and phenomenological description of diffusion, and the grain boundary diffusion are presented. In the following, the total permeation process is explained by introducing governing equations and material properties like the permeability. Experimental methods are presented to determine those material properties. Next, four modes of permeation are distinguished and explained: permeation through a homogeneous material, through parallel or serial materials, and through a defectively coated material. At the end of this chapter, a program to simulate transient permeation is presented. The objective of simulating transient permeation is to obtain characteristic shapes of the flux-time curve, depending on the mode of permeation.

In the third chapter, feasible liner materials and processes are reviewed, evaluated and preselected. First, a literature survey is performed on liners applied or planned for  $\text{LH}_2$  tanks. Second, permeabilities and outgassing rates of different materials are reviewed from the literature. The review includes a large number of publications to enable a meaningful

selection. Third, the required liner permeability and outgassing rate to enable a stable tank vacuum are assessed by performing a sample calculation. Considering both permeation and outgassing, a metallic liner is mandatory to sustain a stable insulating tank vacuum. Feasible processes to produce metallic liners are presented in the following. Considering the producibility on CFRP, the preselected liner production processes are metal plating<sup>2</sup>, adhesion of foils, thermal spraying and physical vapor deposition. The investigated materials include aluminum, copper, gold, nickel, tin and additionally diamond-like carbon.

The next chapter 4 presents and characterizes the selected materials. Considering CFRP and particularly the liners, their basic properties like thermal shock resistance, adhesive strength, structure and potential material defects are discussed. SEM images of the surface and the section of the liners give information about grain-like structures, thickness distribution or the formation of cracks. At the end of this chapter, the size and shape of the utilized specimens are illustrated. A list of all specimens summarizing their properties and production details is presented in appendix C.

Chapter 5 describes the measurement of permeation. Two apparatuses are employed working from 20 K to 293 K, and from 293 K to 373 K respectively. The set-up of both apparatuses is presented and explained. A typical test procedure is exemplarily described in the following section. Because a main focus is laid on high-quality results, the calibration of the experimental set-up is discussed. The last part of this chapter explains the evaluation of the measurements and estimates the maximum experimental error.

In chapter 6, the results of the permeation measurements and simulations are presented, compared and discussed. First, initial tests to verify the reliability of the measurements are performed. Second, the permeation of hydrogen and helium through eleven specimens is compared. Since the permeation performances of both gases are similar and hydrogen is disadvantageous owing to its higher minimum detection limit, it is concluded to use helium as test gas in the following. Third, the influence of the feed pressure and of thermal shocks on the permeability of selected specimens is determined. The following section 6.2 lists the results of the permeation measurements on all specimens. Besides the presentation of the permeabilities, information about the activation energy, diffusivity and the shape of the flux-time is given. In 6.3, the results of the simulations of permeation through parallel grain boundaries, through serial materials and through materials with defective liners are presented. Both, the results of the measurements and simulations are compared and discussed in 6.4. In particular, the mode of permeation through CFRP and through metal-plated CFRP is determined. Finally, the results of the permeation measurements are evaluated together with the material characterization of chapter 4. A recommendation for suitable liners is given.

The last chapter summarized this thesis and gives an outlook on future work.

---

<sup>2</sup>Throughout this thesis, metal plating denotes the generic term for electroless plating and electroplating.



## Chapter 2

# Permeation in Metals and Polymers

*“A theory is something nobody believes, except the person who made it ...”* continued on page 61

This chapter gives a detailed description of permeation in metals and polymers. First, the structure of these materials is explained and fundamental equations to describe gases and their transport are presented. The next two sections deal with sorption and diffusion, the subprocesses of permeation. The permeation process itself is treated afterwards. Finally, the developed program to simulate permeation is presented.

## 2.1 Structure of Metals and Polymers

The mechanism and the rate of permeation are strongly related to the structure of the bulk material. While metals and metal alloys are characterized by their compact crystal structure, polymers are amorphous.

The three types of crystal structure in metals, face-centered cubic (fcc), body-centered cubic (bcc) and hexagonal close-packed (hcp), are shown in figure 2.1. Table 2.1 summarizes the lattice types and the according lattice constants of selected metals. The structure of a true metal, however, is a crystal containing imperfections. Common defects are vacancy or interstitialcy (point defects), edge or screw dislocation (line defects) and grain boundaries (planar defects).

The common feature of all polymers is the co-existence of molecule chains and free volumes [23–26]. The noncrystalline structures of polymers are less tightly packed than metals. Depending on the cross-linkage of the chains one distinguishes between thermoplastics, thermosets and elastomers. In this thesis, only thermosets and thermoplastics are further considered and illustrated in figure 2.2. Thermoplastics consist of linear or less branched but not cross-linked chains. The bonding between the chains are owing to van-der-Waals or hydrogen-bridge forces. The polymer chains of thermosets, on the contrary,

**Table 2.1:** Crystal structure of some metals. The lattice constant  $a$  is taken from [22].

lattice	metals	$a$ / Å
fcc	copper, silver, gold, platinum, aluminum, nickel, lead, palladium	3.52 – 4.95
bcc	iron, vanadium, niobium, tantalum, molybdenum, tungsten	2.87 – 3.31
hcp	titanium, zinc	2.67 – 2.95

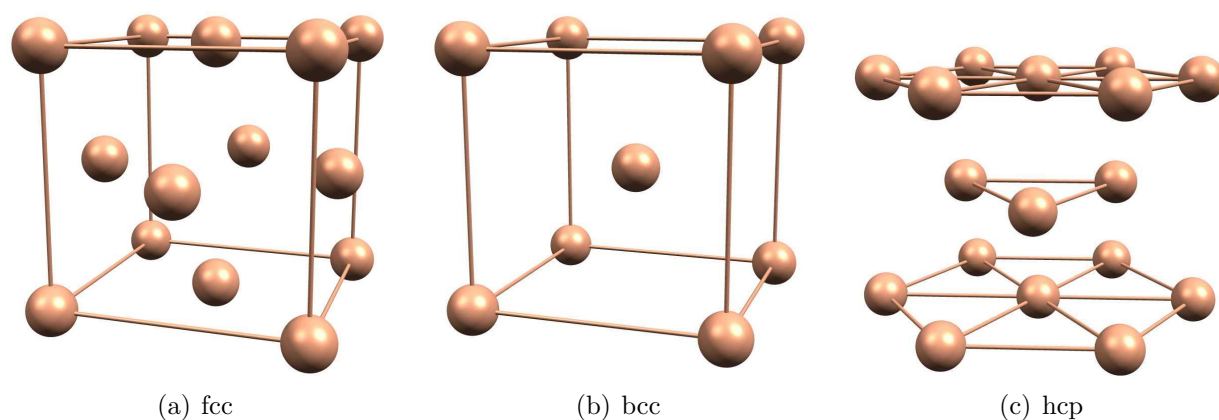


**Figure 2.1:** The three lattice types of metals. The atomic packing factor of fcc, bcc and hcp lattices is 0.74, 0.68 and 0.74, respectively [21].

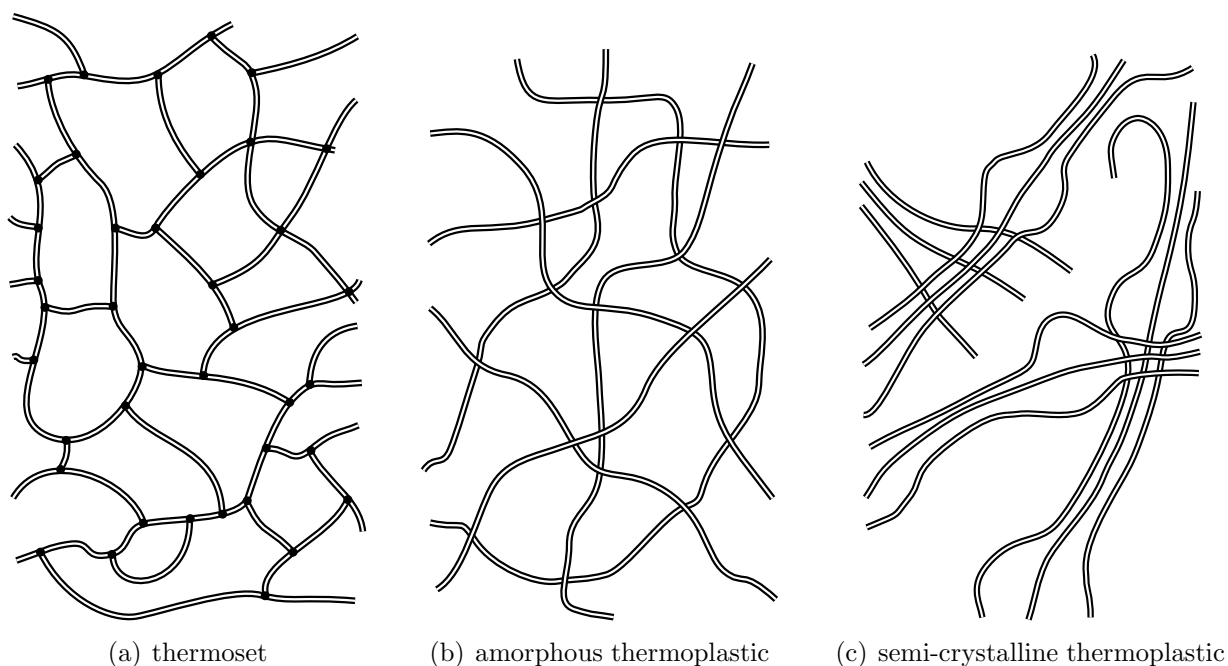


**Figure 2.2:** Molecular structure of thermosets and thermoplastics. Thermosets contain strong covalent bindings between the molecular chains. Thermoplastics form weak van-der-Waals or hydrogen-bridge bindings. Depending on the structure of the chains, one defines amorphous and semi-crystalline thermoplastics. The space not occupied by the molecule chains is called free volume.

are strongly cross-linked to form a net. The existing covalent forces are much stronger than the cohesion forces of thermoplastics.

Free volumes (also: microcavities, holes) exist in both polymer classes. Their size is few Angstroms [27]. They are permanently formed and destroyed caused by oscillations of the macromolecular chains. The oscillations as well as the number of holes increase with increasing temperature. Additionally, the number of holes is proportional to the grade of crystallinity [28; 29]. To quantify the free volumes, the fractional free volume is introduced which is defined by

$$\nu_f = \frac{V_f}{V_{\text{tot}}}, \quad (2.1)$$

where  $V_f$  is the volume not occupied by chains and  $V_{\text{tot}}$  is the total volume.

The properties of polymers are strongly temperature-dependent. With increasing temperature, the chains of thermoplastics contain enough energy to enable rotation around the single C–C bindings. At the glass transition temperature,  $T_g$ , the material becomes soft. A further increase of the temperature leads to overcoming the inter-chain forces and results in melting. Thermosets, on the contrary, do not melt. Breaking apart the covalent forces, the thermoset splits into smaller parts and carbonizes. This characteristic distinguishes thermoplastics from thermosets. While thermoplastics can be repeatedly heated and formed, thermosets can only be once heated and formed.

Epoxy resins are one class of thermosets. The bindings of the epoxy groups are relatively strong and result in very stable materials. Because of their advantageous properties they are used as adhesives or matrices of composites.

## 2.2 Fundamental Equations

The behavior of gases in HV (high vacuum,  $10^{-7}$  mbar –  $10^{-3}$  mbar) and UHV (ultra-high vacuum,  $< 10^{-7}$  mbar) can be described by the state equation of ideal gases

$$pV = NRT, \quad (2.2)$$

where  $p$  is the pressure,  $V$  is the volume,  $N$  is the number of particle in mol,  $R$  is the universal gas constant, and  $T$  is the absolute temperature. The transport of gases is generally quantified by the gas flow

$$Q = \frac{d(pV)}{dt}, \quad (2.3)$$

where  $t$  is the time. The gas flow is per definition an energy flow. The energy expression  $pV$  is called gas amount. Depending on the origin of the gas flow, it can be classified into the leak rate ( $Q_L$ ), outgassing rate ( $Q_G$ ), permeation gas flow ( $Q_P$ ), or throughput ( $Q_T$ ). The throughput is the rate of pumping and is defined as

$$Q_T = s p, \quad (2.4)$$

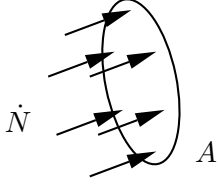


**Figure 2.3:** Definition of the flux  $J$ . The amount of particles  $dN$  crosses the area  $A$  in time  $dt$ .

where  $s$  is the pumping speed and  $p$  is the pressure at the inlet of the pump. In many applications, the area specific gas flow is used to describe transport processes:

$$q = Q/A, \quad (2.5)$$

where  $A$  is the area.

The transport of gases in permeation processes is usually described by the flux,  $J$ . The flux is defined as the rate of particles per unit area, see figure 2.3

$$J = \frac{1}{A} \frac{dN}{dt}. \quad (2.6)$$

Substituting (2.2) and (2.3) in (2.6), the relationship between the flux and the gas flow is

$$J = \frac{1}{A R T} Q. \quad (2.7)$$

The flux can also be expressed by the concentration flow. The concentration of a material is defined as the number of particles  $dN$  per occupied volume  $dV$ :

$$C = \frac{dN}{dV}. \quad (2.8)$$

Substituting (2.8) in (2.6) and considering  $dV/dt = A dx/dt = A v$ , where  $v$  is the average velocity of the particles, one obtains

$$J = C v. \quad (2.9)$$

## 2.3 Sorption

### 2.3.1 Modes of Sorption

Sorption is the general term for all interactions at surfaces between molecules of two phases. In this thesis, only the interactions between molecules of the gas phase (solute) and the surface of a solid (solvent) are considered.

If molecules of the gas phase hit the surface of a solid, they can stick on it with a certain probability. This process is called adsorption. Depending on the existing cohesion forces, one defines physisorption (van-der-Waals forces) and chemisorption (covalent bond forces). The molar sorption energy of physisorption and chemisorption are approximately



30 kJ/mol and 500 kJ/mol, respectively [30; 31]. Desorption is the opposite process of adsorption. Absorption denotes the migration of the solutes into the bulk of the solvent.

Adsorption can be classified into mono-layer and multi-layer adsorption. Mono-layer adsorption is typically described by the Langmuir model [32]. There, only one layer of gas atoms/molecules can stick on the surface of the solvent. The coverage grade,  $\theta$ , is defined for values between 0 (no adsorbed atoms) and 1 (surface is totally covered by one layer of solutes). Additionally, Langmuir presumed that the solutes do not react with each other. Hence, the adsorption rate or the sticking probability, respectively, is proportional to  $1 - \theta$ . The desorption rate is proportional to  $\theta \exp[-E_a/RT]$ . The Boltzmann factor,  $\exp[-E_a/RT]$ , is typical for thermally activated process. It expresses the probability of one atom or molecule accumulating the additional energy  $E_a$  to overcome a barrier [33]. In equilibrium of adsorption and desorption, the according rates are equal and one obtains the Langmuir isotherm

$$\theta = \frac{Bp}{1 + Bp}, \quad (2.10)$$

where  $\theta$  is the surface coverage factor,  $B = B_0 \exp[-E_B/RT]$  is a temperature-dependent material constant reflecting the bond strength of the solute, and  $p$  is the pressure in the gas phase.

Multi-layer adsorption reflects the ability of solutes to stick on already adsorbed solute layers. While mono-layers are physisorbed or chemisorbed, the following layers are condensed gases [30]. Brauner, Emmett and Teller (BET) have developed a model to describe this process. They presumed, that the next layer can only grow if the underlying layer is fully covered. Hence, the adsorption rate is again proportional to  $1 - \theta$ . The desorption process follows the laws of evaporation. The derived surface coverage factor is described by the BET isotherm [30]

$$\theta = \frac{r_{\text{BET}} p}{(p_s - p) [1 + (r_{\text{BET}} - 1) p/p_s]}, \quad (2.11)$$

where  $r_{\text{BET}}$  is the ratio of the sticking times of adsorption and condensation layer,  $p$  is the gas pressure,  $p_s$  is the vapor saturation pressure.

Considering  $\theta \propto C$ , the Langmuir isotherm (2.10) and the BET isotherm (2.11) can be modified respectively to

$$C = \frac{S^* B p}{1 + B p} \text{ and } C = \frac{S^{**} r_{\text{BET}} p}{(p_s - p) [1 + (r_{\text{BET}} - 1) p/p_s]}, \quad (2.12)$$

where  $S^*$  and  $S^{**}$  are material constants. Both isotherms describe the dependency of the surface concentration on the pressure at a constant temperature. The functions are schematically plotted in figure 2.4-b and -d, respectively. The Langmuir isotherm approaches a horizontal asymptote for  $p \rightarrow \infty$ . Similarly to the Langmuir-isotherm, the BET isotherm first converges a saturation region. Near the vapor saturation pressure, the concentration becomes infinity.

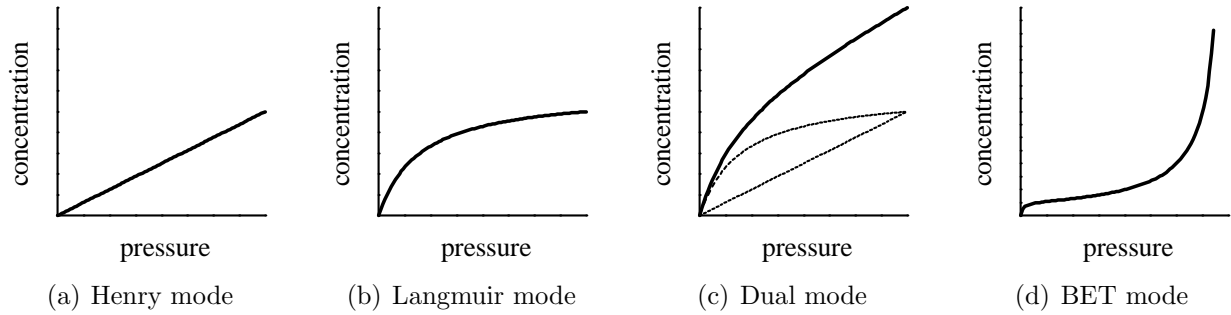


**Figure 2.4:** Sorption modes

In both models describing the mono-layer and the multi-layer adsorption, the concentration is direct proportional to the gas pressure for  $p \rightarrow 0$ . This behavior is expressed by Henry's law:

$$C = S p, \quad (2.13)$$

where  $S$  is called solubility or Henry's constant. The Henry sorption mode is plotted in figure 2.4-a. The solubility includes the probability term for thermally activated processes and is mathematically expressed by the Arrhenius equation

$$S = S_0 e^{-E_S/RT}, \quad (2.14)$$

where  $S_0$  is a temperature-independent but gas-dependent material constant, and  $E_S$  is the activation energy of sorption.

The combination of the Henry and Langmuir isotherms is called Dual mode (see figure 2.4-c). Its importance is described in 2.3.3.

### 2.3.2 Sorption in Metals

The adsorption of gases on metal surfaces can be physisorption or chemisorption. According to Fromm [31], chemisorption is particularly present at active centers on the surface like defects, grain boundaries, corners and edges. In general, the activities of the centers can vary, i.e. the surface is energetically heterogeneous. Depending on the gas type, the adsorption process exhibits different behaviors. In particular, a difference is observed between one and two-atomic gases.

Several publications [31; 34–37] describe the absorption process of two-atomic gases like hydrogen. The molecules first adsorb physically on the surface. The molecules dissociate in a second step and become chemically adsorbed. The adsorbed gas atoms exchange their surface place with the first interstitial layers within the solid (absorption). These reaction steps always exist in both directions, i.e. molecular adsorption counteracts desorption, surface dissociation counteracts recombination. The sum of the reaction steps lead to Sievert's law

$$C = S_S \sqrt{p}, \quad (2.15)$$

where  $S_S$  is the solubility of the dissociative absorption or Sievert's constant.

The absorption process of one-atomic gases like helium in metals is rarely investigated. The process is treated as a sequence of physisorption and movement from the surface to interstitial or vacancy sites within the solid [31]. The relationship between surface concentration and gas pressure is commonly modeled by Henry's law (2.13).

Equations (2.13) and (2.15) are valid as long as gases can be considered to be ideal and to follow equation (2.2). At high pressures and low temperatures, gases show a non-ideal behavior. There, the pressure must be substituted by the fugacity,  $f$  [25; 26]. A simple form of the fugacity is derived from the Abel-Noble equation of state [38–40]

$$f = p \exp \left( \frac{p b}{R T} \right),$$

where  $b$  is the co-volume. In light of the feasible state limits<sup>1</sup> in this work, the relative error when using  $p$  instead of  $f$  is less than 2 %. SanMarchi et al. state that the real gas behavior must only be considered at pressures greater than 150 bar [39].

### 2.3.3 Sorption in Polymers

The absorption process in polymers is independent from the gas type, although the absorption rate varies with the size of the solute. Contrary to metals, two-atomic gases do not dissociate on the surface.

The surface of glassy amorphous polymers ( $T < T_G$ ) can be modeled by a perfect surface coexisting with holes [23; 40; 41]. Elliott [41] explains the existence of the holes with free volume that is frozen into the structure at the glass transition. This surface type is modeled by the Dual sorption mode. While Henry's law (2.13) represents the perfect surface, holes are modeled by the Langmuir isotherm (2.12):

$$C = S p + \frac{S^* B p}{1 + B p}$$

The concentration is direct proportional to  $p$ , for  $p \rightarrow 0$ , as depicted in figure 2.4-c. In this case, the Dual mode can be replaced by Henry's law. In the majority of the reviewed publications about permeation in polymers, Henry's law is employed. In these publications, the gas pressure was near the ambient pressure. Raffaelli [24] even found that the  $H_2$  solubility in CFRP at  $T = 77$  K and  $T = 295$  K is constant for  $p = 0 \dots 11$  bar.

Although this work does not investigate the permeation in rubbery polymers ( $T > T_G$ ), the absorption mode is reviewed for completeness. The absorption of gas molecules is mostly described by the BET isotherm (2.11) or the derived Flory-Huggins-Theory [40; 42]. Again, a direct proportionality between the surface concentration and the applied pressure can be observed for low pressures.

---

<sup>1</sup>The two considered states are ( $p = 8$  bar,  $T = 295$  K) and ( $p = 2$  bar,  $T = 20$  K). The co-volume of hydrogen is  $b = 15.5 \text{ cm}^3/\text{mol}$  [38].

### 2.3.4 General Sorption Equation

The sorption of gases in metals is described by either Henry's law (2.13) or Sievert's law (2.15), depending on the existence of dissociation. The sorption of gases in polymers is mostly expressed by Henry's law. In order to summarize both Henry's and Sievert's law into one equation, the pressure exponent  $n$  is introduced

$$C = S p^n, \text{ with } n = \begin{cases} 1 & \text{if the gas does not dissociate} \\ 0.5 & \text{if the gas dissociates} \end{cases}. \quad (2.16)$$

Equation (2.16) is used throughout this thesis and is termed sorption equation.

## 2.4 Diffusion

### 2.4.1 Phenomenological Description

Transport problems can be described by introducing driving forces [43]. Well known driving forces are for instance the gradient of electrical potential, the temperature gradient, and the gradient of chemical potential. The belonging fluxes and transport phenomena are the current density (Ohm's law), the heat flux (Fourier's law) and the mass flux / diffusion (Fick's first law), respectively.

The general relationship between fluxes  $J$  and forces  $X$  can be represented by a polynomial expression  $J = a_1 X + a_2 X^2 + \dots$ . Kirkaldy [43] states that from kinetic theory and experiments it indicates that the linear form,  $J = a X$ , provides an accurate description of most transport processes.

In thermodynamic transport processes, the driving forces can be summarized by chemical potential gradients, thermal gradients and fields, e.g. the gravity field. In this work, diffusion processes are considered to take place in an isothermal, isobaric and field-free system. Introducing the flux and the driving forces in vector notation, the diffusion transport is [43; 44]

$$\mathbf{J} = -\mathbf{a} \nabla \mu,$$

where  $\mathbf{a}$  is a matrix of phenomenological coefficients and  $\mu$  is the chemical potential. The matrix  $\mathbf{a}$  can be replaced, when considering the expression of the flux in (2.9),  $\mathbf{J} = C \mathbf{v}$ . The average velocity of a particle being under the influence of the generalized force  $\nabla \mu$  is  $\mathbf{v} = -\beta \nabla \mu$  [45], where  $\beta$  is the atom mobility coefficient. The expression of the flux becomes

$$\mathbf{J} = -C \beta \nabla \mu. \quad (2.17)$$

Equation (2.17) describes diffusion processes in general. It covers diffusion in different materials as well as the presence of reactions. In most cases, however, the chemical potential can be substituted by the concentration.

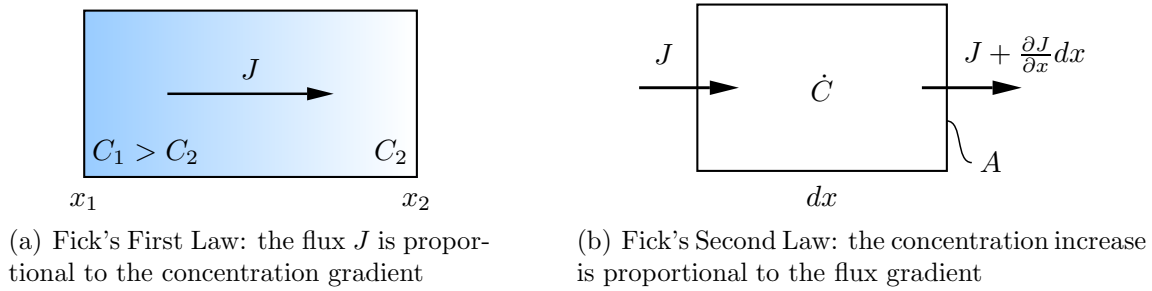


**Figure 2.5:** One-dimensional description of Fick's Laws. The first law gives information about the diffusion rate. The second law denotes the change of the concentration.

Considering a gas dissolved in a condensed phase, the chemical potential is [31]

$$\mu = n \mu^0 + RT \ln \frac{C}{C_{\max}}, \quad (2.18)$$

where  $n$  is the pressure exponent of (2.16),  $\mu^0$  is the standard chemical potential of the non-dissociated gas at a standard pressure and  $C_{\max} = S p_{\max}^n$  is the saturation concentration. Substituting (2.18) in (2.17) one obtains

$$\mathbf{J} = -RT \beta \nabla C.$$

Replacing the term  $RT \beta$  by the new variable  $D$  one derives

$$\mathbf{J} = -D \nabla C. \quad (2.19)$$

Equation (2.19) is entitled Fick's first law and is schematically illustrated in figure 2.5-a. The diffusion flux is proportional to the concentration gradient. The proportionality factor  $D$  is called diffusivity or diffusion coefficient. The diffusivity is a material variable and in general concentration and temperature dependent. It expresses the ability of atoms or molecules to move in a solvent material under the influence of a concentration gradient.

The diffusion movement of the dissolved atoms leads in general to a change of the concentration distribution. Considering the mass conservation principle (see figure 2.5-b), the transient state is described by the second law of Fick:

$$\frac{\partial C}{\partial t} = D \nabla^2 C. \quad (2.20)$$

In the stationary state,  $\frac{\partial C}{\partial t} = 0$ , the flux is constant. Integrating (2.20) for this state, the diffusion flux in one dimension is:

$$\frac{\partial C}{\partial t} = 0 \longrightarrow J(x) = J_{ss} = -D \frac{\Delta C}{\Delta x}. \quad (2.21)$$

### 2.4.2 Atomistic Description

Diffusion is a mass transport process. Driven by the gradient of the chemical potential, or by the concentration gradient in homogeneous materials, dissolved particles move through the bulk. The mechanism of this movement depends on the bulk material and on the diffusing particles. The diffusion of gases like hydrogen and helium in plastics and metals is important in this work and is explained in the following.

#### Diffusion in polymers

It is commonly assumed that diffusion in plastics takes place in free volumes [28; 42]. The diffusion is a stochastic movement of dissolved particles in these free volumes. If the local number of particles is efficiently high, i. e. a concentration gradient is present, then the movement becomes directed.

The jump from one cavity to another involves the overcoming of barriers and requires the activation energy,  $E_D$ . The probability of one atom or molecule accumulating the additional energy to overcome the barrier is proportional to  $e^{-E_D/RT}$ , as deduced in 2.3.1. The jump from one into another free volume also presumes the probability of finding a cavity. Elliot [41] and Wessling [42] mathematically described this probability by  $e^{-b^*/\nu_f}$ , where  $b^*$  is a function of the volume required by the solute, and  $\nu_f$  is the fractional free volume (2.1) of the polymer. The term states that the probability of finding a cavity increases with increasing free-volumes and decreasing gas size. Thran et al. [46] have carried out an extensive correlation between diffusivities and the fractional free volume for a variety of gases. They confirmed the assumption above but also found that small gases like helium and hydrogen also diffuse through the nonfluctuating interstitial free volume.

The rate of diffusion and hence the diffusivity is proportional to jump probabilities. The diffusivity is then expressed by a probability term of finding a hole and the activation term for overcoming barriers:

$$D \propto e^{-b^*/\nu_f} e^{-E_D/RT}.$$

The first term only includes material properties of the bulk and the dissolved gases. Introducing the temperature-independent material constant  $D_0$  one derives:

$$D(T) = D_0 e^{-E_D/RT}. \quad (2.22)$$

Typical values of  $E_D$  in polymers are between 15 kJ/mol and 29 kJ/mol [47; 48].

#### Diffusion in metals

Similar to polymers, the diffusion in metals is a thermally activated, stochastic motion of dissolved particles overcoming barriers. At high concentrations, the diffusion becomes directed. The diffusivity is described by the Arrhenius-type equation (2.22). The diffusion in metals mainly takes place in interstitial sites or vacancies of the lattice. The general

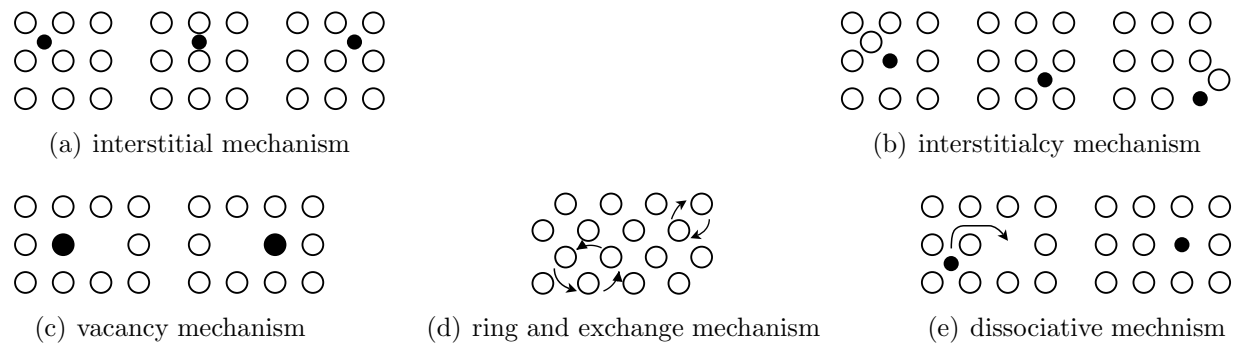


**Figure 2.6:** Mechanisms of diffusion in metals. Source: [45; 50]

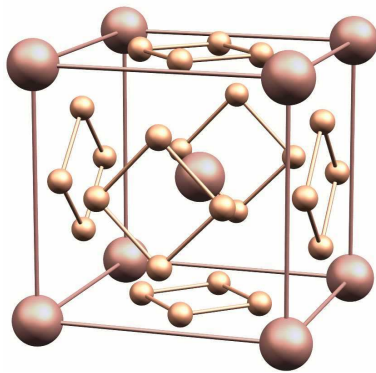


**Figure 2.7:** Tetrahedral interstitial sites of bcc lattice

mechanisms of diffusion in metals are described in [21; 49] and graphically summarized in figure 2.6.

The interstitial mechanism is characterized by the jump from one interstitial site to the adjacent one. The jump can be modeled with the help of the elasticity theory. The diffusing atoms must be relatively small to be able to move through those of the solvent matrix. This mechanism is only valid for few gases and carbon. Exemplarily, figure 2.7 illustrates the tetrahedral interstitial sites of the bcc lattice. The distance between two adjacent interstitial sites is the lattice constant divided by  $\sqrt{8}$ , hence between  $1.0 \text{ \AA}$  and  $1.17 \text{ \AA}$  [51]. The distance between two nearest neighbor interstitial sites in the fcc lattice is  $2.5 \dots 2.9 \text{ \AA}$ .

The vacancy mechanism is very important, because every solid contains vacancies. The vacancy concentration increases with increasing temperature. This mechanism can be used to describe self diffusion, small and large atom diffusion.

The interstitialcy and ring diffusion mechanisms are mainly important for large solutes. The ring mechanism is realistic but not dominating. In the interstitialcy mechanism, the atom dissociates from its vacancy and migrates as interstitial into another vacancy. The interstitialcy mechanism is dominating in self diffusion.

The dissociative mechanism is characterized by alternating atom jumps from a vacancy to an interstitial site and reverse. This mechanism is predominating in small atom diffusion.

Considering hydrogen in metals, only the interstitial, vacancy, and dissociative diffusion

were reported [21; 31; 49; 51–53]. Fromm [31] even stated that only the interstitial site diffusion must be considered. Wipf [51] agreed that hydrogen is mainly existing as an interstitial in metals, but he emphasized the importance of traps in the crystal. The traps are formed by lattice defects like vacancies or dislocations. In general, the traps reduce the diffusivity. Young and Scully [52] investigated the hydrogen diffusion and trapping in high purity aluminum. They observed three distinct diffusion mechanisms with the activation energies 15, 44, and 85 kJ/mol. These diffusion mechanisms are associated with interstitial lattice sites, dislocations, and vacancies, respectively.

The diffusion of inert gases like helium in metals are rarely investigated. Hanika [28] stated that inert gases diffuse extremely badly through metals. Borg and Dienes [49] reviewed the helium diffusion in metals like nickel, gold, aluminum, tungsten and molybdenum. They found that at elevated temperatures the activation energies are much higher than expected for interstitial diffusion. Hence, they concluded that He is predominantly present as a substitutional atom. Borg and Dienes ruled out the vacancy mechanism and stated that helium diffusion follows the dissociative mechanism. Adams and Wolfer [54] investigated the diffusion of helium in nickel. Reviewing measurements and comparing them with their calculations, they concluded that helium primarily exists in substitutional sites. From there, helium may diffuse by interstitial, vacancy or dissociative mechanism. The according activation energies are 52, 126 and 243 kJ/mol, respectively.

The jump frequency of the solute atoms in interstitial sites is the highest compared to other diffusion mechanisms like vacancy and dissociative diffusion. This implies a rapid diffusion process, respectively high diffusivities [49; 55].

### 2.4.3 Solution of Fick's Laws

The two laws of Fick describing diffusion in a homogeneous material, (2.19) and (2.20), are analytically solved for the one-dimensional diffusion in a membrane.

Let there be a homogeneous membrane with area  $A$  and thickness  $l$ , where  $l \ll \sqrt{A}$ . Hence, the diffusion process can be considered as one-dimensional and Fick's laws derive to

$$J = -D \frac{\partial C}{\partial x} \quad \text{and} \quad \frac{\partial C}{\partial t} = D \frac{\partial^2 C}{\partial x^2},$$

where  $x$  is the coordinate in thickness direction. The concentration at the feed side,  $x = 0$ , and permeate side,  $x = l$ , may be termed  $C_f$  and  $C_p$ , respectively. Initially, the concentration is zero throughout the material:  $C(x, t < 0) = 0$ . At  $t = 0$ , a constant concentration is applied at the feed side:  $C_f(t \geq 0) = C_f^0$ . Owing to this change of charge, a flow from the feed side to the permeate side starts and  $C_p$  changes with time. Crank [56] calculated the flux at the permeate side, if  $C_p \approx 0$  and  $C_p \ll C_f$  for all  $t$ :

$$J(t) = \frac{D C_f^0}{l} \left[ 1 + 2 \sum_{n=1}^{\infty} (-1)^n \exp \frac{-D n^2 \pi^2}{l^2} t \right]. \quad (2.23)$$



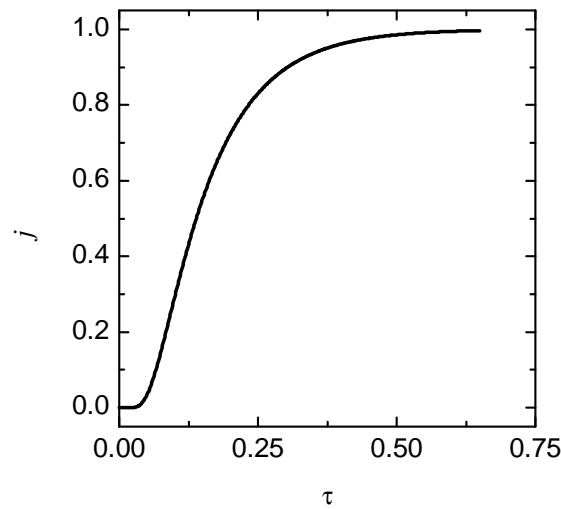


**Figure 2.8:** Fick curve: normalized flux as a function of the dimensionless time. The diffusion flux through a homogeneous membrane was determined by solving Fick's laws.

The steady-state flux is

$$J_{ss} = \lim_{t \rightarrow \infty} J(t) = \frac{D C_f^0}{l} \quad (2.24)$$

The dimensionless form of (2.23) is advantageous to compare different materials. Introducing the normalized flux

$$j = J/J_{ss} \quad (2.25)$$

and the dimensionless time

$$\tau = D t / l^2, \quad (2.26)$$

equation (2.23) derives to

$$j(\tau) = 1 + 2 \sum_{n=1}^{\infty} (-1)^n \exp(-n^2 \pi^2 \tau). \quad (2.27)$$

Equation (2.27) is plotted in figure 2.8. The normalized flux is initially zero, increases afterwards to approach the horizontal asymptote  $j = 1$ . Because of its importance as a reference, the function is called Fick curve throughout this thesis. If any  $j(\tau)$  curve is like the Fick curve, the according material shows Fickian flux-time behavior.

#### 2.4.4 Grain Boundary Diffusion

Grain boundaries are internal interfaces that represent sharp crystallographic orientation changes. They play an important role because they affect material properties. Examples are the stress corrosion cracking in Pb battery electrodes, the creep strength in high temperature alloys and the weld cracking [57]. The diffusion of particles along grain boundaries is of particular interest.

Although the diffusion in grain boundaries is not fully understood, several publications agree in that it is much faster than in the crystals. Brass and Chanfreau [58] investigated the permeation of hydrogen in polycrystalline nickel with grain sizes of 25  $\mu\text{m}$  and 150  $\mu\text{m}$ . The diffusivity along the grain boundaries was found to be 2 – 7 times larger than the lattice diffusivity. Brass and Chanfreau remarked that ratios in the range of 8 – 100 can be found in the literature. Shmayda et al. [59] investigated the hydrogen permeation in electroplated nickel on Ti-substrates. The diffusivity varied with the surface texture, i. e. with the grain sizes. The  $\text{H}_2$  diffusivity in nickel with textured surface was 1.3 to 3.3 times higher than that of untextured nickel. Sohn [53] even estimated that the grain boundary diffusivity is  $10^6$  times greater than the grain diffusivity.

The diffusion mechanism in grain boundaries is different than in grains. Sohn [53] and Cerezo [50] agreed in that grain boundary diffusion is primarily a vacancy motion. This assumption was based on the measurements of the diffusion activation energies. Cerezo [50], Hauffe [60] and Argen [61] reported a generally lower activation energy in grain boundaries than in the crystal. Hauffe found that the activation energy of silver self diffusion in grain boundaries and grains are 20 kJ/mol and 46 kJ/mol, respectively [60]. These values agree well with the rule of thumb given by Argen [61]:

$$\frac{E_{a,G}}{E_{a,B}} \approx 2,$$

where  $E_{a,G}$  and  $E_{a,B}$  are the diffusion activation energy in grains and grain boundaries, respectively.

The diffusion through grain boundaries was classified by Harrison [62] regarding the diffusion distance of the grain. The diffusion distance is proportional to  $\sqrt{D_G t}$ , where  $D_G$  is the grain diffusivity and  $t$  is the diffusion time.

Harrison type A is present, if the diffusion path is much greater than the width of the grain,  $b_G$ :

$$\sqrt{D_G t} \gg b_G. \quad (2.28)$$

Inequality (2.28) also represents the condition, that the migration time between two grain boundaries is much less than the diffusion time  $t$ . Type A kinetics are dominating, if (1) the diffusivities of grain and grain boundary are approximately equal, (2) the diffusion time is large and (3) the grain boundary distance is relatively small. The apparent diffusion coefficient of the overall solid is

$$D = 3 \frac{b_B}{b_G} D_B + \left(1 - 3 \frac{b_B}{b_G}\right) D_G, \quad (2.29)$$

where  $b_G$  and  $b_B$  are the widths of the grain and the grain boundary, respectively, and  $D_G$  and  $D_B$  are the diffusivities of the grain and the grain boundary, respectively. The diffusion process itself can be described by Fick's first law.

Harrison type C describes the diffusion under the condition

$$\sqrt{D_G t} \ll b_B. \quad (2.30)$$

This condition implies that the diffusion distance in the bulk is relatively small compared to the width of the grain boundary. Hence, the particles do not exchange from the bulk into the grain boundary. Type C is dominating at short times, or very high grain boundary diffusivities. The apparent diffusivity is

$$D = \left(3 \frac{b_B}{b_G}\right)^2 D_B, \quad (2.31)$$

and again Fick's first law can be obeyed.

Harrison type B diffusion is the most general situation. It is established if the conditions of type A and C are violated. Diffusion is present in the grain and in the grain boundary, where  $D_B \gg D_G$ . An apparent diffusivity cannot be determined and Fick's laws are not observed.

In any system in which grain boundary diffusion can be studied continuously from very short to very long times, the behavior will initially be type C, and will develop into type B and ultimately type A.

Extensive mathematical studies on grain boundary diffusion were conducted by Kaur, Mishin and Gust [63]. The introduced models included isolated, parallel or mesh grain boundaries. Mathematical treatments were carried out using only the isolated or the parallel grain boundary model. Although many models exist to describe the stationary permeation rate, only few models also consider the transient state.

One of the analyses considering the transient state is based on the model of Hwang and Balluffi [64]. The analyses take Harrison type C diffusion through parallel grain boundaries into account. At  $t = 0$ , a constant concentration is applied at the feed side of the membrane. The particles can accumulate at the surface of the permeate side. Presuming fast surface diffusion, the normalized flux is

$$j = 1 - 2 \sum_{n=1}^{\infty} \exp(-\theta_n^2 \tau_B) \frac{(\theta_n^2 + H^2) \sin \theta_n}{(\theta_n^2 + H^2 + H) \theta_n}, \quad (2.32)$$

where  $\tau_B = \frac{D_B t}{l^2}$  is the dimensionless time, and  $\theta_n$  is the  $n$ th root of  $\theta \tan \theta = H$ . The dimensionless variable  $H$  is defined as

$$H = \frac{S_S}{S_B} \frac{b_B}{b_G} \frac{l}{l_S},$$

where  $S_S$  and  $S_B$  are the solubilities of the accumulation surface and the grain boundary, respectively,  $b_B$  and  $b_G$  are the widths of the boundary and the grain, respectively, and  $l$  and  $l_S$  are the thicknesses of the membrane and the accumulation surface, respectively.

Figure 2.9 shows the different graphs of (2.32) for three values of parameter  $H$ . The dimensionless flux-time behavior is different from that of Fick. In particular, the flux already increases at a very small dimensionless time and the function is less curved.

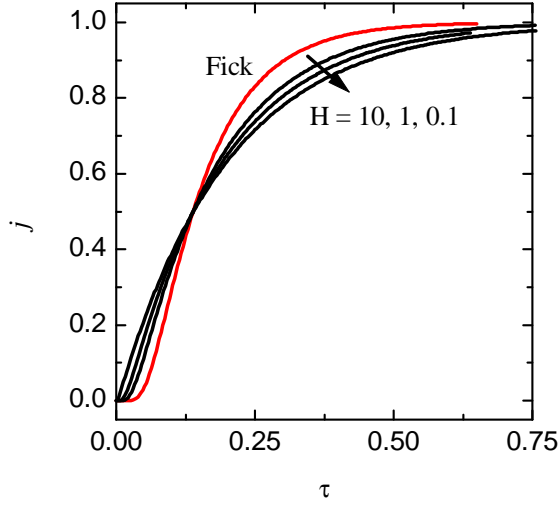


**Figure 2.9:** Simulation of diffusion through grain boundaries according to Hwang and Balluffi [64]. The flux is calculated by (2.32) for three parameters  $H$ . The dimensionless time  $\tau_B$  was scaled to a new time  $\tau$  to fit the Fick curve.

The definition of the parameter  $H$  gives rise to questions. Equal values of  $H$  and hence equal  $j(\tau)$  curves exist if the ratio  $b_B/b_G$  and the remaining variables are kept constant. For example, equal diffusion behavior would be present if  $b_B : b_G : l = 1 : 10 : 100$  or  $b_B : b_G : l = 100 : 1000 : 100$ . However, this behavior is not expected for Harrison type A or B diffusion. Consequently, the transient solution of Hwang and Balluffi may only be applied in few cases.

## 2.5 Permeation

### 2.5.1 Phenomenological Description

In general, permeation is the overall process of a fluid crossing a membrane caused by a pressure difference. In this work, a gas ( $H_2$  or He) permeates a solid as illustrated in figure 2.10. Permeation consists of three processes. Firstly, the gas of the feed side dissolves into the solid, as described in 2.3. Secondly, the dissolved gas diffuses into the bulk, driven by the concentration gradient, refer to 2.4. Finally, the particles being diffused to the permeate side desorb from that surface.

Considering the stationary state and presuming the feed pressure being much greater than the pressure at the permeate side,  $p_f \gg p_p$ , the permeation flux is derived by substituting (2.16) into (2.21)

$$J_{ss} = D S \frac{p_f^n}{l}.$$

Defining the permeability

$$P := D S, \tag{2.33}$$

one obtains

$$J_{ss} = P \frac{p_f^n}{l}. \tag{2.34}$$

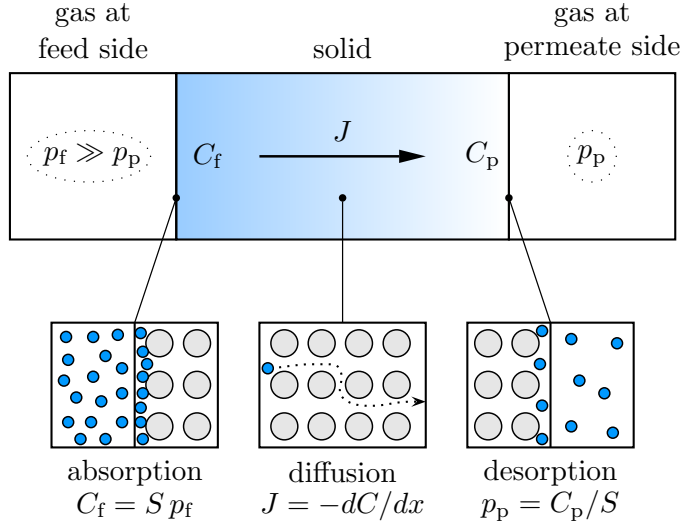


**Figure 2.10:** Schematic diagram of one-dimensional permeation without dissociation. Permeation implies three processes: absorption at the feed side, diffusion, and desorption at the permeate side.

Equation (2.34) relates the flux to the driving pressure gradient. The permeability expresses the material ability to allow gases permeate through a membrane. Considering (2.14) and (2.22), the permeability as defined in (2.33) is expressed by the Arrhenius equation

$$P(T) = P_0 e^{-E_P/RT}, \quad (2.35)$$

where  $P_0$  is a temperature-independent material constant and  $E_P = E_S + E_D$  is the permeation activation energy.

Equation (2.34) is a valid approximation to represent  $H_2$  or  $He$  permeation through metals or polymers in the pressure and temperature range considered in this thesis. Hydrogen permeation in metals, however, is more generally described by the dimensionless permeation equation derived by Ali-Khan et al. [34; 36; 37]

$$W'^2 u^4 + 2 W' u^3 + 2 u^2 = 1, \quad (2.36)$$

where the dimensionless number  $W'$  characterizes the permeation regime and includes the surface roughness factor, the recombination factor, the diffusivity, the thickness, the solubility and the feed pressure. The dimensionless number  $u$  is the ratio of the permeate to the feed concentration. In the high pressure limit, the classical Fickian permeation equation ( $J \propto \sqrt{p_f}$ ) is derived. In the low pressure limit, the recombination process is dominating, and the diffusion is very rapid. In this case, the flux is proportional to the driving pressure and only dependent on surface parameters, i.e. independent from the diffusivity. San Marchi et al. [39] stated that (2.34) is valid and can be used instead of (2.36) for stainless steels, if the feed pressures are greater than 10 Pa and less than  $5 \cdot 10^7$  Pa, and/or the temperature is less than 1373 K.

### 2.5.2 Experimental Determination of $P$ and $D$

A variety of methods exist to experimentally determine the permeability and diffusivity of materials. In general, methods with an initial nonequilibrium setting and subsequent

measuring of the time to reach the equilibrium are established. Examples of these are permeation methods, electrochemical methods (H detection in conductive materials using a Devanathan-Stachurski cell [59; 65]) and coloration methods (H-detection by  $\text{WO}_3$  films [66]). Further transient methods are described by Völkl and Alefeld [67]. On the other hand, three methods are used during stationary diffusion of hydrogen in metals: quasielastic neutron scattering, nuclear magnetic resonance and the Mössbauer effect [68]. However, only the diffusivity but not the permeability is determined in these three techniques.

Two permeation measuring techniques exist that can be used in every gas-membrane combination. On one hand, sorption-desorption tests are performed to directly measure the diffusivity and solubility [69]. The bulk material, mostly a wire or a cuboid, is charged until no further gas is taken up. The subsequent release of the gas is measured. On the other hand, the majority of permeation measurements are performed utilizing the transmission method, which allows the direct determination of  $P$  and  $D$ . The gas is applied to the feed side of a membrane. The flux on the permeate side is measured in either a flowing stream (constant  $p$ ) or a closed chamber (constant  $V$ ).

In this work, the transmission method into a flowing stream is employed. Technically, the permeation flux through the specimen is led into a permanently evacuated chamber. The permeate side of the specimen is considered to be quasi-stationary,  $\partial p/\partial t \approx 0$ . Presuming that no leakage exists, the principle of mass conservation requires that the sum of the gas flows owing to permeation, outgassing and pumping is zero:

$$-Q_T + Q_G + Q_P = 0, \quad (2.37)$$

where  $Q_T$  is the throughput,  $Q_G$  is the outgassing rate, and  $Q_P$  is the permeation gas flow. In most cases, the outgassing can be neglected, if  $Q_G \ll Q_P$  holds valid.

Instead of (2.4), the throughput is represented by the effective pumping speed,  $s_{\text{eff}}$ , of the permeating gas

$$Q_T = s_{\text{eff}} p. \quad (2.38)$$

The effective pumping speed takes the real geometry of the apparatus into account. Hence, the existence of impedances like valves or long pipes is also considered [70; 71]:

$$\frac{1}{s_{\text{eff}}} = \frac{1}{s} + \frac{1}{L},$$

where  $s$  is the nominal pumping speed (2.4) of the permeating gas, and  $L$  is the total conductance of the apparatus. The effective pumping speed is in general depending on the gas, the partial pressure and the temperature. The influence of the temperature can be neglected if that of the measuring instrument is kept constant. The nominal pumping speed is independent from the pressure in the molecular flow state [72]. Hence, the effective pumping speed is not a function of the (partial) pressure in the predominating vacuum regime ( $< 10^{-4}$  mbar).

Replacing  $Q_T$  in the mass conservation law (2.37) by the expression of (2.38) and considering  $Q_G \ll Q_P$ , one obtains:

$$Q_P = s_{\text{eff}} p. \quad (2.39)$$

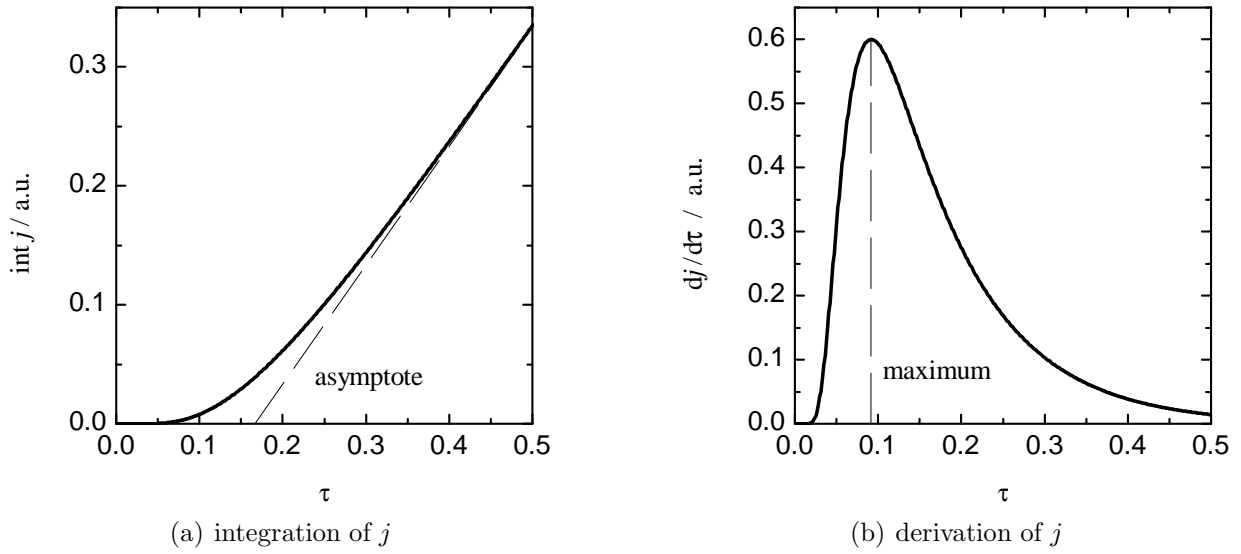


**Figure 2.11:** Integration and derivation of the Fick curve (2.27) with respect to time. In both cases, the characteristic time can be used for determining the diffusivity.

Equation (2.39) correlates the permeation gas flow with the partial pressure of the permeating gas measured in the flowing stream. The proportional factor,  $s_{\text{eff}}$ , must be defined by calibration. In many permeation measurements reported in literature [34; 35; 73–75], however, the permeation flow is calculated using the constant, nominative pumping speed instead of the effective one.

The typical procedure of the permeation measurement into a flowing stream is explained in the following. At  $t < 0$ , the gas concentration of the membrane is near zero. At  $t = 0$ , a constant pressure  $p_f$  is applied at the feed side. The permeate side is permanently kept at UHV, and the flux is recorded. Presuming a homogeneous material and no kinetics in the sorption process, the normalized measured flux is described in 2.4.3, see also figure 2.8. The permeability is calculated by rearranging (2.34):

$$P = \frac{J_{\text{ss}} l}{p_f^n}. \quad (2.40)$$

The diffusivity can be determined in three ways. Firstly, integrating the flux-time curve (2.27), the asymptote of the graph intersects the abscissa at  $\tau_L = 1/6$ , refer to figure 2.11-a. It follows from (2.26) that  $D = l^2/6 t_L$ , where  $t_L$  is the lag time at which the asymptote of the experimental  $J(t)$  curve intersects the abscissa. The accuracy of the lag-time method depends strongly on the drawing of the asymptote and is hence not recommended. Secondly, the derivative of  $j(\tau)$  contains a maximum at  $\tau \approx 0.0918$  (see figure 2.11-b). If  $t_m$  denotes the time at which  $dJ/dt = \text{max}$ , the diffusivity is  $D = 0.0918 l^2/t_m$ . The determination of  $t_m$  and hence of the  $D$  is more accurate than the lag-time method. However, both methods may only be employed if the material shows Fickian behavior. The third method

can always be applied. Thereby, the Fick curve is fitted to the experimental data by the following algorithm

$$[\tau, j]_{\text{Fick}} \circ \left[ \begin{array}{cc} l^2/D & 0 \\ 0 & J_{\text{ss}} \end{array} \right]_{\text{fit parameter}} \longrightarrow [t, J]_{\text{experimental data}} .$$

Knowing  $J_{\text{ss}}$  and  $l$ , only the diffusivity must be varied to fit the experimental data. The relative error of the diffusivity using this method was assessed to be approximately 3 %.

### 2.5.3 Serial and Parallel Permeation

**Serial permeation**, also called multi-layer permeation, is the gas transport through several serial membranes. The total permeability of a material consisting of  $n$  layers is [56]

$$\frac{l}{P} = \sum_{i=1}^n \frac{l_i}{P_i}, \quad (2.41)$$

where  $l_i$  and  $P_i$  are the thickness and permeability of the  $i$ th layer, and  $l$  and  $P$  are the total thickness and permeability, respectively. An analytical expression for the permeation activation energy of the composite of substrate and liner does not exist. However, if the temperature dependent permeabilities of the substrate and the liner are given, the total permeability can be calculated by (2.41) as a function of  $T$ . Subsequently, the activation energy can be determined by (2.35).

In this thesis, the system of two layers consisting of a substrate and a liner is of particular interest. The subscripts s and l may represent the substrate and the liner, respectively. No subscript may represent the composite of substrate and liner. Knowing the permeabilities of substrate and composite, the liner permeability is determined by rearranging the previous equation

$$P_l = l_l \left[ \frac{l}{P} - \frac{l_s}{P_s} \right]^{-1}. \quad (2.42)$$

The reduction of the permeation gas flow owing to the additional liner may be expressed by the barrier constant

$$\iota := \frac{Q}{Q_s}. \quad (2.43)$$

Low values of  $\iota$  represent a good barrier functionality of the liner. Presuming equal areas of the substrate and the liner, (2.43) can be further evaluated when considering (2.7) and (2.34):

$$\iota = \frac{P}{P_s} \frac{l_s}{l} = \left( 1 + \frac{P_s l_l}{P_l l_s} \right)^{-1}. \quad (2.44)$$



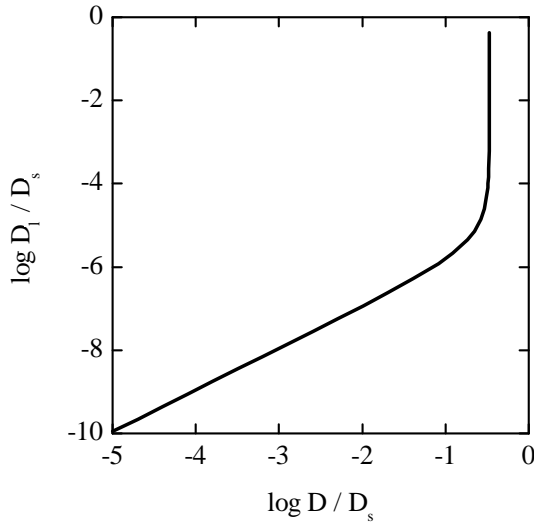


**Figure 2.12:** Liner diffusivity as a function of the total diffusivity in a two-layer material. The equation (2.45) is plotted with the parameters  $\lambda = 300$  and  $\psi = 10^{-5}$ . The function approaches infinity at a certain value of  $D/D_s$ .

The total diffusivity of a two-layer material was analytically deduced by Ash, Barrer and Petropoulos [76]. Assuming the substrate and the composite diffusivity are known, the liner diffusivity can be determined. Introducing the dimensionless variables

$$\lambda = \frac{l_s}{l_l}, \quad \psi = \frac{P_l}{P_s}.$$

the liner diffusivity is

$$\frac{D_l}{D_s} = (1 + 3\psi\lambda) \left( (1 + \psi\lambda)(1 + \lambda)^2 \frac{D_s}{D} - \lambda^2(3 + \psi\lambda) \right)^{-1}. \quad (2.45)$$

Figure 2.12 shows the typical graph of equation (2.45). It is interesting, that the function is not defined for all values of  $D$ . The total diffusivity is always less than a certain value independent from the liner diffusivity

$$D < \frac{(1 + \psi\lambda)(1 + \lambda)^2}{\lambda^2(3 + \psi\lambda)} D_s \neq f(D_l). \quad (2.46)$$

**Parallel permeation.** Permeation through parallel materials occurs for instance in grain boundaries. Let  $b_1$  and  $b_2$  be the widths of two materials and  $P_1$  and  $P_2$  the according permeabilities. The overall permeability is given by [50]:

$$P = \frac{b_1}{b_1 + b_2} P_1 + \frac{b_2}{b_1 + b_2} P_2, \quad (2.47)$$

Equation 2.47 is derived by assuming equal steady-state fluxes in both materials. The overall diffusivity can only be determined if equal solubilities exist in both materials.

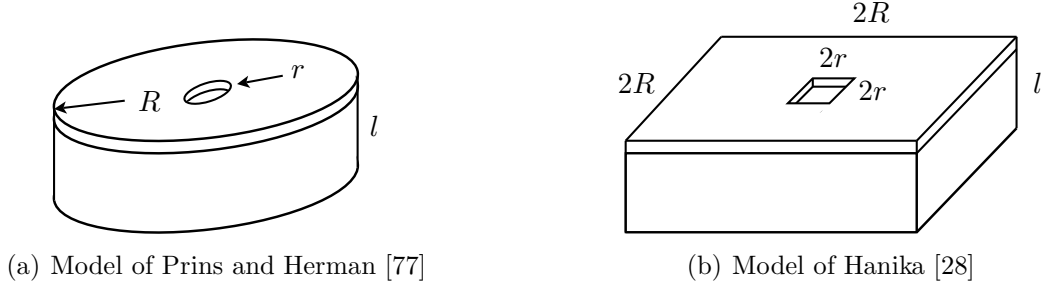


**Figure 2.13:** Two models describing permeation through defectively coated substrates.

#### 2.5.4 Permeation through Substrates with Defective Liners

The permeation of gases through imperfectly coated foils has been an issue in the packaging industry for years. This topic has been the objective of works as early as 1959 [77] and is still being investigated [28; 78]. All reviewed models only considered the stationary condition.

Prins and Herman [77] investigated the permeation through a substrate owing to a concentration difference. One side of the substrate with thickness  $l$  is covered by an impermeable metal layer containing a circular hole with radius  $r$ . Figure 2.13-a explains the model schematically. The defect can be treated separately if the number of holes per area is very low, i. e.  $r/R \ll 1$ .

The permeation flux through the hole was determined by calculating the exact solutions for the cases  $l \ll r$  and  $r \ll l$ . The approximation for the intermediate case is

$$J_{\text{hole}} = -D \frac{\Delta C}{l} \left( 1 + 1.18 \frac{l}{r} \right), \quad \text{for } \frac{l}{r} > 0.3 \text{ and } \frac{l}{r} \ll 1,$$

or with regard to (2.43):

$$\iota = \frac{r^2}{R^2} \left( 1 + 1.18 \frac{l}{r} \right). \quad (2.48)$$

Rossi and Nulman [79] investigated the same problem and found

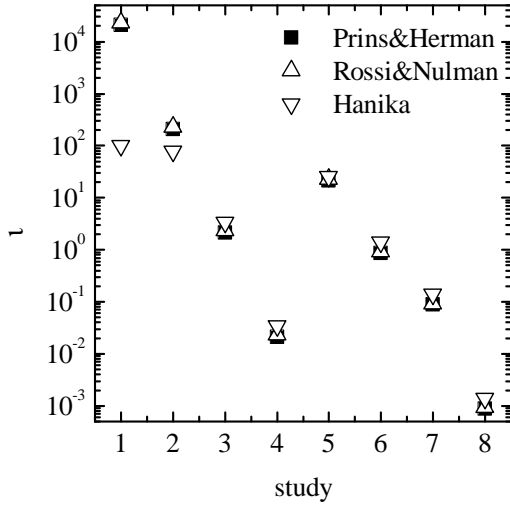
$$\iota = \frac{4rl}{\pi R^2}, \quad \text{for } \frac{l}{r} \gg 1 \quad \text{and} \quad \iota = \frac{r^2}{R^2}, \quad \text{for } \frac{l}{r} \ll 1. \quad (2.49)$$

It can be derived that (2.48) and (2.49) are equal within a certain accuracy.

Hanika [28] summarized several literature models describing permeation through defective metal coatings on polymers. The reviewed models are semi-analytical [77; 80], empirical [81; 82] and numerical [79; 83–85]. They all have in common that the coating contains defects (holes or cracks). The metal itself is treated as impermeable. The models reflecting the experimental results only to a certain accuracy, Hanika developed his own 3D finite-difference model. The model is schematically illustrated in figure 2.13-b. Squared

**Table 2.2:** Comparison of the models to simulate permeation through defectively coated substrates.

study	$r$	$R$	$l$	$r/R$	$l/r$	$\iota$ (2.48)	$\iota$ (2.49)	$\iota$ (2.50)
1	1 nm	10 nm	1.8 mm	$1 \cdot 10^{-1}$	$1.8 \cdot 10^6$	$2.1 \cdot 10^4$	$2.3 \cdot 10^4$	$1.0 \cdot 10^2$
2	1 nm	100 nm	1.8 mm	$1 \cdot 10^{-2}$	$1.8 \cdot 10^6$	$2.1 \cdot 10^2$	$2.3 \cdot 10^2$	$7.8 \cdot 10^1$
3	1 nm	1 $\mu$ m	1.8 mm	$1 \cdot 10^{-3}$	$1.8 \cdot 10^6$	$2.1 \cdot 10^0$	$2.3 \cdot 10^0$	$3.4 \cdot 10^0$
4	1 nm	10 $\mu$ m	1.8 mm	$1 \cdot 10^{-4}$	$1.8 \cdot 10^6$	$2.1 \cdot 10^{-2}$	$2.3 \cdot 10^{-2}$	$3.5 \cdot 10^{-2}$
5	1 $\mu$ m	10 $\mu$ m	1.8 mm	$1 \cdot 10^{-1}$	$1.8 \cdot 10^3$	$2.1 \cdot 10^1$	$2.3 \cdot 10^1$	$2.6 \cdot 10^1$
6	1 $\mu$ m	50 $\mu$ m	1.8 mm	$2 \cdot 10^{-2}$	$1.8 \cdot 10^3$	$8.5 \cdot 10^{-1}$	$9.2 \cdot 10^{-1}$	$1.4 \cdot 10^0$
7	40 $\mu$ m	100 $\mu$ m	1.8 mm	$4 \cdot 10^{-2}$	$4.5 \cdot 10^1$	$8.7 \cdot 10^{-2}$	$9.2 \cdot 10^{-2}$	$1.4 \cdot 10^{-1}$
8	40 $\mu$ m	1 mm	1.8 mm	$4 \cdot 10^{-3}$	$4.5 \cdot 10^1$	$8.7 \cdot 10^{-4}$	$9.2 \cdot 10^{-4}$	$1.4 \cdot 10^{-3}$

**Figure 2.14:** Comparison of the models to simulate permeation through defectively coated substrates. The barrier constant is plotted versus the study parameters listed in table 2.2.

coating defects of width  $2r$  are separated by the characteristic defect distance  $2R$ . The advantage of this model is that interactions of holes are taken into account. The barrier constant is

$$\iota = \frac{(r/R)^2}{1 - \exp(-0.507 r/l) + 0.01 (r/R)^2}. \quad (2.50)$$

The three presented models are compared by calculating the barrier constants of eight geometry constellations. The study parameters and the results are listed in table 2.2. The chosen parameters are representative for expected defects (study 1 – 4: “empty“ grain boundary, 5 – 6: microcracks, 7 – 8: holes). The results of the three models are similar as presented in figure 2.14. The model of Hanika deviates from the two others only for great ratios between the substrate thickness and the defect distance. This behavior is attributed to the influence of neighboring holes which is taken into account only in his model.

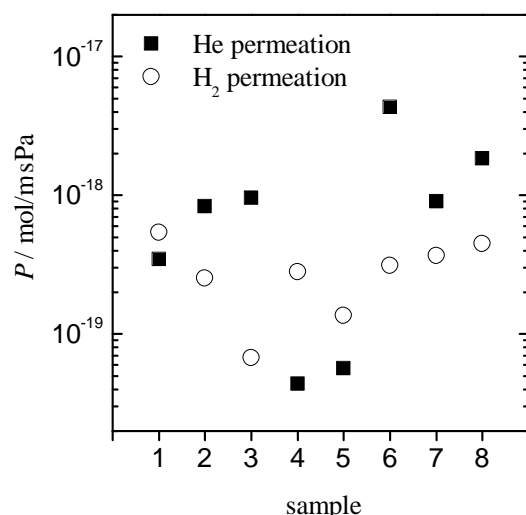


**Figure 2.15:** Comparison of helium and hydrogen permeabilities of CFRP from [86]. Each sample was tested at room temperature with hydrogen and helium. Although the permeabilities vary strongly, in most cases the helium permeability is greater than the hydrogen permeability.

### 2.5.5 Comparison of Hydrogen and Helium Permeation

The measurement of hydrogen permeation is often substituted by helium or argon as test gas for reasons of convenience [86–88]. This section gives a comparison of the H<sub>2</sub> and He permeation in polymers and metals.

Considering polymers, the permeability, being a product of  $D$  and  $S$  (2.33), is mainly dependent on the gas size [41; 46]. While the diffusivity decreases with the penetrant's size, the solubility generally increases with the gas size [41]. Humpenöder [88] reports an exponential dependency of the gas radius on the diffusivity:

$$D_{\text{gas } 1}/D_{\text{gas } 2} = \exp(r_{\text{gas } 2}/r_{\text{gas } 1}).$$

Regarding size and mass, helium is the most similar gas to molecular hydrogen. The van-der-Waals molecular diameter of hydrogen and helium are 276 pm and 266 pm, respectively [89]. With the assumption of Humpenöder above, the diffusivities of hydrogen and helium should have a ratio of  $D_{\text{He}}/D_{\text{H}_2} = 2.8$ . Humpenöder found in experiments with HDPE, PVC, PC and PA that the He diffusivity is 1.6 – 6.6 times greater than that of H<sub>2</sub>.

Measured helium permeabilities in polymers are reported to be comparable to or slightly greater than those of hydrogen. Humpenöder [88], though the diffusivities varied, found similar permeabilities in the considered materials. Goetz et al. [86] investigated the permeation through eight CFRP (IM7/977-2) samples. The results are presented in figure 2.15. Averaging the data, helium permeates slightly stronger than hydrogen. The transport properties of ECTFE, LDPE, PP and PVC are reported in [48; 89–95]. The differences between He and H<sub>2</sub> are minor, though He exhibits a slightly greater permeability. O'Hanlon [96] reviewed the permeabilities of six polymeric materials. He concluded that the helium permeability is greater or equal the hydrogen permeability.

Considering diffusion through metals, hydrogen and helium exhibit different mechanisms, see 2.4.2. Few researches were carried out on the direct comparison of He and H<sub>2</sub>

permeation in metals. Schefer et al. [38] stated qualitatively that the helium diffusivity is several orders of magnitude lower than that of hydrogen. McCool and Lin [97] reported a  $\text{H}_2/\text{He}$  selectivity at 573 K for Pd-Ag membranes in the range of 23 to 4770. Collins and Turnbull [98] investigated the permeation of helium and hydrogen through 0.25 mm thick tubes at 1023 K. Hydrogen permeation was detected through Monel, 304 stainless steel, Kovar, Inconel, nickel, and 52 Alloy ( $\text{Fe}_{50}\text{Ni}_{50}$ ) even at temperatures approaching room temperature. The same metals were not permeated by helium at temperatures as high as 1123 K.

Experiments to directly compare He and  $\text{H}_2$  permeation in grain boundaries have not been performed. However, it can be assumed that the permeation behavior of He and  $\text{H}_2$  in grain boundaries is similar, when considering that primarily a vacancy motion is present, refer to 2.4.4.

Summarizing, helium and hydrogen exhibit comparable diffusivities and permeabilities in plastics and presumably in metals with grain boundaries. In metals, the permeability of hydrogen is much greater than that of helium.

## 2.6 Simulation of Permeation

The Fick curve (2.27) describes one-dimensional transient diffusion or permeation, respectively, in homogeneous membranes. However, this equation may not be employed in multi-layer permeation, grain boundary diffusion or permeation through substrates with defective liners. Hence, presuming inhomogeneous materials in general, the measured flux-time curves can differ from the Fick curve.

The reviewed simulations of grain boundary diffusion in 2.4.4 and permeation through defectively coated membranes in 2.5.4 only cover the stationary state. The only transient consideration — of Hwang and Baluffi — may only be used in Harrison type C grain boundary diffusion.

In order to understand the reason for diversely measured  $J(t)$  curves in this work though, own transient simulations are carried out. The developed model covers the diffusion in two dimensions. Considering the sorption equation (2.16), this model also allows to simulate two-dimensional permeation. Various materials with different transport properties ( $D$  and  $S$ ) and arbitrary geometries can be defined. Additionally, this model can take the dissociation of molecules into account. The physical assumptions underlying the used model and their mathematical implementation into a program are described in the following.

### Definition of the Diffusion Problem

The diffusion problem in one material is described by the two laws of Fick. Considering a body of different materials, Fick's laws may only be applied to each material separately. Knowing the interface conditions, the overall system is determined and can be solved. In the following, the term *phase* is used for a continuous region of one material.



(a) mass of the element and mass fluxes through the boundaries

(b) concentration of the element and fluxes through the boundaries

**Figure 2.16:** Mass conservation of element  $(i,j)$

Numerical methods are always based on the principle of discretizing the continuous media (into elements) and the time (into time steps). The simplest discretization principle is the finite difference method (FDM), which requires initial and boundary conditions.

In this thesis, the body is discretized into rectangular elements. The number of elements in vertical and horizontal direction are denoted by  $v$  and  $w$ , respectively. Introducing a mathematical index, these elements can be assigned. The element in the  $i$ th row and  $j$ th column is indexed  $(i, j)$ . Each element  $(i, j)$  is defined by its properties: width  $dx_j$ , height  $dy_i$ , concentration in the center  $C_{ij}$ , solubility  $S_{ij}$ , diffusivity  $D_{ij}$ , and pressure exponent  $n_{ij}$  (2.16). Discretizing the time into the increment  $\Delta t$ , the explicit solution of the FDM is

$$C_{ij}(t + \Delta t) = C_{ij}(t) + \dot{C}_{ij}(t) \Delta t. \quad (2.51)$$

The unknown derivative of the concentration w.r.t. time can be determined by reformulating Fick's second law (2.20).

### Reformulation of Fick's Second Law

Considering an element  $(i, j)$  as shown in figure 2.16-a, the increase of the mass inside the element equals the sum of all mass flows into and out of the element boundaries

$$\begin{aligned} \dot{m}_{ij} &= \sum \dot{m}|_{\text{bound}} \\ &= \dot{m}_{ij}^{x,\text{in}} - \dot{m}_{ij}^{x,\text{out}} + \dot{m}_{ij}^{y,\text{in}} - \dot{m}_{ij}^{y,\text{out}}. \end{aligned}$$

The mass increase and the mass fluxes can be replaced by adequate expressions of the concentration increase and the fluxes, respectively (refer to figure 2.16-b).

$$\begin{aligned} \dot{m}_{ij} &= M \dot{C}_{ij} dx_j dy_i dz \\ \dot{m}_{ij}^{x,\text{in|out}} &= M J_{ij}^{x,\text{in|out}} dy_i dz \\ \dot{m}_{ij}^{y,\text{in|out}} &= M J_{ij}^{y,\text{in|out}} dx_j dz. \end{aligned}$$

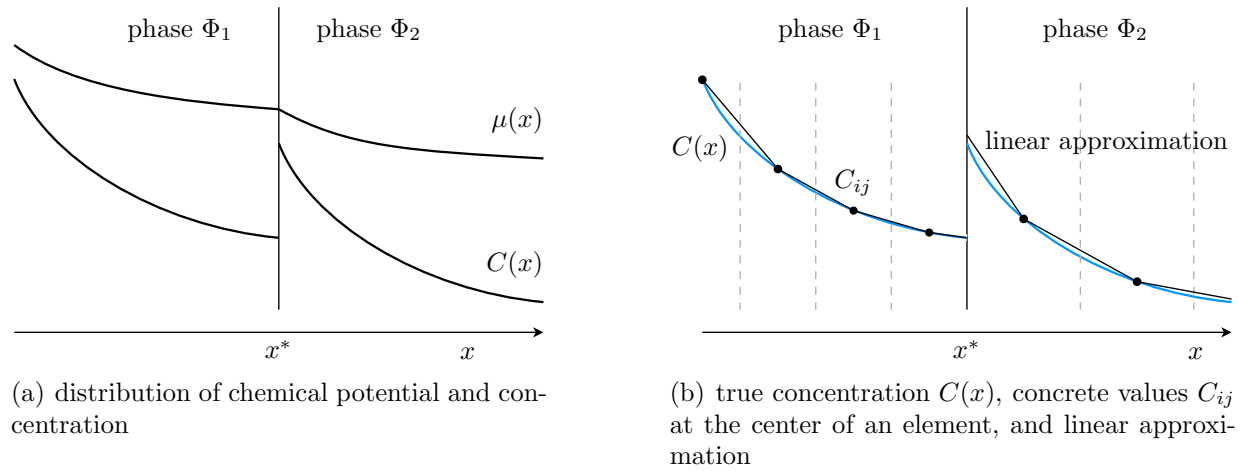


**Figure 2.17:** Concentration distribution at an interface of two phases.

where  $M$  is the molar mass of the permeating gas. Substituting the equations above into the equation of the mass balance one obtains

$$\dot{C}_{ij} = \frac{J_{ij}^{x,\text{in}} - J_{ij}^{x,\text{out}}}{dx_j} + \frac{J_{ij}^{y,\text{in}} - J_{ij}^{y,\text{out}}}{dy_i}. \quad (2.52)$$

Equation (2.52) is another expression of Fick's second law. It states that the sum of the negative flux gradients is equal the concentration increase. The unknown fluxes through the element boundaries in (2.52) are determined in the following.

### Fluxes through Element Boundaries

Figure 2.17 shows the general concentration distribution at the interface between two phases. The chemical potential,  $\mu$ , is per definition continuous. The concentration exhibits a step if the solubilities of both phases are different. Although the flux inside a phase is determined by Fick's first law (2.19), it may not be employed at the interface.

Figure 2.18 illustrates two adjacent elements, 1 and 2, of different phases  $\Phi_1$  and  $\Phi_2$ . The relationship between the concentrations at the interface is derived by considering that

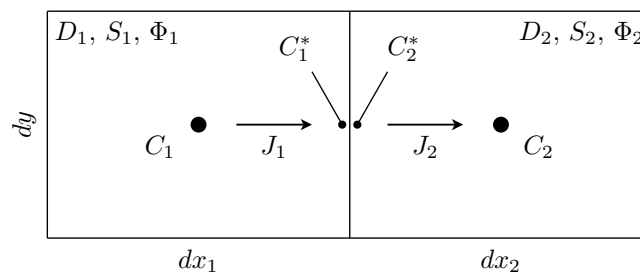


**Figure 2.18:** Concentrations and fluxes in two adjacent elements, 1 and 2.

the chemical potential of the dissolved gas (2.18) is equal in both elements at the interface

$$\frac{1}{n_1} \mu_1(x^*) = \frac{1}{n_2} \mu_2(x^*) \longrightarrow \left( \frac{C_1^*}{S_1} \right)^{1/n_1} = \left( \frac{C_2^*}{S_2} \right)^{1/n_2}, \quad (2.53)$$

where  $n_1$  and  $n_2$  are the pressure exponents.

Presuming no mass accumulation at the common boundary, the mass flows into and out of the interface are equal,  $\dot{m}_1 = \dot{m}_2$ . The mass flow can be substituted by the flux:  $\dot{m} = M \dot{N} = M J A$ , where  $M$  is the molar mass and  $A$  is the interface area. The molar mass of the dissolved gas depends on the existence of dissociation, hence:  $M_1/M_2 = n_1/n_2$ . It follows for the boundary fluxes that

$$\frac{J_1}{J_2} = \frac{n_2}{n_1}. \quad (2.54)$$

Presuming a linear distribution of the concentration from the center to the boundary in each element (see figure 2.17-b), the fluxes are approximated by Fick's first law

$$J_1 = -D_1 \frac{C_1^* - C_1}{dx_1/2}, \quad (2.55)$$

$$J_2 = -D_2 \frac{C_2 - C_2^*}{dx_2/2}. \quad (2.56)$$

Rearranging (2.55) and (2.56) for  $C_1^*$  and  $C_2^*$ , respectively, and substituting these expression in (2.53) considering (2.54) one obtains

$$\left( \frac{C_1}{S_1} - \frac{n_2}{n_1} \frac{J_2}{2 D_1 S_1} dx_1 \right)^{n_2/n_1} = \frac{C_2}{S_2} + \frac{J_2}{2 D_2 S_2} dx_2. \quad (2.57)$$

Defining the variable

$$\gamma_i = \frac{dx_i}{2 D_i S_i} \text{ for } i = 1, 2, \quad (2.58)$$

the fluxes  $J_1$  and  $J_2$  are, depending on the ratio  $n_2/n_1$ ,

$$\begin{aligned} \frac{n_1}{n_2} = 1 : J_1 = J_2 &= (\gamma_1 + \gamma_2)^{-1} \left( \frac{C_1}{S_1} - \frac{C_2}{S_2} \right) \\ \frac{n_1}{n_2} = 2 : 2J_1 = J_2 &= \frac{1}{4\gamma_2} \left( 4\frac{C_2}{S_2} + \frac{\gamma_1}{\gamma_2} \right) \left[ \sqrt{1 - 16 \left( 4\frac{C_2}{S_2} + \frac{\gamma_1}{\gamma_2} \right)^{-2} \left( \frac{C_2^2}{S_2^2} - \frac{C_1}{S_1} \right)} - 1 \right] \\ \frac{n_1}{n_2} = \frac{1}{2} : J_1 = 2J_2 &= \frac{-1}{4\gamma_1} \left( 4\frac{C_1}{S_1} + \frac{\gamma_2}{\gamma_1} \right) \left[ \sqrt{1 - 16 \left( 4\frac{C_1}{S_1} + \frac{\gamma_2}{\gamma_1} \right)^{-2} \left( \frac{C_1^2}{S_1^2} - \frac{C_2}{S_2} \right)} - 1 \right] \end{aligned}$$



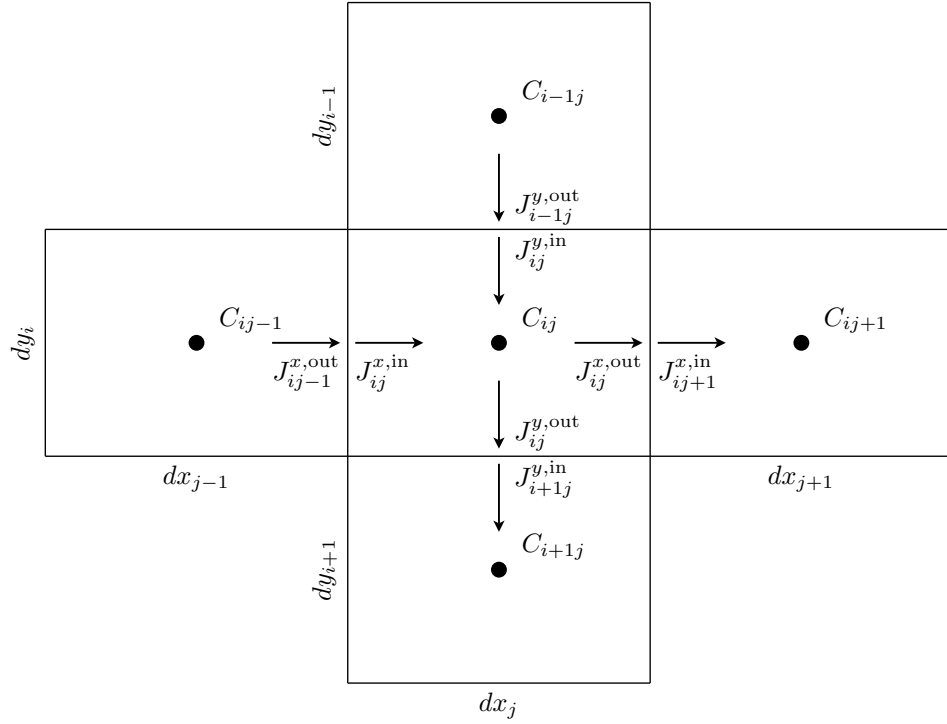


**Figure 2.19:** Element  $(i, j)$ , its adjacent elements, and the fluxes through their common boundaries

The unknown fluxes  $J$  of (2.52), being graphically explained figure 2.19, can now be replaced by given concentrations.

$$J_{ij}^{x, \frac{\text{in}}{\text{out}}} = \begin{cases} \frac{n_{ij\mp 1}}{n_{ij}} = 1 : (\gamma_{ij\mp 1}^x + \gamma_{ij}^x)^{-1} \left( \mp \frac{C_{ij}}{S_{ij}} \pm \frac{C_{ij\mp 1}}{S_{ij\mp 1}} \right) \\ \frac{n_{ij\mp 1}}{n_{ij}} = 2 : \frac{\pm 1}{4\gamma_{ij}^x} \left( 4\frac{C_{ij}}{S_{ij}} + \frac{\gamma_{ij\mp 1}^x}{\gamma_{ij}^x} \right) \left[ \sqrt{1 - 16 \left( 4\frac{C_{ij}}{S_{ij}} + \frac{\gamma_{ij\mp 1}^x}{\gamma_{ij}^x} \right)^{-2} \left( \frac{C_{ij}^2}{S_{ij}^2} - \frac{C_{ij\mp 1}}{S_{ij\mp 1}} \right)} - 1 \right] \\ \frac{n_{ij\mp 1}}{n_{ij}} = \frac{1}{2} : \frac{\mp 1}{8\gamma_{ij\mp 1}^x} \left( 4\frac{C_{ij\mp 1}}{S_{ij\mp 1}} + \frac{\gamma_{ij}^x}{\gamma_{ij\mp 1}^x} \right) \left[ \sqrt{1 - 16 \left( 4\frac{C_{ij\mp 1}}{S_{ij\mp 1}} + \frac{\gamma_{ij}^x}{\gamma_{ij\mp 1}^x} \right)^{-2} \left( \frac{C_{ij\mp 1}^2}{S_{ij\mp 1}^2} - \frac{C_{ij}}{S_{ij}} \right)} - 1 \right] \end{cases} \quad (2.59)$$

$$J_{ij}^{y, \frac{\text{in}}{\text{out}}} = \begin{cases} \frac{n_{i\mp 1j}}{n_{ij}} = 1 : (\gamma_{i\mp 1j}^y + \gamma_{ij}^y)^{-1} \left( \mp \frac{C_{ij}}{S_{ij}} \pm \frac{C_{i\mp 1j}}{S_{i\mp 1j}} \right) \\ \frac{n_{i\mp 1j}}{n_{ij}} = 2 : \frac{\pm 1}{4\gamma_{ij}^y} \left( 4\frac{C_{ij}}{S_{ij}} + \frac{\gamma_{i\mp 1j}^y}{\gamma_{ij}^y} \right) \left[ \sqrt{1 - 16 \left( 4\frac{C_{ij}}{S_{ij}} + \frac{\gamma_{i\mp 1j}^y}{\gamma_{ij}^y} \right)^{-2} \left( \frac{C_{ij}^2}{S_{ij}^2} - \frac{C_{i\mp 1j}}{S_{i\mp 1j}} \right)} - 1 \right] \\ \frac{n_{i\mp 1j}}{n_{ij}} = \frac{1}{2} : \frac{\mp 1}{8\gamma_{i\mp 1j}^y} \left( 4\frac{C_{i\mp 1j}}{S_{i\mp 1j}} + \frac{\gamma_{ij}^y}{\gamma_{i\mp 1j}^y} \right) \left[ \sqrt{1 - 16 \left( 4\frac{C_{i\mp 1j}}{S_{i\mp 1j}} + \frac{\gamma_{ij}^y}{\gamma_{i\mp 1j}^y} \right)^{-2} \left( \frac{C_{i\mp 1j}^2}{S_{i\mp 1j}^2} - \frac{C_{ij}}{S_{ij}} \right)} - 1 \right] \end{cases} \quad (2.60)$$

where

$$\gamma_{ij}^x = \frac{dx_j}{2 D_{ij} S_{ij}} ; \gamma_{ij}^y = \frac{dy_i}{2 D_{ij} S_{ij}}. \quad (2.61)$$

### Implementation in a Program

In the most general case, the body to be simulated consists of different materials, i. e. different phases. It is mandatory to apply equations (2.52), (2.59) and (2.60) for each element. In detail, the following solution steps are run:

1. Set-up (discretization, definition of initial and boundary conditions)
  - (a) Definition of the grid dimension:  $i = 1..v$  and  $j = 1..w$ , where  $v$  and  $w$  are the numbers of elements in vertical and horizontal direction, respectively.
  - (b) Definition of the grid shape:  $dx_j$  and  $dy_i$ ,  $\forall i, j$
  - (c) Definition of the material properties of each element:  $n_{ij}$ ,  $D_{ij}$ ,  $S_{ij}$  and  $\phi_{ij}$ ,  $\forall i, j$
  - (d) Definition of the initial concentration of each element:  $C_{ij}(t=0) = C_{ij}^0$ ,  $\forall i, j$
  - (e) Definition of the boundary elements  $(i, j) \in B$ , where  $B$  is the set of boundary indexes. Boundary elements must be defined at least at the extends of the matrix. The boundary elements must not vary with time.
  - (f) Definition of the boundary conditions for each boundary element. Type 1: Dirichlet boundary condition  $C_{ij}(t>0) = C_{ij}^B$  or type 2: Neumann boundary condition  $J_{ij}^{x/y, \text{in/out}} = 0$ , for  $(i, j) \in B$ . The boundary conditions may vary with time.
  - (g) Definition of the time increment  $\Delta t$ . In advanced programming the time increment can depend on the progress of the simulation.
  - (h) Setting of time variable to zero:  $t = 0$ .

### 2. Solving

- (a) Increase of time:  $t_{\text{new}} = t + \Delta t$
- (b) Calculation of the fluxes  $J_{ij}^{x, \text{in}}$ ,  $J_{ij}^{x, \text{out}}$ ,  $J_{ij}^{y, \text{in}}$ ,  $J_{ij}^{y, \text{out}}$  according to (2.59) and (2.60) for all non-boundary elements  $(i, j) \notin B$ .
- (c) Calculation of the mandatory fluxes in the boundary elements  $(i, j) \in B$ . In general, one or more fluxes of (2.59) and (2.60) are zero.
- (d) Calculation of the concentration increase  $\dot{C}_{ij} \forall (i, j)$  according to (2.52).
- (e) Calculation of the concentration at time  $t_{\text{new}}$  according to (2.51):  
 $C_{ij}^{\text{new}} = C_{ij} + \dot{C}_{ij} \Delta t$  for all  $(i, j)$

- (f) Reallocation of the concentration and time variable:

$$C_{ij} = C_{ij}^{\text{new}}, t = t_{\text{new}}$$

- (g) Loop to step 2 (a) until simulation is finished

### 3. Post-processing

- (a) Plotting of concentration distribution versus time  
 (b) Plotting of flux versus time  
 (c) Export of the data

### Special Case: Different Phases without Dissociation

The solving method presented above requires a high computing effort. The equations (2.59) and (2.60) are calculated  $n_i \times n_j$  times at every time step. Furthermore, these equations are case-sensitive, which requires an “if-then” programming. The computing durance with a personal computer is too high for extensive simulations being efficient. In many cases, different phases exist which have different diffusivities and solubilities, but the same pressure exponent,  $n$ . For these cases, a method with increased efficiency is presented.

By considering  $n_{ij} = n \forall (i, j)$ . Equations (2.59) and (2.60) become simple:

$$J_{ij}^{x,\text{in|out}} = (\gamma_{ij\mp 1}^x + \gamma_{ij}^x)^{-1} \left( \mp \frac{C_{ij}}{S_{ij}} \pm \frac{C_{ij\mp 1}}{S_{ij\mp 1}} \right)$$

$$J_{ij}^{y,\text{in|out}} = (\gamma_{i\mp 1j}^y + \gamma_{ij}^y)^{-1} \left( \mp \frac{C_{ij}}{S_{ij}} \pm \frac{C_{i\mp 1j}}{S_{i\mp 1j}} \right).$$

Inserting these expressions for the fluxes into (2.52), the concentration increase is

$$\begin{aligned} \dot{C}_{ij} = & \frac{1}{dx_j} (\gamma_{ij}^x + \gamma_{ij-1}^x)^{-1} \left[ \frac{C_{ij-1}}{S_{ij-1}} - \frac{C_{ij}}{S_{ij}} \right] + \frac{1}{dx_j} (\gamma_{ij}^x + \gamma_{ij+1}^x)^{-1} \left[ \frac{C_{ij+1}}{S_{ij+1}} - \frac{C_{ij}}{S_{ij}} \right] \\ & + \frac{1}{dy_i} (\gamma_{ij}^y + \gamma_{i-1j}^y)^{-1} \left[ \frac{C_{i-1j}}{S_{i-1j}} - \frac{C_{ij}}{S_{ij}} \right] + \frac{1}{dy_i} (\gamma_{ij}^y + \gamma_{i+1j}^y)^{-1} \left[ \frac{C_{i+1j}}{S_{i+1j}} - \frac{C_{ij}}{S_{ij}} \right]. \end{aligned} \quad (2.62)$$

Equation (2.62) contains only constant material properties, constant geometry variables, and the variable concentrations of the elements. Furthermore, the unknown concentration increase  $\dot{C}_{ij}$  is linearly dependent on the input variables,  $C_{ij}$ . Hence, this equation can be transformed to a linear matrix equation  $\dot{\mathbf{C}} = f(\mathbf{T}, \mathbf{C})$ , where  $\mathbf{C}$  is the concentration matrix and  $\mathbf{T}$  is a constant coefficient matrix. In particular, the usage of linear algebra enables enhanced and fast simulations. The results of the performed simulations are presented in 6.3.



## Chapter 3

# Preselection of Feasible Liner Materials and Production Processes

In order to narrow the wide range of liner materials, a preselection is done on basis of permeation and outgassing rates found in the literature. First of all, this chapter surveys existing or planned liners of LH<sub>2</sub> tanks. H<sub>2</sub> permeabilities of metals, polymers and glasses reported in the literature are reviewed and compared in the following. Afterwards, the outgassing process is briefly introduced and typical outgassing rates of several materials are presented. After performing sample calculations to assess the required liner properties to enable a stable tank vacuum, potential liner materials are preselected. Finally, liner production processes are reviewed and evaluated.

### 3.1 Literature Review of LH<sub>2</sub> Tank Liners

Mainly the space and aircraft industry has performed studies, tests and prototyping of CFRP tanks. These tank systems can be categorized into four classes regarding their insulation technique. First amongst these are cryogenic tanks with one CFRP shell but neither insulation nor liner, produced by Wilson Composites [99] and Microcosm [100]. Both tank systems are primarily conceived for liquid oxygen. Secondly, NASA and McDonnell Douglas have produced a LH<sub>2</sub> tank consisting of one CFRP shell and an outside foam insulation but containing no liner [101; 102]. Thirdly, sandwich solutions were employed in several tank systems. The sandwich is made of CFRP skins and an insulating foam core. Three of these tank systems were produced or planned without liners [86; 99; 103; 104]. Three other tank systems by ESA [105–108], Northrop Grumman [99; 109] and NASA [87] consider the usage of liners. Finally, vacuum insulated storage systems were produced or studied. ILK Dresden [110] produced LHe cryostats made of glass fiber reinforced plastics without liners for the measurement of low magnetic fields [111]. However, the vacuum stability was limited to 1 – 2 months. Hartwig [112] studied fiber reinforced materials and liners for the operation in LH<sub>2</sub> tanks. In the following, the liners employed or investigated by ESA, NASA, Northrop Grumman and Hartwig are presented in more detail.

**ESA.** Since 1994, the European Space Agency has worked on reusable launch vehicles. Within the project FESTIP, two different tank concepts were developed but not produced. The first tank concept implied an aluminum-lithium waffle structure, a foam insulation and a liner facing the hydrogen [105]. The liner was planned to be a 0.1 mm thin aluminum foil. The second tank concept consisted of a CFRP sandwich solution with a liner [106]. Five liner types were studied.

Three liner types facing the hydrogen were investigated by Diaz et al. [107]. The first among these types was a metal foil made of stainless steel or aluminum. The single foil segments were joined by laser welding. The second liner consisted of collapsible metallic foils or organic films. The ends of the liner were secured by retainer rings at the access ports. The third liner type was made of PBO and produced by an extrusion blow-molding process. Although tests revealed low permeation rates, the inherent manufacturing difficulties could not be solved.

Two alternative liners were studied by Antonenko et al. [108]. Firstly, metalized plastic films were proposed. The metallization, made of silver, gold or aluminum, should be applied on organic base materials like PI, PTFE, PVC or PETP. Secondly, water dispersion coatings based on PU, VdC or PE were investigated. Thermal cycles between LN<sub>2</sub> temperature and 333 K did not result in cracks or peeling-off. For both alternative liners, no information is given about liner thickness or permeation behavior.

Trading off all liner concepts, ESA selected foils made of 0.1 mm thick aluminum (AA6061-TO). The trade off was carried out without any permeation tests on that liner.

**NASA.** In NASA's X-33 program, a planned successor of the Space Shuttle should have been developed. The employed LH<sub>2</sub> tank consisted of a sandwich, made of CFRP face sheets and an insulating core, but no liners. The tank was destroyed in 1999 during testing. The subsequent investigation determined the most probable failure cause. Microcracks appeared in the inner facesheet and cold, gaseous hydrogen gas could infiltrate the core. The reduced bondline strength and high pressure inside the core led to the delamination of the outer facesheet [86].

The X-33 program was canceled in 2001 [113]. The investigations and improvements, however, have been continued by Grimsley et al. [87]. Their work concentrated on the application of polymer film liners in and on the CFRP substrate. The permeation tests were performed using Argon instead of hydrogen.

Aluminized Mylar films provided the highest potential considering the permeation. The 0.023 mm or 0.1 mm thick Mylar films were coated with 300 Å aluminum by means of physical vapor deposition. Although the potential of reducing the permeability was shown, a high scatter of the results was also reported. The scatter was attributed to variations in the process conditions. Mechanical tests performed on CFRP with an interleaf aluminized Mylar film resulted in delamination.

**Northrop Grumman Corporation** developed a cryogenic fuel tank made from composite materials for NASA's Marshall Space Flight Center [114], see figure 3.1. The tank was made of a composite sandwich structure with a liner. The liner consisted of a thin aluminum foil enclosed by epoxy resin films [99]. The epoxy-aluminum-epoxy film was applied between the consolidated inner skin and the honeycomb core. Starting in November 2003, tests were performed for the next 9 months. Joan Funk, NASA's cryogenic tanks project leader, reported: "We didn't prove that composite fuel tanks don't leak! In fact we have a hydrogen leak we just don't know if its from the tank or the plumbing." [115]

**Hartwig** [112] investigated fiber reinforced materials enhanced with different liners. All investigated surface liners (12 µm sputtered TiN, 2 µm sputtered amorphous carbon, 0.5 µm chemical NiP and 10 µm chemical/electrochemical Cu) did not reduce the permeation rate.



**Figure 3.1:** Composite liquid hydrogen tank manufactured by Northrop Grumman. From [109].

Embedded foil liners made of Al (240  $\mu\text{m}$ ) and Sn (100 – 200  $\mu\text{m}$ ) were not permeated by helium and hydrogen. Because the aluminum foil separated from the CFRP, Hartwig recommended a thin tin foil as a liner.

Summarizing, the few liners used or planned for composite  $\text{LH}_2$  tanks can be categorized into foils or coatings. Metallic foil liners were proposed by ESA, Northrop Grumman and Hartwig. The investigated foils were made of aluminum, stainless steel and tin. Metalized plastic films were investigated by ESA and NASA. The coating materials were aluminum, silver and gold. None of these liners were applied on a vacuum-insulated  $\text{LH}_2$  tank made of CFRP.

## 3.2 Literature Review of Hydrogen Permeabilities

This section reviews the  $\text{H}_2$  permeabilities and, if available, the related activation energies found in the literature. A distinction between metals, polymers and glasses is made. The reviewed data are listed in table A.1 – table A.9 of appendix A and partly plotted in figure A.1 – figure A.5. For a wide range of diffusivities in metals, it is referred to the publications of Wipf [51] and Völkl & Alefeld [116].

The literature review leads to the following statements: 1. For some materials, only very few or even only one measurement is existing. 2. In few cases, the measured permeabilities of one metal vary more than five orders of magnitude. 3. The permeabilities of metals is mostly determined at high temperatures. The extrapolation to room temperature (RT) must be considered carefully. 4. A direct relationship between the structure of the metal lattice (refer to 2.1) and the measured permeabilities does not exist.

The permeabilities of metals on one hand and those of polymers or glasses on the other hand are defined differently, depending on the existence of dissociation (see 2.5.1). The dimension of  $P$  in metals and polymers is  $\text{mol}/\text{m s Pa}^{0.5}$  and  $\text{mol}/\text{m s Pa}$ , respectively. Consequently, the permeabilities cannot be compared directly. Instead, the permeation fluxes owing to a defined pressure difference are evaluated. Considering feed pressures between 1 bar and 6 bar, equal permeation fluxes through metals and polymers exist, if  $|P_{\text{metal}}| \approx 500 |P_{\text{polymer}}|$ .

Regarding their room temperature permeabilities, metals and alloys are here classified

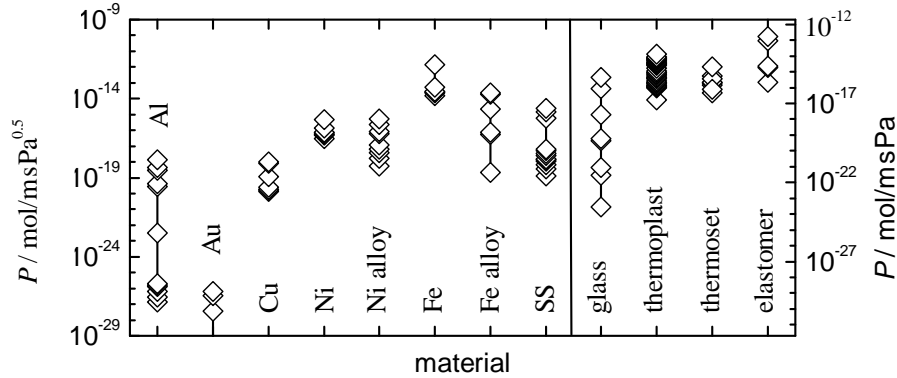


**Figure 3.2:** Comparison of room temperature  $H_2$  permeabilities in some metals, polymers and glasses. The scales for metals and polymers are arranged so that the resulting permeation fluxes for  $p_f = 1 \dots 5$  bar are approximately equal. The plotted data are from appendix A.

into 3 categories: extra-low permeation materials ( $|P| < 10^{-20}$ ), low permeation materials ( $10^{-20} < |P| < 10^{-17}$ ) and high permeation materials ( $|P| > 10^{-17}$ ). Extra-low permeabilities are found in germanium, tungsten, gold, aluminum and silver. Platinum and copper can be classified between extra-low and low permeation materials. Low permeation materials are cobalt, beryllium and nickel. Stainless steel, iron and nickel alloys can be high or low permeation materials, depending on their composition. Iron and titanium are high permeation materials with  $P \approx 10^{-13} \text{ mol/ms Pa}^{0.5}$ . Very high permeabilities can be found in palladium, vanadium, tantalum and yttrium.

The RT permeabilities of glasses are between  $10^{-16}$  and  $10^{-24} \text{ mol/ms Pa}$ . The polymer permeabilities are all within a bandwidth of three orders of magnitude, if six highly permeable materials are neglected.  $P(\text{RT})$  ranges between  $10^{-17}$  and  $10^{-14}$ , while the average is approximately at  $10^{-15} \text{ mol/ms Pa}$ . The RT permeabilities of glasses and polymers are graphically compared with those of some metals in figure 3.2. The lowest permeabilities can be found in some metals followed by glasses. The permeabilities of polymers are relatively high.

The permeabilities of all polymers and all low or extra-low permeation metals extrapolated to  $T = 20 \text{ K}$  are negligible. The permeabilities are less than  $10^{-53} \text{ mol/ms Pa}$  or  $10^{-62} \text{ mol/ms Pa}^{0.5}$ , respectively. The extrapolated permeability of gold at  $20 \text{ K}$  is even  $10^{-306} \text{ mol/ms Pa}^{0.5}$ .

### 3.3 Outgassing and Literature Review of Outgassing Rates

Outgassing is the gas release from a solid's surface. It can be classified into two different processes. Firstly, molecules dissolved in the bulk diffuse to the surface and desorb from it. This process is denoted thermal outgassing [117]. Secondly, particles that have previously been adsorbed, e.g. at high pressures during venting a vacuum chamber, desorb from the surface again. This process is called short-time outgassing [118]. In general, both processes are existing concurrently. The predominant outgassing molecule in polymers is water vapor



**Table 3.1:** Area specific outgassing rates in mbar l/s m<sup>2</sup> of stainless steel as a function of bake-out time and bake-out temperature  $T$ . The data are taken from [128].

$T / ^\circ\text{C}$	bake-out time			
	20 h	40 h	100 h	200 h
150	$9.0 \cdot 10^{-07}$	$7.6 \cdot 10^{-07}$	$4.0 \cdot 10^{-07}$	$2.9 \cdot 10^{-07}$
250	$9.0 \cdot 10^{-08}$	$7.6 \cdot 10^{-08}$	$4.0 \cdot 10^{-08}$	$2.9 \cdot 10^{-08}$
400	$5.7 \cdot 10^{-09}$	$2.4 \cdot 10^{-09}$	$1.4 \cdot 10^{-09}$	$1.4 \cdot 10^{-09}$
500	$1.1 \cdot 10^{-10}$	$1.1 \cdot 10^{-11}$	$5.7 \cdot 10^{-13}$	$1.1 \cdot 10^{-14}$

[119]. In metals, water vapor and mainly hydrogen are the sources of outgassing [120–122].

Besides thermal and short-time outgassing, atoms or molecules are released from the surface if the vapor saturation pressure is higher than the vacuum pressure. The vapor saturation pressure of most metals is lower than  $10^{-8}$  mbar at room temperature and much less at 20 K [70; 96]. Some polymers vaporize at high pressures, for instance Teflon at  $10^{-7}$  mbar and Perbunan at  $5 \cdot 10^{-4}$  mbar, respectively.

The outgassing rate is defined in two different ways. In space applications, the total mass loss ( $TML$ ) is used to characterize polymers [123; 124]:

$$TML = \frac{\Delta m}{m \Delta t},$$

where  $m$  is the mass of the subjected material at the beginning and  $\Delta m$  is the mass loss during time  $\Delta t$ . The test procedure is described in [125]. The investigated material with  $m \approx 250$  mg is placed inside a copper chamber. This chamber is heated to  $125^\circ\text{C}$  for 24 hours. The released gas can escape only through a 6.3 mm diameter exit port. The disadvantages of this method are the standard temperature of  $125^\circ\text{C}$ , the non-existence of vacuum, no relation to an area and the very low accuracy.

In most publications, the outgassing rate is defined as a gas flow or an area-specific gas flow

$$Q_G = \frac{d(pV)}{dt} \text{ or } q_G = \frac{1}{A} Q_G. \quad (3.1)$$

The outgassing rate depends on the temperature and on the time. At high temperatures, the outgassing is accelerated. Presuming thermal outgassing, Calder and Lewin [126] have analytically shown that the outgassing rate is proportional to  $\exp(-\frac{1}{T})$ . Kishiyama et al. [127] state that below 373 K, the outgassing rate doubles with each temperature increase of 15 K. The bake-out process takes advantage of the strong temperature dependency. After heating and subsequent cooling, the outgassing rate is dramatically decreased. Table 3.1 shows the strong emphasis of the bake-out temperature in comparison to the bake-out time exemplarily for hydrogen outgassing from stainless steel.

Wutz, Adam and Walcher [30] distinguished between three functions of  $Q_G(t)$ . While the outgassing kinetics of metals are generally described by  $Q_G \propto t^{-1}$ , polymers can follow

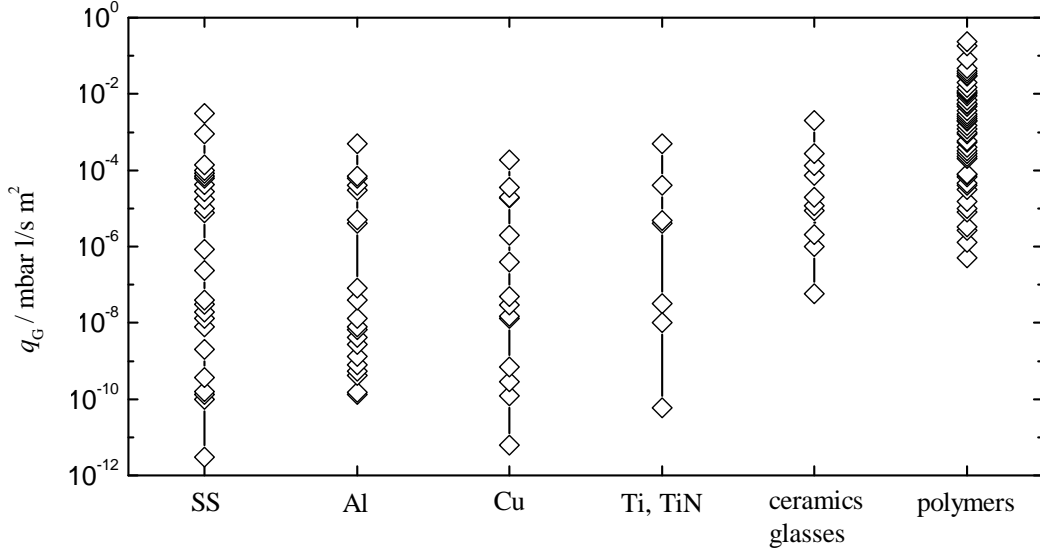


**Figure 3.3:** Area specific outgassing rates at RT of stainless steel, aluminum, copper, titanium, ceramics, glasses and polymers from literature. The plotted data are from appendix B.

either  $Q_G \propto t^{-1/2}$  or  $Q_G \propto \exp(-t)$ . Dylla et al. [129] measured the outgassing rates of stainless steel and aluminum and found that  $Q_G \propto t^{-n}$  with  $n = 0.9 \dots 1.3$ .

The outgassing rates of various materials are reviewed from the literature and listed in appendix B. Figure 3.3 compares the outgassing rate of stainless steel, aluminum, copper, titanium, ceramics/glasses and various polymers. The minimum area specific outgassing rate of various polymers is  $5 \cdot 10^{-7}$  mbar l/s m<sup>2</sup> at room temperature. The minimum values of metals are much less. Outgassing rates of approximately  $10^{-11}$  mbar l/s m<sup>2</sup> are reported for stainless steel and copper.

### 3.4 Vacuum Stability and Material Preselection

The parameters to mathematically describe the LH<sub>2</sub> tank of chapter 1 are presented in figure 3.4. The approximate values of these parameters are  $V_v \approx 0.06$  m<sup>3</sup>,  $A_i \approx 1.6$  m<sup>2</sup>,  $p_{H_2} \approx 6$  bar and  $T_v \approx 293$  K. In a first assessment, the pressure of the vacuum insulation may not exceed  $5 \cdot 10^{-4}$  mbar within 2 years. It follows that the maximum allowable total gas flow into the insulation space is

$$Q_{\max} = \frac{d(pV)}{dt} = \frac{\Delta p_v}{\Delta t} V_v \approx \frac{5 \cdot 10^{-4} \text{ mbar}}{2 \text{ a}} 0.06 \text{ m}^3 = 5 \cdot 10^{-10} \text{ mbar l/s}. \quad (3.2)$$

To assess the maximum allowable permeation and outgassing rate, it is assumed that

$$\begin{aligned} Q_{P,\max} &= Q_{G,\max} = 0.5 Q_{\max} = 2.5 \cdot 10^{-10} \text{ mbar l/s, or} \\ q_{P,\max} &= q_{G,\max} = 0.5 Q_{\max}/A_i = 1.5 \cdot 10^{-10} \text{ mbar l/s m}^2. \end{aligned} \quad (3.3)$$

At low temperatures, no significant outgassing will occur. On the contrary, cryopumping can even improve the vacuum. However, it must be assumed that the inner tank can

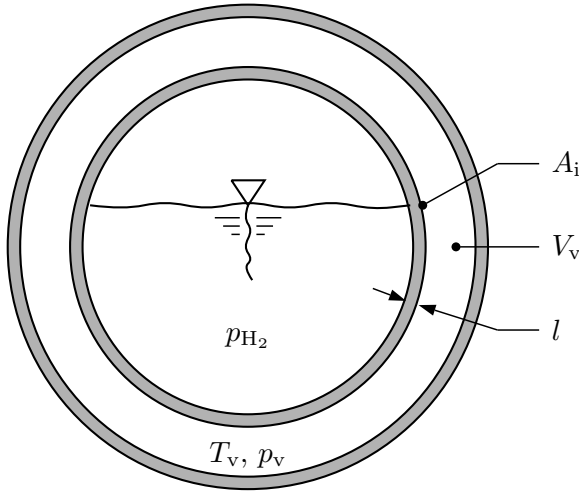


**Figure 3.4:** Parameters to describe the LH<sub>2</sub> tank.  $A_i$ ,  $V_v$  and  $l$  denote the surface area of the inner tank, the volume of the vacuum and the thickness of the inner tank, respectively.  $p_{H_2}$  and  $p_v$  are the pressures of the stored hydrogen and the vacuum, respectively.  $T_v$  is the temperature of the vacuum.

also reach room temperature, for instance during manufacturing, delivery or service times. The minimum area specific outgassing rates of metals and polymers from 3.3 are compared to the requirement (3.3):

$$\begin{aligned} q_{G,\min,\text{metals}} &= 1 \cdot 10^{-11} \text{ mbar l/s m}^2 < q_{G,\max} \\ q_{G,\min,\text{polymers}} &= 1.3 \cdot 10^{-6} \text{ mbar l/s m}^2 \gg q_{G,\max}. \end{aligned}$$

The high outgassing rate of polymers at room temperature would correspond to a vacuum stability time of only four minutes. Hence, regarding outgassing, it is mandatory to apply a metallic liner on the CFRP.

The permeation gas flow strongly depends on the temperature. At high temperatures, e.g. at RT, the gas flow is maximal and hence critical. With (2.7) and (2.34), the steady-state H<sub>2</sub> permeation rate through the inner tank is

$$q_P = R T_v P(T) \frac{p_{H_2}^n}{l}. \quad (3.4)$$

Let  $q_P < q_{P,\max}$ , the maximum allowable permeability is

$$\begin{aligned} P &< 1.656 \cdot 10^{-17} \frac{\text{mol}}{\text{m s Pa}^{1/2}} \frac{l}{\text{m}} \quad \text{for metals, and} \\ P &< 2.138 \cdot 10^{-20} \frac{\text{mol}}{\text{m s Pa}} \frac{l}{\text{m}} \quad \text{for polymers and glasses.} \end{aligned}$$

These equations relate the permeability of a material to the required thickness, or vice versa. The CFRP of the inner tank with  $l \approx 2 \text{ mm}$  would require a permeability of  $4 \cdot 10^{-23} \text{ mol/m s Pa}$  or less. This value is not feasible for polymers at room temperature, refer to 3.2. The minimum RT permeability found in the literature is  $10^{-17} \text{ mol/m s Pa}$ , which results in a steady-state gas flow of  $10^{-4} \text{ mbar l/s}$ . This value corresponds to a vacuum stability time of only 5 seconds.

**Table 3.2:** Required liner thicknesses  $l_{\min}$  for several metals presuming a vacuum stability of two years at 293 K (RT). The permeabilities are taken from appendix A.

metal	$P(293\text{ K}) / \text{mol/m s Pa}^{0.5}$	$l_{\min}$	remarks
Ag	$1.2 \cdot 10^{-24}$	73 nm	extrapolated from $T \gg 293\text{ K}$
Al	$1.4 \cdot 10^{-27} \dots 4.4 \cdot 10^{-19}$	0.08 nm – 26 mm	
Au	$6.3 \cdot 10^{-34} \dots 6.2 \cdot 10^{-27}$	$4 \cdot 10^{-17} - 4 \cdot 10^{-10}\text{ m}$	
Cu	$1.3 \cdot 10^{-20} \dots 9.9 \cdot 10^{-19}$	0.8 ... 60 mm	
Ge	$3.2 \cdot 10^{-41}$	$2 \cdot 10^{-24}\text{ m}$	extrapolated from $T \gg 293\text{ K}$
Mo	$9.3 \cdot 10^{-22} \dots 2.1 \cdot 10^{-17}$	56 $\mu\text{m}$ ... 1 m	
SS	$1.3 \cdot 10^{-19} \dots 2.5 \cdot 10^{-15}$	8 mm ... 150 m	
W	$4.9 \cdot 10^{-32} \dots 7.3 \cdot 10^{-24}$	$3 \cdot 10^{-15} \dots 10^{-7}\text{ m}$	extrapolated from $T \gg 293\text{ K}$

Feasible permeation barriers are either glass or metals. The minimum permeability of glasses from literature is  $3 \cdot 10^{-24}\text{ mol/m s Pa}$  (see table A.6). This would imply a minimum liner thickness of 140  $\mu\text{m}$ . Considering metals as liner, the required thicknesses are calculated for potential low and extra-low permeation materials and are listed in table 3.2. The thicknesses range from  $10^{-24}\text{ m}$  for Germanium to 150 m for stainless steel.

Summarizing, the outgassing and permeation rates of polymers at room temperature are too high to enable a long-time stable vacuum. Hence, fiber reinforced plastics can only be introduced as a structural material of a vacuum-insulated  $\text{LH}_2$  tank if a liner is added. The mandatory liner must be applied at least on the surface pointing to the vacuum, that means on the outside of the inner tank. The material of the liner should be either a metal or glass. Considering the availability, producibility and existing applications in UHV, gold, aluminum, and copper are preselected. With regard to the literature survey of liners in 3.1, tin will also be further investigated.

### 3.5 Literature Review and Preselection of Liner Production Processes

Liners can be categorized into foils/sheets or coatings. Foils and sheets are manufactured in advance and then adhered on the substrate. Coatings are generally produced directly on the substrate. Figure 3.5 gives a graphical overview of existing liner production methods which are explained in the following.

**Foils or sheets** can be produce in different thicknesses by means of rolling or deep drawing [131]. Rolling implies a dense structure of these liners. The foils can be adhered on or laminated into the CFRP. Another technique is the lamination of CFRP on foils or sheets. The joining of separate foil segments is difficult. A feasible joining method is welding but the produced heat and its impact on the CFRP must be considered. It is reasonable though, to adhere different foil segments on the CFRP and close the joining lines by a subsequent coating process.

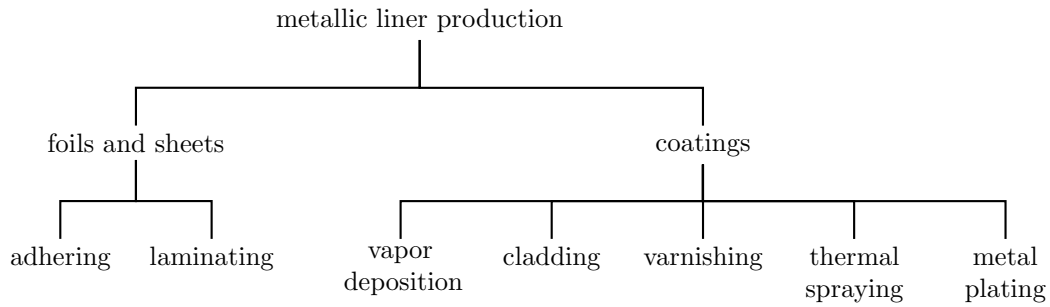


**Figure 3.5:** Technologies to produce metallic liners. Partial source: [130].

The two variants of **vapor deposition** are physical vapor deposition (PVD) and chemical vapor deposition (CVD). PVD is defined if vapor is created by evaporation or sputtering. If the vapor is produced by chemical reactions, the process is called CVD. The process temperature of CVD is generally very high ( $>700\text{ }^{\circ}\text{C}$ , [132]). In all vapor deposition techniques, the vapor is transported in vacuum to the target and precipitates there. Vapor deposition is characterized by low deposition rates and brittle coatings. Brittle coatings on soft substrates like CFRP tend to the formation of microcracks (eggshell effect, [133–135]).

**Cladding** liners can be produced by welding, hot dip coating or roll-bonding [130]. All cladding technologies are disadvantageous because of the high production temperatures (near melting temperature of the metal) or pressures. They are not suitable for coating of polymers.

**Varnishes** can be produced with metallic or organic particles. Metallic varnishes are baked at temperatures higher than  $350\text{ }^{\circ}\text{C}$  to vaporize the solvent [130]. Consequently, they are not suitable for the application on CFRP. Organic varnishes are characterized by high outgassing rates and are not an appropriate liner, either.

Different variants of **thermal spraying** exist. Commonly employed technologies are the atmospheric and low-pressure plasma spraying and cold spraying [136; 137]. All thermal spray techniques have in common that the metal is melted and then carried to the substrate. Further information about the process is given in [136]. Depending on the coating material, the process temperatures are very high. Song et al. [138] reports a generally existing porosity of the coating.

**Metal plating** is a coating process in which ions of the coating metal are dissolved in an electrolyte and, by supplying electrons, are discharged and deposited onto the surface of the target (refer to figure 3.6). Depending on the source of the electrons one distinguishes

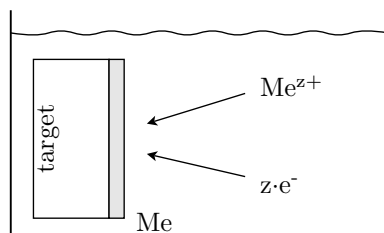
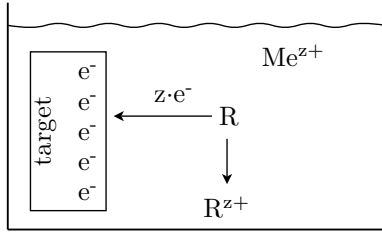
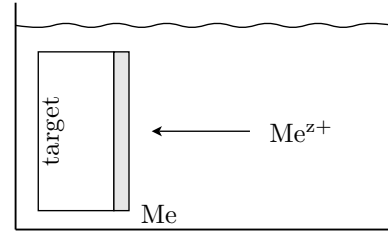


**Figure 3.6:** Principle of metal plating: metal ions  $\text{Me}^{z+}$  are discharged and deposit on the target's surface.



(a) The reduction agent R oxidizes and delivers electrons to the target's surface

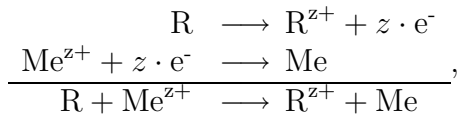


(b) The metal ions  $Me^{z+}$  are discharged by the electrons on the surface and form the coating.

**Figure 3.7:** Principle of electroless plating

between electroless plating (without outer voltage source, also known as chemical deposition, electroless deposition) and electroplating (with outer voltage source, also known as electrochemical deposition and electrodeposition). While the deposition rate of electroless plating is rather low ( $\approx 1 \dots 3 \mu\text{m/h}$ ), the rates of electroplating can be much higher ( $\approx 12 \mu\text{m/h}$ ) [139]. Because fiber reinforced plastics are non-conducting, they must initially be covered by an electroless coating and can subsequently be coated by means of electroplating. The process temperatures of metal plating can be as low as  $25^\circ\text{C}$ . A full coverage of the CFRP is feasible. The two classes of metal plating are further explained in the next paragraphs.

Industrial-relevant methods of **electroless plating** utilize reducing agents for the supply of electrons. There are two processes describing the chemical deposition: the oxidation of the reducing agent and the discharge of the metal ions (refer to figure 3.7). The sum of both processes is [130]



where R is the reducing agent and  $Me^{z+}$  is the  $z$ -valent metal.

Common electroless depositions on polymers are chemical copper (cCu) and chemical nickel phosphor (cNiP). Exemplarily, the cNiP process is presented. The two main components of the electrolyte are the metallic salt, nickel sulfate ( $\text{NiSO}_4$ ) and the reducing agent, mostly sodium hypophosphite ( $\text{NaH}_2\text{PO}_2$ ). The stability of the electrolyte can be affected by many factors like local heating, too high concentration of the reducing agent or dirt particles. Stabilizing agents, complexing agents, pH-regulators and accelerators are added to the electrolyte, in order to maintain its stability and allow a controlled deposition process. The target's surface is activated in advance by means of palladium atoms, which act as germ cells. Subsequent, small crystals of the metal adsorb on the surface, move to and primarily deposit at these germs. Depending on the type of the growth, the different germs form a grain-like surface morphology. These grain-like structures are not monocrystalline and must be distinguished from the grains defined in the crystallography. The shape and

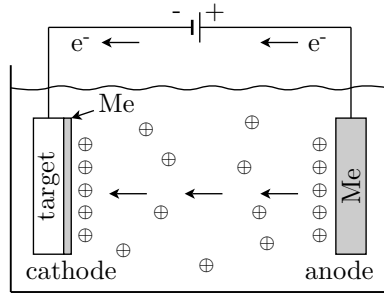
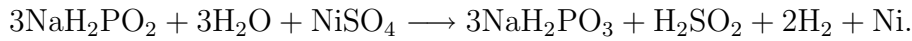


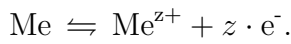
**Figure 3.8:** Principle of electroplating: metal ions  $\text{Me}^{z+}$  (denoted with  $\oplus$  in the diagram) are discharged and deposit on the target's surface.

size of these grain-like structures depend on the current density, the electrolyte, the shape and the material of the substrate. The typical size of these grains is several micrometers.

The cNiP deposition is a sum of several reactions. The simplified net equation is



The **electroplating** process consists of three subprocesses. In the first step, the coating material, Me, is provided by an anode (refer to figure 3.8). In contact with the electrolyte and under specific conditions, the metal can spontaneously leave the lattice of the anode and form metal ions in the electrolyte. As a result, the anode becomes negative because of an oversupply of electrons. This process is called anodic metal dispersion:



The equilibrium can be changed to the right-hand side if an external voltage source is applied so that the electrons are extracted from the anode.

In the second step, the metal ions diffuse to the target driven by an electric field. The electric field is created by supplying the target (cathode) with electrons, see figure 3.8. In the last step, the metal ions discharge at the surface of the target and form the coating. Similar to electroless plating, the deposition starts at favored spots (germs) and forms grain-like structures.

### Preselection of Liner Production Processes

Considering the production of the liner, the following requirements and criteria must be fulfilled:

- feasibility to produce a closed, metallic liner in general
- feasibility to produce a liner on large structures (at the outside of the inner tank shown in figure 1.5-a)
- feasibility to produce a liner on complex geometries (free-form geometry of the LH<sub>2</sub> lightweight tank)
- low costs, outlay, complexity and application time.

Taking these qualitative specifications into account, the metal-plating process shows the highest potential. Hence, the majority of the liners investigated in this work are produced by this process. Considering the statements from 3.1, foils and sheets are also tested. Few PVD and thermal spray coatings are also investigated.



## Chapter 4

# Materials

This chapter presents and characterizes the materials used in the permeation measurements. First, the CFRP substrates are introduced in 4.1. The following section 4.2 describes the materials, application methods and properties of the used liners. Section 4.3 explains the geometry and preparation of the specimens.

The materials are classified into material systems. A material system is represented by a code starting with “M” and followed by two numbers, e.g. M01. The specimens are analogously indexed by the abbreviations S01, S02, . . . . Numbers ending with *c* denote specimens used at cryogenic temperatures.

### 4.1 Substrates

Different CFRP substrates exist, because the polymeric material of the tank structure was developed and defined parallel to the liner application pretests. Hence, the liners were produced on two different substrates, denoted by M02 and M03. Further CFRP samples (M04) were not employed for the liner production but for comparing the permeability with those of M02 and M03. PVC specimens (M01) were used for validating the permeation apparatus because of their well-known transport properties. An overview of the polymeric material systems and their properties is given in table C.1 on page 129. In the following, the material systems M02 and M03 are presented in more detail.

The substrates representing the chosen tank material (M02) were produced by company C02. The composite (Sigratex KDK 8054/120 carbon fibers and Araldite LY 564 with hardener HY 2954 epoxy resin) consists of six plies of woven fabric. The epoxy resin was infiltrated by means of the VARI (vacuum assisted resin infusion) technique. There, an aluminum tool is firstly painted by a release agent. The laid-up fiber plies are then covered by a perforated foil, a resin distribution medium and the vacuum bag<sup>1</sup>. At one location of the vacuum bag, a low vacuum is generated. At the opposite side of the vacuum bag, the heated, viscous resin is introduced to the carbon fiber lay-up. Driven by the pressure difference between atmosphere and vacuum, the resin infiltrates the lay-up. After infiltration, the material is cured to let the epoxy groups fully react. The thickness of the M02 specimens is between 1.4 and 1.8 mm. A cross section is shown in figure 4.1.

The substrates of M03 were produced by company C01. They are made of Zoltek HT carbon fibers and Bakelite epoxy resin (EPR04695 with hardener EPH05357). In opposite

---

<sup>1</sup>The influence of the resin, fibers, mold release agent, peel-ply and distribution medium on the ability to apply a liner on the substrate was investigated in extensive tests. Based on these investigations, the resin and the helpers were chosen.

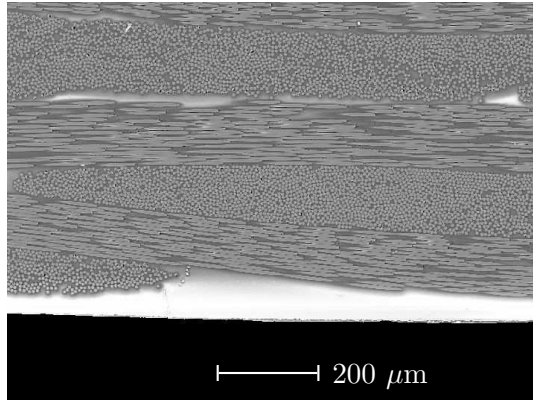
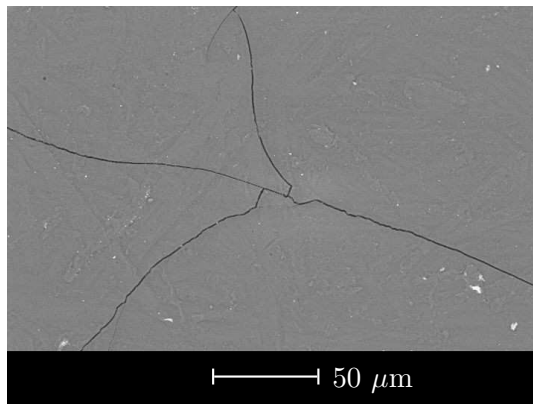
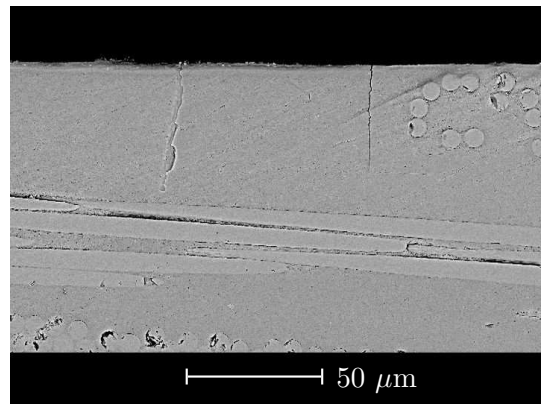


**Figure 4.1:** SEM image of the polished section of a CFRP sample (M02). The woven carbon fibers can be recognized. Resin rich areas (bright) exist between the plies and at the surface (bottom of image).



(a) surface



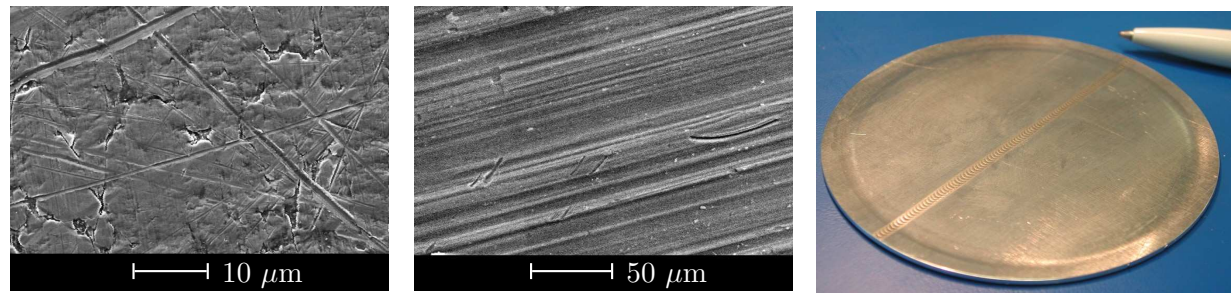
(b) polished section

**Figure 4.2:** SEM images of a CFRP sample (M02) after thermal shock. Microcracks form a network on the surface. The polished section image shows that the microcracks tend to originate in resin rich areas.

to M02, the substrates of M03 were produced by means of RTM (resin transfer molding) and cured in an autoclave. The thickness of the samples is approximately 2.5 mm.

Composites tend to the formation of microcracks during thermal shock owing to their heterogeneity. The thermal expansion coefficient of epoxy resin at 20 K and 300 K is approximately  $4 \cdot 10^{-6} \text{ K}^{-1}$  and  $90 \cdot 10^{-6} \text{ K}^{-1}$ , respectively [112]. In comparison, the thermal expansion coefficient of carbon fibers is near zero or even negative in fiber direction [112]. Cooling from RT to 77 K (condensation temperature of nitrogen), the difference of the thermal strain between epoxy resin and carbon fibers is more than 1 %. Figure 4.2 depicts the microcracks of M02 after a thermal shock in  $\text{LN}_2$ . The cracks form a network on the surface. No microcracks were found that traverse the whole CFRP plate. In various tests it was shown that the microcrack density became maximal after 3 – 15 thermal shocks.

The maximum application temperature of the used epoxy resins is between 128 °C and 145 °C. Consequently, the temperature of the liner production and the bake-out process is restricted to these values.



(a) SEM of the surface of a stainless steel sheet (M06) (b) SEM of the surface of an aluminum foil (M08) (c) welded aluminum sheet (M05)

**Figure 4.3:** SEM images and photos of sheets and foils.

## 4.2 Liners

This section introduces the liners studied in this work. Their basic properties like outgassing, thermal shock resistance, adhesive strength, structure and potential material defects are discussed. First, the methods to determine these properties are briefly explained.

Although quantitative measurements of the outgassing rate were not performed, qualitative statements can be given by evaluating the vacuum pressure during the permeation measurements. All samples containing a liner, independent from the liner material, revealed a reduced outgassing rate compared to CFRP by factor 10 – 100. The general appearance and the structure of the liner was determined by means of SEM. There, the surface as well as the section of the liner was inspected for grains, holes, uncoated spots, microcracks or other material defects. EDX scans were performed to determine the composition of the liner if necessary. The thermal shock resistance was tested by immersing the samples three times into liquid nitrogen. Before each immersion, the samples were kept at room temperature. After the thermal shock, potential microcracks were detected by means of SEM. A possible peeling of the liner was observed by eye or by inspecting polished-cut images. Grid tests according to DIN EN ISO 2409 [140] were performed to determine the adhesive strength.

### Foils and Sheets

The foil and sheet liners (see table C.2) were made of aluminum, stainless steel, tin and copper. The thickness of the sheets was between 0.21 mm and 1.0 mm. The foils were 25 – 130 μm thick and either adhered on substrates or single. The surface of sheets and foils was free from defects like holes or microcracks but contained scratches (see figure 4.3). The adhesive strength of foils on the substrates was very low in some cases and resulted in a total peeling-off. Three samples of an aluminum sheet (M05) were welded to investigate a feasible sheet joining process (see figure 4.3-c).

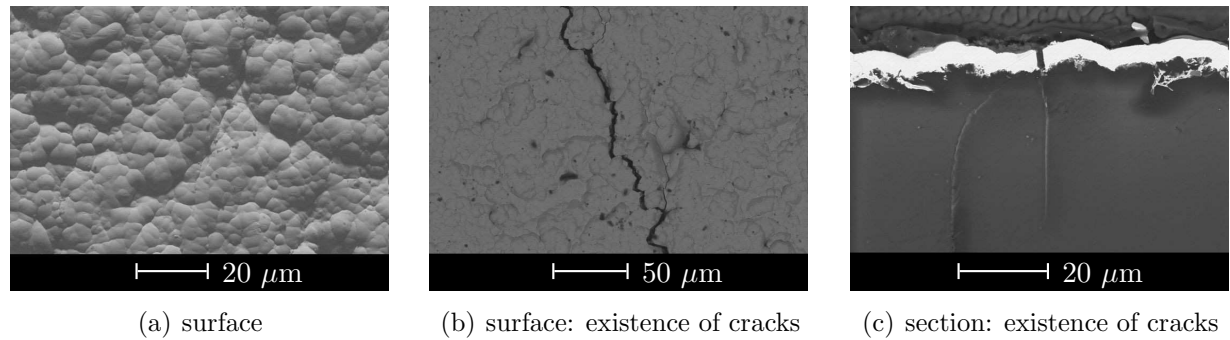


**Figure 4.4:** SEM images of the cNiP coating (M12)

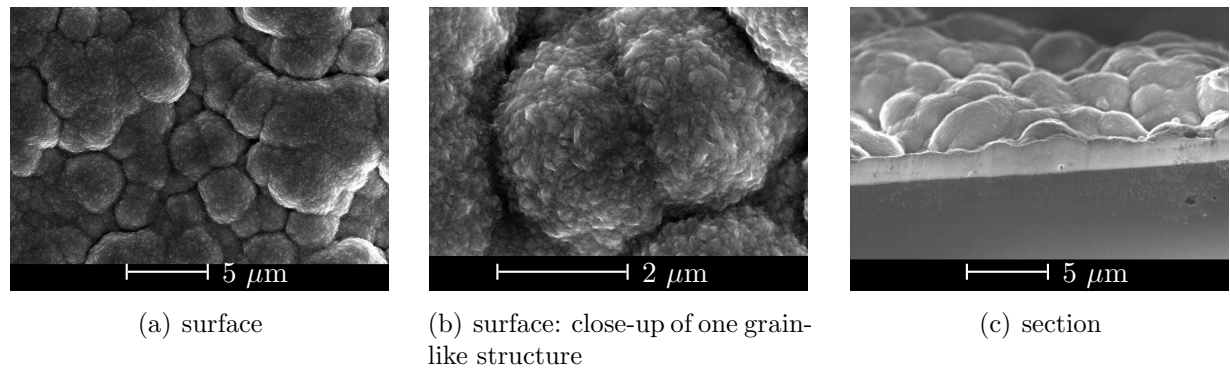


**Figure 4.5:** SEM images of the cCu coating (M31).

## Metal Platings

The various studied metal platings and their basic properties, like liner material and thickness, are summarized in table C.4. All liners consisted of a chemical deposition layer to establish a conductive area. This starting layer was followed by one or more functional layers. The functional layer(s) was (were) mostly produced by means of electroplating. The metal platings can be classified regarding their starting layer.

The starting layer of M12 – M17 was a chemical nickel layer phosphor (cNiP) with approximately 4 – 10  $\mu\text{m}$  in thickness (see figure 4.4). This cNiP coating contained regular, circular, grain-like structures (figure 4.4-a), and microcracks (figure 4.4-b,c). The size of these grains was between 3 and 8  $\mu\text{m}$ . The microcracks, mainly located along the grain boundaries, became more developed after thermal shock. The cracks totally traversed the coating and extended into the resin. The existence of microcracks before the thermal shock points to a brittle behavior of the chemical nickel.

The initial layer of the material systems M18 – M26 was made of chemical copper (cCu, see figure 4.5). The cCu coating with circa 2  $\mu\text{m}$  in thickness was strongly textured. The grain-like features were regular, nearly circular and between 1 and 3  $\mu\text{m}$  in diameter. In opposite to cNiP, cCu did not contain microcracks.

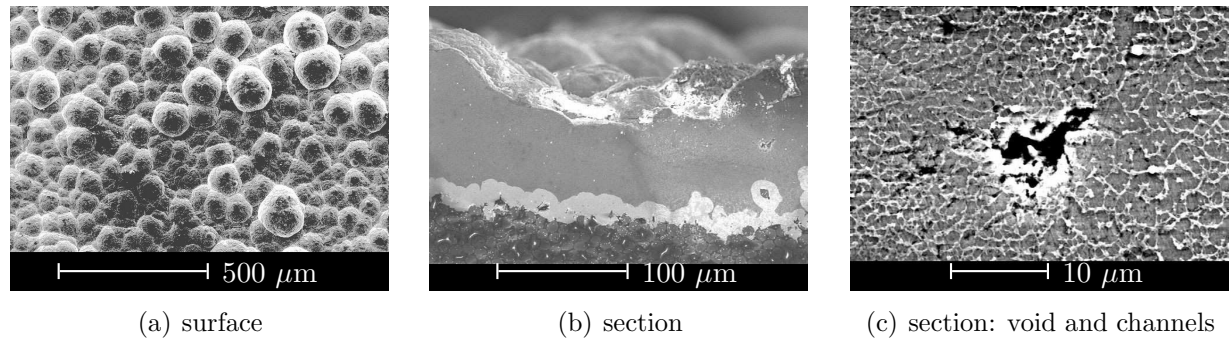


**Figure 4.6:** SEM images of the cNiP-Al coating (M13, S64)

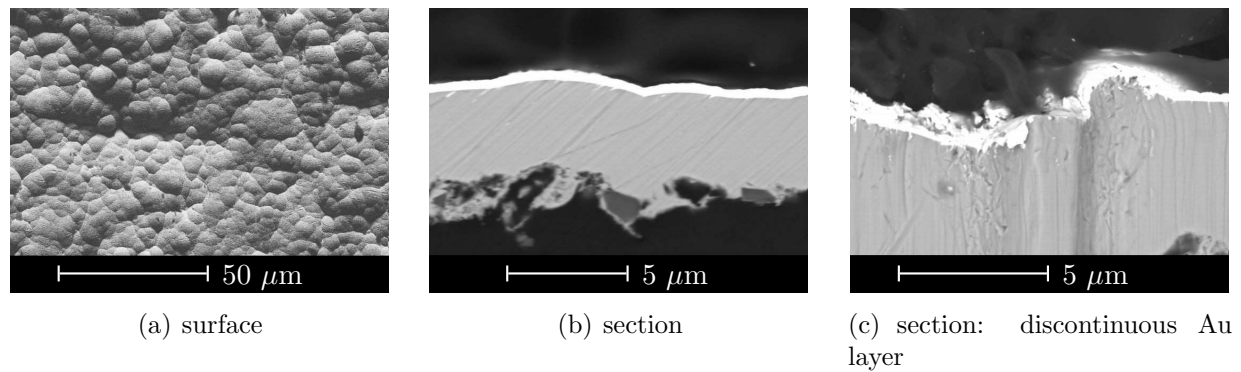


**Figure 4.7:** SEM images of the cNiP-cAu coating (M14)

The functional coatings following the cNiP layer were made of aluminum, chemical gold (cAu), copper, tin or nickel sulfamate (Ni)<sup>2</sup>. Aluminum coatings were produced from aprotic electrolytes [141; 142]. The thickness of the gold layer was 0.3 μm, those of the other functional layers were between 20 and 88 μm.

The surfaces of M13 – M15 contained regular, circular, grain-like structures, refer to figures 4.6-a, 4.7-a and 4.8-a. The size of these grains was between 3 and 8 μm for cNiP+cAu (M14), between 25 and 55 μm for cNiP+Cu (M15) and between 80 and 160 μm for cNiP-Al (M13). Considering the cNiP-cAu and cNiP-Cu coatings, the cross sections showed that the heights of these grain-like features were small compared to the diameter (figures 4.7-b and 4.8-b). The height of the grain-like structures of the cNiP-Al liner was maximal 20 μm (figures 4.6-b) and hence considerable. The cNiP-Ni coating contained irregular, nearly crystalline, grain-like features, refer to figure 4.10. The size of these grains varied from less than 100 nm to 3 μm. The cNiP-Sn coatings (M16, figure 4.9) did not contain a recognizable surface texture but regularly formed dents.

Besides grain-like structures, microcracks were observed in the Sn coatings (M16) after

<sup>2</sup>Nickel sulfamate coatings contain 100 % nickel. The term is derived from the electrolyte, Ni(SO<sub>3</sub>NH<sub>2</sub>)×H<sub>2</sub>O. This Ni coating was additionally proposed by the producer.

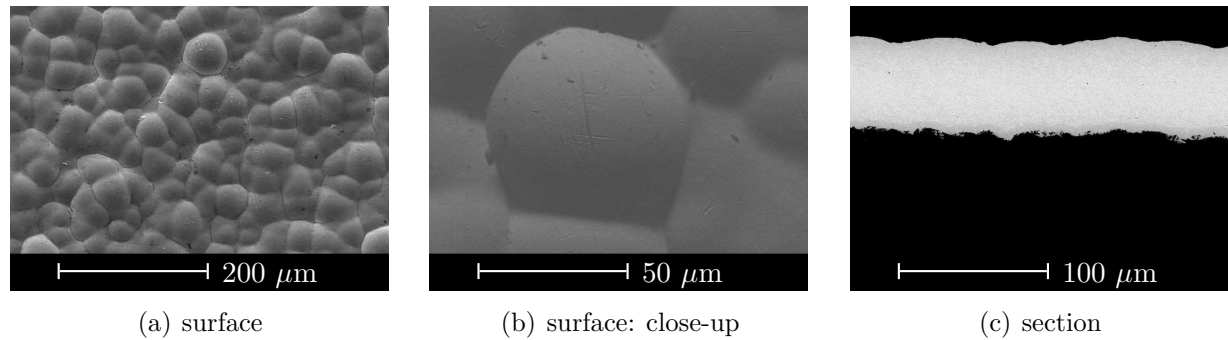


**Figure 4.8:** SEM images of the cNiP-Cu coating (M15)

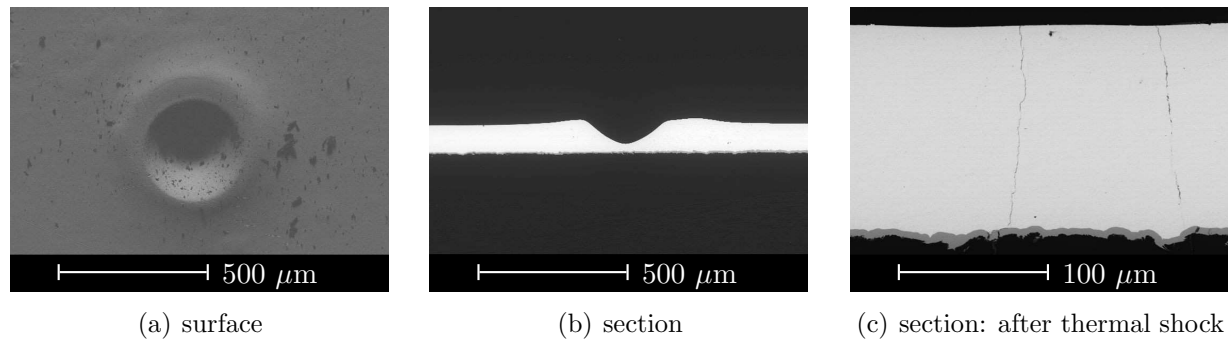


**Figure 4.9:** SEM images of the cNiP-Sn coating (M16). Dents are existing in the coating (figure a and b). Microcracks appeared during thermal shock.

thermal shocks (figure 4.9-c). This behavior can be explained by the phase transition of tin. When tin is cooled below  $13.2^{\circ}\text{C}$ , it changes from  $\beta$ -tin ( $7.29\text{ g/cm}^3$ ) to  $\alpha$ -tin ( $5.77\text{ g/cm}^3$ ) [143; 144]. In the remaining coatings, no microcracks were observed before or after thermal shocks.

The cross sections of the coatings revealed two features. First, the Al coating was interspersed by channels (figure 4.6-b,c). Another specimen (S07) was not fully covered by the aluminum layer. Second, the Au coatings were partly not fully deposited (see figure 4.7-c). The remaining coatings showed a homogeneous thickness and a full coverage.

The adhesive strengths of the coatings were variable. The adhesive strength of the cNiP layer on CFRP was approximately  $21\text{ MPa}$  [145]. In contrast to this high value, the cNiP-Ni coating of M17 peeled off from the substrate during sawing. The grid tests of the remaining coatings revealed a sufficient high adhesive strength.

The functional coatings following the cCu layer were made of Cu (M18 – M22), Cu-Ni-Au (M23), Ni (M24), Ni-Au (M25) and Sn (M26), refer to table C.4. While the coatings of M18 were deposited using standard process parameters, those of M19 – M22 were produced by a varied current density and sulfuric acid ( $\text{H}_2\text{SO}_4$ ) concentration of the electrolyte, see table C.4. Thereby, the influence of the parameters on the coating was investigated.

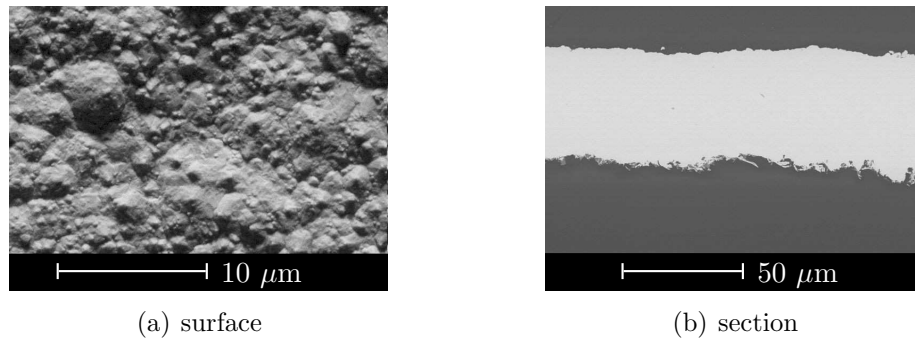


**Figure 4.10:** SEM images of the cNiP-Ni coating (M17).

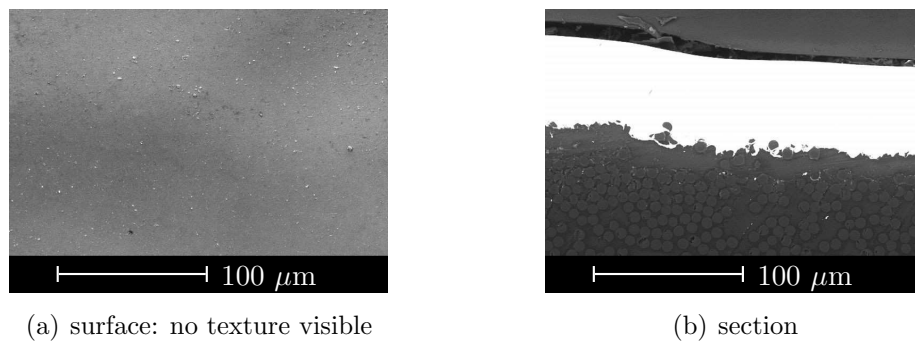


**Figure 4.11:** SEM images of the cCu-Cu coating (M18, S42).

The surfaces of the cCu-Cu coating of M18 did not contain a recognizable textured structure (see figure 4.11). On the contrary, the surface of the cCu-Cu liners of M19 – M22 were characterized by grain-like structures, see figure 4.12. Especially the decrease of the  $\text{H}_2\text{SO}_4$  concentration resulted in a strong development of the grain size. The size of these grains was between 30 and 50  $\mu\text{m}$ . The coatings of M24 – M26 also contained grain-like structures (figures 4.13 and 4.14). The grains of the cCu-Ni and the cCu-Ni-Au liners were circular and between 3 and 20  $\mu\text{m}$  in diameter. The nickel layer itself was very brittle and contained cracks (figure 4.13-a). Figure 4.13-c shows that these cracks, not traversing the whole Ni layer, were fully covered by the gold layer of M25. The cCu-Sn coating was extremely textured with nearly-crystalline, grain-like structures (figure 4.14-a).

In all coatings except that of nickel, no microcracks were found before thermal shock. Thermal shock tests on specimens with cCu-Cu or cCu-Ni-cAu liners did not result in the formation of cracks. The tin coating, however, showed new cracks after thermal shocks (refer to figure 4.14-c). The adhesive strength of all coatings was high. Grid tests on thin coatings were always successful. Flatwise tensile tests on samples of M18 – M22 revealed an adhesive strength of approximately 7 MPa [146].

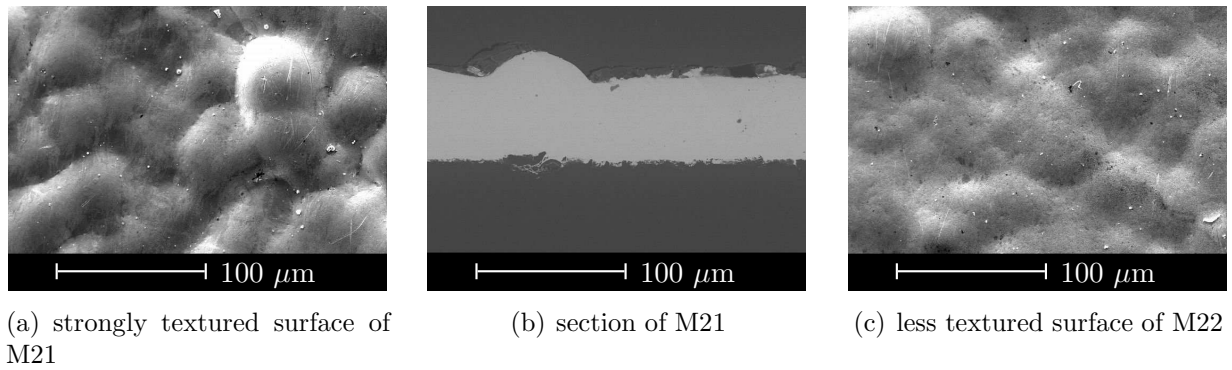


**Figure 4.12:** SEM images of cCu-Cu coating with decreased and increased sulfuric acid concentration (M21 and M22, respectively).

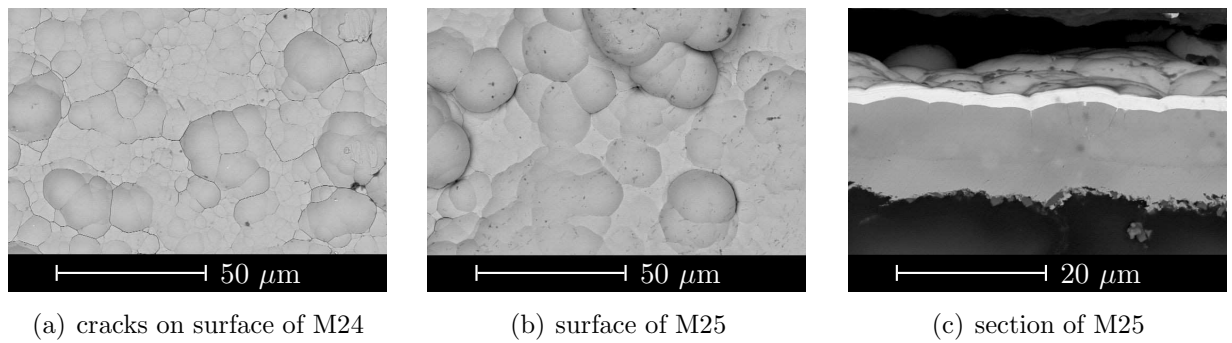


**Figure 4.13:** SEM images of cCu-Ni (M24) and cCu-Ni-cAu (M25) coating.

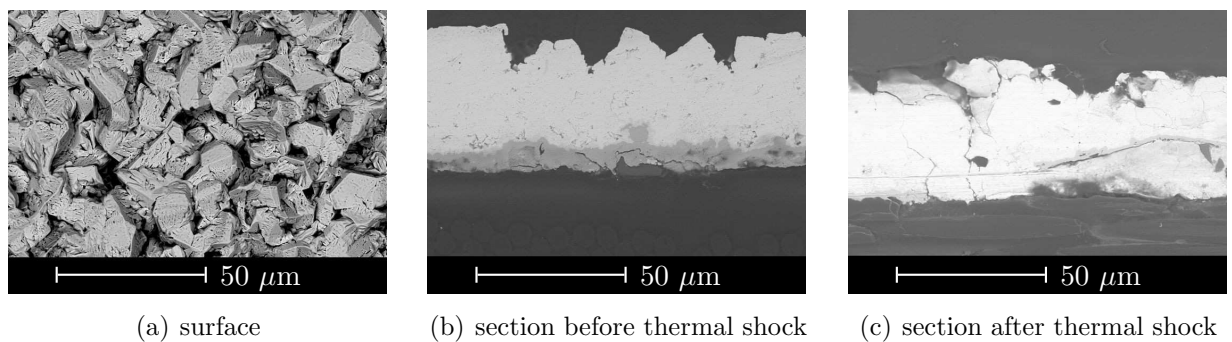


**Figure 4.14:** SEM images of cCu-Sn coating (M26).



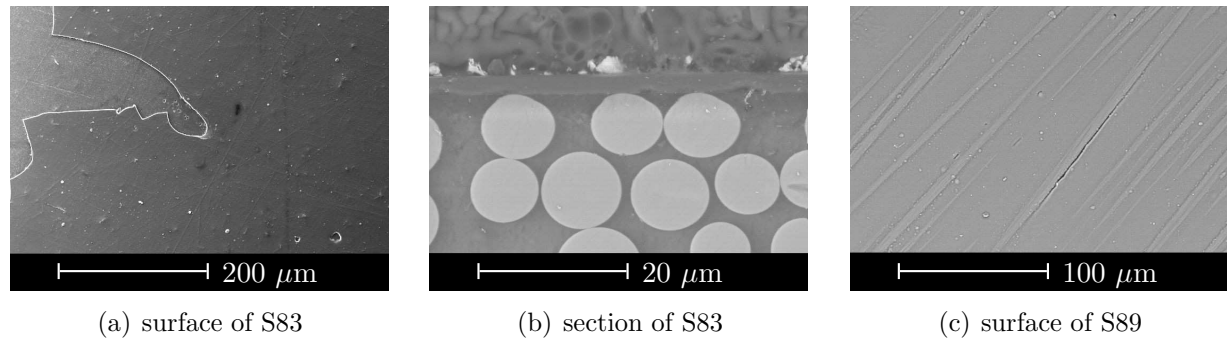


**Figure 4.15:** SEM images of DLC coatings (M83). The coating of S83 is very brittle and leads to planar peeling-off. The hardness of S89 is reduced and implies only local cracks.

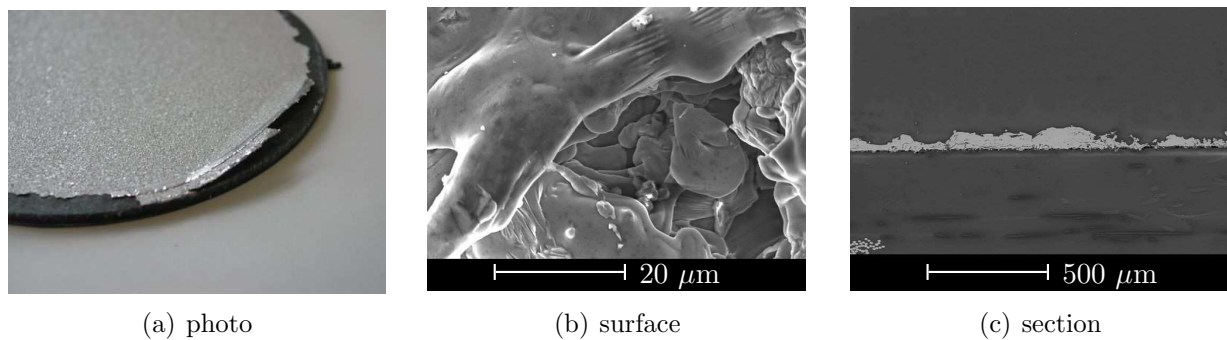


**Figure 4.16:** Photo and SEM images of thermal spray Al coatings (M29).

### Miscellaneous Coatings

Table C.3 summarizes three further investigated liners. The PVD coatings of M28 are made of amorphous hydrogen-containing diamond-like carbon (DLC) doped with Si. The DLC coatings were synthesized by plasma immersion ion implantation and deposition [147]. The typical deposition rate was  $< 1 \mu\text{m/h}$ . DLC coatings mostly feature a high hardness  $> 10 \text{ GPa}$ . The brittleness of the three investigated samples of M28 was successively decreased by increasing the number of layers and reducing the hardness. Figure 4.15 shows SEM images of the brittle DLC coating of S83 and the more ductile coating of S89. Still, the coating of S89 contained cracks resulting from too high internal stresses. Thermal shocks with  $\text{LN}_2$  did not change the coatings remarkably.

The coating of material system M29 was made of thermally-sprayed aluminum. The coating was characterized by a low adhesive strength and macroscopic material defects (see figure 4.16).

The liner of M30 was made of nickel and deposited by means of electroless plating and PVD. Figure 4.17 shows the brittle behavior of the coating. The liner partially flaked off from the CFRP substrate which points to a low adhesive strength.

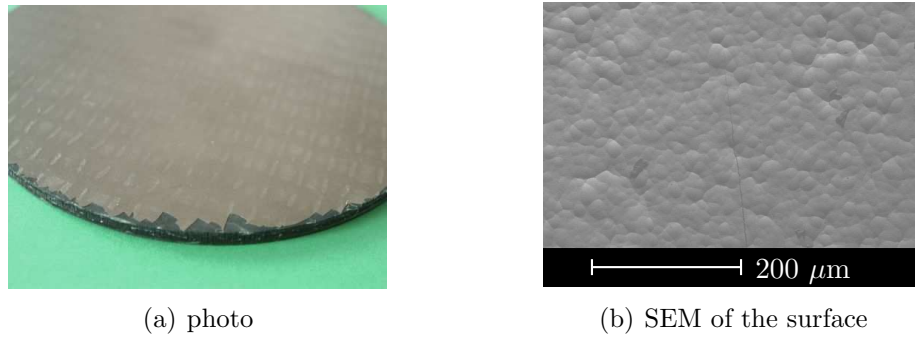


**Figure 4.17:** Photo and SEM image of the Ni coating (M30).

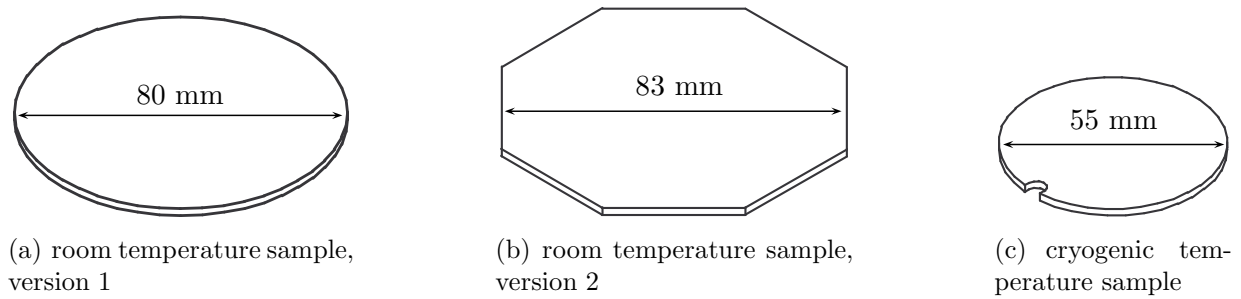


**Figure 4.18:** Geometry and dimension of the specimens used for the permeation measurement.

### 4.3 Specimens

All CFRP substrates were produced as rectangular plates with different sizes. Common dimensions of the plates were  $200 \times 100 \text{ mm}^2$  and  $400 \times 200 \text{ mm}^2$ . The liners were produced on these plates. The specimens for the permeation measurements were cut out of the plates by means of two techniques. On one hand, a water jet with 0.5 mm in diameter and a pressure of more than 1000 bar was applied. In some cases, the liner was locally separated from the substrate, when the water was partly reflected at the interface between the CFRP and the liner. Additionally, the usage of water implied a source of oxidation. On the other hand, specimens were prepared by means of a circular saw with a diamond coated blade. This technique enabled sharp cut lines without any destruction of the liner. The ability to saw only straight lines and the creation of fine carbon dust were disadvantageous.

The permeation measurements were performed in two different apparatuses (refer to chapter 5). The according specimens are shown in figure 4.18. The thickness of all permeation specimens was between 1.4 mm and 3 mm. The diameter of the RT specimens was approximately 80 mm, while that of the cryogenic temperature specimens was only 55 mm. The circular samples were prepared by means of water-jet cutting; the octagonal samples were prepared by means of a circular saw. The cryogenic temperature specimens additionally contained a clearance for easier dismounting after the permeation tests.

## Chapter 5

# Measurement of Permeation

*“...An experiment is something everybody believes, except the person who made it.”* Albert Einstein

### 5.1 Room Temperature Permeation Measurement Apparatus (RTPMA)

#### 5.1.1 Test Set-up

The permeation measurements at room temperature were performed at the RTPMA. A heating system additionally allowed permeation tests at temperatures up to 100 °C. The design of the RTPMA is schematically shown in figure 5.1. The following explanations refer to this figure.

The apparatus can be subdivided into the gas supply-, evacuation- and measuring chamber. The three chambers are separated by the specimen and a valve (18), respectively. Each chamber can be heated, pressurized, vented or evacuated separately.

The gas supply chamber consists of the upper specimen holder (9), a controllable heating system (7, 8,  $T_{1a}$ ,  $T_{1b}$ ), a piezo-resistive pressure gauge (6) and the gas feed system (1-3). The chamber can be pressurized with hydrogen or helium up to 6 bar or evacuated by means of a scroll pump (17). The two thermocouples ( $T_{1a}$ ,  $T_{1b}$ ) give information about the temperature of the upper specimen holder and the feed gas, respectively. While the heating system is controlled by  $T_{1a}$ ,  $T_{1b}$  is continuously recorded for verification.

The discoid specimen (refer to 4.3) is mounted between the lower and upper specimen holder, see figure 5.2. In order to guarantee no leakage, the specimen is sealed with indium wires (1 mm in diameter). The ends of the indium wire are cut angularly and are joined subsequently. The two specimen holders are tightened by means of eight bolts to squeeze the indium wire.

The permeate side of the sample is divided into the evacuation- and the measuring chamber to prevent any contamination of the measuring instruments. The evacuation chamber is open during the assembly of the specimen and can be separately pumped afterwards. The measuring chamber consists of a pressure gauge (19) and a quadrupole mass spectrometer (QMS, 20) to record the total pressure and partial pressures. Because of their sensitivity to contamination, both devices must not be exposed to pressures higher than  $10^{-4}$  mbar. At ambient pressures, the devices would absorb a high amount of molecules which could only be released after a long and high-temperature bake-out process. Baking-out the mass spectrometer degrades its filaments. The measuring chamber is permanently

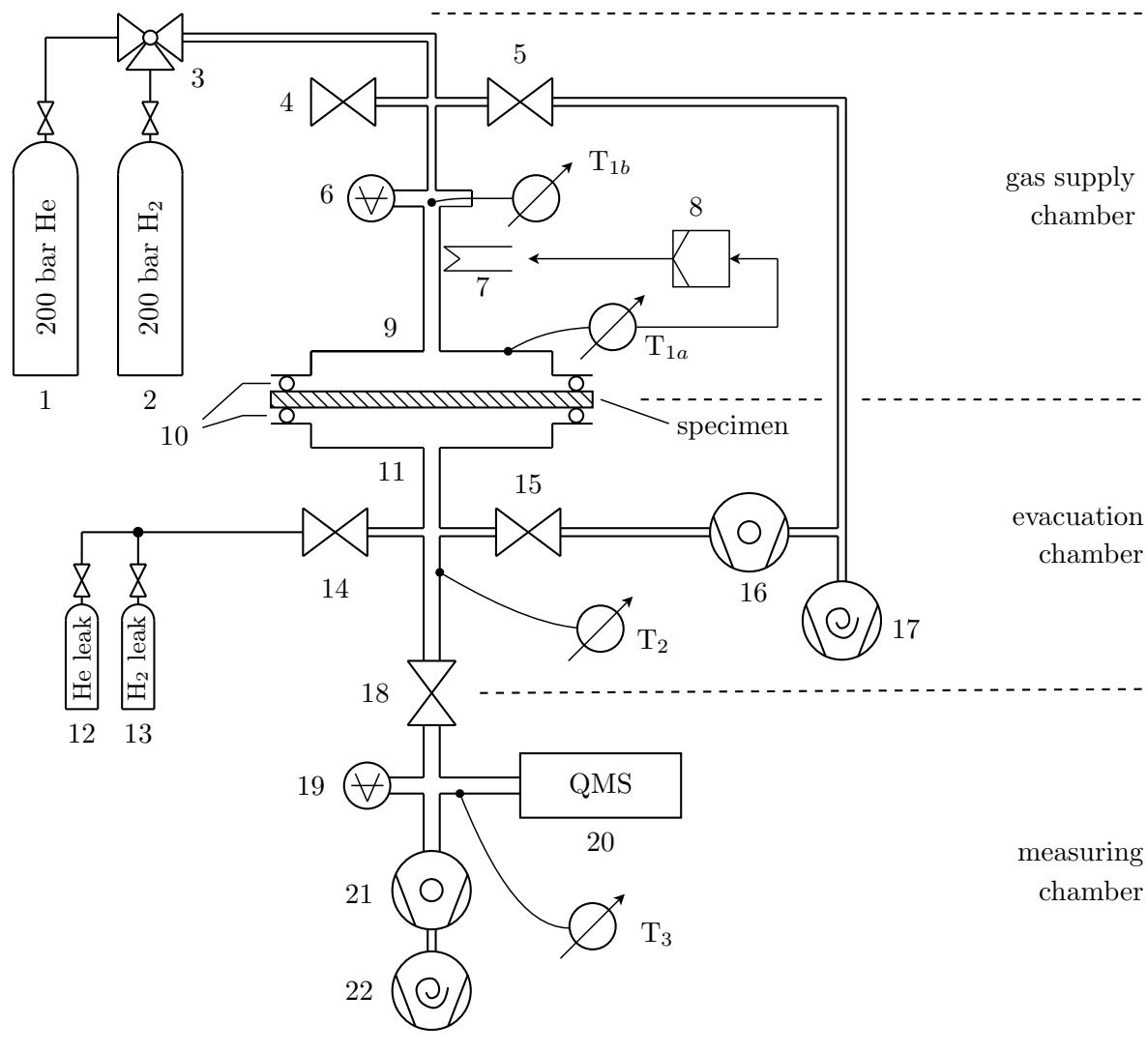


**Figure 5.1:** Schematic diagram of the RTPMA. 1: helium gas bottle with pressure regulator; 2: hydrogen gas bottle with pressure regulator; 3: three-way valve; 4: relief valve; 5: ball valve; 6: piezo pressure gauge, Pfeiffer APR 266; 7: heating; 8: heating control; 9: upper specimen holder; 10: sealing (indium wire); 11: lower specimen holder; 12: helium calibrated leak, Pfeiffer CT 446; 13: hydrogen calibrated leak, VTI CL-6-H<sub>2</sub>-MCFF-1000DOT-MFV; 14: all metal dosing valve; 15: gate valve; 16: turbomolecular pump, BOC Edwards EXT70/4; 17: scroll pump, BOC Edwards XDS 10; 18: pneumatic gate valve; 19: inverted magnetron gauge, BOC Edwards AIM-X-DN40CF; 20: quadrupole mass spectrometer, MKS e-Vision+; 21: turbomolecular pump, Leybold HyCone 200; 22: scroll pump, BOC Edwards XDS 10; T<sub>1a</sub>...T<sub>3</sub>: thermocouples.

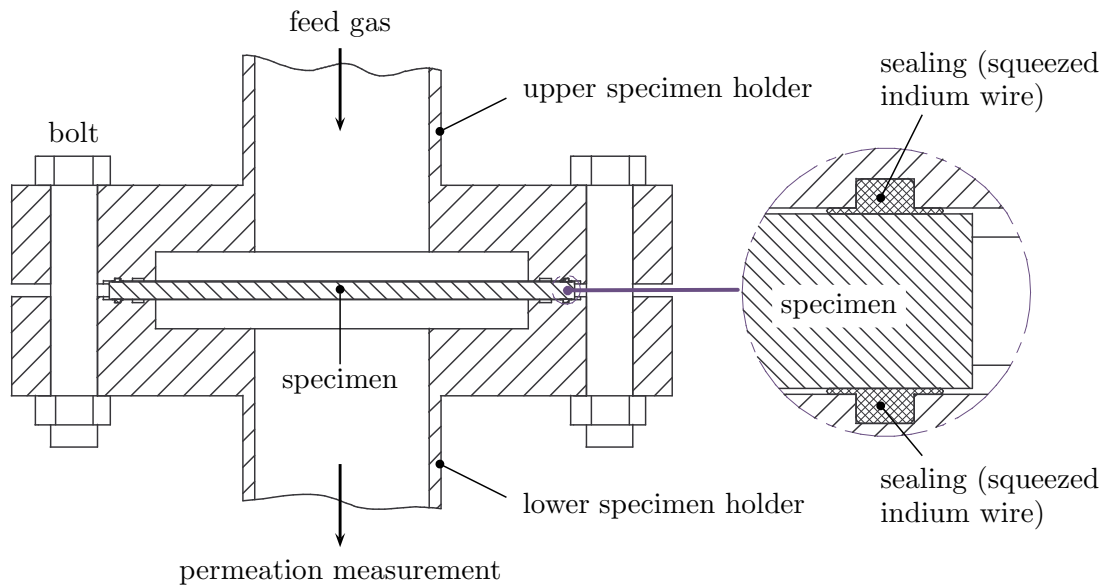


**Figure 5.2:** Drawing of the specimen holders and of the sample's sealing.

evacuated by a turbomolecular pump (21), that means the permeation measurement is performed in a flowing stream (refer to 2.5.2).

The usage of hydrogen as permeating gas requires the employment of safety equipment. The room, in which the RTPMA and CPMA (see 5.2) are located in, is instrumented with three hydrogen sensors. The sensors give input to a control system. If the maximum allowable hydrogen concentration is exceeded, the hydrogen gas supply is closed by means of a magnetic valve. Furthermore, an acoustic and a visual signal are output.

### 5.1.2 Test Procedure

The typical test procedure included three main steps: the assembly of the sample and preparations, the permeation test, and the disassembly of the sample.

The assembly and sealing of the sample were carried out very carefully to provide a leak-free permeation measurement. The ends of the indium wire were joined by pressing them slightly together. The bolts were tightened to squeeze the indium wire into the microscopically rough surface of the specimen. Trials showed that gradual tightening in peripheral direction is optimal for squeezing the indium wire.

After the assembly, the tightness of the sealing was roughly checked. Therefore, the evacuation chamber was pumped approximately 5 minutes. Afterwards it was briefly connected with the measurement chamber and then disconnect again. A strong leakage was present if the total pressure was very high ( $\gtrsim 10^{-5}$  mbar) and mainly defined by the partial pressures of nitrogen,  $p_{N_2}$ , and oxygen,  $p_{O_2}$ . If the ratio  $p_{N_2}/p_{O_2}$  was greater than three, a high leakage could be excluded.

After the successful checking of the sealing, the evacuation chamber including the leak supply was baked out at 120 °C for 24 hours. Because of its thermal connection to the

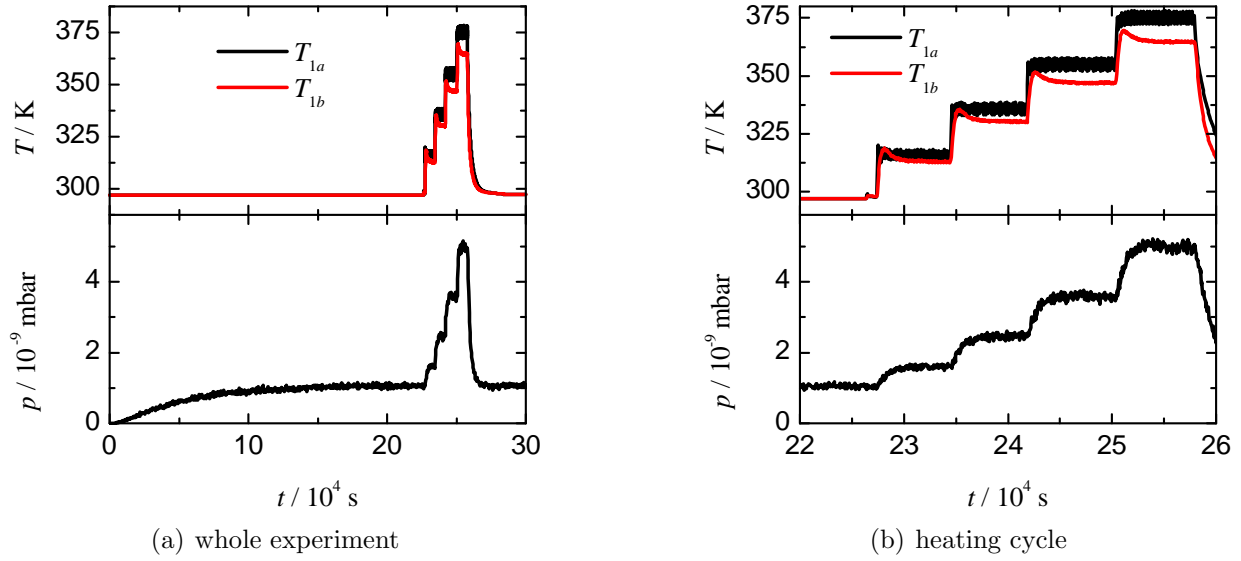


**Figure 5.3:** Example of a permeation measurement, sample S89. The temperature of the feed gas ( $T_{1b}$ ), the heating control temperature ( $T_{1a}$ ) and the measured partial pressure of the permeating gas ( $p$ ) are plotted as a function of the time,  $t$ .

chamber, the specimen was also heated. Measurements revealed that the sample's temperature never exceeds  $80^\circ\text{C}$ . The bake-out accelerated the outgassing of the evacuation chamber as well as the specimen.

After cooling, the evacuation- and measuring chamber were connected again and valve 15 was closed. The calibration of the QMS was carried out to relate the measured partial pressure of the permeating gas with the according gas flow. Because of its importance for high-quality results, the calibration process is described in more detail in 5.1.3. Following the calibration, valve 14 was closed to shut off the calibration gas. Helium was sprayed at the outside of the sample's sealing to check the tightness between the specimen and the lower specimen holder. The tightness of the gas supply chamber was inspected by opening valve 5 to evacuate the chamber. Closing the valve again, a possible pressure increase gave information about the tightness.

The permeation experiment started by feeding the test gas to the specimen. During the experiment, the following quantities were measured and recorded: the feed pressure,  $p_f$  (6), the temperature of the feed gas,  $T_f$  ( $T_{1b}$ ), and the residual gas spectrum of the permeate side. The partial pressure of the permeating gas,  $p$ , was of particular importance. After reaching the steady-state condition (refer to 2.4.3), the temperature of the feed gas was increased by means of the heating system (7, 8,  $T_{1a}$ ).

Figure 5.3 shows exemplarily the measured values during the permeation experiment of sample S89. Starting at room temperature, the steady-state condition was reached after approximately 2.5 days. Subsequently, the control temperature of the feed chamber,  $T_{1a}$ , was increased. The temperature of the feed gas,  $T_{1b}$ , showed a overshooting response and

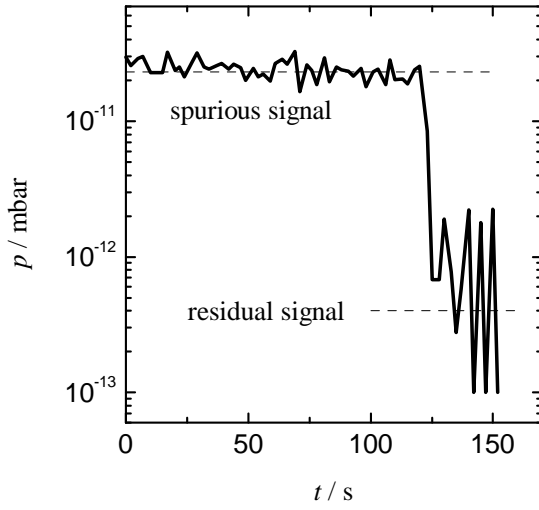


**Figure 5.4:** Calibration of the mass spectrometer by means of a helium leak. The partial helium pressure is plotted as a function of the time. At  $t = 120$  s, the leak is disconnected and the residual helium pressure is measured.

became constant after approximately one hour (see figure 5.3-b). The partial pressure of the permeating gas, and hence the permeation flux, increased accordingly until a new steady-state flux was established. The temperature increase was repeated three more times. Afterwards, the system was cooled to room temperature again.

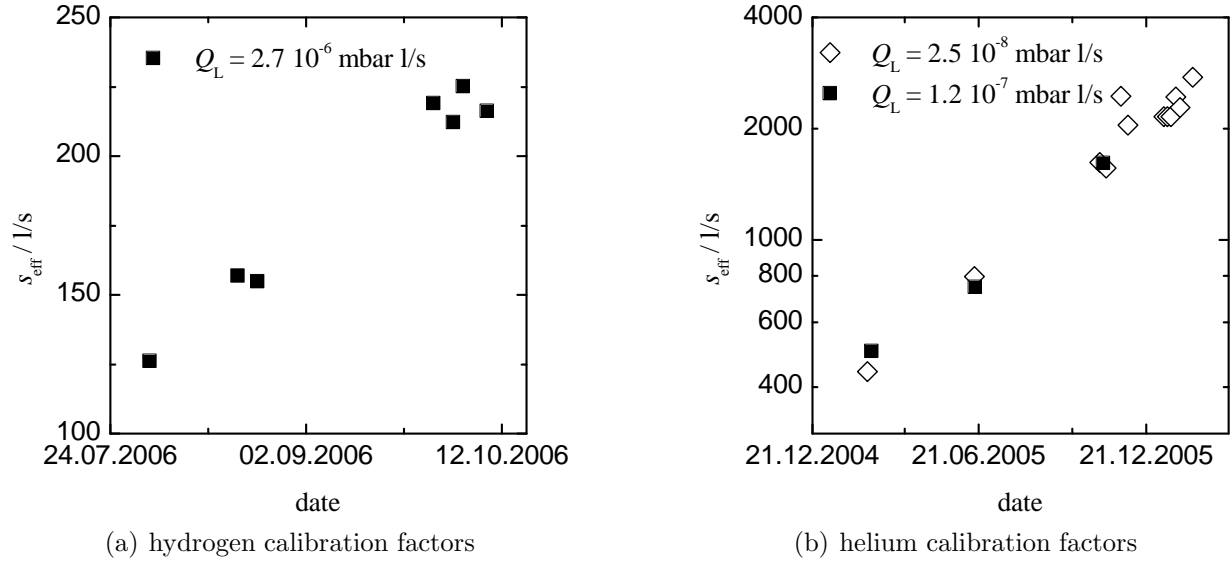
The last part of the test procedure consisted of the specimen's disassembly. Therefore, the feed gas was released and the measuring chamber was disconnected from the evacuation chamber. The calibrated leaks being disconnected, valve 14 was opened to flood the evacuation chamber. The specimen holders were dismounted, and the sample itself was detached. The detachment had to be carried out without the help of metallic instruments to not harm the surface of the specimen holders. After the detachment of the specimen, the sealing surface of the holders was cleaned from residual indium.

### 5.1.3 Calibration

The calibration procedure is explained by referring to the elements drawn in figure 5.1. After the successful assembly of the specimen and the subsequent bake-out, valves 14 and 18 were opened, and valve 15 was closed. Thereby, the calibrated leak was connected with the measuring chamber. The mass conversation principle of this case leads to  $-Q_T + Q_L = 0$ , where  $Q_T$  is the throughput and  $Q_L$  is the rate of the calibrated leak. Considering the term of the throughput (2.38), one obtains

$$s_{\text{eff}} = \frac{Q_L}{p}. \quad (5.1)$$

Equation 5.1 denotes the determination of the calibration factor. The introduced, well-defined leak rate,  $Q_L$ , results in the increase of the partial pressure of the calibration gas,  $p$ , recorded by the QMS. The value of  $p$  is spurious and must be corrected by the residual signal. The residual pressure of the calibrating gas was measured by closing the valve of the leak.



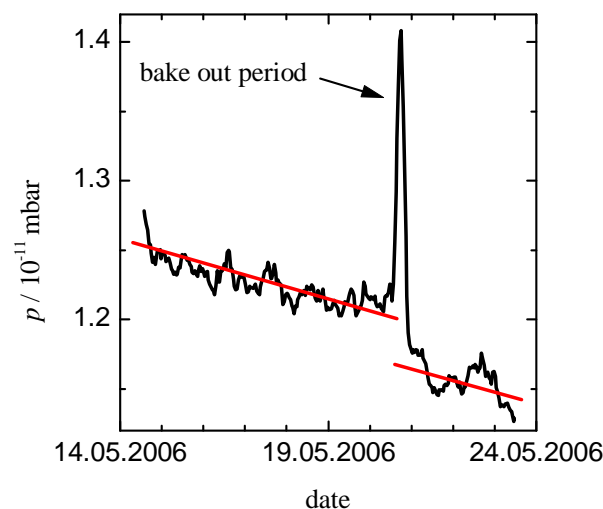
**Figure 5.5:** The calibration factor of the QMS,  $s_{\text{eff}}$ , as a function of the time. The generally observed increase of  $s_{\text{eff}}$  is believed to result from a degeneration of the mass spectrometer.

Figure 5.4 shows exemplarily the results of one helium calibration. The calibrated leak with  $Q_{\text{L,He}} = 2.5 \cdot 10^{-8}$  mbar l/s increased the helium pressure to  $p = 2.43 \cdot 10^{-11}$  mbar. The residual helium pressure was approximately  $4 \cdot 10^{-13}$  mbar and much less than the spurious signal. Consequently, the corrected signal ( $2.39 \cdot 10^{-11}$  mbar) did not differ strongly from the spurious signal (2 %). The effective pumping speed in this case was  $s_{\text{eff}} = 1046$  l/s.

In order to investigate the influence of the leak rate on the QMS signal, three different helium and three different hydrogen calibrated leaks were utilized. Introducing helium leak rates of  $2.5 \cdot 10^{-8}$ ,  $1.2 \cdot 10^{-7}$  and  $5.1 \cdot 10^{-6}$  mbar l/s, the calculated effective pumping speed was approximately equal. Since the calibrated leak with  $Q_L = 2.5 \cdot 10^{-8}$  mbar l/s was most similar to the expected permeation rates, it was employed in the following. Introducing hydrogen leak rates of  $3 \cdot 10^{-8}$  and  $1.3 \cdot 10^{-7}$  mbar l/s, the measured spurious signals were only 2 – 3 times higher than the residual signal. Hence, all hydrogen calibrations were carried out with a  $2.7 \cdot 10^{-6}$  mbar l/s leak.

Figure 5.5 displays the calibration factor of helium and hydrogen, respectively, for selected periods of time.  $s_{\text{eff}}$  varied from one experiment to the other and generally increased by time. Considering helium, the calibration factor increased nearly by factor 10 within one year. A drift of the calibrated leak can be excluded, because the manufacturer [148] reports a decrease of the leak rate between 1 % and 4 % per year. Furthermore, the validation with a second calibrated leak confirmed the great increase of  $s_{\text{eff}}$  (see figure 5.5-b). Hence, with regard to (5.1), an increasing  $s_{\text{eff}}$  and a nearly constant  $Q_L$  implies a decreasing measured partial pressure,  $p$ . It is assumed, that the filaments of the mass spectrometer degraded and hence the detection rate decreased. An exchange of the filaments by the manufacturer revealed a strong oxidation. To confirm the oxidation theory, a long-term He





**Figure 5.6:** Long-term helium calibration of the mass spectrometer. The partial helium pressure is plotted as a function of the time. On 20.05.2006, a bake out period was carried out. The measured signal decreases gradually in general, and strongly after heating.

calibration including a heating period of the evacuation chamber at 120 °C was performed. The measured partial pressure decreased gradually by time and significantly after a heating period, see figure 5.6.

Summarizing, the calibration of the mass spectrometer before each permeation measurement is mandatory for high-quality results. The usage of the nominal pumping speed to calculate the permeation gas flow does not cover a potential degeneration of the measuring device and leads to wrong results.

## 5.2 Cryogenic Permeation Measurement Apparatus (CPMA)

The permeation measurements at temperatures between 20 K and room temperature were performed at the CPMA. The main part of the CPMA was the continuous flow cryostat produced by CryoVac. Its design is schematically drawn in figure 5.7. The cryostat was a modified version based on that used in the work of Humpenöder [88].

The sample was mounted in the middle of the cryostat between the heat exchanger plate and the feed gas cap. The sealing are, similar to the RTPMA, two 1 mm indium wires. The indium wires were squeezed by tightening the bolts of the feed gas cap. The heat exchanger plate and hence the sample and the feed gas cap were cooled by means of liquid helium. The liquid helium was introduced on one side of the cryostat and flew through several heat exchangers driven by a low pressure applied at the outlet. Two heat shields were employed and the space inside the cryostat was evacuated in order to insulate the cold parts. The outer heat shield was additionally connected with a heat exchanger. The temperature was recorded by two gauges (Si-diodes DT-670-A/CU) located at the heat exchanger plate near the sample and at the feed gas cap. The temperature was set by regulating the LHe throughput and activating the heating on demand.

The overall set-up of the CPMA is illustrated in figure 5.8. A photograph of it is shown in figure 5.9. The LHe inlet of the cryostat was connected to a LHe can by a detachable transfer tube. A helium-tight vacuum pump (1) generated the vacuum to let

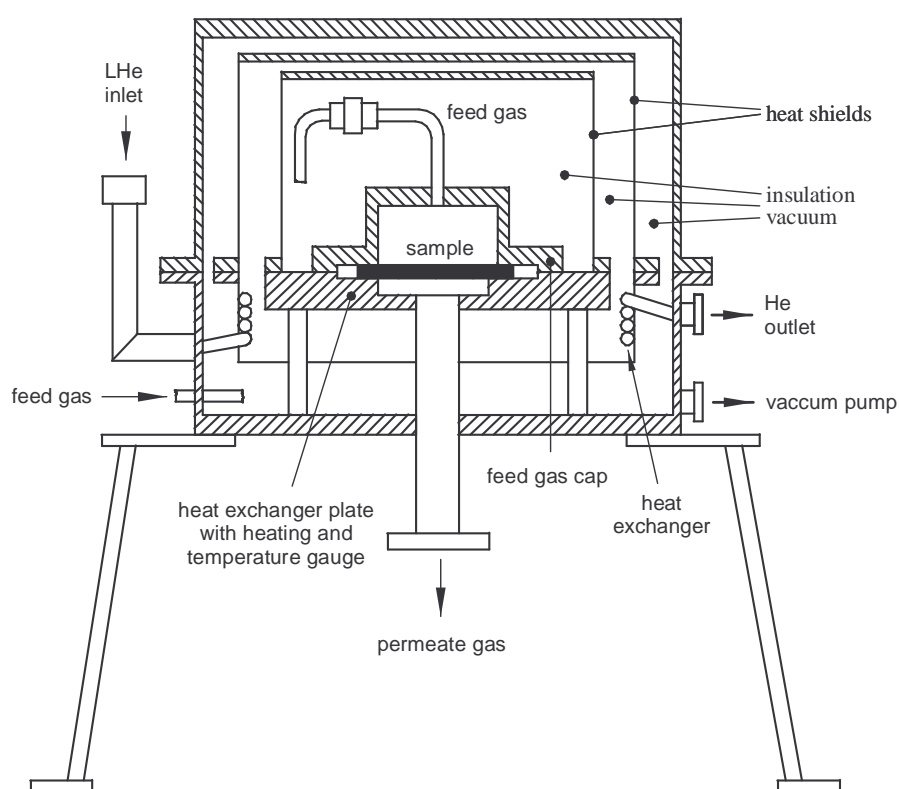


**Figure 5.7:** Schematic diagram of the cryostat. Bolts and electrical components like the resistive heating system and temperature gauges are not drawn. The feed gas pipe is drawn discontinuously. Partly redrawn from [88].

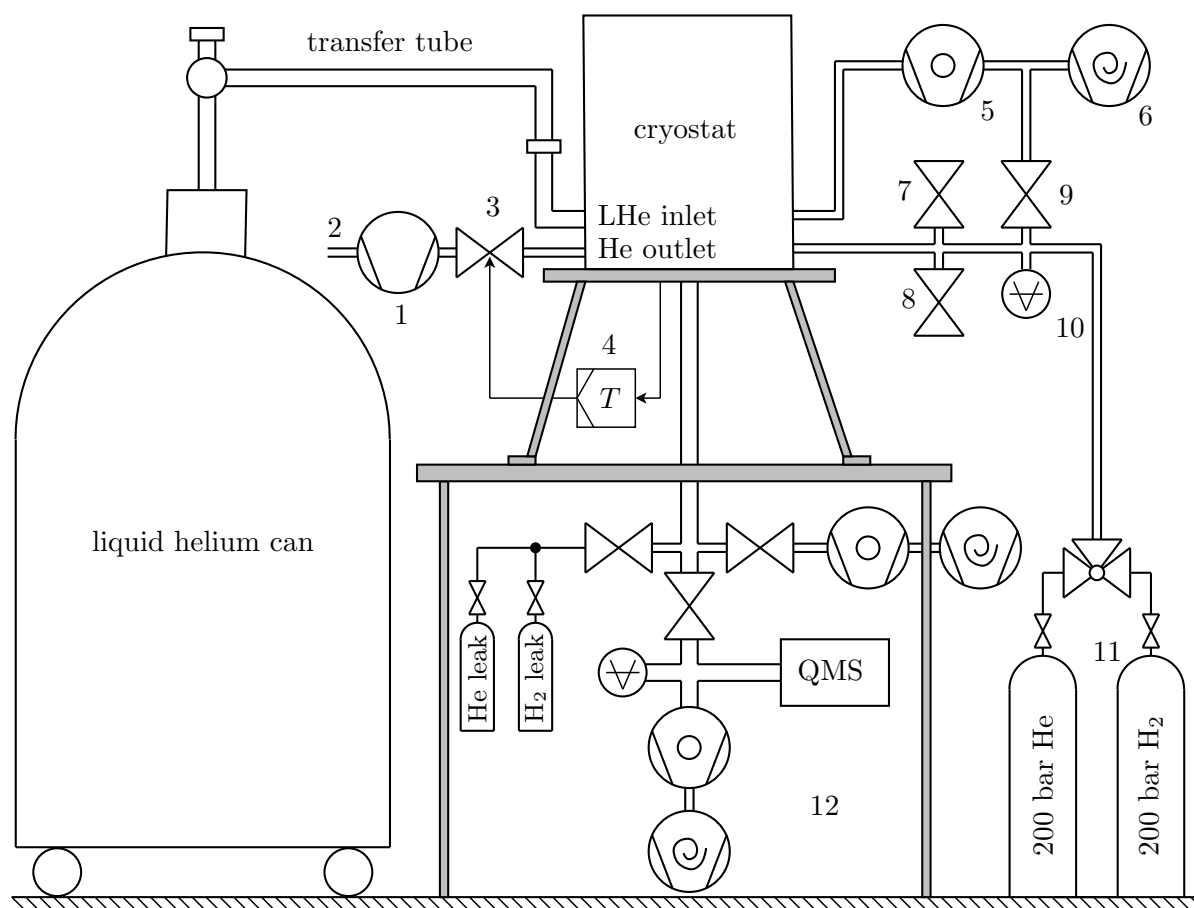


**Figure 5.8:** Schematic diagram of the CPMA. The set-up can be subdivided into (a) the cryostat including the specimen; (b) the cooling system: LHe can, transfer tube, He-tight pump (1), recirculation to the He liquefier (2), control valve (3) and temperature control system (4); (c) the feed pressure system: 200 bar He and H<sub>2</sub> bottles (11), safety valves (7, 8), evacuation valve (9), and pressure gauge (10); (d) the vacuum generation system: turbomolecular pump (5) and scroll pump (6); and (e) the permeation measurement system (12): consisting of an evacuation and measuring chamber as described in figure 5.1.

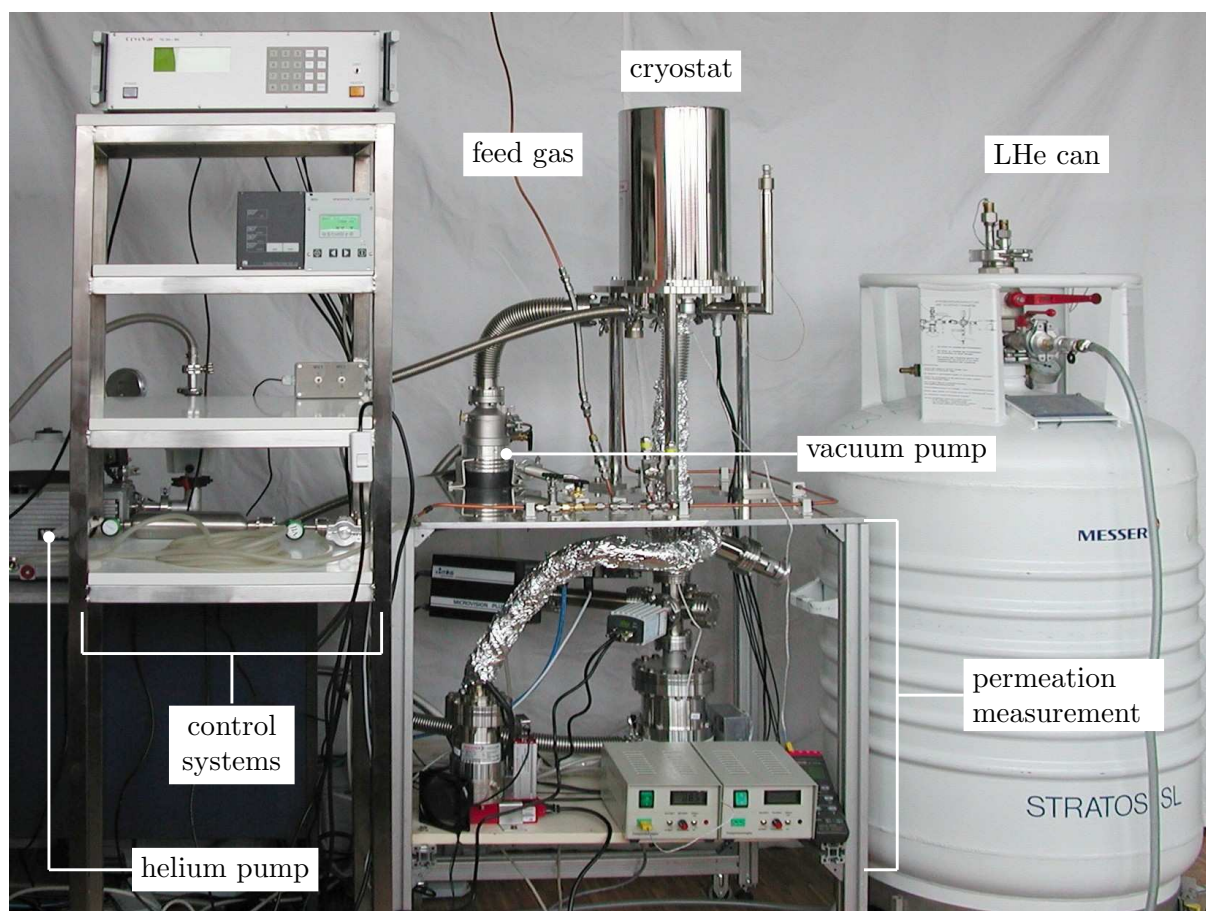


**Figure 5.9:** Photography of the CPMA. Scroll pumps, the LHe transfer tube and the computer are not shown.

the LHe flow through the cryostat. The throughput was regulated by a valve (3) which was set by a temperature control system (4). An in-house liquefaction equipment (2) recycled the transferred helium. The insulating vacuum of the cryostat was produced by the combination of a turbomolecular and a scroll pump (5, 6). The feed pressure system was analogous to that of the RTPMA. Considering the temperature range and a potential expansion of the feed gases, two separate safety valves (7, 8) were additionally employed. The permeate side of the cryostat was connected with the measuring system (12). Its design corresponds to that of the RTPMA. Again, the separation into an evacuation and a measuring chamber enabled a reduced contamination of the measuring instruments.

The test procedure of the CPMA was similar to that of the RTPMA (refer to 5.1.2). The preparations before the experiment additionally included the assembly of the heat shields of the cryostat. Following the calibration, the permeate gas was fed at room temperature to the specimen. After the steady-state condition was established, the specimen and the feed gas were cooled at successive steps. If the permeation signal was as low as the residual signal, the cooling process was carried out continuously to 20 K.

### 5.3 Evaluation and Error Estimation

In both permeation measurement apparatuses, the partial pressure of permeating gas,  $p(t)$ , the variable temperature of the feed gas,  $T(t)$ , and the feed pressure,  $p_f$ , were recorded. The apparatuses only differed from each other regarding the effective permeation area of the specimen. The effective permeating area is given by the diameter of the sealing ring. The diameters of the sealing in the RTPMA and CPMA were 72 mm and 43 mm respectively. The recorded data were evaluated by the following algorithm:

1. Calculation of the permeation gas flow, (2.39):  $Q_P(t) = s_{\text{eff}} p(t)$ .
2. For each feed gas temperature, reading of the steady-state permeation gas flow:  $Q_{\text{ss}}(T_1), Q_{\text{ss}}(T_2), \dots$
3. For each feed gas temperature, calculation of the permeability using (2.7) and (2.40):

$$P(T) = \frac{Q_{\text{ss}}(T) l}{A R T_{\text{mc}} p_f^n}, \quad (5.2)$$

where  $l$  is the thickness of the specimen,  $A$  is the permeation area of the specimen,  $R$  is the universal gas constant,  $T_{\text{mc}}$  is the temperature of the measuring chamber,  $p_f$  is the feed pressure, and  $n$  is the pressure exponent.

4. Fitting the Arrhenius equation (2.35) to the  $[T, P]$  data  $\rightarrow$  determination of  $P_0$  and  $E_P$ .
5. Determination of the diffusivity as described in 2.5.2.

The relative error of the permeability is assessed in the following. Equation 5.2 determines the permeability using measured quantities, a natural constant and two derived variable,  $Q_{\text{ss}}$  and  $A$ . Considering (2.39) and (5.1),  $Q_{\text{ss}}$  can be substituted by  $Q_L p_{\text{ss}}/p_{\text{cal}}$ , where  $Q_L$  is the rate of the calibrated leak,  $p_{\text{ss}}$  is the partial, steady-state pressure of the permeating gas, and  $p_{\text{cal}}$  is the partial pressure of the permeating gas during calibration. The effective permeation area can be replaced by the diameter of the sealing ring,  $d$ . The permeability as a function of non-derived quantities is

$$P(T) = \frac{4}{\pi} \frac{Q_L p_{\text{ss}}(T) l}{R T_{\text{mc}} p_f p_{\text{cal}} d^2}.$$

The law of error propagation leads to the sum of the relative errors:

$$\frac{\Delta P}{P} = \frac{\Delta Q_L}{Q_L} + \frac{\Delta p_{\text{ss}}}{p_{\text{ss}}} + \frac{\Delta l}{l} + \frac{\Delta R}{R} + \frac{\Delta T_{\text{mc}}}{T_{\text{mc}}} + \frac{\Delta p_f}{p_f} + \frac{\Delta p_{\text{cal}}}{p_{\text{cal}}} + 2 \frac{\Delta d}{d}.$$

The single variables and their relative errors are listed and explained in table 5.1. Thereby, the relative error of the permeability is determined to

$$\frac{\Delta P}{P} = 55 \%. \quad (5.3)$$

**Table 5.1:** Relative errors of variables to determine the permeability. All errors are random.

var	description	rel. err.	description
$Q_L$	leak rate of the calibrated leak	30 %	uncertainty specified by the producer
$p_{ss}$	partial pressure of permeating gas at the steady-state condition	10 %	reading error, estimated uncertainty
$l$	thickness of the specimen	1.2 %	mean value of all relative standard deviations
$R$	molar gas constant	0 %	exact: $1.2 \cdot 10^{-4}$ % [149]
$T_{mc}$	temperature of the measuring chamber	1.6 %	estimated uncertainty: $T_{mc} \approx 300$ K, $\Delta T < 5$ K
$p_f$	feed pressure	0.5 %	estimated uncertainty: $p_f \approx 2$ bar, $\Delta p_f < 0.01$ bar
$p_{cal}$	partial pressure of calibrated leak gas	9 %	reading error, standard deviation
$d$	diameter of the sealing ring	1.2 %	instrument limit of error, $d_{CPMA} = 43$ mm, $d_{RTPMA} = 72$ mm, $\Delta d = 0.5$ mm

The main influence on this great error is caused by the calibration. The uncertainty of the calibrated leak and the reading error of the calibration signal are already 39 % in sum. The second greatest error is caused by reading the permeation signal. This error includes the relative standard deviation of the steady-state signal as well as the uncertainty of having reached the steady-state condition. In general, the relative error increases if the measuring signal approaches the level of the residual signal.

## Chapter 6

# Results and Discussion

*“The most exciting phrase to hear in science, the one that heralds the most discoveries, is not 'Eureka!', but 'That's funny...'”* Isaac Asimov

This chapter presents and discusses the results of the permeation measurements and simulations. The quality of the liners with respect to their barrier function are evaluated.

In the first section 6.1, the results of initial permeation tests are presented. There, the reliability of the measuring apparatuses is confirmed. Furthermore, the permeation behavior of helium and hydrogen in selected materials is compared. Helium is used as permeating gas in the following. Finally, the influence of the feed pressure and thermal cycles on the permeability are investigated. The second section 6.2 presents the results of the permeation measurements on the selected material systems. The results of the permeation simulations are described in 6.3. Section 6.4 finally discusses the permeation results and compares them with those of the simulation.

## 6.1 Initial Permeation Tests

### 6.1.1 Reliability of the Measurement Apparatuses

The reliability of experimental results strongly depends on the repeatability and on the agreement with literature data. In order to neglect material deviations, two homogeneous (Al, PVC) and one nearly-homogeneous (CFRP) material system were investigated. The results obtained by both apparatuses are compared with each other and finally validated with literature data.

The helium permeation flux through nine tested aluminum sheets (M05) was always lower than the detection limit (refer to 6.2.2). The repeatability of the test results was not feasible to prove in this case.

The results of three tested PVC specimens (M01: S76, S82 and S88c) are summarized in table D.1 and graphically shown in figure 6.1. The He permeabilities at RT were well coinciding. The relative standard deviation of the three permeabilities was 1.72 % but that of the diffusivities varied by 15 %. The flux-time behaviors were moderately different, but all specimens showed Fickian behavior (see figure 6.2).

The six CFRP samples of material system M02 revealed well-correlated measuring results (see figure 6.3). Fitting the Arrhenius-type equation (2.35) to the data, the coefficient of determination was  $R^2 = 0.98$ . The band width around the fit, for all data points being enclosed, was 65 %. The RT permeabilities, which were measured either at the RTPMA or

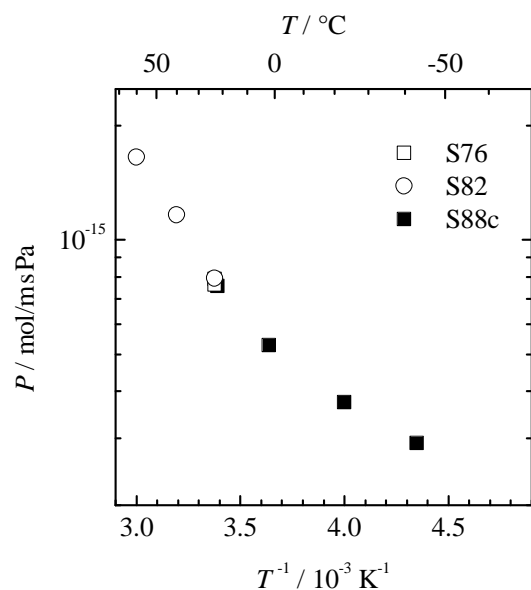


**Figure 6.1:** He Permeability of PVC as a function of the temperature. Hollow and filled symbols denote measurements at the RTPMA and CPMA, respectively. The two last data points of S88c are spurious (near detection limit).

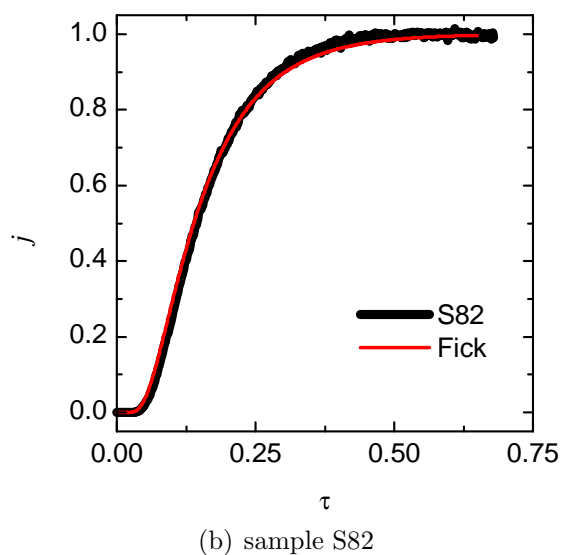
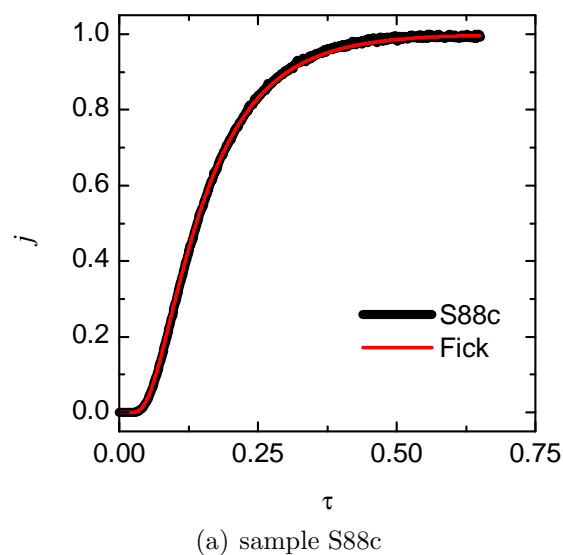


**Figure 6.2:** Flux-time behavior of two PVC samples. In both figures, the experimental data (bold black line) and the theoretical curve according to Fick (thin red line) are plotted. Sample S88c shows exact agreement with Fick's law, while sample S82 exhibits a minor deviation from it.



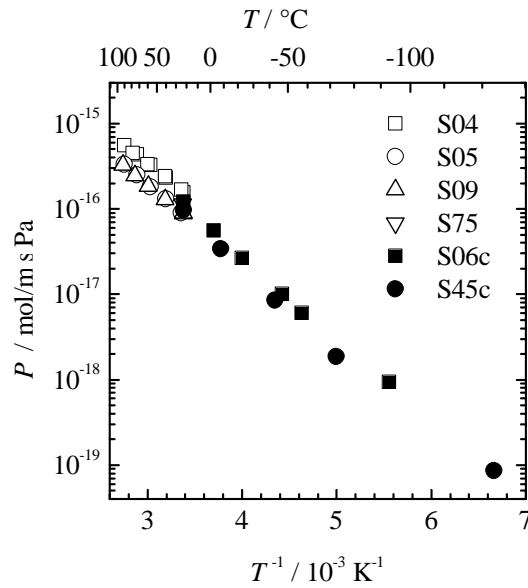


**Figure 6.3:** He Permeability of CFRP as a function of the temperature. Hollow and filled symbols denote measurements at the RTPMA and CPMA, respectively. The data can be fitted by the Arrhenius equation:

$$P = 2.024 \cdot 10^{-13} \exp \left( \frac{-18.607 \text{ kJ/mol}}{RT} \right).$$

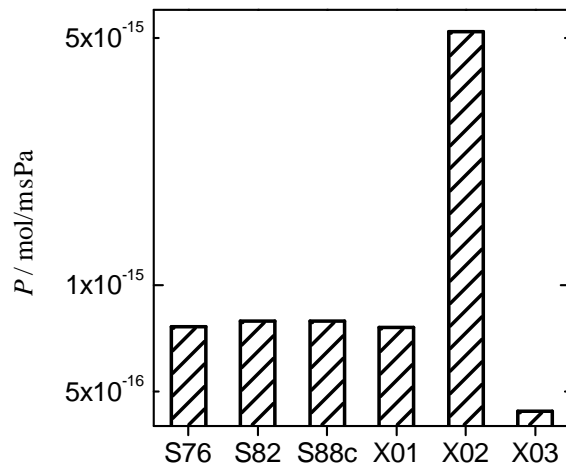


**Figure 6.4:** Comparison of the helium permeabilities of PVC from this work (S76, S82, S88c) and from the literature (X01, X02, X03). The data are plotted in logarithmic scale. X01, X02 and X03 represent the data from [90], [150] and [89], respectively.

CPMA, coincide well (relative standard deviation: 26 %). In the following, the results of the measurements on PVC and CFRP are compared with the data from literature.

The reported helium permeability of PVC at room temperature ranges from  $4.4 \cdot 10^{-16}$  to  $5.2 \cdot 10^{-15}$  mol/m s Pa [89; 90; 150]. This scatter can be explained by differences in the density of PVC. The permeabilities measured in this work being approximately  $7.8 \cdot 10^{-16}$  mol/m s Pa are within this range, which is graphically emphasized in figure 6.4. Humpenöder [150] determined the activation energy of helium permeation through PVC to be 15.752 kJ/mol. The calculated activation energies of specimens S82 and S88c are 16.361 and 12.587 kJ/mol, respectively. Neglecting the latter value, which was derived using spurious signals, the activation energy coincides well.

The structure and hence the transport properties of CFRP varies strongly depending on the fiber type, resin type, and the fiber volume fraction. The He permeabilities reported by Humpenöder [88; 150] range from  $8.62 \cdot 10^{-17}$  mol/m s Pa to  $1.71 \cdot 10^{-16}$  mol/m s Pa, with

$E_P \approx 20$  kJ/mol. Raffaelli [24] determined a very low permeability ( $7.71 \cdot 10^{-20}$  mol/m s Pa) but stated that this value does not agree with those reported by others. The helium permeability of equal CFRP samples of the X33 LH<sub>2</sub> tank [86] varied from  $4.37 \cdot 10^{-20}$  mol/m s Pa to  $4.31 \cdot 10^{-18}$  mol/m s Pa. A feasible explanation of this great scatter (2 orders of magnitude) could be the existence of interlaminar diffusion. The measured He permeabilities of CFRP in this work are all between  $3.73 \cdot 10^{-17}$  and  $3.62 \cdot 10^{-16}$  mol/m s Pa (refer to section 6.2.1 on page 82). The activation energies vary between 14.6 kJ/mol and 19.7 kJ/mol. Considering the potential differences between CFRPs, the obtained values are reasonable.

Summarizing, both permeation measurement apparatuses provide reliable and conforming results. The measured permeabilities of CFRP and PVC agree with those found in the literature.

### 6.1.2 Comparison of Hydrogen and Helium Permeation

The measurement of the partial pressure of hydrogen is more difficult and less accurate than that of helium. The minimum values of the residual pressure of H<sub>2</sub> and He in ultra-high vacuum are circa  $10^{-9}$  and  $10^{-13}$  mbar, respectively. The H<sub>2</sub> signal can even be much higher depending on the hydrogen and water outgassing of the specimen. Considering the typical calibration factors of H<sub>2</sub> and He,  $s_{\text{eff,H}_2} \approx 125 \dots 300$  l/s and  $s_{\text{eff,He}} \approx 400 \dots 4000$  l/s, the minimum detectable permeation gas flows (2.39) are

$$Q_{\text{H}_2, \min} \approx 1.3 \cdot 10^{-7} \text{ mbar l/s, and } Q_{\text{He}, \min} \approx 4 \cdot 10^{-11} \text{ mbar l/s.}$$

Although the minimum detectable gas flow of helium is mostly higher than  $4 \cdot 10^{-11}$  mbar l/s, the difference of more than three orders of magnitude is significant.

The permeation of helium and hydrogen was mainly investigated and compared on those materials, where a high H<sub>2</sub> permeation flux was expected. The tested material systems were PVC, CFRP, DLC-coated CFRP, metal-plated CFRP and steel. The investigated samples and the measured permeabilities are listed in table 6.1. Hydrogen permeation could be detected in seven specimens. In all except one of these, the He permeability was greater than that of H<sub>2</sub> with  $P_{\text{He}}/P_{\text{H}_2} = 0.7 \dots 28$ . The rightmost column of table 6.1 lists the ratios between the hydrogen steady-state signal and the hydrogen residual signal. Except that of PVC, all ratios are less than six and many even less than one. Hence, the quality of all measured H<sub>2</sub> permeabilities is very low.

The characterization of the  $j(\tau)$  curves and the diffusivities is listed in table 6.2. Samples not showing any permeation were not further evaluated. The diffusivity of helium was 3 – 6 times greater than that of hydrogen, i.e. helium permeated 3 – 6 times faster than hydrogen. This agrees well with the theory of 2.5.5. Regarding the  $j(\tau)$  curves, hydrogen exhibited a more pronounced Fickian behavior than helium. Figure 6.5 illustrates exemplarily this behavior of one CFRP specimen. The He flux increased earlier than expected from the Fickian theory, while the H<sub>2</sub> flux was in accordance with Fick's law.

The temperature dependency of the He and H<sub>2</sub> permeabilities is compared for two CFRP samples in table 6.3 and figure 6.6. The activation energy of hydrogen was 36 %

**Table 6.1:** Comparison of He and H<sub>2</sub> permeabilities (mol/msPa) at room temperature.  $Q_{\text{H}_2,\text{ss}}/Q_{\text{H}_2,\text{r}}$  denotes the ratio of the hydrogen steady-state signal to the hydrogen residual signal.

sample	characterization	$P_{\text{He}}$	$P_{\text{H}_2}$	$P_{\text{He}}/P_{\text{H}_2}$	$Q_{\text{H}_2,\text{ss}}/Q_{\text{H}_2,\text{r}}$
S76 (M01)	PVC	7.63E-16	2.32E-16	3.3	37
S09 (M02)	CFRP	8.73E-17	7.84E-17	1.1	3.9
S85 (M04)	CFRP	3.62E-16	4.55E-17	8.0	2.7
S90 (M03)	CFRP	1.24E-16	8.34E-17	1.5	5.2
S89 (M28)	CFRP+DLC	4.38E-17	2.95E-17	1.5	1.7
S20c (M14)	CFRP+cNiP-cAu	4.71E-17	1.69E-18	27.8	1.5
S23 (M14)	CFRP+cNiP-cAu	1.86E-17	2.83E-17	0.7	3.7
S32c (M17)	CFRP+cNiP-Ni	$\leq 5.47\text{E-}20$	$\leq 7.32\text{E-}19$	—	$\leq 1$
S44 (M15)	CFRP+cNiP-Cu	$3.68\text{E-}19$	$\leq 1,71\text{E-}18$	—	$\leq 1$
S80 (M11)	GFRP+cCu-Cu	$\leq 1.57\text{E-}20$	$\leq 1.64\text{E-}18$	—	$\leq 1$
S84 (M06)	Fe	$\leq 2.32\text{E-}21$	$\leq 8.52\text{E-}19$	—	$\leq 1$

**Table 6.2:** Comparison of the He and H<sub>2</sub> permeation performance at room temperature. The unit of the diffusivities is  $\text{m}^2\text{s}^{-1}$ .

sample	He flux-time behavior	H <sub>2</sub> flux-time behavior	$D_{\text{He}}$	$D_{\text{H}_2}$	$D_{\text{He}}/D_{\text{H}_2}$
S76	near Fickian	exact Fickian	3.0E-10	5.2E-11	5.8
S09	near Fickian	exact Fickian	4.2E-11	1.1E-11	3.8
S85	exact Fickian	exact Fickian	1.4E-10	3E-11	4.7
S90	exact Fickian	exact Fickian	8E-11	1.6E-11	5.0
S89	not Fickian	near Fickian	2E-11	6E-12	3.3
S20c	not Fickian	—	2E-11	—	—
S23	—	near Fickian	—	2E-11	—

**Table 6.3:** Comparison of temperature-dependent He and H<sub>2</sub> permeation. The permeabilities of helium and hydrogen are expressed by means of the pre-exponential factor  $P_0$  (mol/m s Pa) and the activation energy  $E_P$  (kJ/mol).

sample	temperature range	$P_{0,\text{He}}$	$P_{0,\text{H}_2}$	$E_{P,\text{He}}$	$E_{P,\text{H}_2}$	$E_{P,\text{He}}/E_{P,\text{H}_2}$
S90	296 – 365 K	$6.20 \cdot 10^{-14}$	$2.25 \cdot 10^{-12}$	15.364	25.092	0.61
S09	296 – 349 K	$8.48 \cdot 10^{-14}$	$9.67 \cdot 10^{-13}$	16.936	23.121	0.73

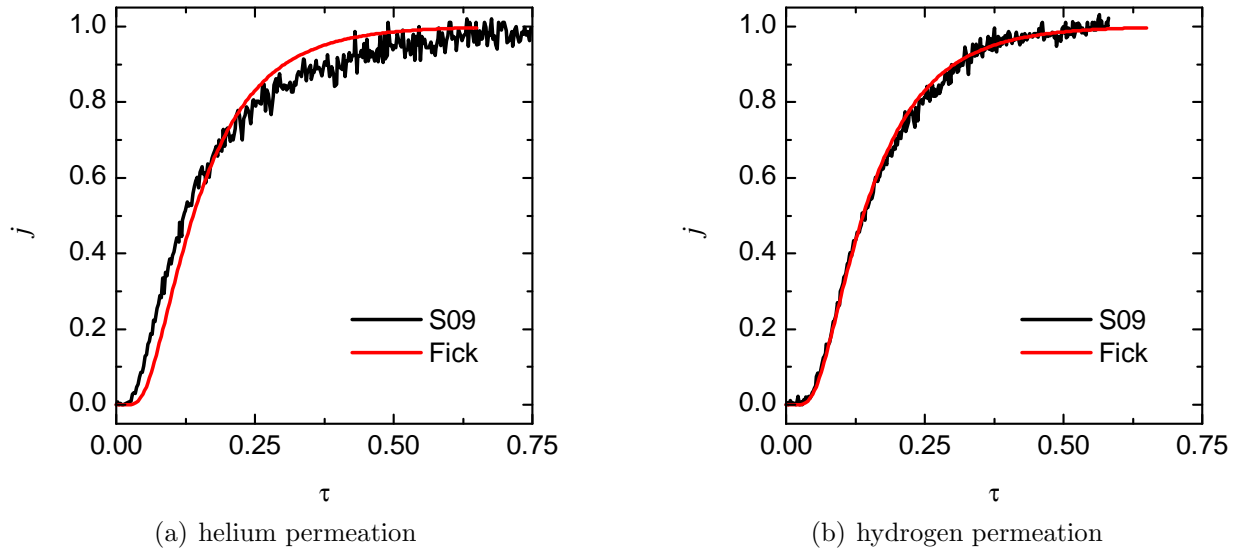


**Figure 6.5:** Comparison of the He and H<sub>2</sub> flux-time behavior of CFRP (S09). While the He permeation exhibits a minor deviation from the Fickian behavior, H<sub>2</sub> permeates according to it.

and 64 %, respectively, higher than that of helium. This result confirms the theory, that atoms with greater molecular radius require more energy to jump from one free volume to the next.

The measurement of H<sub>2</sub> permeation was not only challenging because of its low measuring-to-residual ratio, but also because of a strong environmental influence on the measuring signal. He and H<sub>2</sub> permeation tests, performed on a CFRP+DLC specimen (S89) for 61 and 120 hours, respectively, produced repeating excursions of the  $Q(t)$  curves, see figure 6.7. While the measured hydrogen gas flow oscillated strongly within one day, the excursions of the helium gas flow were comparably low. The maximum excursion of the hydrogen gas flow between morning and afternoon was 23 %, that of helium less than 5 %.

In order to determine possible reasons for the excursions, another long-term (13 days) experiment was performed. The H<sub>2</sub> gas flow through the CFRP+cNiP-cAu specimen (S23) is plotted as a function of time in figure 6.8. Again, the frequency of the excursions was one day. It was assumed that environmental influences like sunshine durance, temperature or air pressure can cause these excursions. While the air pressure and the temperatures did not exhibit any correlation to the excursions, the sunshine durance and the difference between maximum and minimum day temperature show a partial correlation<sup>1</sup>. Figure 6.9 displays these two parameters in relation to the measured daily excursion of the steady-state gas flow (29.08.-06.09.2006). Although a linear correlation does not exist, a trend and hence a dependency is recognizable. Mainly the sunshine durance seems to have an influence on the hydrogen measuring signal. It is believed that the changing temperature strongly affects the ad- or desorption of hydrogen into or from the stainless steel chambers

<sup>1</sup>Weather data for the investigated period in Augsburg, Germany was found in [151].

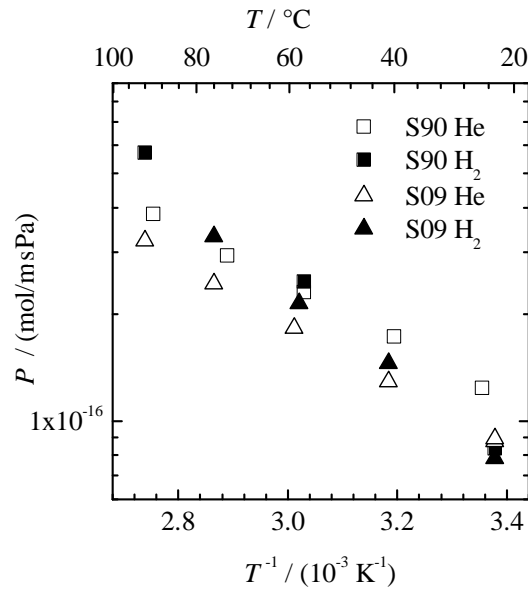
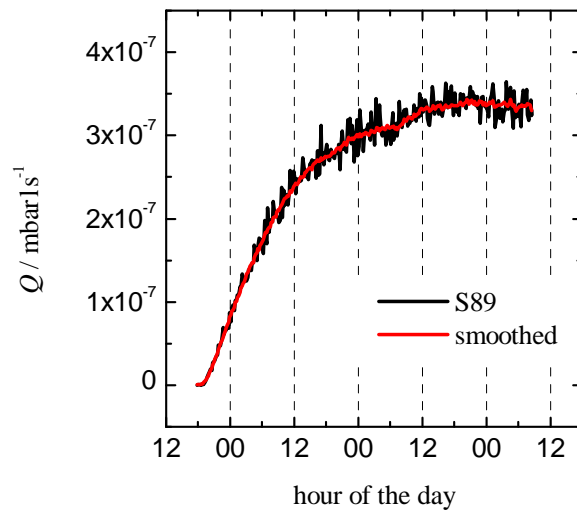
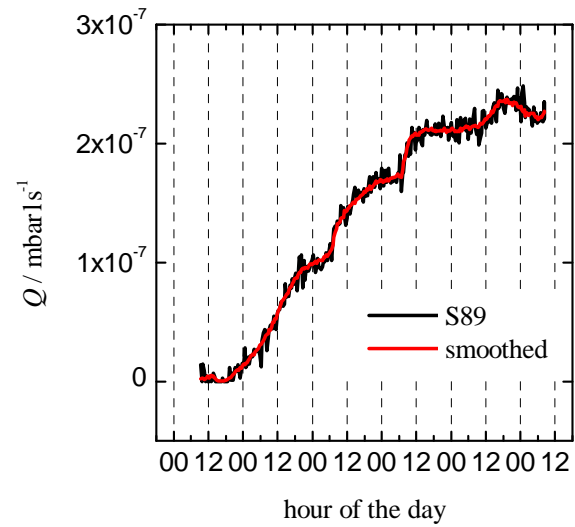


**Figure 6.6:** Helium and hydrogen permeabilities of two CFRP samples. The helium and hydrogen permeabilities are displayed with hollow and filled symbols, respectively. The activation energy of hydrogen permeation is higher than that of helium in both samples.



(a) helium permeation



(b) hydrogen permeation

**Figure 6.7:** Comparison of the He and  $\text{H}_2$  gas flow behavior of a CFRP+DLC specimen (S89). In both cases, the permeation gas flow is characterized by steps in the morning hours of each day. The excursions are minor for helium but strongly developed for hydrogen.

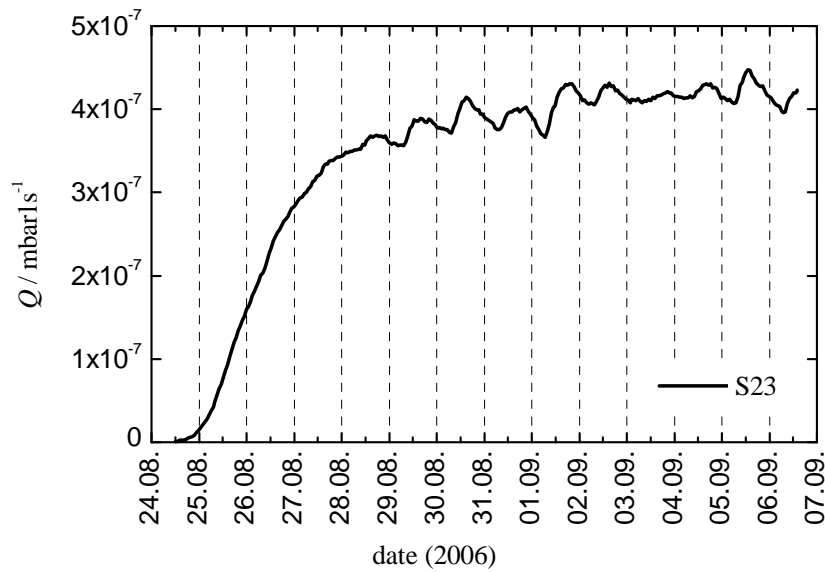


**Figure 6.8:**  $\text{H}_2$  permeation through CFRP+DLC (S23). The data was smoothed in order to emphasize the daily excursions. The excursions in the beginning of the permeation process are not visible owing to the great gradient of  $Q$ . Approaching the steady-state gas flow, the excursions are well to determine.

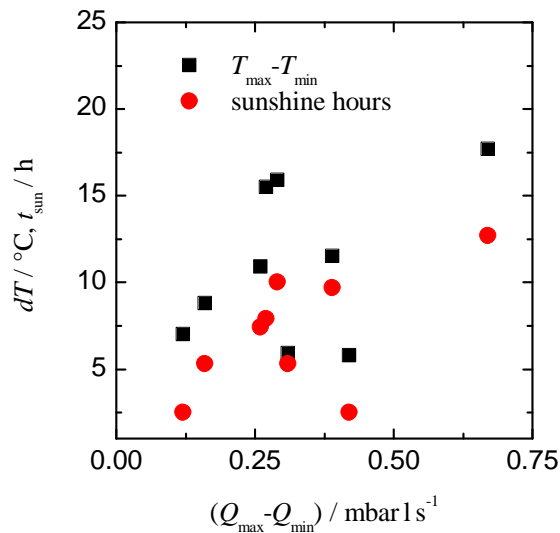


**Figure 6.9:** Correlation between the daily gas flow excursions of S23 (see figure 6.8) and environmental factors. The difference between the maximal and minimal measured gas flow is compared to the sunshine duration (hollow circles) and the difference between maximum and minimum day temperature (filled squares).

of the measuring apparatus.

Summarizing, hydrogen and helium permeated similarly through the tested materials. However, the usage of  $\text{H}_2$  as permeation gas is disadvantageous because of two reasons. Firstly, the residual signal is too high to detect low measuring signals. Secondly, environmental parameters like the daily sunshine duration strongly influence the measured signal. Both facts lead to a low quality of the hydrogen permeation measurements in comparison to those with helium. In the following, only He permeation tests are performed.

### 6.1.3 Influence of the Feed Pressure

The dependency of the permeability on the feed pressure is assumed to be linear, i. e. Henry's law (2.13) is valid. In order to verify this assumption, tests were performed on two CFRP

**Table 6.4:** Feed pressure dependency of the permeability in three specimens. The rightmost column denotes the linear regression gradient in mol/m s Pa bar. This gradient gives information about the grade of the pressure dependency.

sample	characterization	$T / ^\circ\text{C}$	$p_f / \text{bar}$	$P / \text{mol/m s Pa}$	$dP/dp_f$
S67 (M03)	CFRP	22	0.566	$1.34 \cdot 10^{-16}$	$-7.5 \cdot 10^{-18}$
			1.052	$1.27 \cdot 10^{-16}$	
			1.541	$1.22 \cdot 10^{-16}$	
			1.986	$1.24 \cdot 10^{-16}$	
S79 (M04)	CFRP	23	0.911	$3.95 \cdot 10^{-17}$	$1.1 \cdot 10^{-17}$
			1.390	$4.37 \cdot 10^{-17}$	
			1.960	$5.13 \cdot 10^{-17}$	
		89	0.911	$1.69 \cdot 10^{-16}$	$2.7 \cdot 10^{-17}$
			1.390	$1.82 \cdot 10^{-16}$	
S18 (M14)	CFRP+cNiP-cAu	22	0.506	$3.92 \cdot 10^{-17}$	$5.0 \cdot 10^{-18}$
			1.004	$4.52 \cdot 10^{-17}$	
			1.493	$4.39 \cdot 10^{-17}$	
			1.968	$4.78 \cdot 10^{-17}$	

samples (S67 and S79) and one metal-plated CFRP sample (S18). Samples S67 and S18 were tested at room temperature at four different feed pressures. Sample S79 was tested at three different pressures and at 22 °C and 89 °C. The results are summarized in table 6.4 and shown in figure 6.10. The permeability of S67 was nearly independent from the feed pressure. Considering S18 and S79, the permeability increased with growing feed pressure. However, the influence of  $p_f$  is small enough to justify the usage of Henry's law.

#### 6.1.4 Influence of Thermal Cycling

Thermal cycles were performed on five material systems (see table 6.5) including CFRP and metal-plated CFRP. The tests before and after thermal shock were carried out on different specimens, because specimens dismounted from the permeation apparatus were mostly damaged. Hence, a comparison of the results before and after thermal shock was difficult to accomplish.

The permeability of CFRP was lower after thermal cycling. Such a behavior must be doubted and be ascribed to measurement errors or material variations. The permeability of tin coated CFRP (S24, S26) increased by factor 100 after thermal shock and approached the value of uncoated CFRP. The inefficient barrier function of tin coatings after thermal shock can be explained by the formation of cracks (see 4.2, figure 4.9-c). The three remaining metal-plated CFRP samples showed a minor increase of the permeability after thermal cycling. Because it is uncertain if this increase was caused by thermal cycling, measuring errors or material variations, the change of the activation energy, the diffusivity and the  $j(\tau)$  curve after thermal shock was investigated. Table 6.6 lists these three parameters. Excluding CFRP and tin-coated CFRP, these three parameters did not change systemati-

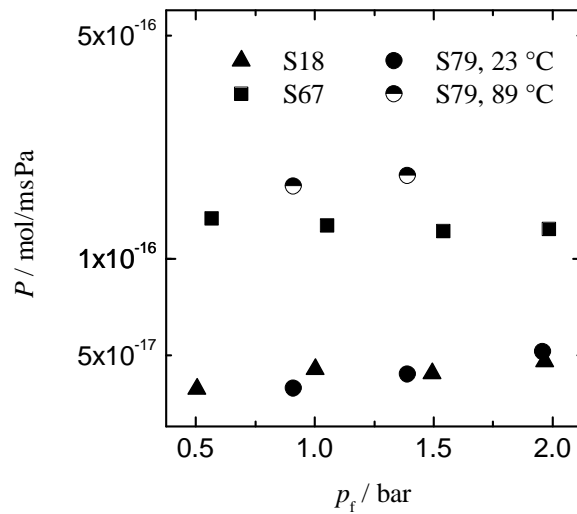


**Figure 6.10:** Pressure dependency of the permeability. The data of table 6.4 are plotted. Samples S18 and S79 show a small dependency from the applied pressure at the feed side.

**Table 6.5:** Influence of thermal cycling on the permeability.  $P_{uc}$  and  $P_{tc}$  denote the permeabilities in mol/m s Pa of uncycled and thermal cycling specimens, respectively.

material system	uncycled		thermally cycled		$P_{tc}/P_{uc}$
	sample	$P_{uc}$	sample	$P_{tc}$	
M02: CFRP	S04	$1.55 \cdot 10^{-16}$	S05	$8.88 \cdot 10^{-17}$	0.6
M15: CFRP+cNiP-Cu	S08	$7.42 \cdot 10^{-19}$	S10	$1.38 \cdot 10^{-18}$	1.9
M14: CFRP+cNiP-cAu	S21	$4.79 \cdot 10^{-17}$	S22	$8.01 \cdot 10^{-17}$	1.7
M16: CFRP+cNiP-Sn	S24	$4.08 \cdot 10^{-19}$	S26	$5.48 \cdot 10^{-17}$	134
M17: CFRP+cNiP-Ni	S30	$1.85 \cdot 10^{-19}$	S31	$4.97 \cdot 10^{-19}$	2.7

cally after thermal shock. It is assumed that thermal cycles did not significantly influence the permeation performance of the samples.

## 6.2 Results of the Permeation Measurements

This section summarizes the results of the permeation measurements on the various material systems. As far as available, the permeability, the activation energy, the permeation behavior ( $j(\tau)$  curve), the diffusivity and special incidents of each sample are reported.

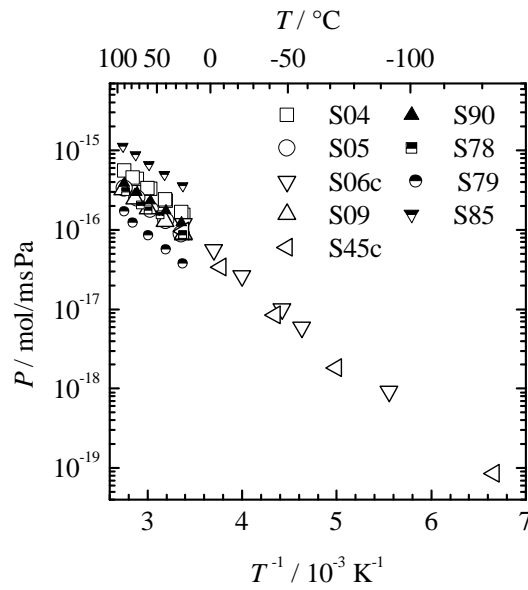
### 6.2.1 CFRP Substrates

The results of the permeation measurements are listed in table D.2 and graphically shown in figure 6.11. The permeabilities of the three different CFRP material systems (M02 – M04) were within a bandwidth of one order of magnitude. Typical values of the RT permeability were around  $10^{-16}$  mol/m s Pa with activation energies between 15 and 20 kJ/mol. The diffusivities of M02 and M03 were approximately  $6 \cdot 10^{-11}$  and  $8 \cdot 10^{-11}$  m<sup>2</sup>/s, respectively. All specimens exhibited a flux-time behavior similar to the Fickian distribution. CFRP samples of M03 showed the best agreement with Fick's law, while samples of M02 contained



**Table 6.6:** Influence of thermal cycling on the permeation activation energy,  $E_P$  in kJ/mol, and on the diffusivity in  $10^{-11} \text{ m}^2/\text{s}$ .

uncycled				thermally cycled				$\frac{E_{P,tc}}{E_{P,uc}}$	$\frac{D_{tc}}{D_{uc}}$
sample	$E_{P,uc}$	$D_{uc}$	$j(\tau)$ behavior	sample	$E_{P,tc}$	$D_{tc}$	$j(\tau)$ behavior		
S04	16.4	8.0	near Fickian	S05	17.7	6.0	near Fickian	1.08	0.8
S08	14.2	1.3	not Fickian	S10	16.3	3.5	not Fickian	1.15	2.7
S21	12.0	2.5	not Fickian	S22	11.5	2.2	not Fickian	0.96	0.9
S24	14.8	2.0	not Fickian	S26	13.3	3.0	not Fickian	0.90	1.5
S30	12.2	—	—	S31	15.0	2.0	not Fickian	1.23	—

**Figure 6.11:** Permeabilities of CFRP specimens as function of the temperature. Hollow symbols: material system M02; fully filled symbols: material system M03; semi-filled symbols: material system M04.

minor deviations in the beginning of the permeation process (refer to figure 6.12). For further consideration when evaluating coated CFRP specimens, the available measured data of M02 and M03 are averaged and summarized in table 6.7.

### 6.2.2 Metal Sheets and Foils

The results of the helium permeation tests on metal sheets, foils and foils adhered on CFRP are summarized in table D.3. All sheets (M06: Al, M07: SS) did not show any permeation. Even the mechanically treated or welded Al sheets were impermeable for helium.

The measurement of permeation through thin foils without substrate was not feasible in some cases, owing to the mechanical softness of the specimens. In these cases, the foils (one 10  $\mu\text{m}$  thick aluminum foil and two 25  $\mu\text{m}$  thick tin foils) were destroyed during the sealing process. Foils with greater thickness could be successfully sealed and tested. A 136  $\mu\text{m}$  tin foil (S77, M07) did not show a permeation flux for 140 hours until suddenly a high and further increasing gas flow occurred. The test was immediately stopped to protect the measuring chamber. The subsequent inspection of the sample revealed the occurrence

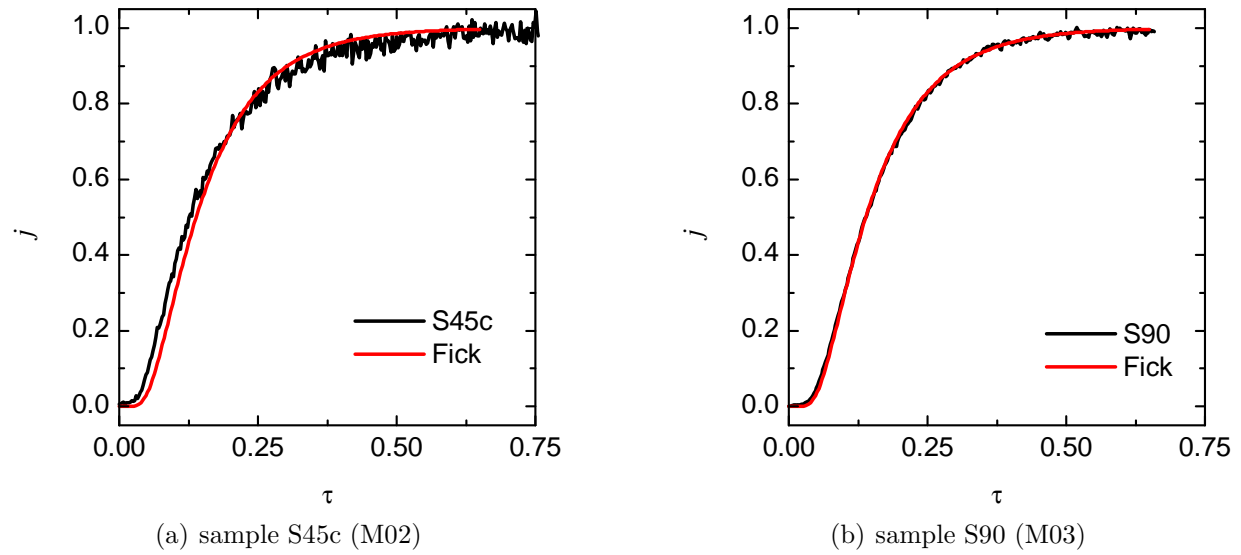
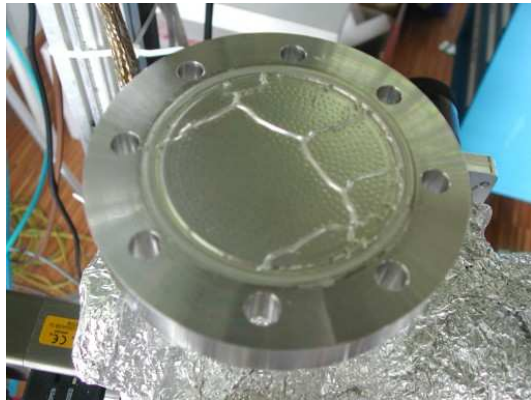


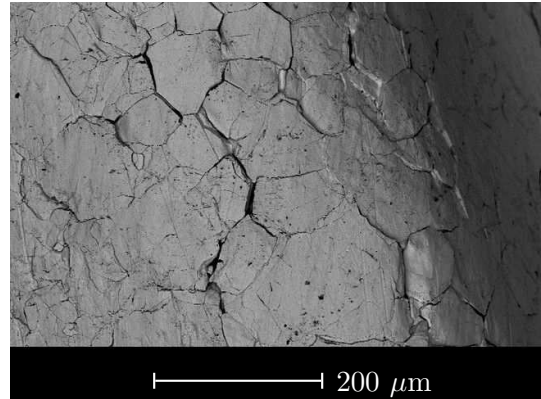
**Figure 6.12:** Flux-time behavior of two CFRP samples. The experimental data (black line) and the theoretical curve according to Fick (red line) are plotted. While S90 shows exact agreement with Fick's law, sample S45c exhibits a minor deviation from Fick's law.

**Table 6.7:** Fitted He permeation properties of CFRP substrates for further consideration.

samples	material system	$P$ (295 K) mol/m s Pa	$P_0$ mol/m s Pa	$E_P$ kJ/mol	$D$ (295 K) m <sup>2</sup> /s
S04, S05, S06c, S09, S45c, S75	M02	$1.027 \cdot 10^{-16}$	$2.024 \cdot 10^{-13}$	18.607	$6 \cdot 10^{-11}$
S67, S90	M03	$1.24 \cdot 10^{-16}$	$6.20 \cdot 10^{-14}$	15.031	$8 \cdot 10^{-11}$



(a) photo of S77 after the permeation test



(b) SEM shot of one knit line

**Figure 6.13:** Tin foil (S77) after the permeation test. The foil is knitted because of its low stiffness and the pressure difference between feed and permeate side (a). Cracks occurred along the knit lines (b).

of knit lines (figure 6.13-a) which were formed by the pressure difference between feed and permeate side. The SEM image of a knit line (figure 6.13-b) proved the existence of cracks. The formation of cracks probably resulted from a long-time creep process. In the tested 30  $\mu\text{m}$  aluminum foil (S74, M08), no permeation gas flow was detected.

The CFRP specimens with adhered Al, Cu and Sn foils (M10, M11, M27) were impermeable within the measuring time. Only the composite with a 25  $\mu\text{m}$  Sn foil (S70, M09) showed a permeation flux. The inspection of sample S70 after the permeation test revealed that the foil was partly damaged at the sealing line.

Summarizing, the permeabilities of foils and sheets were very low compared to those of CFRP. Considering CFRP covered with an 25  $\mu\text{m}$  Cu foil, the foil permeability was less than  $1.9 \cdot 10^{-22} \text{ mol/msPa}$ , refer to table D.3.

### 6.2.3 Metal-plated CFRP

The results of the permeation measurements on the specimens of M12 – M17 and M18 – M26 are summarized in tables D.4 and D.5, respectively. First, the permeabilities of the single material systems are presented, followed by a description of the permeation activation energies, diffusivities and  $j(\tau)$  curves.

The three tested specimens of CFRP+cNiP (M12) had comparable permeabilities at room temperature with a mean value of  $6.2 \cdot 10^{-17} \text{ mol/msPa}$ . This value was only slightly lower than that of CFRP (M02, refer to table 6.7). Sudden increases of the gas flow could be observed when cooling the specimens S02c and S03c, see figure 6.14. The RT permeability after the cooling cycle was similar to that of CFRP. It is assumed that cracks appeared in the cNiP layer between 273 K and 230 K.

The RT permeabilities of the CFRP+cNiP-Al (M13) specimens were approximately  $5 \cdot 10^{-17} \text{ mol/msPa}$ . This value is comparable with that of CFRP coated with cNiP.

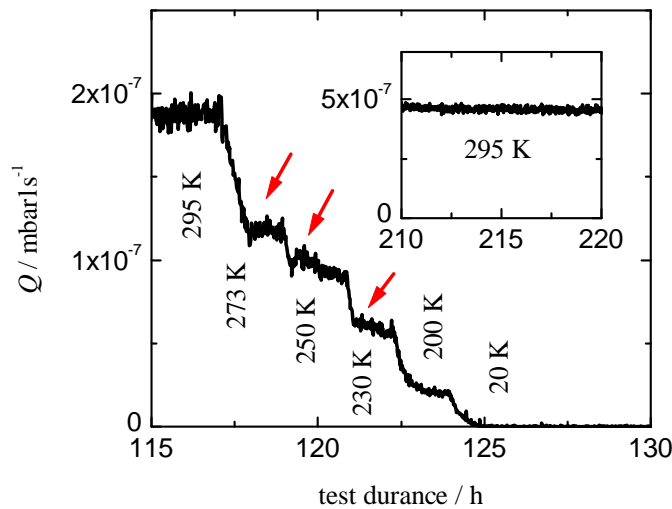


**Figure 6.14:** Measured gas flow of the CFRP+cNiP specimen S03c during cooling. Before cooling, the steady-state gas flow is approximately  $2 \cdot 10^{-7}$  mbar l/s. During cooling, the gas flow shows sudden increases (red arrows) which points to the formation of leaks. No permeation is measurable at 20 K. When reaching room temperature again, the gas flow is about  $5 \cdot 10^{-7}$  mbar l/s.

Hence, the additional aluminum layer was fully permeable which can be ascribed to existing channels (figure 4.6-c) or uncoated spots.

In the seven specimens with a cNiP-cAu coating (M14), permeabilities from  $7.6 \cdot 10^{-18}$  to  $8.9 \cdot 10^{-17}$  mol/m s Pa were measured. While the latter value was comparable with that of cNiP-coated CFRP, the first value was an improvement by factor 10. Considering the thickness of the gold layer ( $0.35 \mu\text{m}$ ), the permeability of gold was only  $1.8 \cdot 10^{-20}$  mol/m s Pa. Cooling the specimen S20c, peaks similar to those in M12 occurred between 273 K and 240 K. On the contrary, S19c did not show these peaks during cooling. Considering the higher RT permeability of S19c, it can be assumed that the coating already contained microcracks before cooling.

The eight cNiP-Cu coated specimens (M15) showed a great scatter of the measured permeabilities. The RT permeabilities ranged from  $1.4 \cdot 10^{-17}$  to less than  $5.4 \cdot 10^{-20}$  mol/m s Pa (see figure 6.15). These values correspond to liner permeabilities from  $4.2 \cdot 10^{-20}$  to less than  $1.8 \cdot 10^{-21}$  mol/m s Pa. The two samples tested between 293 K and 20 K did not show a sudden increase of the gas flow. It can be concluded that no cracks appeared in the cNiP-Cu coating owing to cooling.

The permeation measurements of tin coated specimens (M16) affirmed the cryogenic ineligibility derived from the SEM inspections. Although the permeabilities of S24, S27c and S28c were approximately  $5 \cdot 10^{-19}$  mol/m s Pa, that of the thermally shocked S25 was 100 times greater. A second thermally cycled specimen could not be sealed, which is deduced to the existence of microcracks along the sealing line. The permeation gas flows of S27c and S28c showed peaks during the cooling phase. The RT permeability of S27c increased by factor 100 after the cooling at 20 K. The resulting permeability was similar to that of an uncoated CFRP. Figure 6.16 proves the existence of cracks in the coating.

The specimens containing a cNiP-Ni coating (M17) showed very low permeation rates. Two of four specimens were fully impermeable, even during and after cooling. However, the coatings were partly or even fully peeled off the substrate after the disassembly of the samples. It is not known if the liners were already peeled off during the permeation

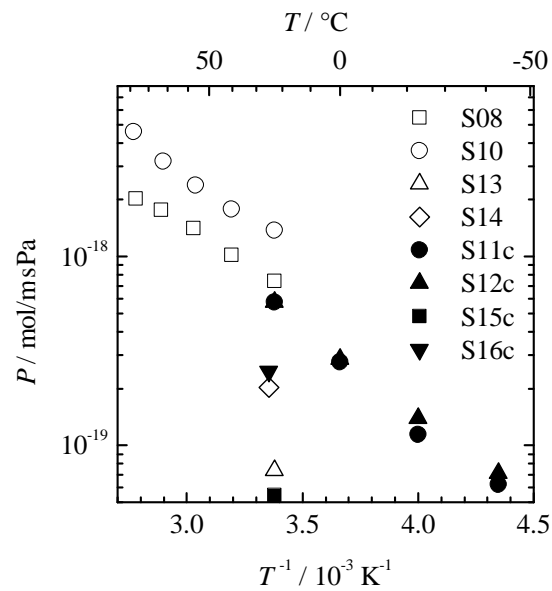


**Figure 6.15:** Great scatter of RT permeabilities of material system M15. Hollow symbols denote data from the RTPMA, filled symbols denote data from the CPMA.

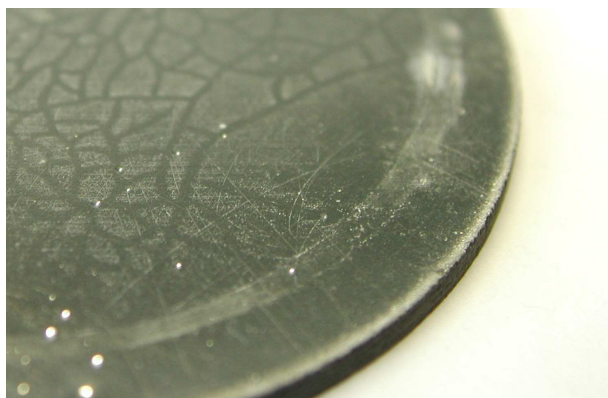


**Figure 6.16:** Close-up photography of the tin-coated CFRP specimen S27c after the permeation measurement at 20 K. The crack network is made responsible for the 100 times greater permeation flux after cooling to 20 K.

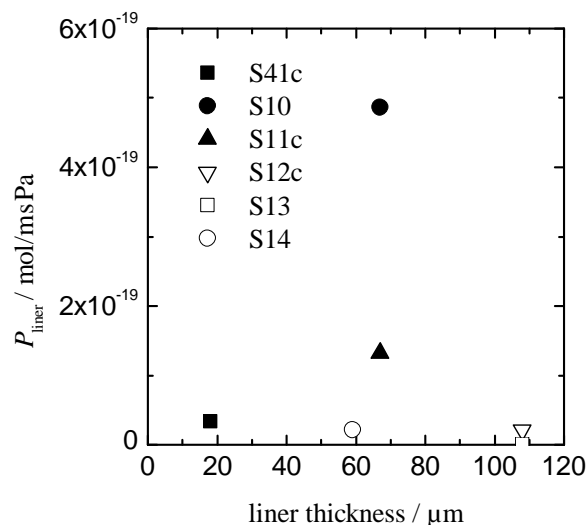


**Figure 6.17:** Liner permeability of M18 as a function of the liner thickness. No correlation between both variables is recognizable.

measurements. Presuming this case, a potentially existing flux along the interface between substrate and liner would imply an error of the measurement.

The cCu-Cu coatings of M18 were produced with different thicknesses to investigate the influence of the liner thickness on the liner permeability. However, the measurements revealed no correlation between these two variables, see figure 6.17. One specimen (S46c) was impermeable for helium, the others showed partly very high permeation rates. During cooling at 20 K, no permeation was measured in S46c. Specimen S43c became impermeable at temperatures below 250 K. The measurement of S41c at low temperatures was interrupted by a leakage at the sealing line.

The cCu-Cu coatings of M19 – M22 were produced with varied process parameters, refer to 4.2. The variation of the current density did not effect the permeation rate. The decrease of the sulfuric acid content yielded to a higher measured permeability. The specimen produced with increased sulfuric acid content was impermeable.

Gold coating were investigated in material systems M23 and M25. The functional coating of M23, Cu-Ni-cAu, was not permeated by helium. While the permeability of cCu-Ni coated CFRP (M24) was negligibly lower than that of CFRP, the additional 1.55  $\mu\text{m}$  gold layer in M25 reduced the permeation gas flow by factor 2. The permeability of the gold layer was  $5 \cdot 10^{-20} \text{ mol/msPa}$ . However, the cooling of a M25 specimen at 20 K resulted in a suddenly increased gas flow similar to that in figure 6.14. The RT permeation flux after the cooling cycle increased by factor 5 to that of uncoated CFRP. The subsequent investigation did not reveal cracks but a partial flaked off coating near the sealing line.

Only one specimen of cCu-Sn coated CFRP was tested because a second specimen could not be sealed successfully. The RT permeability was slightly lower than that of CFRP. No permeation measurement at low temperatures was performed.

The permeation activation energies of the metal-plated CFRP specimens varied strongly, from 7 to 20 kJ/mol. The values were similar to those of CFRP in few cases but mostly much lower. Even within one material system, the activation energies scattered strongly.

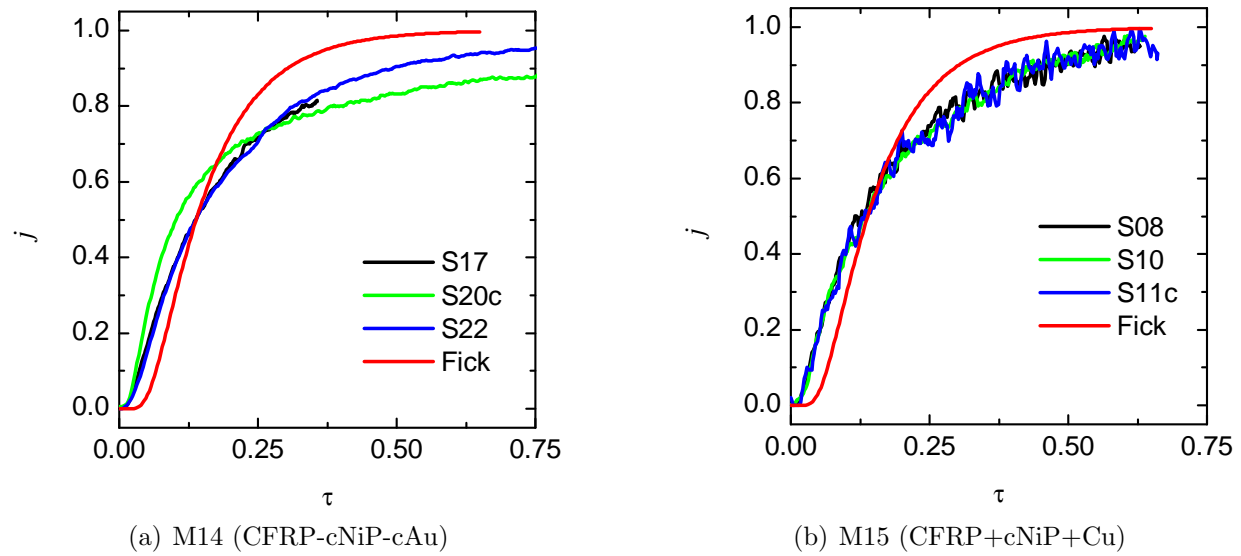


**Figure 6.18:** Flux-time behavior of selected specimens of M12 and M15. The deviations from the Fick curve are strongly developed at early and late times.

The total diffusivities also varied in all metal-plated CFRPs as well as within a single material system. The majority of the determined diffusivities was between 1 and  $3 \cdot 10^{-11} \text{ m}^2/\text{s}$  and hence approximately three times lower than that of CFRP.

The flux-time behaviors of all considered specimens except of S07 were different from the Fickian distribution. In the majority of the specimens, the  $j(\tau)$  curves even showed a strong deviation from the Fick curve. As an example, the flux-time curves of specimens with cNiP-cAu (M14) and cNiP-Cu (M15) coatings are illustrated in figure 6.18.

Evaluating the measured data ( $P$ ,  $E_P$ ,  $D$  and characteristics of the  $j(\tau)$  curves), no correlation between those variables can be found. In particular, the strong varying activation energies do not correlate to the measured permeabilities or diffusivities.

#### 6.2.4 Miscellaneous Coatings on CFRP

The results of the permeation measurement on DLC, PVD and thermal spray liners are summarized in table D.6.

The three specimens with a  $2.3 \mu\text{m}$  DLC liner (M28) were characterized by similar permeation behaviors. Although the composite permeabilities were not reasonably less than those of CFRP, the calculated liner permeabilities were as low as  $7.6 \cdot 10^{-20} \text{ mol/m s Pa}$ . The activation energies were in the range of those of CFRP. The diffusivity was reduced by factor 2 – 4.

Thermal spray aluminum liners (M29) did not exhibit a permeation barrier function. Two specimens could not be sealed owing to the great surface roughness (see figure 4.16). One tested specimen showed permeation and diffusion constants similar to those of uncoated CFRP.

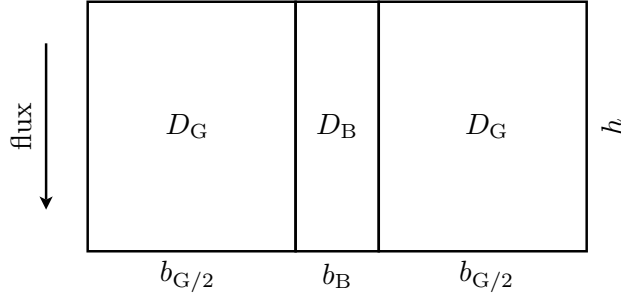


**Figure 6.19:** Parallel grain boundary model. One grain boundary (B) separates two grains (G). Repeating the single grain boundary and its neighboring grains in horizontal direction, one obtains the parallel grain boundary model.

The 24  $\mu\text{m}$  cNiP-Ni PVD coated CFRP specimen (M30) did not reduce the permeation rate significantly, either. The diffusivity was similar to that of CFRP, but the permeation activation energy was reduced.

### 6.3 Simulation of Transient Permeation

The results of the permeation measurements on the metal-plated CFRP specimens showed a great scatter of the permeabilities, diffusivities, activation energies and flux-time distributions. Before these results are discussed in 6.4, the simulated  $j(\tau)$  curves of selected cases are presented in this section.

#### 6.3.1 Simulation of Grain Boundary Diffusion

The simulation of grain boundary diffusion was performed similarly to the studies of Hwang and Baluffi, see 2.5.3. The used parallel grain boundary model is shown in figure 6.19. Opposite to Hwang and Baluffi, it does not contain a surface accumulation surface. The geometry of the model is defined by the thickness of the membrane  $l$  and the widths of the grain and boundary,  $b_G$  and  $b_B$ , respectively. The material properties include the diffusivity and the solubility of the grain and grain boundary. For reasons of simplification, the solubilities of grain and grain boundary are presumed to be identical.

To assess the sensibility of the parameters on the  $j(\tau)$  curve, initial simulations with approximately 200 different parameter sets were carried out. It was found that equal  $j(\tau)$  curves are obtained if

1. the ratio of the diffusivities,  $D_B/D_G$ , is constant, or
2. the geometry is equivalent, i. e.  $b_G : b_B : l$  is constant (Hwang and Baluffi:  $\frac{b_B l}{b_G}$  is constant).

In the parameter studies, the  $j(\tau)$  curves varied strongly. With increasing ratio of  $D_B/D_G$ , the  $j(\tau)$  curves showed greater deviations from Fick. The deviations occurred at earlier times with growing grain size,  $b_G$ . The deviations became less distinct in case of increased membrane thickness.

In order to illustrate the extremes of the deviations in the  $j(\tau)$  curves from Fick, one example is shown figure 6.20. There, the diffusion through a parallel grain boundary with



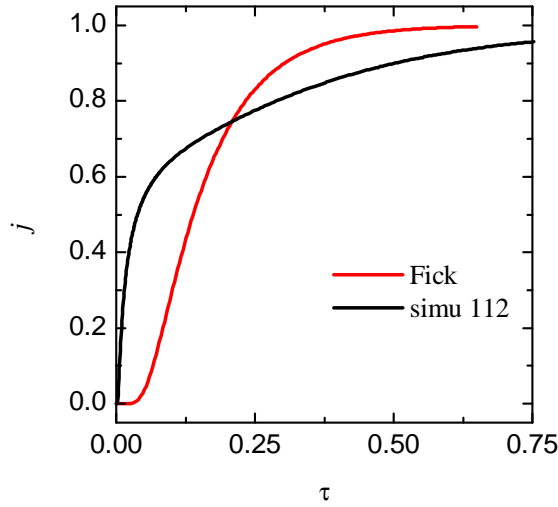


**Figure 6.20:** Simulation of grain boundary diffusion with the parameters  $D_B/D_G = 50$ ,  $b_G = 33 \mu\text{m}$ ,  $b_B = 2 \mu\text{m}$  and  $l = 19 \mu\text{m}$ . The deviation from the Fick curve is strongly developed.

parameters  $D_B/D_G = 50$ ,  $b_G = 33 \mu\text{m}$ ,  $b_B = 2 \mu\text{m}$  and  $l = 19 \mu\text{m}$  (simu112) is presented. The flux increases immediately but reaches the steady-state condition at very late time,  $\tau > 0.75$ . The concentration distribution within the material at different times is plotted in figure 6.21. At early times  $\tau \leq 0.008$ , the particles have already diffused into the grain boundary but not into the grain, i.e. Harrison diffusion type C is present. For  $\tau \geq 0.28$ , the diffusion in the grain is also developed and Harrison diffusion type A is reached.

The activation energy of permeation through a material containing grain boundaries can vary depending on the temperature. The following example illustrates this behavior. Presuming a material with  $b_G = 33 \mu\text{m}$ ,  $b_B = 2 \mu\text{m}$  and  $l = 19 \mu\text{m}$ . The permeabilities of the grain and the boundary may follow the Arrhenius equations with

$$\begin{aligned} P_{0,G} &= 10^{-14} \text{ mol/m s Pa}, \quad E_{P,G} = 50 \text{ kJ/mol}, \\ P_{0,B} &= 10^{-17} \text{ mol/m s Pa}, \quad E_{P,B} = 10 \text{ kJ/mol}. \end{aligned}$$

The total permeability,  $P$ , is calculated by (2.47). Figure 6.22 depicts  $P$ ,  $P_G$ ,  $P_B$  and  $E_P$  as a function of the temperature. The activation energy is dominated by the grain boundary at low temperatures ( $E_P \approx E_{P,B}$ ), whereas it is dominated by the grain at high temperatures ( $E_P \approx E_{P,G}$ ).

### 6.3.2 Simulation of Two-layer Permeation

The objective of this section is to investigate the possible  $j(\tau)$  curves for a composite consisting of a substrate and a liner. In accordance to 2.5.3, the substrate and liner are denoted by the subscripts s and l, respectively, while the composite contains no subscript. Both, substrate and liner, are presumed to be homogeneous in this simulation.

The investigation was performed exemplarily at a system similar to M15. The properties of the substrate were chosen to conform to M02 (CFRP):

$$P_s = 1 \cdot 10^{-16} \text{ mol/m s Pa}, \quad D_s = 1 \cdot 10^{-10} \text{ m}^2/\text{s}, \quad l_s = 1.43 \cdot 10^{-3} \text{ m}.$$

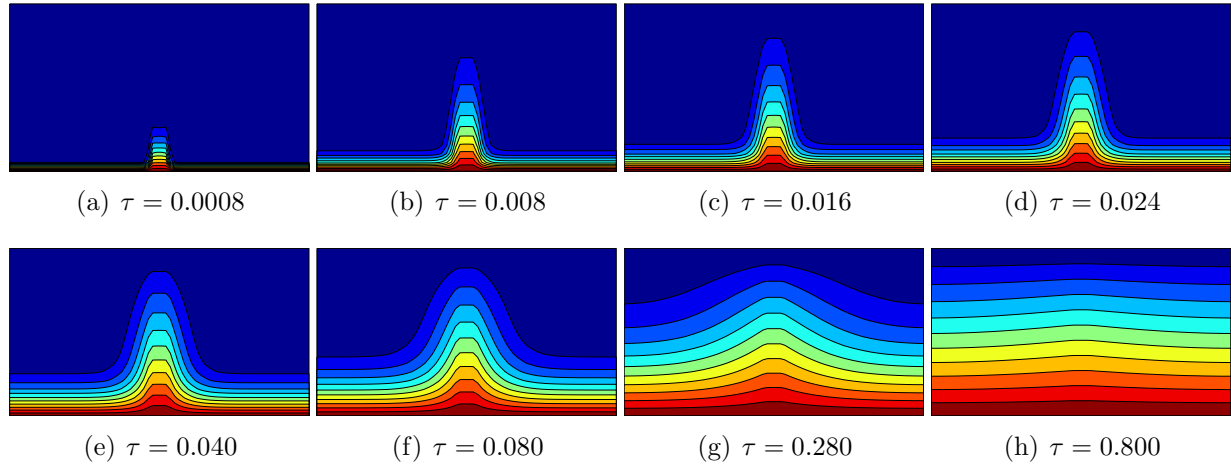


**Figure 6.21:** Concentration distribution in the parallel grain boundary simulation number 112. The concentration is plotted in colors (dark red: high concentration, dark blue: low concentration) as a function of the place and the dimensionless time.

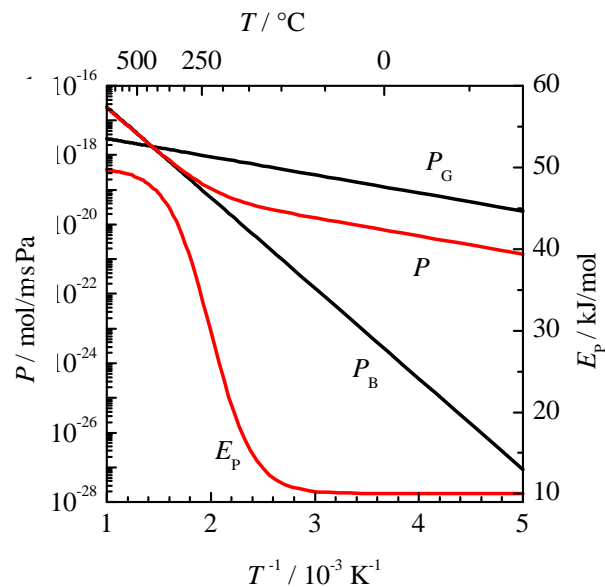


**Figure 6.22:** Permeation activation energy as a function of the temperature in a grain boundary material.  $E_p$  is proportional to the negative gradient of the  $\log P(T^{-1})$  curve. The parameters of the curves are given in the text.

**Table 6.8:** Parameters of the simulations of two-layer diffusion.  $D$  is calculated by (2.45).

simu no.	substrate			liner			composite	
	$P_s$ mol/m s Pa	$D_s$ m <sup>2</sup> /s	$l_s$ mm	$P_l$ mol/m s Pa	$D_l$ m <sup>2</sup> /s	$l_l$ μm	$P$ mol/m s Pa	$D$ m <sup>2</sup> /s
1					$1 \cdot 10^{-16}$			$9.58 \cdot 10^{-14}$
2					$1 \cdot 10^{-15}$			$9.35 \cdot 10^{-13}$
3					$1 \cdot 10^{-14}$			$7.56 \cdot 10^{-12}$
4					$5 \cdot 10^{-14}$			$2.04 \cdot 10^{-11}$
5					$8 \cdot 10^{-14}$			$2.43 \cdot 10^{-11}$
6	$10^{-16}$	$10^{-10}$	1.43	$10^{-21}$	$1 \cdot 10^{-13}$	47.5	$3.10 \cdot 10^{-20}$	$2.60 \cdot 10^{-11}$
7					$2 \cdot 10^{-13}$			$3.00 \cdot 10^{-11}$
8					$1 \cdot 10^{-12}$			$3.43 \cdot 10^{-11}$
9					$1 \cdot 10^{-11}$			$3.55 \cdot 10^{-11}$
10					$1 \cdot 10^{-10}$			$3.56 \cdot 10^{-11}$
11					$1 \cdot 10^{-09}$			$3.56 \cdot 10^{-11}$
12					$1 \cdot 10^{-08}$			$3.56 \cdot 10^{-11}$

The Cu liner was approximated by

$$P_l = 1 \cdot 10^{-21} \text{ mol/m s Pa}, l_l = 47.5 \cdot 10^{-6} \text{ m},$$

with diffusivities from  $10^{-16}$  to  $10^{-9} \text{ m}^2/\text{s}$  (see table 6.8 for the total parameter set, and figure 6.23 for the  $[D, D_l]$  parameter set). Mainly liner diffusivities greater than  $10^{-14} \text{ m}^2/\text{s}$  are interesting, because the according composite diffusivities are circa  $2 \dots 4 \cdot 10^{-11} \text{ m}^2/\text{s}$  and hence similar to those found in the experiments, see table D.4 and D.5.

The simulated  $j(\tau)$  curves varied but the deviations from Fick were minor. Remarkably, all curves had one common data point at approximately  $(\tau = 0.186, j = 0.68)$ . The  $j(\tau)$  curves of simulations 1 and 2 showed Fickian behavior. With increasing liner diffusivity (simu 3 and 4), a negative deviation from Fick at small  $\tau$  was found, see figure 6.24-a. This behavior was never observed in the experiments. For a very small range of  $D_l$  (simu 5 and 6), Fickian behavior was observed again. Further increasing of  $D_l$  (simu 7-12) resulted in a positive deviation from the Fick curve at small  $\tau$ , see figure 6.24-b. The deviations at late times were very small. A second series of simulations performed with  $P_l = 10^{-20} \text{ mol/m s Pa}$  showed similar results.

The activation energy of permeation through a two-layer material was investigated at two examples. First, the substrate and the liner was homogeneous. In the second example, the liner contained grain boundaries as described in 6.3.1. The parameters of both examples are summarized in table 6.9. The total permeabilities and hence the activation energies were calculated by (2.47) and (2.41). In both examples, the activation energy is dominated by that of the substrate at low temperatures. With increasing temperatures,  $E_P$  approaches the activation energy of the liner. In case of a liner consisting of grain boundaries,  $E_P$  is first dominated by that of the boundary and then by that of the grain.

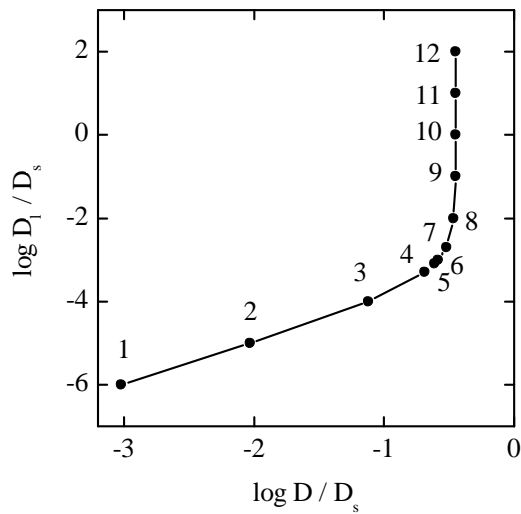
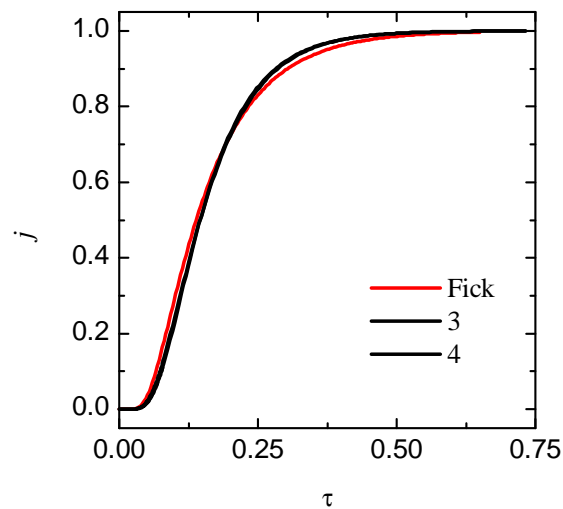
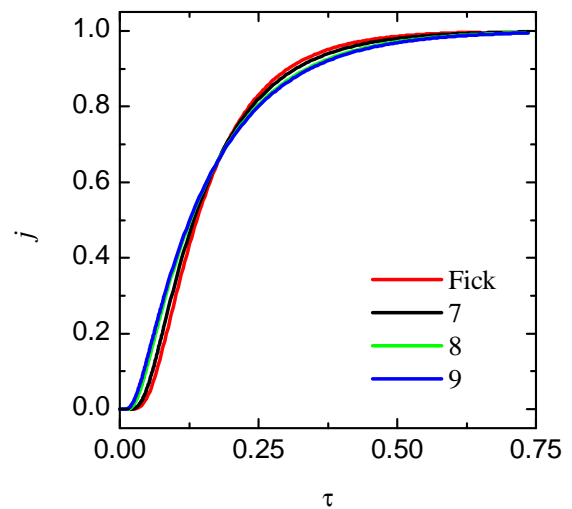


**Figure 6.23:** The parameter set of  $D_l$  and  $D$  in the two-layer diffusion simulation. Each  $(D_l, D)$  parameter point is labeled by the according simulation number of table 6.8. The curve follows equation (2.45) with  $\lambda = 30$  and  $\psi = 10^{-5}$  and  $D_s = 10^{-10} \text{ m}^2/\text{s}$ .



(a) negative deviation from Fick at low  $\tau$



(b) positive deviation from Fick at low  $\tau$

**Figure 6.24:** Flux-time behavior of a two-layer material. The numbers refer to the simulations defined in table 6.8.

**Table 6.9:** Parameters to calculate the permeation activation energy.

Example 1	Example 2
$P_{0,s} = 2 \cdot 10^{-13} \text{ mol/m s Pa}$	$P_{0,s} = 2 \cdot 10^{-13} \text{ mol/m s Pa}$
$E_{P,s} = 18.6 \text{ kJ/mol}$	$E_{P,s} = 18.6 \text{ kJ/mol}$
$l_s = 1.8 \text{ mm}$	$l_s = 1.8 \text{ mm}$
$P_{0,l} = 10^{-17} \text{ mol/m s Pa}$	$P_{0,G} = 10^{-14} \text{ mol/m s Pa}$ $P_{0,B} = 10^{-17} \text{ mol/m s Pa}$
$E_{P,l} = 10 \text{ kJ/mol}$	$E_{P,G} = 50 \text{ kJ/mol}$ $E_{P,G} = 10 \text{ kJ/mol}$
$l_l = 19 \mu\text{m}$	$b_G = 33 \mu\text{m}, b_B = 2 \mu\text{m}, l_l = 19 \mu\text{m}$

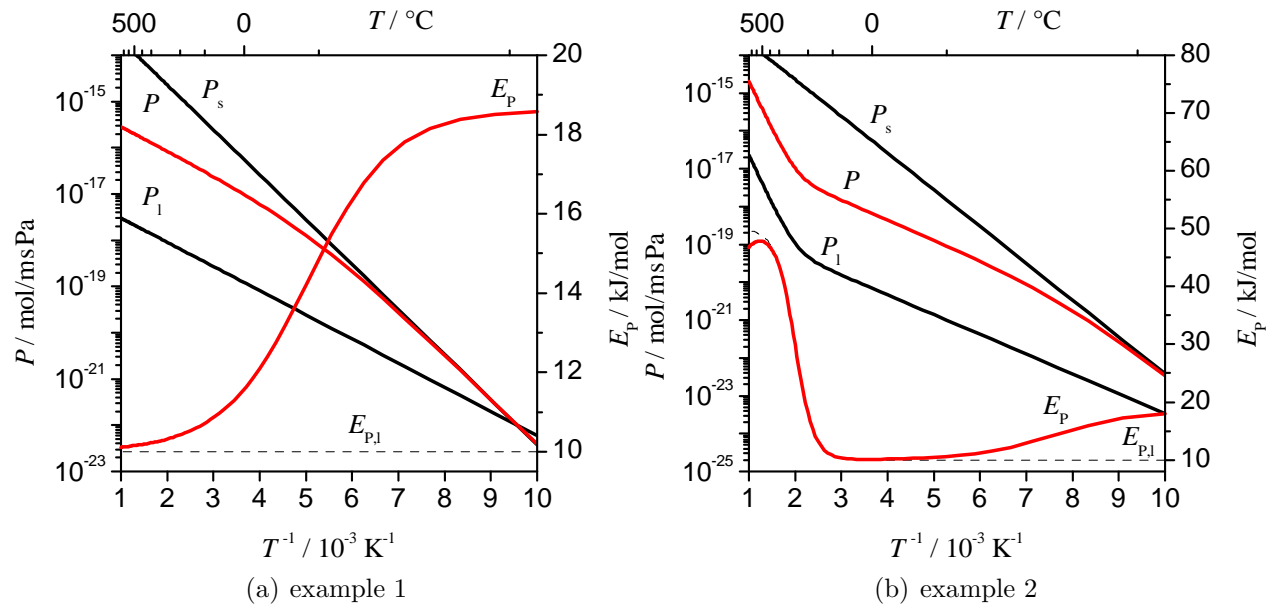


**Figure 6.25:** Permeation activation energy as a function of the temperature in a 2-layer composite.  $E_p$  is proportional to the negative gradient of the  $\log P(T^{-1})$  curve. The parameters of the curves are given in the table 6.9.

### 6.3.3 Simulation of Permeation through Substrates with Defective Liner

The simulations of transient permeation through substrates with a defective liner were performed using the model illustrated in figure 6.26. The used model considered two-dimensional diffusion in a homogeneous substrate. Hence, the defects are regarded as lines instead of holes. The width of the defect and the distance between two defects are denoted in accordance to 2.5.4 by  $2r$  and  $2R$ , respectively. The liner itself is treated impermeable. The substrate with thickness  $l_s$  is defined by its transport properties,  $P_s$  and  $D_s$ . The permeability and diffusivity of the composite are denoted by  $P$  and  $D$ , respectively.

Initial simulations showed that the permeation gas flow through a substrate with a defective liner is less than that without a liner, i.e. the barrier constant was  $\iota < 1$ . The barrier constant was independent from the substrate's diffusivity/permeability and only dependent on the geometry. This implies that the permeation activation energy of the composite equals that of the substrate:

$$E_p = E_{p,s}.$$

The diffusivity of the composite of substrate and liner was less than that of the substrate:  $D < D_s$ . The  $j(\tau)$  curve was independent from the material properties of the substrate.

In the following, the  $j(\tau)$  curves and diffusivities of selected examples are reviewed. The parameters of the simulations are summarized in table 6.10. The size and the distance of the defects were chosen so that they represent expectable coating defects. The simulation 1 represents cracks in the liner, the remaining simulations represent greater material defects.

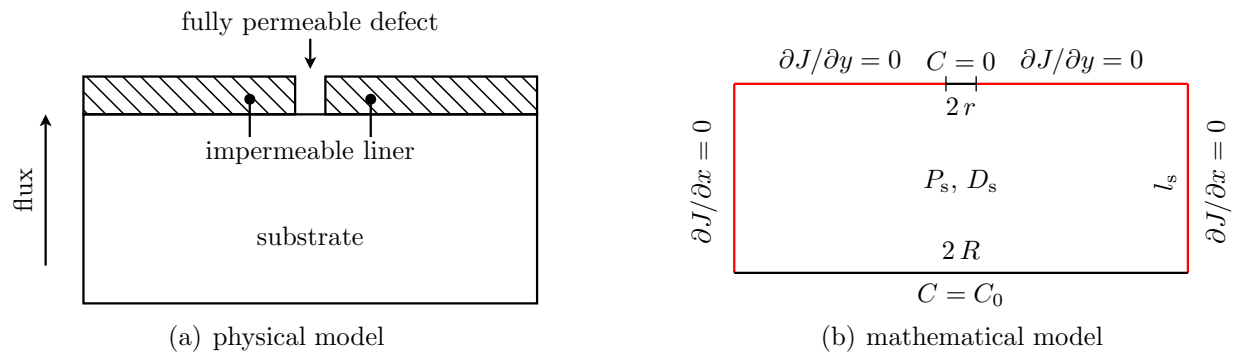


**Figure 6.26:** Model to simulate permeation through defectively coated CFRP.

**Table 6.10:** Simulation parameters of permeation through substrates with defective liner and their results.

simu no.	parameters			results			
	$2r$ $\mu\text{m}$	$2R$ $\text{mm}$	$l_s$ $\text{mm}$	$\iota$	$\iota_{\text{Prins}}$ (2.48)	$D/D_s$	$j(\tau)$ behavior
1	2	0.052	1.4	0.052	0.095	1.00	exact Fickian
2	26	72.026	1.8	0.003	$2 \cdot 10^{-5}$	0.36	not Fickian
3	40	1.040	1.8	0.255	0.172	0.66	near Fickian
4	40	10.040	1.8	0.041	0.002	0.40	not Fickian
5	80	1.080	1.8	0.366	0.346	0.70	near Fickian
6	80	10.080	1.8	0.060	0.003	0.42	not Fickian

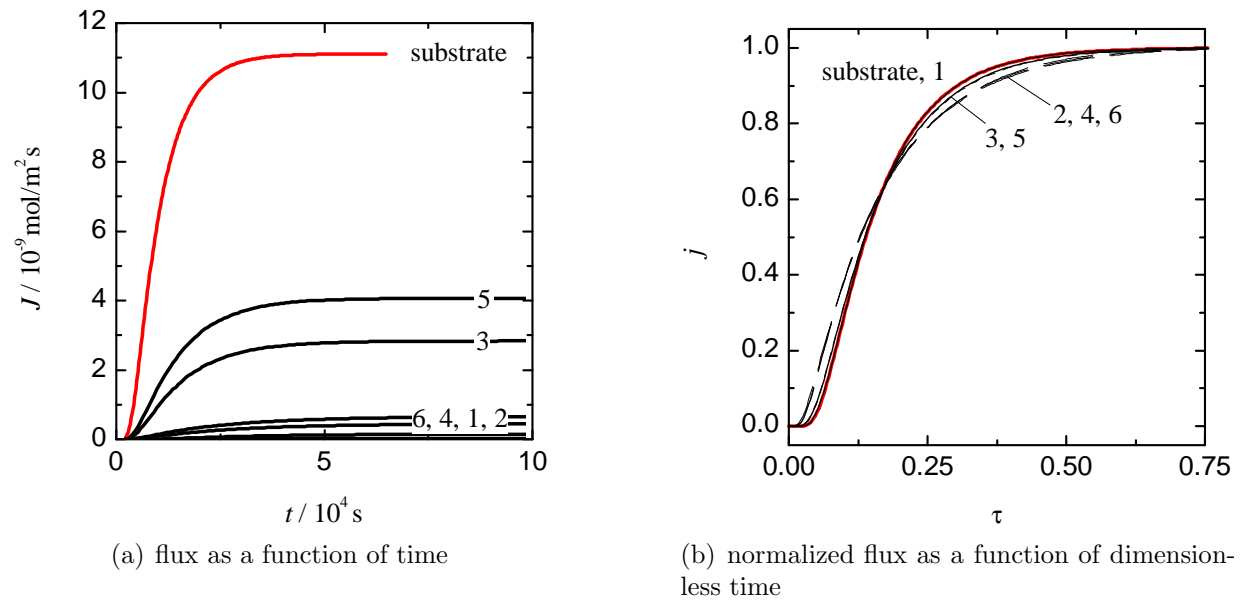


**Figure 6.27:** Simulated flux-time behavior of defectively coated CFRP. The labels refer to the simulation numbers of table 6.10

The results of the simulations are presented in table 6.10 and shown in figure 6.27. The reduction of the steady-state flux is remarkable if the defect distance is great. The diffusivities are in the range  $1.9 \cdot 10^{-11} \text{ m}^2/\text{s}$  and  $3.5 \cdot 10^{-11} \text{ m}^2/\text{s}$  and hence remarkably less than those of CFRP and similar to those found in the experiments. Figure 6.27-b displays the  $j(\tau)$  curves in comparison to that of Fick. The flux-time curves are similar to the Fick-curve, but a positive deviation in the beginning of the permeation process can be recognized. The deviations mainly depend on the defect distance. The deviations are, however, not as distinct as found in the experiments, see figure 6.18

Table 6.10 also lists the barrier factor derived from the simulation of Prins & Herman (2.48). The barrier factor of this simulation and that of Prins & Herman agree well for large defect size and small defect distances. For small defects being largely separated, the simulated steady-state flux does not coincide with the results of circular defects.

## 6.4 Discussion

### 6.4.1 Permeation through CFRP

The permeation measurements on CFRP specimens revealed deviations of the flux-time curves from the Fickian theory, see figures 6.5-a and 6.12-a. These deviations were observed in eight of ten investigated CFRP samples. Because the homogeneous PVC specimens did not show those deviations (see figure 6.2), CFRP can be considered to be inhomogeneous.

It is assumed that highly diffusive paths exist in CFRP which lead to an earlier rise of the permeation flux. These paths might follow the structure of the reinforcement texture and are in general curved and cross-linked. The following simulation of permeation through CFRP takes a simpler model into account. Instead of curved and cross-linked paths, parallel paths are employed. In analogy to grain boundary diffusion, the resin and the fibers represent the grain boundary and the grain, respectively.

The diffusivities and widths of the fiber region as well as the resin region were varied until the best fit to the experimental  $j(\tau)$  curve was found. Taking specimen S45c as an example, figure 6.28 presents the results of the simulation in comparison to the experimental results. The simulated flux-time curve matches exactly the experimental data. The simulation was performed with the following parameters

width of fiber region:	$b_G = 0.42 \text{ mm}$
width of resin region:	$b_B = 0.78 \text{ mm}$
diffusivity of fiber region:	$D_G = 8.7 \cdot 10^{-12} \text{ m}^2/\text{s}$
diffusivity of resin region:	$D_B = 1.74 \cdot 10^{-10} \text{ m}^2/\text{s}$

Considering the width values of the simulation, the fiber volume fraction of S45c would be  $f_f = b_G / (b_G + b_B) = 35 \%$ . This value is approximately 15 % lower than that of the real material. Although the simulations took a simplified model into account, the existence of highly-diffusive paths in CFRP would explain the deviations of the  $j(\tau)$  curves from Fick.

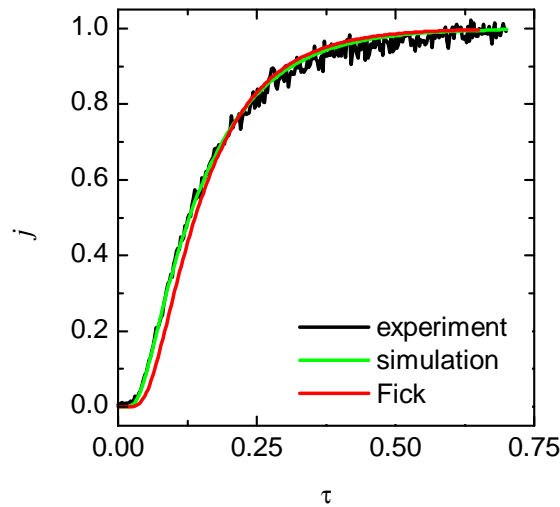


**Figure 6.28:** Simulation of the flux-time behavior of sample S45c. The minor deviation of the experimental data from the Fick distribution can be simulated by the parallel grain boundary model and parameters as listed in the text.

#### 6.4.2 Permeation through Metal-plated CFRP

The results of the permeation measurements on metal-plated CFRP revealed a great scatter of the total permeability, the activation energy and the  $j(\tau)$  behavior. In particular, the results within some material systems varied strongly. Possible explanations are investigated and discussed in the following, considering the cNiP-Cu plated CFRP specimens of M15.

The RT permeabilities of the M15 specimens varied from  $1.4 \cdot 10^{-17}$  mol/m s Pa to less than  $5.4 \cdot 10^{-20}$  mol/m s Pa (see figure 6.15). The activation energies were determined to be between 14 and 19 kJ/mol. All  $j(\tau)$  curves showed great deviations from the Fick curve, refer to figure 6.18-b. Assuming a CFRP substrate with nearly constant permeabilities and activation energies, the high scatter must be caused by a varying coating. The following explanations are considered and investigated:

1. strong variation of the liner thickness
2. existence of grain boundary diffusion
3. existence of defects in the coating
4. a combination of the three previous points.

To 1. A variation of the liner thickness was proven during the characterization of the materials in chapter 4. In polished-cut images of M15, the Cu liner thickness ranged from 48 to 59  $\mu\text{m}$  (refer to table C.4). Assuming an ideal two-layer permeation process in homogeneous materials, as described in 2.5.3 and 6.3.2, the total permeability is calculated by (2.41). Table 6.11 lists the total permeability as a function of the liner permeability for the two extremes of the liner thickness. The difference of the total permeabilities between these two extremes is always less than 23 %. Hence, the scattered results are not caused by a variation of the liner thickness of  $\pm 5 \mu\text{m}$  only.

To 2. The existence of grain-like structures was shown in chapter 4. In order to find a possible correlation between the structure of the liner and the measured permeabilities,



**Table 6.11:** Total permeability  $P$  as a function of the liner permeability  $P_l$  and the liner thickness  $l_l$ .  $P$  is calculated by (2.41) with  $P_s = 10^{-16}$  mol/m s Pa and  $l_s = 1.8$  mm.

	$\log P_l$	-23.00	-22.00	-21.00	-20.00	-19.00	-18.00	-17.00	-16.00
$l_l = 48 \mu\text{m}$ :	$\log P$	-21.41	-20.41	-19.41	-18.42	-17.43	-16.55	-16.09	-15.99
$l_l = 59 \mu\text{m}$ :	$\log P$	-21.50	-20.50	-19.50	-18.50	-17.51	-16.62	-16.10	-15.99
	rel. diff. of $P$ in %	22	22	22	22	21	16	4	0

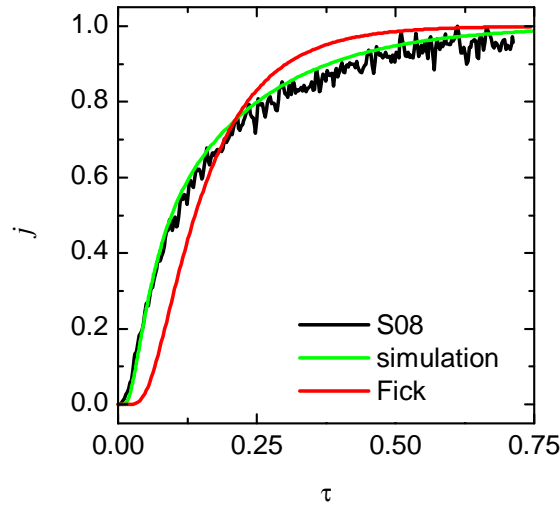


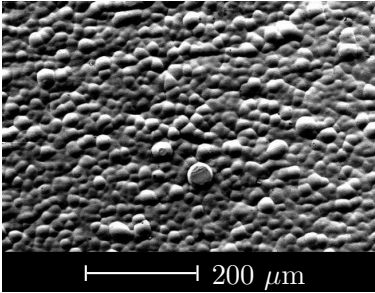
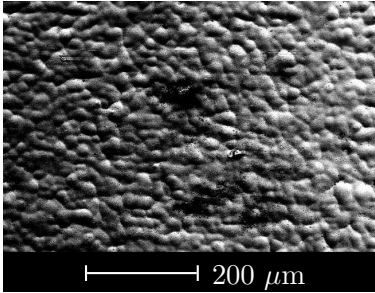
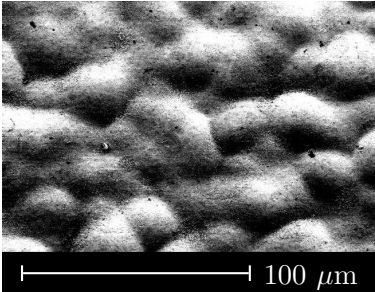
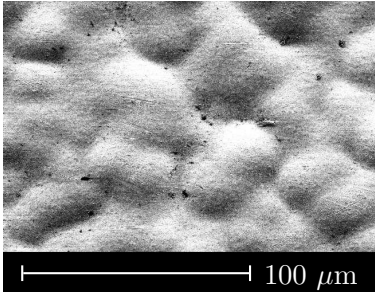
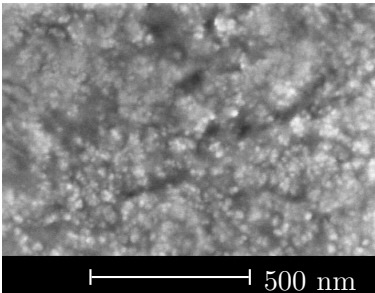
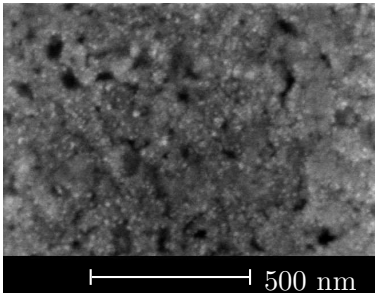
**Figure 6.29:** Simulation of the flux-time behavior of sample S08. The experimental data can be reproduced well by employing the parallel grain boundary model. The used parameters were  $D_B/D_G = 100$ ,  $b_B : b_G : l \approx 1 : 1.65 : 9.5$ .

specimens S10 and S14 were investigated more intensively. While S10 was characterized by a high permeation rate, S14 showed a low permeability. Table 6.12 compares the structure of the liner surface of both specimens. In both samples, circular, grain-like structures with 25...50  $\mu\text{m}$  in diameter are visible (table 6.12 a,b). At higher magnifications it is recognizable, that these grain-like structures consist of smaller grains with approximately 23 nm for S10 and 20 nm for S14 in diameter (table 6.12 c). EDX line scans along the grain-like structures revealed similar element distributions in both specimens (table 6.12 e). While the copper content was dominant, that of oxygen was around 5 atom percent. Carbon could be detected proportionally strongly near the boundaries of the grain-like structures. It is assumed that organic dirt accumulates better along these boundaries.

Although no distinctive differences between the liner surfaces of S10 and S14 were found to understand the enormous deviation of the measured permeabilities, the diffusion through grain boundaries would explain the strong deviations of the measured  $j(\tau)$  curves and the low activation energies. Figure 6.29 shows the  $j(\tau)$  curve of S08 in comparison with the Fickian distribution and the curve derived from the simulations. Although a substrate is not considered in the simulations, the trend to reproduce the experimental data with grain boundary diffusion simulation is visible.

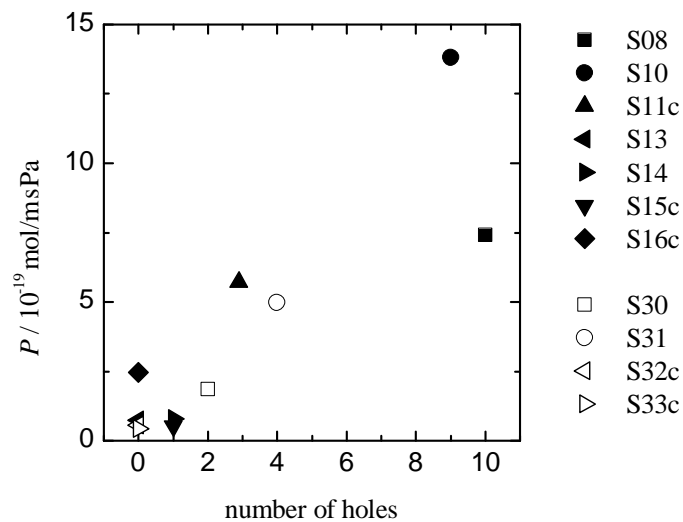
To 3. The third possible explanation of the great experimental scatter are defects in the coating. Therefore, each specimen of M15 and additionally of M17 was inspected more intensively. Scanning the surface of the liner by means of a stereo microscope and SEM, no uncoated areas were found. Subsequently, the coatings were peeled off, if feasible. Placing

**Table 6.12:** Comparison of the surface structure of two cNiP-Cu coated CFRP specimens.

	S10	S14
(a) surface x100 outlens detector		
(b) surface x500 outlens detector		
(c) surface x100000 inlens detector		
(d) EDX scans across the boundaries of grain- like structures	Cu: 50...85 % C: 12...50 % O: max 5 %	Cu: 55...85 % C: 8...45 % O: max 10 %
(e) $P(\text{RT})$ / (mol/m s Pa) $E_P$ / (kJ/mol)	$1.38 \cdot 10^{-18}$ 16.3	$7.79 \cdot 10^{-20}$ n/a

**Table 6.13:** Correlation between the number of holes (n. o. h.) in the coating of M15 and M17 and the measured permeabilities.

M15 (CFRP+cNiP-Cu)				M17 (CFRP+cNiP-Ni)			
sample	n. o. h.	$P(\text{RT})$ mol/m s Pa	$E_P$ kJ/mol	sample	n. o. h.	$P(\text{RT})$ mol/m s Pa	$E_P$ kJ/mol
S08	10	$7.42 \cdot 10^{-19}$	14.2	S30	1	$1.85 \cdot 10^{-19}$	12.2
S10	9	$1.38 \cdot 10^{-18}$	16.3	S31	4	$4.97 \cdot 10^{-19}$	15.0
S11c	3	$5.72 \cdot 10^{-19}$	19.3	S32c	0	$< 5.48 \cdot 10^{-20}$	n/a
S13	0	$7.38 \cdot 10^{-20}$	n/a	S33c	0	$< 4.29 \cdot 10^{-20}$	n/a
S14	1	$7.79 \cdot 10^{-20}$	n/a				
S15c	1	$< 5.44 \cdot 10^{-20}$	n/a				
S16c	1	$2.46 \cdot 10^{-19}$	n/a				

**Figure 6.30:** Measured permeabilities of material system M15 (S08 – S16c) and M17 (S30 – S33c) in correlation to the number of holes in the coating. The plotted permeabilities of S15c, S32c and S33c are the minimum detectable signals.

the liners in front of a light, circular holes were found. The number of the found holes are summarized in table 6.13, although the real number of holes might be even higher. The diameter of these holes ranged from 26  $\mu\text{m}$  to 100  $\mu\text{m}$ . Figure 6.30 displays the number of holes in correlation to the measured permeability. It is well to recognize that the measured permeabilities generally increase with the number of holes.

The origin of the holes is explained exemplarily for specimen S08 in figure 6.31. The substrate contained cavernous spots at the same locations where holes were found in the coating. These cavernous spots in the substrate were also coated but the thickness of the coating was negligible. In order to understand the existence of caverns in the substrate, a micrograph of specimen S12c was prepared, see figure 6.32. A spherical cavern which tapers toward the surface is visible. The diameter of the cavern is approximately 210  $\mu\text{m}$ . The diameter of the hole in the coating increases from 40  $\mu\text{m}$  to 240  $\mu\text{m}$ . The micrograph reveals that the cavern is located at the resin-richest area. The manufacturer of the CFRP stated, that this hole was very likely caused by an air bubble during the production.

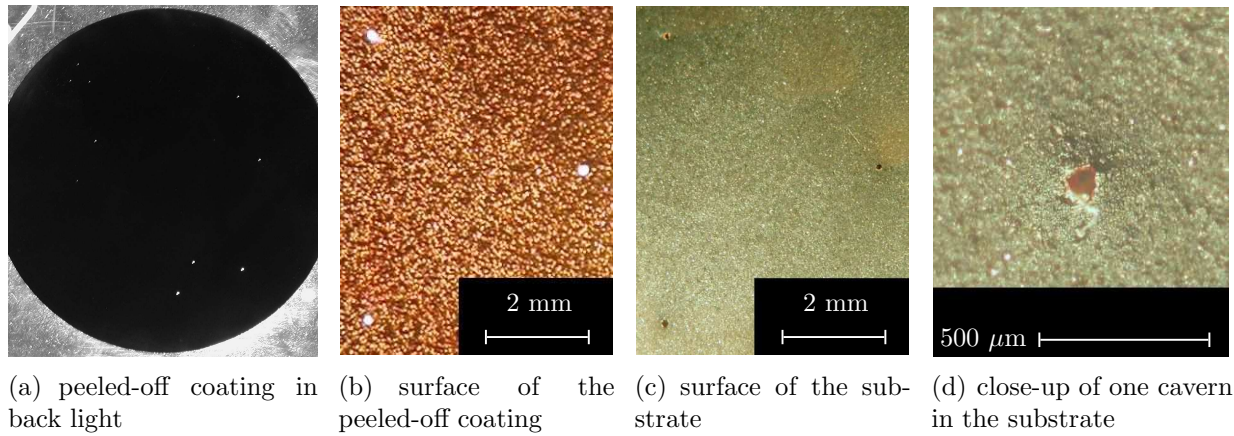


**Figure 6.31:** Microscope images of sample S08. In the back light, 10 holes are visible in the peeled-off coating (a). Cavernous spots in the CFRP substrate (c) are located at the same coordinates as the holes of the coating (b). The caverns are coated (d).

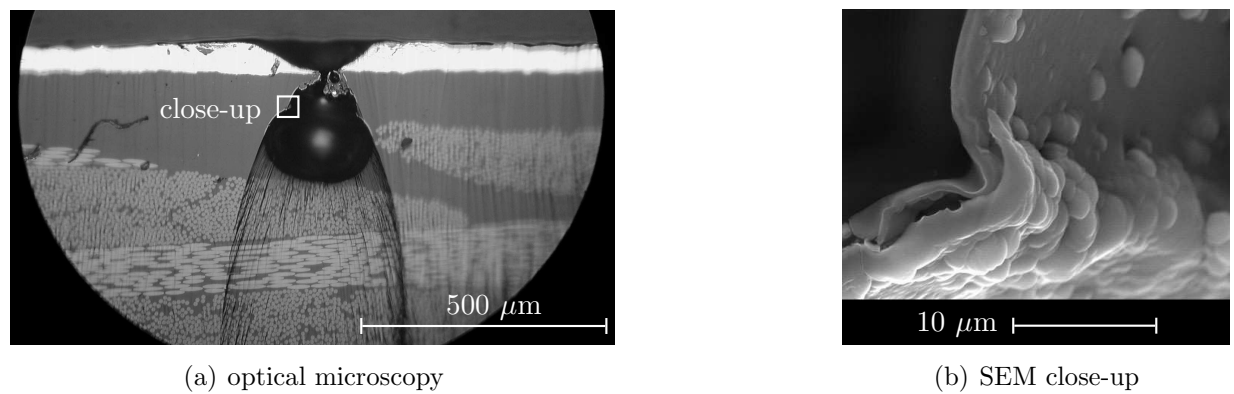


**Figure 6.32:** Micrograph of a cavernous spot of S12c. The hole in the coating is crater-like shaped. The surface of the cavern is coated (b). Note: the black vertical lines are grooves created during the polishing with ion beams.

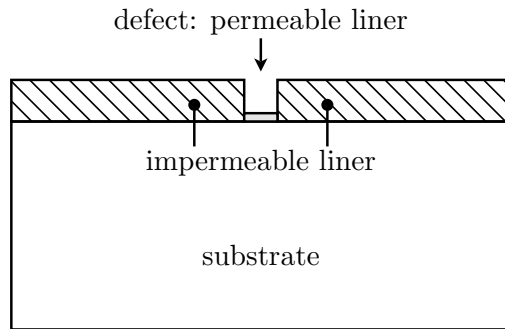


**Figure 6.33:** Model of the metal-plated CFRP specimens. The metal plating itself is treated impermeable. Potentially existing defects of the liner are modeled by a low thickness and grain boundaries.

The micrograph unveils two further important facts. Firstly, the thickness of the coating on the surface of the cavernous spot is partly as low as  $1\text{ }\mu\text{m}$ . It is assumed that other caverns can also contain uncoated areas. Secondly, the hole of the liner follows the shape of a sinkhole. This implies, that the coating does not get closed with increasing coating thickness. Such a behavior is probably caused by flow problems out of the cavern [152].

Knowing about the existence of holes in the coating, the remaining metal-plated CFRP specimens were investigated again. Only coatings with sufficient thickness ( $\gtrsim 40\text{ }\mu\text{m}$ ) could be peeled off from the substrate to be placed in the back light. The coatings of the remaining specimens were investigated under the microscope. Although it is not known if all holes were found, the following statements can be given:

- Holes in the coating were found in approximately 50 % of the metal-plated specimens. No correlation exists between the coating material and the number of holes.
- In general, the permeability increases with the number of holes in microcrack-free, thick ( $l \gtrsim 30\text{ }\mu\text{m}$ ) coatings.
- The distribution of holes is statistical, this means no pattern of the holes exists.
- The underlying caverns in the CFRP surface are mainly located in resin-rich areas, i. e. between two filament yarns.

Summarizing, the great scatter of the experimentally determined permeabilities of metal plated CFRP is caused by statistically existing caverns in the CFRP. While the defect-free surface of the CFRP is coated by the nominal thickness, the caverns are insufficiently coated. A simplified model to explain the permeation through such a body is shown in figure 6.33. The liner on the “perfect” part of the CFRP surface is treated as impermeable. The thin liner at the caverns is permeable and consists of grain boundaries. The permeation through the thin part of the liner is responsible for the lower values of  $E_P$ , compared to those of uncoated CFRP, and for the remarkable deviations of the measured  $j(\tau)$  curves from the Fickian distribution.

### 6.4.3 Evaluation of the Barrier Function of the Liners

All sheets, foils, and foils adhered on CFRP, except those made of Sn, were impermeable within the limit of the measuring apparatus. The minimum detection limit varied from

one experiment to the next owing to changing calibration factors and residual pressures within the measuring chamber. The lowest liner permeability limits were found in a 25  $\mu\text{m}$  Cu (S71) and a 30  $\mu\text{m}$  Al foil (S72) adhered on CFRP with  $P_l < 1.9 \cdot 10^{-22} \text{ mol/m s Pa}$ , see table D.3. Considering a CFRP substrate with  $l_s = 1.8 \text{ mm}$  and  $P_s = 10^{-16} \text{ mol/m s Pa}$ , the barrier constants (2.44) were  $< 1/7400$  and  $< 1/9100$ , respectively.

The metal-plated specimens showed very scattered barrier properties, depending on the existence of holes in the coating. Considering the optimal case of hole-free coatings in S15c, S33c, S46c, S51 and S65, the permeation rates were below the detection limit. The lowest liner permeability limit was found in S46c and S65 with  $P_l < 8 \cdot 10^{-22} \text{ mol/m s Pa}$ . The permeation flux through CFRP was reduced at least by factor 7400.

The remaining coatings of M28 (DLC), M29 (thermal spray aluminum) and M30 (PVD Ni) did not reduce the permeation flux through CFRP significantly. The barrier constant of M28 was between 0.37 and 0.70 which is still remarkable for an only 2.3  $\mu\text{m}$  thick coating. The barrier constants of M29 and M30 were  $\approx 1$  and 0.44, respectively.

Evaluating the permeation properties and the material characterization from chapter 4 of all specimens, metal platings and foils are recommended to use as a permeation barrier. If foils could be joined leak-freely, they were the favored liner.

The determined liner permeabilities are used in the following to estimate the permeation gas flow through the tank system presented in 3.4. Considering (3.4), the steady-state permeation gas flow would be

$$Q_P = 2.339 \cdot 10^{10} \frac{\text{mbar l}}{\text{s}} \frac{P}{\text{mol/m s Pa}} \frac{\text{m}}{l}.$$

Values of  $P$ ,  $l$  and  $Q_P$  are presented in table 6.14 for five liner solutions. The right-most column of this table lists the minimum limit of the vacuum stability time at room temperature. In all cases, the maximum limit of the expected gas flow through the CFRP tank is higher than the required maximum allowable gas flow, see (3.3). Hence, in order to achieve measurement results which can prove the requirement (3.3), specimens with a surface area similar to that of the tank would be required.

**Table 6.14:** Four possible liner solutions and their permeation properties. The CFRP substrate is represented by  $l_s = 1.8 \text{ mm}$  and  $P_s = 10^{-16} \text{ mol/m s Pa}$ .  $Q_P$  denotes the permeation gas flow through the CFRP inner tank.  $t^*$  is the time to reach the maximum allowable vacuum pressure:  $t^* = (p_{v,\max} V_v) / Q_P$ , with  $p_{v,\max} = 5 \cdot 10^{-4} \text{ mbar}$  and  $V_v = 60 \text{ l}$ , see 3.4.

substrate	liner	$l_l$ $\mu\text{m}$	$P_l(\text{RT})$ $\text{mol/m s Pa}$	$P(\text{RT})$ $\text{mol/m s Pa}$	$Q_P(\text{RT})$ $\text{mbar l/s}$	$t^*(\text{RT})$ $\text{d}$
CFRP	Cu foil	25	$< 1.87 \cdot 10^{-22}$	$< 1.36 \cdot 10^{-20}$	$< 1.75 \cdot 10^{-7}$	$> 2.0$
CFRP	Al foil	30	$< 1.83 \cdot 10^{-22}$	$< 1.12 \cdot 10^{-20}$	$< 1.43 \cdot 10^{-7}$	$> 2.4$
CFRP	Cu coating	50	$< 8.00 \cdot 10^{-22}$	$< 2.96 \cdot 10^{-20}$	$< 3.74 \cdot 10^{-7}$	$> 0.9$
CFRP	Cu coating	100	$< 8.00 \cdot 10^{-22}$	$< 1.52 \cdot 10^{-20}$	$< 1.87 \cdot 10^{-7}$	$> 1.9$
—	Al sheet	1000	$< 1.71 \cdot 10^{-21}$	$< 1.71 \cdot 10^{-21}$	$< 4.00 \cdot 10^{-8}$	$> 8.7$

## Chapter 7

# Conclusions

*“Basic research is like shooting an arrow into the air and, where it lands, painting a target.”* Homer Burton Adkins

### Summary

The objective of this thesis was to find an appropriate liner for the inner shell of an LH<sub>2</sub> tank made of CFRP. The liner — located at the outside surface of the shell — is required to prevent permeation of hydrogen through and outgassing from the inner tank into the insulating vacuum. Although outgassing was taken into account, too, the main objective was the permeation measurement of various liner types.

Surveying the outgassing rates and permeabilities from literature, only few metals and glasses satisfy the high requirements for the liners to enable a stable vacuum. Possible production processes to apply those materials on CFRP were studied and evaluated. The maximum allowable temperature of CFRP ( $\approx 120 \dots 140^\circ\text{C}$ ) and the applicability on the large and from-adapted structure of the LH<sub>2</sub> tank restricted the number of feasible processes. The chosen liner materials and production processes were

- Foils/sheets: Al, Cu, Sn and SS
- Metal platings with cNiP starting layer: Al, Au, Cu, Sn, and Ni
- Metal platings with cCu starting layer: Cu, Au and Sn
- Thermal spray Al
- PVD: C (DLC) and Ni.

All material tests and investigations were performed on flat specimens (plates, discs). Except for sheets and some of the foils, all liners were applied on CFRP substrates.

Besides permeation tests, the investigation of the various liners included the characterization by means of SEM, thermal shock experiments and adhesive strength tests. The permeation measurements were performed in two separate apparatuses, working between 293 K and 373 K (RTPMA) and between 20 K and 293 K (CPMA), respectively. Both apparatuses were designed and built to investigate CFRP, metals or the combination of both. The transmission method was used to imitate the real load case of the tank as good as possible. Feeding the test gas at one side of the specimen, the molecules permeate through the membrane into a flowing stream. There, the partial pressure of the permeating

gas was measured by means of a mass spectrometer and subsequently converted into the corresponding permeation rate.

The relationship between measured pressure and permeation flux was found by calibrating the mass spectrometer instead of using the constant pumping speed. The acquired calibration factors varied statistically around a mean value. Considering long terms, the mean value increased gradually by time. This increase was found to originate from a degradation of the filaments. Within one year, the sensitivity of the mass spectrometer decreased by factor 10. Hence, an error of 1000 % or more is possible if the speed of the turbomolecular pump is used instead of a calibration factor.

A typical permeation test consisted of the assembly of the specimen, the permeation measurement and the disassembly. During the assembly, an indium wire was squeezed between the specimen and two specimen holders to enable a leak-free sealing. This process was very critical and could not be successfully performed for every specimen. Mainly a rough surface of the specimen or mechanically weak liners were reasons for failing seals. After the subsequent bake-out at approximately 120 °C for 24 hours, the calibration was carried out. The actual permeation measurements were started at room temperature. Depending on the material, the steady-state permeation flux was typically reached after one or two days — if permeation was measurable at all. The change in temperature resulted in a change of the flux approaching a new steady-state within few hours. In very few cases, leaks in the sealing occurred during the change of the temperature.

Initial permeation tests were carried out to prove the functionality and reliability of both apparatuses. The measurements on CFRP and PVC showed consistent results at the RTPMA and CPMA. The permeabilities agreed well with those from the literature. The initial tests also revealed disadvantages of hydrogen as a test gas. The minimum detectable signal of hydrogen was almost four orders of magnitude higher than that of helium. Furthermore, hydrogen permeation was strongly influenced by environmental factors like the daily sunshine duration or the temperature. It is believed that the adsorption and release of hydrogen in the stainless steel chambers is very sensitive to the temperature and causes errors in the measurement. Because the permeabilities of helium and hydrogen were found to be similar in seven specimens, helium was used as test gas in the following.

Important for the quality of the measurement results is the minimum detectable gas flow. The minimum detectable gas flow is the product of the minimum detectable pressure and the calibration factor. Both factors can vary from one experiment to the other, depending on the material of the specimen, the quality of the sealing, and the state of the mass spectrometer's filaments. The typical limit of the detectable He gas flow was between  $4 \cdot 10^{-11}$  and  $5 \cdot 10^{-10}$  mbar l/s. Related to the permeating area of the RTPMA specimens, the minimum detectable area-specific gas flow was between  $1 \cdot 10^{-8}$  and  $1.2 \cdot 10^{-7}$  mbar l/s m<sup>2</sup>. In order to prove the requirement of the maximum allowable area-specific permeation gas flow through the tank vessel at room temperature (3.3),  $q < 1.5 \cdot 10^{-10}$  mbar l/s m<sup>2</sup>, the sensibility of the measuring apparatus would have to be between 66 and 800 times better. Hence, the employed measurement apparatuses enabled a comparison of the single liners and a general qualification/feasibility of them. In order to quantitatively prove the requirements, tests on specimens as large as the tank are necessary. On the other hand,



considering the best minimum detectable signal ( $1 \cdot 10^{-8}$  mbar l/s m<sup>2</sup>) ever measured, a tank vacuum stability time at room temperature of more than 56 days is feasible to prove.

Evaluating the results of the permeation measurements together with those of the adhesive strength and thermal shock tests, the foil/sheet liners and metal platings exhibited the highest potentials. Still, both liner types face some to-be solved challenges.

The structure of foils and sheets was compact and defect-free, which is characteristic for the production process (rolling, extrusion). The adhesive strength of some foils on CFRP was too low which resulted in a partial peeling. With the exception of tin specimens, the permeation gas flow through foils and sheets was lower than the detection limit. Remarkably, a 25  $\mu$ m Cu foil adhered on CFRP and three welded, 1 mm thick Al sheets did not allow any measurable permeation. Considering the 25  $\mu$ m Cu foil, the permeation flux through the protected CFRP was reduced at least by factor 7400 compared to CFRP. The measured He permeability of copper was less than  $2 \cdot 10^{-22}$  mol/m s Pa. Introducing sheets or foils as a liner on a free-form CFRP inner tank, the application of them would require a leak-free joining method with low heat production. This issue was not investigated in this thesis.

In contrast to foils, full metal platings can be produced on the outside of an inner LH<sub>2</sub> tank vessel. The investigated metal platings consisted of at least two layers. The first layer was produced by chemical deposition of copper or nickel. The typical thickness of this initial layer was between 1 and 10  $\mu$ m. Subsequently, the functional layer was applied by either chemical or electrochemical deposition. The materials of the functional layers were copper, nickel, gold, tin and aluminum. Depending on the material and the process parameters, the coatings contained grain-like structures on the surface. While the diameter of these grain-like structures was only 1 – 3  $\mu$ m for chemical copper, those of aluminum were up to 160  $\mu$ m in diameter. The coatings consisting of chemical nickel contained cracks which can be explained by their brittleness. Tin coatings were fully traversed by cracks after thermal shock which was ascribed to the phase transition at 286 K. The gold layers, having a thickness of only few micrometers, were not fully deposited but contained holes. The aluminum liners either exhibited uncoated spots or channels. Some of the metal platings, independent from the material and thickness, were characterized by circular holes. These holes, being maximal 100  $\mu$ m in diameter, originated from defects (voids, caverns) on the surface of the substrate. The caverns on the CFRP surface were only coated by material few micrometers thick or not at all. The existence of holes had a substantial impact on the measured permeabilities. Functional liners made of nickel sulfamate or copper containing no holes were impermeable within the accuracy of the measurements. In this case, the permeation gas flow through CFRP was reduced by more than factor 7400 (S46c, S65). On the contrary, a copper coating with nine holes (S10) reduced the permeation flux through CFRP only by factor 67. It was shown that — independent from the coating material — the total permeability is approximately proportional to the number of holes.

Temperature-dependent permeation measurements on metal-plated and uncoated CFRP specimens were performed between 20 K and 373 K. The measured permeation flux generally decreased with decreasing temperature. For temperatures below approximately 200 K,

no permeation could be detected in all investigated specimens. In particular, no permeation gas flow could be measured at 20 K. The extrapolated permeability of uncoated CFRP (worst case) at 20 K is  $5 \cdot 10^{-62}$  mol/m s Pa.

In some specimens containing either a cNiP, cNiP-cAu or cNiP-Sn coating, sudden and short increases of the permeation flux were recorded during the cooling phase. The subsequent measurement at RT revealed an increase of the permeation rate to values of uncoated CFRP. Hence, the peaks of the flux resulted from the formation of cracks in the according liners. Specimens with a copper or nickel functional layer did not show any peaks and did not form microcracks during cooling.

The measured activation energies of permeation through metal-plated CFRP were between 7 and 20 kJ/mol, but mostly below 15 kJ/mol. These activation energies are lower than those of uncoated CFRP ( $18 \pm 1$  kJ/mol). Simulations and calculations proved, that this behavior only occurs if the activation energy of permeation through the liner is low. Permeation through CFRP with an impermeable but defective coating would result in the same activation energy as uncoated CFRP. The low activation energy of the coating is assumed to be caused by grain boundary diffusion.

The assumption of grain boundary diffusion is emphasized by transient simulations performed with a self-written **Matlab** program. The aim of the simulations was to understand the various existing flux-time curves obtained from the experiments. In particular, some measured  $j(\tau)$  curves showed strong deviations from the Fickian curve, which describes permeation through a homogeneous material. Three models were employed: grain boundary diffusion, permeation through two homogeneous layers and permeation through a substrate with a defective liner. The parameters of the simulations were chosen to reflect the experiments as good as possible. Neither the simulation of two-layer permeation nor those of permeation through defectively coated CFRP could reproduce the  $j(\tau)$  curves found in the experiments. On the contrary, the simulation of grain boundary diffusion could describe the  $j(\tau)$  shape obtained from the experiments. It was found that the deviations from the Fickian curve depend on the size of the boundaries, the distance between those and the ratio between the grain and grain boundary diffusivity.

Considering the scattering in the values of the permeabilities, the low activation energies, and the partly found strong deviations of the  $j(\tau)$  curve from the Fickian curve, the permeation through metal-plated CFRP specimens can be described as followed: A closed, defect-free metal plating is impermeable for helium. If defects in the coating or very low coating thicknesses exist, then the barrier function of the coating is reduced. The permeation through these coating defects with low thickness is dominated by grain boundary diffusion. The existence of grain boundaries additionally justifies the usage of helium instead of hydrogen. In grain boundaries, vacancy diffusion is assumed to be present and results in a similar diffusion behavior of He and H<sub>2</sub>.

Besides sheets/foils and metal platings, thermal spray aluminum and physical vapor deposited carbon and nickel coatings were investigated. The three latter coatings did not reduce the permeation flux dramatically. While the PVD Ni and the DLC coatings contained cracks presumably owing to high internal stresses, the thermally sprayed Al coating did not form a closed layer.

Evaluating and comparing the permeation properties, sheets/foils and defect-free metal platings enabled a reduction of the permeation flux through CFRP below the minimum detection limit. Using this detection limit to calculate the stability time of the insulating tank vacuum, only a lower limit of the time can be given. At room temperature, a 30  $\mu\text{m}$  Al foil, a 25  $\mu\text{m}$  Cu foil or a 100  $\mu\text{m}$  Cu metal plating would enable a vacuum stability for at least 2 days. An aluminum sheet with 1 mm in thickness would even increase the minimum expectable time to 9 days. At 20 K, no reasonable permeation is expected.

The results of this work were used to choose an appropriate liner for the CFRP inner tank introduced in chapter 1. Considering and evaluating all properties of the various liners, the CFRP tank was coated by means of metal plating (see figure of the title page). The coating consisted of a chemical copper layer, followed by an electrochemical copper layer. Although the tank was fully coated, permeation tests could not be performed owing to predominating leaks in the CFRP structure.

Summarizing, a promising liner material and the according production process were found to prevent permeation through CFRP at temperatures between 20 and 373 K. The final qualification of this liner, however, must be performed on a tank itself.

## Future Work

This work has shown that metallic liners are feasible to apply on CFRP and to reduce the permeation rate below the detection limit. Still, there is a lot of space for improvements and future work.

The minimum detection limit of the measurements was too high to present results that can prove the tank requirements for the vacuum stability. An improvement can be achieved by either using larger specimens or applying higher feed pressures. When increasing the feed pressure, the limited ultimate strength of the specimens and the sensitivity of the sealing must be considered. Larger specimens are more difficult to seal, especially when measuring at varying temperatures. The lower stiffness and strength of larger specimens must also be taken into account. The usage of tubes instead of flat specimens would be an alternative. A promising approach to enhance the sensitivity of the mass spectrometer is given by Firpo and Pozzo [153]. There, the pumping speed of the gas of interest is reduced, while all other gases are evacuated constantly. Employing this method, the minimum detectable signal could be reduced by factor 10.

It was shown, that electroplatings on CFRP can be a permeation barrier if they do not contain defects. This implies that the surface of the CFRP must be free of caverns. Studies on the CFRP production process could indicate and subsequently prevent factors that favor the formation of those caverns. A promising approach is the usage of the resin transfer molding (RTM) process instead of the VARI process. In the RTM process, air enclosures are more present within the CFRP but less near the surface [154]. At the end of this work, four 200×100 mm<sup>2</sup> CFRP plates were produced by means of RTM and subsequently coated by 50  $\mu\text{m}$  copper. Only one hole was found in the four liners having an area of 800 cm<sup>2</sup>. Additionally to the improvement of the CFRP surface, the coating process can

be further investigated. Emphasis should be laid on understanding why caverns cannot be fully coated with increasing liner thickness.

All tests were performed on flat, nearly perfect specimens. However, the produced free-form CFRP tank contained leaks which were probably formed owing to different load cases and/or imperfections in the CFRP. Presuming an always existing potential of leakage in the CFRP structure, the size of the cracks causing this leakage should be determined. Subsequently, the ability to cover these cracks by coating should be investigated. Another option is a liner consisting of two layers. The first layer is very ductile, insensitive to thermal shocks or mechanical loads, and does not form cracks. Hence, this layer shall work as a crack stopper and prevent leakage. The second layer consists of a liner presented in this work and prevents permeation and outgassing.

Foils showed a great potential as a permeation barrier. However, leak-free joining methods must be found to employ foils as a liner. Processes like welding (high temperatures) or adhering (leakage) are not feasible. An alternative solution would be the application of single foil parts and the subsequent coating of the joining lines.

The qualification of the liners also requires the measurement of their outgassing rates. In order to be able to prove very low outgassing rates, large specimens — preferably the tank itself — should be used. The influence of the bake-out temperature and bake-out time can be determined by sensitivity studies. Cleaning methods, like chemical or glow discharge cleaning, should be investigated to further reduce the outgassing rate.

## Appendix A

# Literature Survey of H<sub>2</sub> Permeabilities

**Table A.1:** Permeabilities of metals.  $P_0$  and  $P$  in mol/m s Pa<sup>0.5</sup>,  $E_P$  in kJ/mol.

metal	$P_0$	$E_P$	$T$ / K	$P(293\text{ K})$	ref.
Ag	8.51E-07	100	887-998	1.24E-24	[155]
Al	5.80E-05	123	400-800	6.70E-27	[156]
Al	2.46E-04	129	200-500	2.84E-27	[157]
Al	3.98E-05	121	833-998	1.28E-26	[155]
Al	1.00E-09	52	400-800	4.38E-19	[38]
Al	3.30E-10	97	1273-1673	1.41E-27	[158]
Al	5.80E-05	123	420-520	6.70E-27	[159]
Al	5.20E-05	121	666-994	1.62E-26	[43]
Al oxidized	1.01E-09	52	733-823	4.44E-19	[160]
Al oxidized	7.50E-14		823		[160]
Al oxidized	1.61E-10	54	763-823	4.34E-20	[160]
Al oxidized	6.04E-10	57	683-738	4.01E-20	[160]
Al oxidized	5.48E-11	46	763-823	3.04E-19	[160]
Al oxidized	4.36E-11	42	763-823	1.41E-18	[160]
Al oxidized	1.86E-09	77	793-823	3.06E-23	[160]
Al oxidized	1.26E-10	54	763-823	2.85E-20	[160]
Al <sub>2</sub> O <sub>3</sub>	8.82E-02	322	1459-1721	2.82E-59	[161]
Al	2.00E-26		300	2.00E-26	[162]
Au	1.98E-06	115	300-640	6.23E-27	[163]
Au	1.89E-03	171	967-998	6.33E-34	[155]
Au	1.14E-06	115	400-800	3.59E-27	[38]
Au	3.10E-06	123	500-900	3.58E-28	[159]
Be	5.80E-14	18	670-1170	3.18E-17	[159]
Co	6.30E-09	57	400-670	4.43E-19	[159]
Cu	5.50E-07	75	623-973	2.51E-20	[164]
Cu	1.34E-07	63	1075-1172	8.51E-19	[165]
Cu	1.28E-07	72	200-500	1.72E-20	[157]
Cu	7.05E-07	76	684-998	1.93E-20	[155]
Cu	8.40E-07	77		1.33E-20	[38]
Cu	1.10E-05	98		9.90E-19	[166]
Cu	8.40E-07	77	470-700	1.29E-20	[159]

metal	$P_0$	$E_P$	$T / K$	$P(293 K)$	ref.
Cu	7.18E-09	61	667-997	1.12E-19	[43]
Fe	1.99E-07	39	628-681	1.45E-12	[34]
Fe	4.90E-05	35	623-973	2.92E-14	[164]
Fe	2.09E-06	35	200-500	1.43E-12	[157]
Fe	4.03E-08	35	625-1002	2.47E-14	[155]
Fe	5.72E-08	37	355-645	1.54E-14	[73]
Fe	4.10E-08	35	375-500	2.44E-14	[159]
Fe	5.35E-08	34		5.48E-14	[38]
Ge	1.20E-05	200	1040-1200	3.20E-41	[159]
Mo	2.30E-07	81	500-1700	9.32E-22	[159]
Mo	8.05E-09	48	666-994	2.10E-17	[43]
Nb	6.50E-09	-29	692-1000	9.55E-04	[155]
Nb	6.30E-09	-36	700-1000	1.34E-02	[159]
Nb	1.53E-08	5	751-995	2.32E-09	[43]
Ni	4.40E-07	55	673-1123	7.19E-17	[164]
Ni	1.28E-06	59	200-500	4.73E-17	[157]
Ni	3.17E-07	55	418-773	5.70E-17	[167]
Ni	9.62E-08	63		4.53E-16	[166]
Ni	6.16E-07	58	396-722	2.95E-17	[73]
Ni	4.00E-07	55	300-775	6.60E-17	[159]
Ni	8.40E-08	49	313-455	1.41E-16	[98]
Pd	3.33E-07	15	285-667	7.81E-10	[168]
Pd	2.16E-07	16	574-1165	3.55E-10	[169]
Pd	1.12E-07	13	624-1150	5.82E-10	[165]
Pd	4.08E-07	17	623-1173	4.33E-10	[170]
Pd	1.89E-07	15	625-998	4.29E-10	[155]
Pd	2.20E-07	16	300-709	3.54E-10	[159]
Pd	1.34E-07	14	667-994	4.69E-10	[43]
Pt	5.41E-08	64	709-1000	2.35E-19	[155]
Pt	1.20E-07	71	540-900	3.02E-20	[159]
Ta	5.46E-09	-21	625-998	2.86E-05	[155]
Ta	5.80E-09	-20	625-944	2.32E-05	[159]
Ti	4.86E-05	49	666-945	8.13E-14	[43]
V	4.90E-06	3		2.04E-06	[166]
V	4.00E-09	-25	600-900	1.08E-04	[159]
V	1.94E-04	59	667-912	5.07E-15	[43]
W	1.47E-09	80	873-1072	7.31E-24	[171]
W	7.80E-07	141	1100-2400	4.94E-32	[159]
W	1.61E-06	129	839-997	1.62E-29	[43]
Y	3.61E-09	-26	625-998	1.42E-04	[155]

**Table A.2:** Permeabilities of stainless steels.  $P_0$  and  $P$  in mol/m s Pa<sup>0.5</sup>,  $E_P$  in kJ/mol.

stainless steel	$P_0$	$E_P$	$T$ / K	$P(293\text{ K})$	ref.
Eurofer 97	4.08E-08	40	473-673	2.50E-15	[171]
stainless steel	1.20E-07	60	423-700	2.62E-18	[39]
stainless steel	2.80E-07	65	473-703	6.48E-19	[39]
stainless steel	5.40E-08	56	373-623	5.39E-18	[39]
SS 300 series	4.10E-08	60		6.82E-19	[156]
SS 303	3.60E-07	67	773-1173	3.53E-19	[164]
SS 304	4.99E-08	55	392-650	6.48E-18	[98]
SS 304	5.10E-07	71	823-1173	1.28E-19	[164]
SS 309S	1.20E-07	59	425-875	3.59E-18	[159]
SS 316	2.36E-07	63	416-1018	1.13E-18	[172]
SS 316L	3.90E-07	64		1.46E-18	[38]
SS 321	5.53E-08	59	497-933	1.42E-18	[172]
SS 403	5.90E-08	43		1.44E-15	[38]
SS 430	1.12E-07	46	796-1118	5.86E-16	[173]
stainless steel	2.47E-07	63	668-1000	1.37E-18	[43]

**Table A.3:** Permeabilities of nickel alloys.  $P_0$  and  $P$  in mol/m s Pa<sup>0.5</sup>,  $E_P$  in kJ/mol.

nickel alloy	$P_0$	$E_P$	$T$ / K	$P(293\text{ K})$	ref.
ANL-1	1.50E-05	65	973-1173	5.96E-17	[170]
Haynes	2.12E-07	63	500-1000	1.73E-18	[159]
Inconel	1.45E-09	41	313-455	7.87E-17	[98]
Inconel	9.30E-07	69	773-1173	5.44E-19	[164]
Inconel 600	6.40E-08	48	873-1173	2.23E-16	[170]
Inconel 600	3.99E-08	57	423-673	3.72E-18	[36]
Inconel 625	2.57E-07	60	423-1007	6.55E-18	[172]
Inconel 718	9.59E-08	56	364-1051	1.13E-17	[172]
Monel	6.97E-07	52	313-423	5.39E-16	[98]
Monel	1.87E-07	53	723-1223	6.10E-17	[164]

**Table A.4:** Permeabilities of iron alloys.  $P_0$  and  $P$  in mol/m s Pa<sup>0.5</sup>,  $E_P$  in kJ/mol.

iron alloy	$P_0$	$E_P$	$T / K$	$P(293 K)$	ref.
52 Alloy	2.79E-10	37	357-588	7.31E-17	[98]
Cold-drawn steel	4.70E-08	36	573-873	1.99E-14	[164]
iron alloy	8.09E-08	37	667-992	2.28E-14	[43]
Kovar	4.67E-09	44	373-666	5.68E-17	[98]
Kovar Interpolated	4.56E-07	69	641-998	2.14E-19	[155]
mild steel	4.10E-08	35		2.44E-14	[156]
Steal 4130	2.91E-08	40	350-900	2.23E-15	[159]

**Table A.5:** Permeabilities of various alloys.  $P_0$  and  $P$  in mol/m s Pa<sup>0.5</sup>,  $E_P$  in kJ/mol.

alloy	$P_0$	$E_P$	$T / K$	$P(293 K)$	ref.
Cu0.2Pd0.8	1.22E-07	21	627-1160	2.13E-11	[165]
Cu0.47Pd0.53	4.15E-08	28	623-1172	4.20E-13	[165]
Fe(321-SS)1.3 mm+4 $\mu$ m Al	3.42E-09	59	473-923	9.05E-20	[174]
Fe0.98Al0.02 (430-SS) and oxidation	2.34E-09	58	626-1112	9.70E-20	[174]
Fe0.98Al0.02 (430-SS)	3.40E-09	51	530-1115	2.78E-18	[174]
Hf36Ni64	3.00E-08	21	473-623	5.41E-12	[175]
Pd0.92Al0.08 partially oxidized	2.57E-09	13	423-504	1.49E-11	[176]
V-10mol%Al	3.67E-08	-7	523-624	7.64E-07	[177]
V-20mol%Al	5.46E-09	-10	523-624	3.95E-07	[177]
V-25mol%Al	4.62E-08	9	523-624	1.06E-09	[177]
V-30mol%Al	4.71E-08	18	523-624	2.52E-11	[177]
Zr36Ni64	8.00E-08	17	473-623	7.45E-11	[175]
Zr36Ni64(0.2) Ti39Ni61(0.8)	6.00E-08	26	473-623	1.39E-12	[175]

**Table A.6:** Permeabilities of glasses.  $P_0$  and  $P$  in mol/m s Pa,  $E_P$  in kJ/mol.

glass	$P_0$	$E_P$	$T / K$	$P(293 K)$	ref.
glass	4.86E-14	34	273-973	4.37E-20	[159]
glass	1.29E-13	60	273-973	2.94E-24	[159]
glass	2.86E-13	51	273-973	2.79E-22	[159]
Pyrex	8.20E-14	26	192-493	1.95E-18	[178]
Pyrex	7.67E-14	45	274-1246	8.44E-22	[30]
Quarzglas	5.08E-14	33	273-1246	5.65E-20	[30]
Zellglas	4.46E-16		293	4.46E-16	[92]
Zellglas, polymerlackiert	8.93E-17		293	8.93E-17	[92]



**Table A.7:** Permeabilities of thermoplastics.  $P_0$  and  $P$  in mol/m s Pa,  $E_P$  in kJ/mol.

thermoplastic	$P_0$	$E_P$	$T$ / K	$P(293\text{ K})$	ref.
ASA	2.55E-15		296	2.55E-15	[91]
CTFE	8.60E-11	32	257-343	1.75E-16	[91]
CTFE	6.69E-16		293	6.69E-16	[92]
ECTFE	2.85E-10	33	251-341	4.51E-16	[91]
EDPM	1.12E-10	24	317-349	5.02E-15	[47]
FEP	4.46E-15		298	4.46E-15	[179]
FEP	9.23E-11	27	257-341	1.70E-15	[91]
HDPE	9.13E-11	28	296	8.98E-16	[150]
HDPE	1.11E-10	29	255-341	8.09E-16	[91]
HDPE	1.12E-15		293	1.12E-15	[92]
HDPE	8.07E-16		298	8.07E-16	[180]
LDPE	3.57E-15		298	3.57E-15	[93]
LDPE	2.45E-15		293	2.45E-15	[92]
Noryl	8.66E-13	12	291-343	5.55E-15	[47]
PA 12	6.69E-16		293	6.69E-16	[92]
PA 12	7.30E-12	26	296	1.42E-16	[150]
PA 6	2.23E-16		293	2.23E-16	[92]
Parylene	1.07E-15		298	1.07E-15	[91]
PBT	6.69E-16		298	6.69E-16	[181]
PC	4.90E-11	23	224	4.27E-15	[112]
PC	8.93E-15		293	8.93E-15	[92]
PC	4.01E-15		298	4.01E-15	[182]
PE	1.07E-15		293	1.07E-15	[90]
PET	1.82E-16		298	1.82E-16	[183]
PET	1.98E-16		298	1.98E-16	[91]
PETP	1.79E-16		293	1.79E-16	[92]
PI	4.46E-16		298	4.46E-16	[184]
PP	2.66E-15		293	2.66E-15	[90]
PP	2.90E-15		293	2.90E-15	[92]
PP	1.34E-14		298	1.34E-14	[94]
PPS	8.31E-16		297	8.31E-16	[91]
PS	6.69E-15		293	6.69E-15	[92]
PS	7.58E-15		298	7.58E-15	[185]
PSU	3.56E-15		296	3.56E-15	[91]
PTFE	3.12E-15		298	3.12E-15	[186]
PTFE	3.44E-12	17	347-433	3.62E-15	[47]
PVC	3.92E-16		293	3.92E-16	[90]
PVC	3.57E-16		293	3.57E-16	[92]
PVC	2.33E-11	20	296	6.92E-15	[150]

thermoplastic	$P_0$	$E_P$	$T / K$	$P(293 K)$	ref.
PVC	1.34E-16		298	1.34E-16	[95]
PVC-E	4.46E-16		293	4.46E-16	[92]
PVDC	2.68E-16		293	2.68E-16	[92]
PVDF	9.74E-17		293	9.74E-17	[90]
PVDF	1.34E-16		293	1.34E-16	[92]
PVDF	1.07E-16		296	1.07E-16	[91]
PVDF	1.12E-16		298	1.12E-16	[187]
PVF	1.41E-16		298	1.41E-16	[188]
Santoprene	4.96E-13	25	293-333	1.66E-17	[47]
TFE	1.40E-11	20	255-341	3.49E-15	[91]
UPVC	5.25E-16		298	5.25E-16	[189]
UPVC	6.69E-16		298	6.69E-16	[190]

**Table A.8:** Permeabilities of thermosets.  $P_0$  and  $P$  in mol/m s Pa,  $E_P$  in kJ/mol.

thermoset	$P_0$	$E_P$	$T / K$	$P(293 K)$	ref.
CFEP (60%)	8.0E-12	26	200-300	1.9E-16	[150]
EP	5.6E-11	28	200-300	5.7E-16	[150]
EP	2.2E-16		298	2.2E-16	[91]
GFEP (56%)	5.9E-12	26	200-300	1.4E-16	[150]
GFRP	4.6E-17		308	4.6E-17	[191]
Polypyrrole	3.5E-16		296	3.5E-16	[91]
PUR	2.0E-15		293	2.0E-15	[91]
IM7/BMI	8.0E-17		293	8.0E-17	[192]

**Table A.9:** Permeabilities of elastomers.  $P_0$  and  $P$  in mol/m s Pa,  $E_P$  in kJ/mol.

elastomer	$P_0$	$E_P$	$T / K$	$P(293 K)$	ref.
CA, 2.5-Acetate	2.32E-15		293	2.32E-15	[92]
Kautschukhydrochlorid	1.79E-15		293	1.79E-15	[92]
Silicone	1.78E-13		298	1.78E-13	[193]
Silicone	8.90E-14		298	8.90E-14	[91]
Viton	7.06E-08	47.7	336-402	2.21E-16	[47]

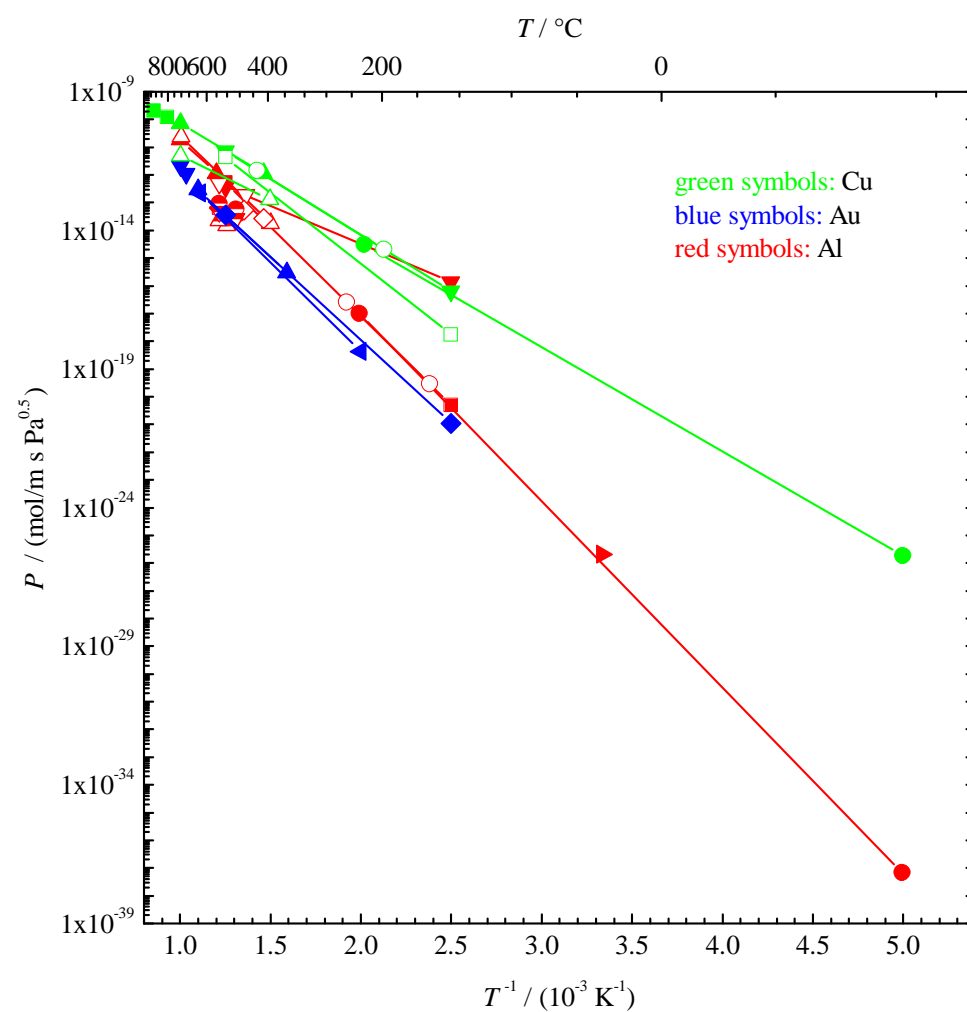


**Figure A.1:** Hydrogen permeabilities of copper, gold and aluminum from literature. The data of table A.1 is plotted.

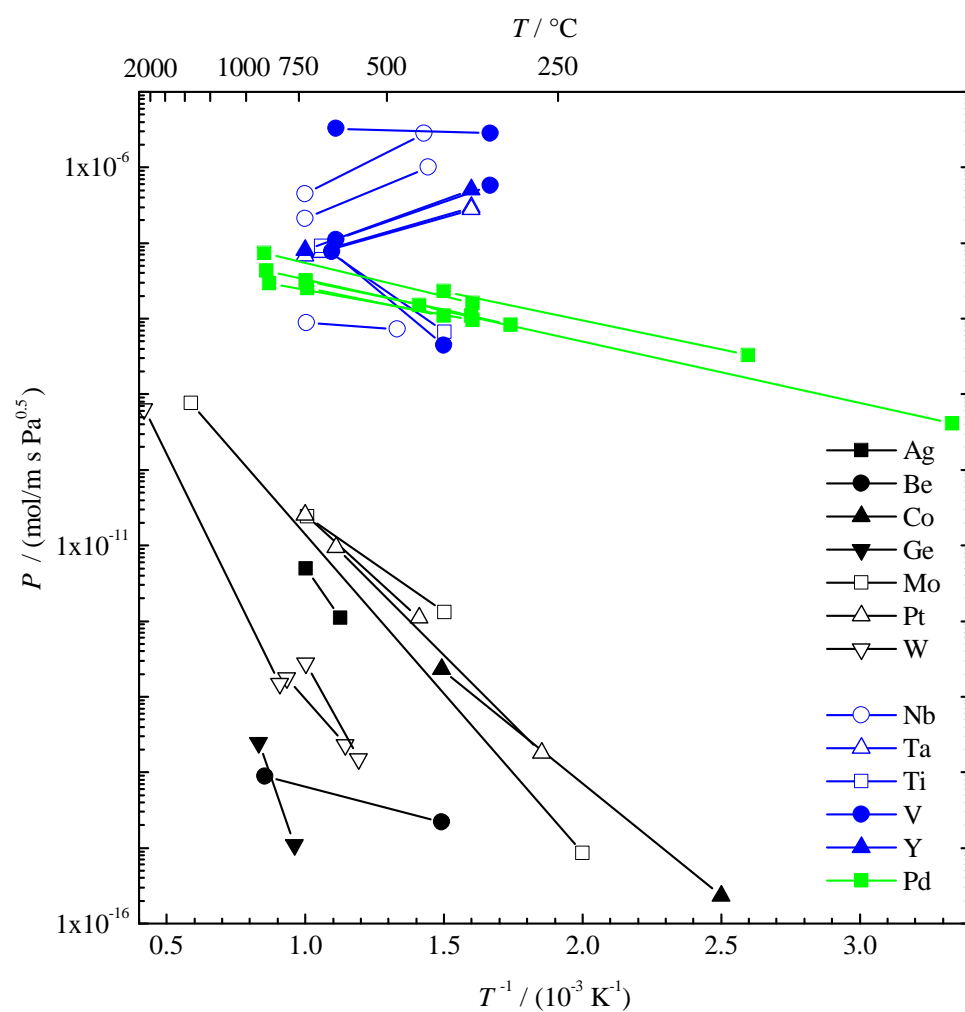


**Figure A.2:** Hydrogen permeabilities of silver, beryllium, cobalt, germanium, molybdenum, platinum, tungsten, niobium, tantalum, titanium, vanadium, yttrium and palladium. The data of table A.1 is plotted.

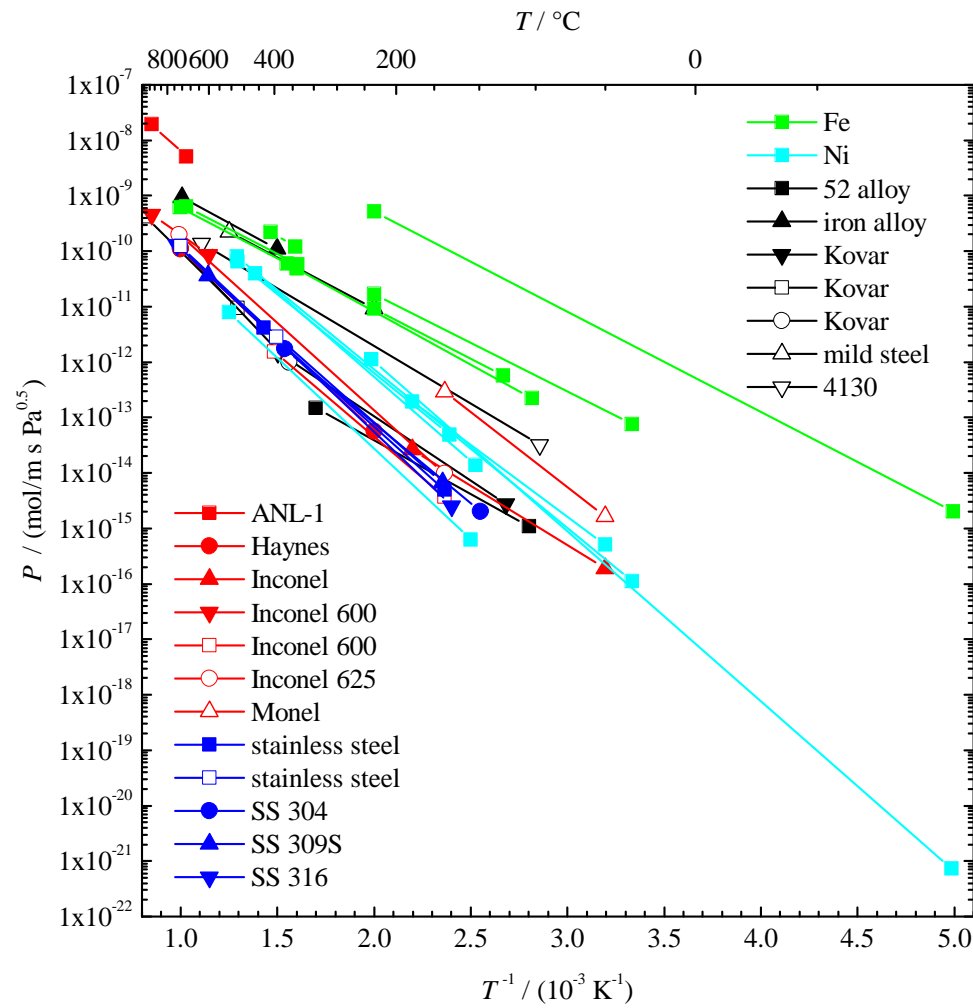


**Figure A.3:** Hydrogen permeabilities of iron, nickel and their alloys. The data of Fe (green) and Ni (light blue) are taken from table A.1. The data of stainless steel (dark blue), nickel alloy (red) and iron alloy (black) are taken from table A.2, table A.3 and table A.4, respectively.

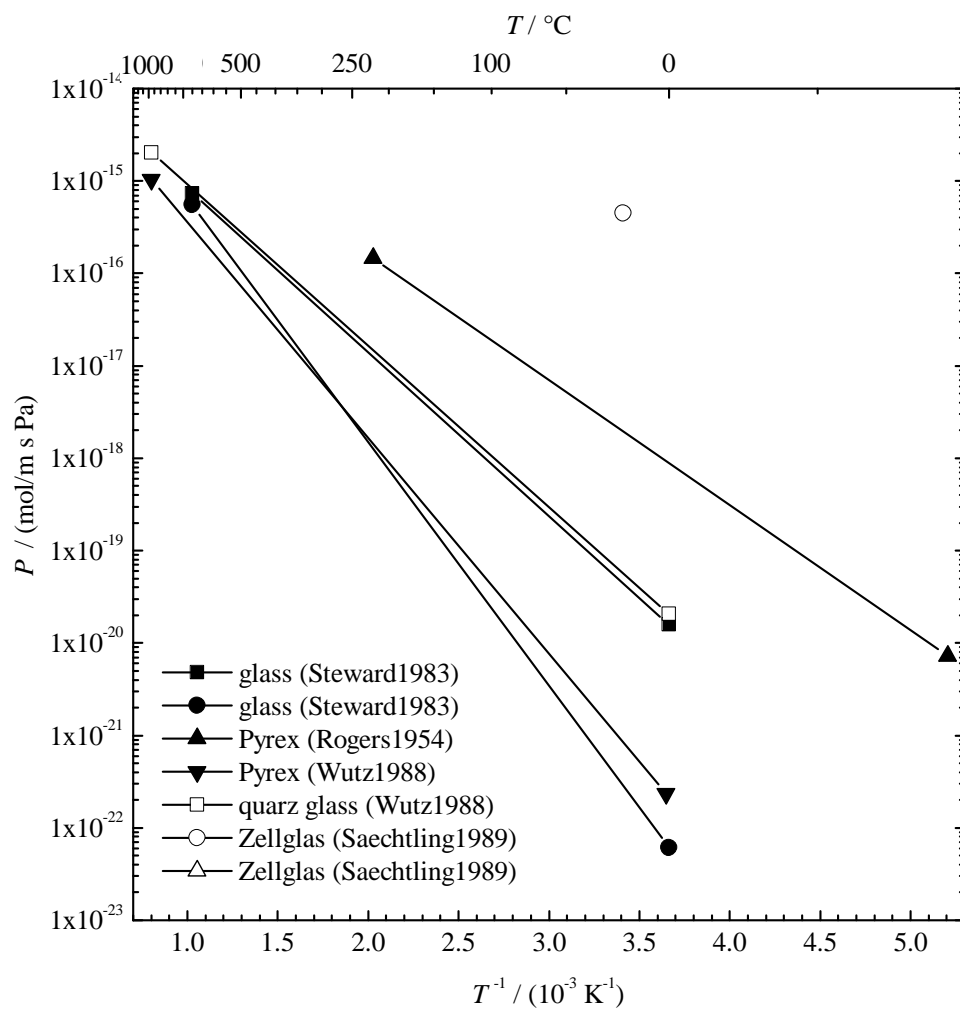


**Figure A.4:** Hydrogen permeabilities of glasses. The data are taken from table A.6.

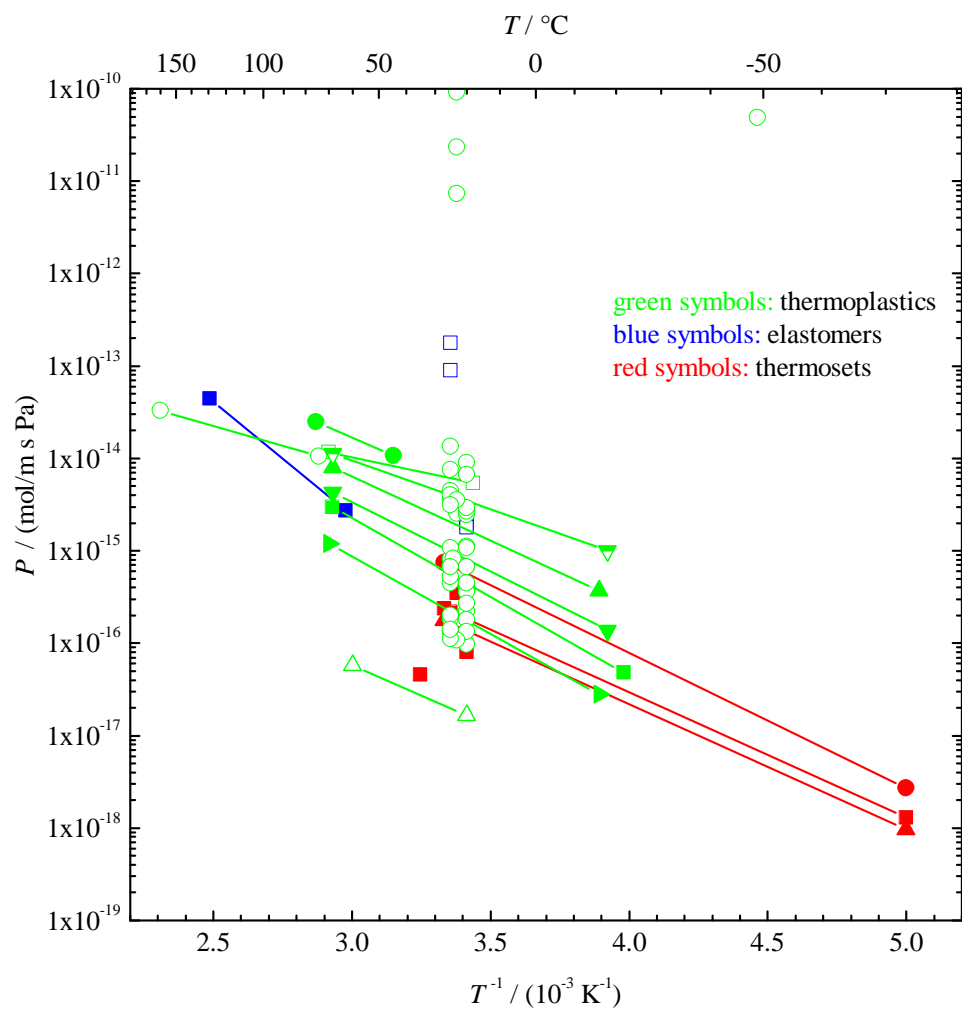


**Figure A.5:** Hydrogen permeabilities of polymers. The data of thermoplastics (green), thermosets (red) and elastomers (blue) are taken from table A.7, table A.8 and table A.9, respectively.





## Appendix B

# Literature Survey of Outgassing Rates

If not noted, the outgassing rates,  $q_G$ , are measured at room temperature (RT). The unit of the area specific outgassing rates is  $\text{mbar l s}^{-1} \text{m}^{-2}$ . The term “ $xx$  h at  $yyy$  °C” denotes the bake-out at  $yyy$  °C for  $xx$  hours.

**Table B.1:** Area specific outgassing rates of stainless steels

material	preparation / treatment	$q_G$	ref.
SS	1 h at RT	2.8E-05	[30]
SS	1 h at RT	4.2E-05	[30]
SS	1 h at RT	7.1E-05	[30]
SS	1 h at RT	8.3E-05	[30]
SS	1 h at RT	1.4E-04	[30]
SS	1 h at RT	9.0E-04	[30]
SS	1 h at RT	3.1E-03	[30]
SS	2 h at RT	7.7E-06	[129]
SS	2 h at RT	6.3E-05	[194]
SS	5 h at RT	1.0E-04	[195]
SS	10 h at RT	1.0E-05	[96]
SS	20 h at 150 °C	8.4E-07	[128]
SS	21 h at 200 °C	1.3E-10	[196]
SS	22 h at 212 °C	1.0E-10	[196]
SS	100 h at 430 °C, 100 h at 480 °C	3.0E-12	[196]
SS	electropolished	3.0E-08	[197]
SS	electropolished, 1 h at RT	4.3E-05	[30]
SS	mechanically polished, 1 h at RT	1.7E-05	[30]
SS	sand-blasted, 1 h at RT	8.3E-05	[30]
SS (304)	30 h at 250 °C	4.0E-08	[96]
SS (304)	baked and cleaned	1.3E-08	[198]
SS (304)	oxidized (3.5 nm CrOxide)	1.6E-10	[199]
SS (304)	venting with N <sub>2</sub> , 8 h at 180 °C	2.0E-09	[200]
SS (316)	baked and cleaned	1.3E-08	[198]
SS (316L)	10 h at 20 °C, 40 h at 140 °C, 50 h at 20 °C	7.7E-09	[201]
SS (401)	24 h at 300 °C	2.4E-07	[120]
SS (U15C)	45 h at 360 °C	1.9E-08	[126]
SS (U15C)	baked in situ at 360 °C for 24 h	3.7E-10	[126]

**Table B.2:** Area specific outgassing rates of Al

material	preparation / treatment	$q_G$	ref.
Al	? h at 200 °C	1.3E-10	[96]
Al	100 h at RT	4.0E-08	[200]
Al	10 h at 20 °C, 40 h at 140 °C, 50 h at 20 °C	1.5E-10	[201]
Al	10 h at 300 °C	4.0E-08	[135]
Al	10 h at RT	4.0E-06	[96]
Al	1 h at RT	4.1E-05	[30]
Al	1 h at RT	6.3E-05	[30]
Al	20 h at 100 °C	5.3E-10	[96]
Al	2 h at RT	3.0E-05	[129]
Al	2 h at RT	6.9E-05	[194]
Al	5 h at RT	5.0E-06	[195]
Al	dipped in sodium hydroxide, rinsed in de-mineralized water, thermally processed in an oxygen/argon atmosphere for 24 hrs	1.3E-09	[198]
Al		5.0E-04	[135]
Al		4.1E-05	[30]
Al (5083)	45 h at 140 °C	1.3E-10	[127]
Al (5083-H <sub>321</sub> )	several preparations to get an oxide layer	4.1E-09	[202]
Al (6061)	degreasing in acetone, 24 h at 100 °C	8.0E-08	[203]
Al (6061)	degreasing in acetone, 24 h at 150 °C	1.3E-08	[203]
Al (6061)	degreasing in acetone, 24 h at 200 °C	8.0E-09	[203]
Al (6061)	degr. in acetone, glow discharge in Ar, 24 h at 100 °C	6.7E-09	[203]
Al (6061)	degr. in acetone, glow discharge in Ar, 24 h at 150 °C	2.7E-09	[203]
Al (6061)	degr. in acetone, glow discharge in Ar, 24 h at 200 °C	8.0E-10	[203]
Al (6061)	several preparation, 24 h at 200 °C	1.3E-10	[203]
Al (6063)	10 h at 20 °C, 40 h at 140 °C, 50 h at 20 °C	4.1E-10	[201]

**Table B.3:** Area specific outgassing rates of Cu

material	preparation / treatment	$q_G$	ref.
Cu		3.5E-05	[30]
Cu	1 h at RT	1.9E-04	[30]
Cu	mechanically polished, 1 h at RT	1.9E-05	[30]
Cu	5 h at RT	2.0E-05	[195]
Cu	10 h at RT	2.0E-06	[96]
Cu	20 h at 100 °C	1.5E-08	[96]
Cu	24 h at 100 °C	2.9E-08	[204]
Cu	24 h at 250 °C	4.9E-08	[205]

material	preparation / treatment	$q_G$	ref.
Cu	24 h at RT, 24 h at 300 °C, venting, 24 h@RT, 24 h@100 °C	6.9E-10	[204]
Cu	25 h at 370 °C	1.2E-10	[122]
Cu	baked and cleaned	1.3E-08	[198]
Cu	electropolished, 10 h at 20 °C	4.0E-07	[206]
Cu	electropolished, 10 h at 20 °C, 24 h at 100 °C	2.9E-10	[206]
Cu	electropolished, 10 h at 20 °C, 24 h at 100 °C, 48 h at 300 °C	6.2E-12	[206]

**Table B.4:** Area specific outgassing rates of Ti and TiN

material	preparation / treatment	$q_G$	ref.
Ti		5.0E-04	[135]
Ti	chemical, electrical, buffing and mechanochemical polishing	4.0E-06	[135]
Ti	10 h at 300 °C	1.0E-08	[135]
Ti	10 h at RT	4.9E-06	[96]
Ti	1 h at RT	4.0E-05	[30]
TiN	192 h at ?	3.2E-08	[207]
TiN	48 h at 150 °C	6.0E-11	[194]

**Table B.5:** Area specific outgassing rates of further metals

material	preparation / treatment	$q_G$	ref.
Au	1 h at RT	1.6E-04	[30]
Au	1 h at RT	1.6E-04	[30]
Brass	10 h at RT	1.3E-04	[96]
Duraluminium	1 h at RT	1.7E-03	[30]
Fe	1 h at RT	5.4E-03	[30]
FeO	1 h at RT	6.0E-03	[30]
Messing	1 h at RT	4.0E-03	[30]
Mo	1 h at RT	5.2E-05	[30]
Ni	1 h at RT	2.3E-05	[30]
Zn	1 h at RT	2.2E-03	[96]
Zn	10 h at RT	4.3E-04	[30]

**Table B.6:** Area specific outgassing rates of polymers

material	preparation / treatment	$q_G$	ref.
1338 (epoxy)	24 h at 140 °C, 10 h at RT	3.1E-05	[208]
828 (epoxy)	24 h at 140 °C, 10 h at RT	2.0E-04	[208]
Araldite	10 h at RT	1.0E-02	[195]
Araldite	10 h at RT	4.7E-03	[96]
Araldite		1.2E-02	[30]
Araldite		1.5E-02	[30]
Araldite AT1	51 h at RT	6.0E-04	[209]
Araldite CT200+HT901	51 h at RT, 98 h at 100 °C	2.7E-06	[209]
Araldite MY740	51 h at RT	2.0E-04	[209]
Boron nitride M	clean in alcohol, dry air, 100 h at RT	3.0E-03	[121]
Butyl	4 h at RT	5.3E-03	[96]
CY-179 (epoxy)	24 h at 140 °C, 10 h at RT	4.5E-05	[208]
ERL4221 (epoxy)	24 h at 140 °C, 10 h at RT	2.0E-04	[208]
Kel-F	10 h at RT	2.3E-04	[96]
Kel-F		4.0E-04	[30]
Lexan (polycarbonate resin)	clean in alcohol, dry air, 100 h at RT	1.2E-03	[121]
Mycalex	51 h at RT	1.0E-05	[209]
Mylar	10 h at RT	2.0E-03	[195]
Mylar	10 h at RT	5.3E-03	[96]
Neopren		3.0E-02	[30]
Neoprene	4 h at RT	2.4E-01	[96]
Nylon	10 h at RT	4.0E-02	[195]
Nylon	10 h at RT	8.0E-02	[96]
Nylon 31	51 h at RT, 80 h at 120 °C	8.0E-06	[209]
Nylon 51	51 h at RT, 82 h at 120 °C	1.3E-06	[209]
PE	262 h at RT, 496 h at 80 °C	6.7E-05	[209]
PE	10 h at RT	1.1E-02	[96]
PE		2.3E-03	[30]
Perbunan		3.5E-02	[30]
Perspex	51 h at RT, 102 h at 85 °C	8.0E-05	[209]
PI	12 h at 300 °C	5.0E-07	[96]
Plexiglas	10 h at RT	3.6E-03	[96]
Plexiglas		7.0E-03	[30]
Polysil	24 h at 140 °C, 10 h at RT	3.2E-04	[208]
Polystyrol		5.6E-03	[30]
PRC-446-1387 (rubber)	clean in alcohol, dry air, 100 h at RT	4.7E-02	[121]
PRC-446-4387 (rubber)	clean in alcohol, dry air, 100 h at RT	2.9E-02	[121]
PTFE	48 h at RT	3.3E-06	[209]
PTFE	10 h at RT	1.0E-03	[195]

material	preparation / treatment	$q_G$	ref.
PTFE	10 h at RT	2.6E-03	[96]
PTFE		3.0E-03	[30]
PVC	24 h at 95 °C	2.7E-04	[96]
RF4000 (bisphenol resin)	24 h at 140 °C, 10 h at RT	7.6E-05	[208]
Silastomer 80	51 h at RT, 101 h at 200 °C	1.5E-05	[209]
Silicone	5 h at RT	2.0E-02	[195]
Silicone		1.8E-01	[30]
Steatit		9.0E-04	[30]
Teflon	10 h at RT	3.3E-04	[96]
Urethane 3000/AH-18	clean in alcohol, dry air, 100 h at RT	1.9E-03	[121]
Vespel (polyimide resin)	clean in alcohol, dry air, 100 h at RT	5.3E-04	[121]
Vespel (polyimide resin)		9.0E-03	[30]
Viton	5 h at RT	1.5E-03	[195]
Viton	12 h at 200 °C	2.7E-06	[96]
Viton		1.1E-02	[30]
Viton	degased	4.0E-05	[30]
Viton 77-545	clean in alcohol, dry air, 100 h at RT	2.0E-03	[121]

**Table B.7:** Area specific outgassing rates of glasses and ceramics

material	preparation / treatment	$q_G$	ref.
AlN-15% glassy C ceramics		2.0E-05	[210]
AlN-15% glassy C ceramics	24 h at 150 °C	5.7E-08	[210]
Mykrey 750 ceramics	clean in alcohol, dry air, 100 h at RT	2.0E-05	[121]
Mykrey 1100 ceramics	clean in alcohol, dry air, 100 h at RT	8.7E-06	[121]
Pyrex glass	10 h at RT	1.0E-06	[195]
Pyrex glass	10 h at RT	2.1E-06	[96]
Pyrex glass	1 month in air	1.2E-05	[30]
Pyrex glass		7.4E-05	[30]
Pyrophyllite glass	10 h at RT	2.7E-04	[96]
Pyrophyllite glass		2.0E-03	[30]
Steatite glass	10 h at RT	1.3E-04	[96]



## Appendix C

### List of Materials

**Table C.1:** List of substrates and polymers.  $l$  denotes the thickness.

mat. syst.	samples	matrix	fibers	production	$l$ / mm	producer	usage
M01	S76, S85, S88c	PVC			$\approx 2.0$	n/a	comparison with literature
M02	S04, S05, S06c, S09, S45c, S75	Araldite LY 564 / HY 2954 (100/35)	Sigratex KDK 8054/120	VARI	1.4..1.8	C02	metal plating
M03	S67, S90	Bakelite EPR04695/ EPH05357 (100/22)	Zoltec PX35 UD0300	wet laminate	$\approx 2.5$	C01	foils, thermal spraying, PVD
M04	S78	MGS RIM 935/ RIMH 937	SGL KDK 8054	VARI	$\approx 2.4$	C03	comparison of permeability of M02 and M03
	S79		see M03		$\approx 2.0$	C01	
	S85				$\approx 3.0$		

**Table C.2:** List of sheet and foil liners.  $l$  denotes the thickness of the liner.

material system	samples	substrate	liner	liner form	$l / \mu\text{m}$	producer	notes
M05	S52-S54		Al	sheet	$\approx 1000$	C10	no treatment
	S55-S57		(AA				welded
	S59-S61		5083)				bended
M06	S84		Fe	sheet	210	C11	1.4310
	S87				970	C12	1.4571
M07	S77		Sn	foil	130	unknown	
M08	S74		Al	foil	30	C14	
M09	S70	M03	Sn	foil	130	unknown	
M10	S72	M03	Al	foil	30	C14	
M27	S71	M03	Cu	foil	25	C13	
M11	S62	GFRP	Al	foil	2·101	unknown	no data of
	S63, S66	GFRP	Sn	foil	2·130	unknown	substrates
	S80	GFRP	Cu	foil	66	C05	availbale

**Table C.3:** List of miscellaneous coatings.  $l$  denotes the thickness of the liner.

material system	samples	substr.	liner	production	$l / \mu\text{m}$	producer	notes
M28	S83				2.37		produced
	S86	M03	C	DLC	2.30	C09	by Götz
	S89				2.32		Thorwarth
M29	S68, S69, S73	M03	Al	thermal spraying	0 ... 103 (48)	C07	
M30	S81	M03	Ni	PVD / chemical deposit.	22 ... 29 (24)	C08	no documentation available



**Table C.4:** List of metal platings. All coatings are produced on substrate M02. Abreviations: mat. sys.: material system;  $l$ : liner thickness, mean value in paranthesis; chem: chemical deposition; el-ch: electrochemical deposition.

mat. sys.	samples	liner	process	producer	$l$ / $\mu\text{m}$	notes
M12	S01, S02c, S03c	Ni	chem	C04	3.0 .. 4.6 (3.5)	cNiP
M13	S07	Ni	chem	C04	8 .. 13 (10)	
		Al	el-ch	C06	0 .. 28 (20)	
M13	S64	Ni	chem	C04	12 .. 23 (20)	
		Al	el-ch	C06	55 .. 94 (88)	
M14	S17, S18, S19c, S20c, S21, S22, S23	Ni	chem	C04	3.4 .. 4.2 (3.5)	
		Au	chem	C04	0.14 .. 0.4 (0.3)	
M15	S08, S10, S11c, S12c, S13, S14, S15c, S16c	Ni	chem	C04	3.7 .. 7.6 (5.0)	
		Cu	el-ch	C04	48 .. 59 (58)	
M16	S24, S25, S26, S27c, S28c	Ni	chem	C04	3.5 .. 6.0 (3.6)	
		Sn	el-ch	C04	77 .. 82 (80)	
M17	S29, S30, S31, S32c, S33c	Ni	chem	C04	3.3 .. 6.7 (3.7)	
		Ni	el-ch	C04	35 .. 39 (36)	nickel sulfamat
M31	S92	Cu	chem	C05	1.5 .. 10 (1.7)	cCu
M18	S40, S41c	Cu	chem	C05	$\approx 2$	
	S47				18	parameters:
	S42, S43c	Cu	el-ch	C05	57	2.0 A/dm <sup>2</sup>
	S44, S46c				67	200 g/l H <sub>2</sub> SO <sub>4</sub>
					108	
M19	S48	Cu	chem	C05	$\approx 2$	1.5 A/dm <sup>2</sup>
		Cu	el-ch	C05	42 .. 46 (44)	200 g/l H <sub>2</sub> SO <sub>4</sub>
M20	S49	Cu	chem	C05	$\approx 2$	3.0 A/dm <sup>2</sup>
		Cu	el-ch	C05	51 .. 60 (53)	200 g/l H <sub>2</sub> SO <sub>4</sub>
M21	S50, S91	Cu	chem	C05	$\approx 2$	2.0 A/dm <sup>2</sup>
		Cu	el-ch	C05	54 .. 63 (60)	180 g/l H <sub>2</sub> SO <sub>4</sub>
M22	S51	Cu	chem	C05	$\approx 2$	2.0 A/dm <sup>2</sup>
		Cu	el-ch	C05	51 .. 55 (52)	250 g/l H <sub>2</sub> SO <sub>4</sub>
M23	S65	Cu	chem	C05	$\approx 2$	
		Cu	el-ch	C05	81	
		Ni	el-ch	C05	17	
		Au	chem	C05	4	
M24	S36, S37c	Cu	chem	C05	3 .. 5 (3.1)	
		Ni	el-ch	C05	6 .. 8 (7.2)	
M25	S34, S35c	Cu	chem	C05	3 .. 7 (4)	
		Ni	el-ch	C05	6 .. 8 (7.7)	
		Au	chem	C05	1.4 .. 1.6 (1.55)	
M26	S38, S39c	Cu	chem	C05	1.5 .. 3 (2)	
		Sn	el-ch	C05	27 .. 43 (32)	



## Appendix D

### Measured Data

**Table D.1:** Summary of He permeation tests on PVC samples

sample	thickness	$P(RT)$	$P_0$	$E_P$	flux-time	$D$
	mm	mol/m s Pa	mol/m s Pa	kJ/mol	behavior	m <sup>2</sup> /s
S76	2.037	$7.62 \cdot 10^{-16}$			Fickian	$3.0 \cdot 10^{-10}$
S82	2.022	$7.91 \cdot 10^{-16}$	$6.14 \cdot 10^{-13}$	16.361	Fickian	$3.5 \cdot 10^{-10}$
S88c	2.017	$7.90 \cdot 10^{-16}$	$2.22 \cdot 10^{-11}$	12.587	Fickian	$2.4 \cdot 10^{-10}$

**Table D.2:** Summary of He permeation tests on CFRP samples

sample	material	$P(RT)$	$P_0$	$E_P$	flux-time	$D$
	system	mol/msPa	mol/msPa	kJ/mol	behavior	m <sup>2</sup> /s
S04	M02	$1.56 \cdot 10^{-16}$	$1.44 \cdot 10^{-13}$	16.389	near Fickian	$8.0 \cdot 10^{-11}$
S05		$8.88 \cdot 10^{-17}$	$1.35 \cdot 10^{-13}$	17.739	near Fickian	$6.0 \cdot 10^{-11}$
S06c		$1.21 \cdot 10^{-16}$	$2.19 \cdot 10^{-13}$	18.252	n/a	n/a
S09		$8.73 \cdot 10^{-17}$	$8.48 \cdot 10^{-14}$	16.569	near Fickian	$4.0 \cdot 10^{-11}$
S45c		$9.60 \cdot 10^{-17}$	$3.37 \cdot 10^{-13}$	19.759	near Fickian	$5.7 \cdot 10^{-11}$
S75		$1.15 \cdot 10^{-16}$	—	—	near Fickian	$6.0 \cdot 10^{-11}$
S67	M03	$1.24 \cdot 10^{-16}$	—	—	near Fickian	$8.0 \cdot 10^{-11}$
S90		$1.24 \cdot 10^{-16}$	$6.20 \cdot 10^{-14}$	15.031	Fickian	$8.0 \cdot 10^{-11}$
S79	M04	$3.73 \cdot 10^{-17}$	$1.13 \cdot 10^{-13}$	19.367	near Fickian	$1.1 \cdot 10^{-11}$
S85		$3.62 \cdot 10^{-16}$	$1.58 \cdot 10^{-13}$	14.673	Fickian	$1.4 \cdot 10^{-10}$
S78		$8.41 \cdot 10^{-17}$	$7.79 \cdot 10^{-14}$	16.373	near Fickian	$6.0 \cdot 10^{-11}$

**Table D.3:** Summary of He permeation tests on samples made of metal sheets or foils. MS: material system,  $t_{\text{test}}$ : test time,  $T_{\text{max}}$ : maximum test temperature,  $P$  and  $P_{\text{liner}}$ : permeability in mol/m s Pa of the sample and the liner, respectively.

sample	MS	material	liner	$t_{\text{test}} / \text{h}$	$T_{\text{max}}$	$P$	$P_{\text{liner}}$
S52	M05	Al	sheet	24	RT	$< 3.15 \cdot 10^{-21}$	$< 3.15 \cdot 10^{-21}$
S53				24	RT	$< 3.26 \cdot 10^{-21}$	$< 3.26 \cdot 10^{-21}$
S54				48	RT	$< 2.40 \cdot 10^{-21}$	$< 2.40 \cdot 10^{-21}$
S55				21	RT	$< 2.30 \cdot 10^{-21}$	$< 2.30 \cdot 10^{-21}$
S56				22	RT	$< 2.21 \cdot 10^{-21}$	$< 2.21 \cdot 10^{-21}$
S57				23	RT	$< 2.33 \cdot 10^{-21}$	$< 2.33 \cdot 10^{-21}$
S59				22	RT	$< 1.67 \cdot 10^{-21}$	$< 1.67 \cdot 10^{-21}$
S60				21	RT	$< 1.71 \cdot 10^{-21}$	$< 1.71 \cdot 10^{-21}$
S61				96	RT	$< 1.71 \cdot 10^{-21}$	$< 1.71 \cdot 10^{-21}$
S84	M06	Fe	sheet	24	362 K	$< 2.32 \cdot 10^{-21}$	$< 2.32 \cdot 10^{-21}$
S87				95	363 K	$< 7.03 \cdot 10^{-21}$	$< 7.03 \cdot 10^{-21}$
S77	M07	Sn	foil	$< 140$	RT	$< 1.21 \cdot 10^{-21}$	$< 1.21 \cdot 10^{-21}$
				$\geq 140$	RT	$> 3.66 \cdot 10^{-16}$	$> 3.66 \cdot 10^{-16}$
S74	M08	Al	foil	64	RT	$< 5.02 \cdot 10^{-22}$	$< 5.02 \cdot 10^{-22}$
S70	M09	CFRP/Sn	foil		RT	$2.56 \cdot 10^{-17}$	$3.71 \cdot 10^{-19}$
S72	M10	CFRP/Al	foil	15	RT	$< 1.33 \cdot 10^{-20}$	$< 1.83 \cdot 10^{-22}$
S71	M27	CFRP/Cu	foil	95	RT	$< 1.61 \cdot 10^{-20}$	$< 1.87 \cdot 10^{-22}$
S63	M11	GFRP/Sn	foil	68	RT	$< 1.67 \cdot 10^{-20}$	$\approx 1.62 \cdot 10^{-21}$
S66		GFRP/Sn	foil	94	RT	$< 1.84 \cdot 10^{-20}$	$\approx 2.06 \cdot 10^{-21}$
S62		GFRP/Al	foil	37	RT	$< 1.32 \cdot 10^{-20}$	$\approx 1.05 \cdot 10^{-21}$
S80		GFRP/Cu	foil	163	365 K	$< 1.57 \cdot 10^{-20}$	$\approx 7.45 \cdot 10^{-22}$

**Table D.4:** Summary of He permeation tests on metal-plated CFRP samples of material systems M12 – M17

sample	material system	$P(RT)$ mol/msPa	$P_0$ mol/msPa	$E_p$ kJ/mol	flux-time behavior	$D(RT)$ $10^{-11}$ m <sup>2</sup> /s	$P_{\text{liner}}(RT)$ mol/msPa
S01	M12	$9.90 \cdot 10^{-17}$	$6.40 \cdot 10^{-14}$	16.0	not Fickian	2.5	$4.97 \cdot 10^{-18}$
S02c		$3.60 \cdot 10^{-17}$		12-17	not Fickian	1.4	$1.03 \cdot 10^{-19}$
S03c		$5.09 \cdot 10^{-17}$		13-17	not Fickian	1.5	$1.91 \cdot 10^{-19}$
S07	M13	$4.73 \cdot 10^{-17}$	$6.31 \cdot 10^{-14}$	17.6	exact Fickian	8.0	$1.36 \cdot 10^{-18}$
S64		$5.40 \cdot 10^{-17}$	$1.17 \cdot 10^{-13}$	18.8	near Fickian	3.8	$\approx 5.72 \cdot 10^{-18}$
S17	M14	$7.62 \cdot 10^{-18}$	$1.65 \cdot 10^{-13}$	19.8	not Fickian	2.5	$1.86 \cdot 10^{-20}$
S18		$4.78 \cdot 10^{-17}$	$2.61 \cdot 10^{-14}$	14.1	not Fickian	2.0	$1.96 \cdot 10^{-19}$
S19c		$8.91 \cdot 10^{-17}$	$6.67 \cdot 10^{-15}$	11.9	not Fickian	2.0	$1.46 \cdot 10^{-18}$
S20c		$4.71 \cdot 10^{-17}$	$6.50 \cdot 10^{-15}$	12.0	not Fickian	1.6	$1.96 \cdot 10^{-19}$
S21		$4.79 \cdot 10^{-17}$			not Fickian	2.5	$2.13 \cdot 10^{-19}$
S22		$8.01 \cdot 10^{-17}$			not Fickian	2.5	$8.56 \cdot 10^{-19}$
S23		$1.86 \cdot 10^{-17}$			not Fickian	1.9	$5.52 \cdot 10^{-20}$
S08	M15	$7.42 \cdot 10^{-19}$	$2.43 \cdot 10^{-16}$	14.2	not Fickian	1.3	$2.57 \cdot 10^{-20}$
S10		$1.38 \cdot 10^{-18}$	$9.68 \cdot 10^{-16}$	16.3	not Fickian	3.6	$4.20 \cdot 10^{-20}$
S11c		$5.72 \cdot 10^{-19}$	$1.36 \cdot 10^{-15}$	19.3	not Fickian	1.0	$1.84 \cdot 10^{-20}$
S12c		$5.71 \cdot 10^{-19}$	$7.70 \cdot 10^{-16}$	17.8	not Fickian	2.2	$1.88 \cdot 10^{-20}$
S13		$7.38 \cdot 10^{-20}$					$2.51 \cdot 10^{-21}$
S14		$7.79 \cdot 10^{-20}$					$2.66 \cdot 10^{-21}$
S15c		$< 5.44 \cdot 10^{-20}$					$< 1.82 \cdot 10^{-21}$
S16c		$2.46 \cdot 10^{-19}$					$8.22 \cdot 10^{-21}$
S24	M16	$4.08 \cdot 10^{-19}$	$1.72 \cdot 10^{-16}$	14.8	not Fickian	2.0	$1.88 \cdot 10^{-20}$
S25		no sealing feasible	$1.21 \cdot 10^{-14}$	13.3	not Fickian	3.0	$5.02 \cdot 10^{-18}$
S26		$5.48 \cdot 10^{-17}$					
S27c		$6.25 \cdot 10^{-19}$					
S28c		$3.69 \cdot 10^{-19}$	$6.34 \cdot 10^{-16}$	17.1	not Fickian	2.0	$2.77 \cdot 10^{-20}$
S29	M17	no sealing feasible	$2.61 \cdot 10^{-17}$	12.2	not Fickian	2.0	$4.12 \cdot 10^{-21}$
S30		$1.85 \cdot 10^{-19}$					
S31		$4.97 \cdot 10^{-19}$					
S32c		$< 5.48 \cdot 10^{-20}$					$< 1.17 \cdot 10^{-21}$
S33c		$< 4.29 \cdot 10^{-20}$					$< 9.18 \cdot 10^{-22}$

**Table D.5:** Summary of He permeation tests on metal-plated CFRP samples of material systems M18 – M26

sample	material system	$P(RT)$ mol/msPa	$P_0$ mol/msPa	$E_P$ kJ/mol	flux-time behavior	$D(RT)$ $10^{-11}$ m <sup>2</sup> /s	$P_{\text{liner}}(RT)$ mol/msPa
S40		no sealing feasible					
S41c		$2.96 \cdot 10^{-18}$		9.9	not Fickian	4.0	$3.32 \cdot 10^{-20}$
S42		$1.20 \cdot 10^{-17}$	$2.19 \cdot 10^{-16}$	7.2	not Fickian	2.0	$4.86 \cdot 10^{-19}$
S43c	M18	$5.83 \cdot 10^{-19}$	$1.13 \cdot 10^{-15}$	18.6	near Fickian	3.0	$1.32 \cdot 10^{-19}$
S44		$3.68 \cdot 10^{-19}$	$1.70 \cdot 10^{-17}$	15.1	not Fickian	2.5	$2.13 \cdot 10^{-20}$
S46c		$< 6.26 \cdot 10^{-20}$					$< 8.09 \cdot 10^{-22}$
S47		$6.13 \cdot 10^{-18}$	$1.04 \cdot 10^{-15}$	12.9	near Fickian	2.0	$2.13 \cdot 10^{-20}$
S65	M23	$< 1.97 \cdot 10^{-20}$					$< 7.96 \cdot 10^{-22}$
S36		$8.31 \cdot 10^{-17}$	$2.06 \cdot 10^{-14}$	13.6	near Fickian	7.0	$2.33 \cdot 10^{-18}$
S37c	M24	no sealing feasible					
S34		$4.31 \cdot 10^{-17}$	$6.09 \cdot 10^{-15}$	12.3	not Fickian	4.0	$5.28 \cdot 10^{-19}$
S35c	M25	$3.21 \cdot 10^{-17}$			not Fickian	2.0	$3.31 \cdot 10^{-19}$
S38		$5.86 \cdot 10^{-18}$				5.0	$1.13 \cdot 10^{-19}$
S39c	M26	no sealing feasible					
S48	M19	$8.55 \cdot 10^{-19}$	$3.35 \cdot 10^{-17}$	9.1	not Fickian	2.0	$2.24 \cdot 10^{-20}$
S49	M20	$4.05 \cdot 10^{-19}$	$9.46 \cdot 10^{-17}$	13.4			$1.27 \cdot 10^{-20}$
S50	M21	$3.84 \cdot 10^{-18}$	$4.94 \cdot 10^{-15}$	17.6	not Fickian	1.5	$1.39 \cdot 10^{-19}$
S51	M22	$< 7.56 \cdot 10^{-20}$					$< 2.30 \cdot 10^{-21}$

**Table D.6:** Summary of He permeation tests on coated CFRP samples of material systems M28 – M30

sample	material system	$P(RT)$ mol/msPa	$P_0$ mol/msPa	$E_P$ kJ/mol	flux-time behavior	$D(RT)$ $10^{-11}$ m <sup>2</sup> /s	$P_{\text{liner}}(RT)$ mol/msPa
S83		$8.63 \cdot 10^{-17}$	$6.89 \cdot 10^{-14}$	16.4	near Fickian	4.2	$2.94 \cdot 10^{-19}$
S86	M28	$6.83 \cdot 10^{-17}$	$9.42 \cdot 10^{-14}$	17.8	near Fickian	3.8	$1.47 \cdot 10^{-19}$
S89		$4.38 \cdot 10^{-17}$	$1.76 \cdot 10^{-13}$	20.5	not Fickian	2.0	$7.64 \cdot 10^{-20}$
S68		no sealing feasible					
S69	M29	no sealing feasible					
S73		$1.69 \cdot 10^{-16}$			near Fickian	6.5	high
S81	M30	$5.71 \cdot 10^{-17}$		12.9	Fickian	5.5	$1.06 \cdot 10^{-18}$

# Bibliography

- [1] IFMO. Szenarien für das Jahr 2020. Technical report, Institut für Mobilitätsforschung, 2002.
- [2] M. A. Weiss et al. On the road in 2020. Technical report, MIT Energy Laboratory, 2000.
- [3] Kraftstoffstrategie der Bundesregierung – Matrixbericht. Technical report, Expertenarbeitsgruppe der Bundesregierung, 2004.
- [4] F. Birol. World energy outlook 2002. Technical report, International Energy Agency, 2002.
- [5] L. Mantzos. European energy and transport trends to 2030. Technical report, European Commission, Directorate-General for Energy and Transport, 2003.
- [6] AFCG. Market development of alternative fuels. Technical report, Alternative Fuels Contact Group, 2003.
- [7] L-B-Systemtechnik. Assumptions, visions and robust conclusions from project phase I. Technical report, HyWays, 2005.
- [8] McKinsey. Drive study. Technical report, 2005.
- [9] W. Stegers. Alles – ausser Benzin. *P.M.*, 5:46–50, 2005.
- [10] W. Tauscher. Wie lange reichen die Reserven von Erdöl und Erdgas?, 2002. Lecture series, Österreichischer für Kraftfahrzeugtechnik, Wien.
- [11] BP. Statistical review of world energy. Technical report, 2006.
- [12] M. von Baratta. *Der Fischer Weltalmanach 2004*. Fischer Taschenbuch Verlag, 2003.
- [13] WMO. Statement on the status of the global climate in 2005. Technical Report 998, World Meteorological Organization, 2006.
- [14] S. Dunn. Hydrogen futures: toward a sustainable energy system. *International Journal of Hydrogen Energy*, 27(3):235–264, 2002.
- [15] R. Alley et al. Climate change 2007: The physical science basis, summary for policymakers. Technical report, Intergovernmental Panel on Climate Change, 2007.
- [16] A. Raffray et al. Effect of outer insulating porous plastic foam layer on target thermal response during injection. Technical Report UCSD-ENG-096, University of California, San Diego, 2002.

- 
- [17] W. Lehmann. Thermische Isolation. In *Kryotechnik - VDI Seminar in Karlsruhe*. 1997.
- [18] V. Strubel. First periodic activity report. Technical report, StorHy, 2005.
- [19] P. Ermanni. Composites Technologien, 2003. Lecture notes at Eidgenössische Technische Hochschule Zürich.
- [20] R&G Faserverbundwerkstoffe GmbH. Handbook composite materials. URL [http://www.swiss-composite.ch/pdf/i-handbuch\\_komplett.pdf](http://www.swiss-composite.ch/pdf/i-handbuch_komplett.pdf), 2003.
- [21] W. Möbius. Mechanismen und Modelle der Festkörperdiffusion. In *Sommerakademie in Alpbach*. 2003.
- [22] D. R. Lide. *CRC handbook of chemistry and physics, 1996 - 1997*. CRC Press, 77th edition, 1996.
- [23] B. Duncan et al. Review of measurement and modelling of permeation and diffusion in polymers. Technical Report DEPC MPR 012, NPL, Division of Engineering and Process Control, 2005.
- [24] L. Raffaelli. *Thermomechanics of fibre reinforced epoxies for cryogenic pressurized containment*. Ph.D. thesis, Fakultät für Maschinenwesen der Technischen Universität München, 2006.
- [25] C. Hibshman. *Polyimide-Organosilicate Hybrid Materials*. Master's thesis, Department of Chemical Engineering, Virginia Polytechnic Institute and State University Blacksburg, 2002.
- [26] C. Cornelius. *Physical and gas permeation properties of a series of novel hybrid inorganic-organic composites based on a synthesized fluorinated polyimide*. Ph.D. thesis, Virginia Polytechnic Institute and State University, 2000.
- [27] V. Ravindrachary et al. Thermally induced microstructural changes in undoped and doped polyacrylonitrile: A positron-annihilation study. *Physical Review B*, 46(18):11471–11478, 1992.
- [28] M. Hanika. *Zur Permeation durch aluminiumbedampfte Polypropylen- und Polyethylenterephthalatfolien*. Ph.D. thesis, Technische Universität München, 2003.
- [29] A. Michaels et al. Solution of gases in polyethylene terephthalate. *Journal of Applied Physics*, 34(1):1–12, 1963.
- [30] M. Wutz et al. *Theorie und Praxis der Vakuumtechnik*. Friedrich Vieweg & Sohn, Braunschweig, 4th edition, 1988.
- [31] E. Fromm and E. Gebhardt. *Gase und Kohlenstoff in Metallen*. Springer, 1976.



- 
- [32] I. Langmuir. The constitution and fundamental properties of solids and liquids. *Journal of the American Chemical Society*, 38(95):2221–2295, 1916.
- [33] H. Vogel and C. Gerthsen. *Physik*. Springer, 1995.
- [34] I. Ali-Khan et al. The rate of hydrogen release out of clean metallic surfaces. *Journal of Nuclear Materials*, 76(11):337–343, 1978.
- [35] P. B. Lloyd et al. Surface and bulk interactions of hydrogen with copper. *Applied Surface Science*, 119(3-4):275–287, 1997.
- [36] E. Rota et al. Measurements of surface and bulk properties for the interaction of hydrogen with inconel 600. *Journal of Nuclear Materials*, 111-112:233–239, 1982.
- [37] F. Waelbroeck et al. Hydrogen solubilisation into and permeation through wall materials. *Journal of Nuclear Materials*, 85-86:345–349, 1979.
- [38] R. Schefer et al. Characterization of leaks from compressed hydrogen dispensing systems and related components. *International Journal of Hydrogen Energy*, 31(9):1247–1260, 2006.
- [39] C. S. Marchi et al. Permeability, solubility and diffusivity of hydrogen isotopes in stainless steels at high gas pressures. *International Journal of Hydrogen Energy*, article in press, 2006.
- [40] M. Klopffer and B. Flaconnèche. Transport properties of gases in polymers: Bibliographic review. *Oil & Gas Science and Technology*, 56(3):223–244, 2001.
- [41] J. Elliott. Polymeric materials - diffusion in polymers, 2003. Lecture notes at the University of Cambridge.
- [42] M. Wessling. *Relaxation phenomena in dense gas separation membranes*. Ph.D. thesis, University of Twente, 1993.
- [43] J. Kirkaldy and D. Young. *Diffusion in the Condensed State*. The Institute of Metals, London, 1987.
- [44] J. Philibert. *Atom movements - Diffusion and mass transport in solids*. Les Éditions de Physique, 1991.
- [45] M. Glicksman. *Diffusion in Solids. Field Theory, Solid-State Principles, and Applications*. John Wiley & Sons, Inc., 2000.
- [46] A. Thran et al. Correlation between fractional free volume and diffusivity of gas molecules in glassy polymers. *Journal of Polymer Science: Part B: Polymer Physics*, 37(23):3344–3358, 1999.

- 
- [47] D. Stodilka et al. A tritium tracer technique for the measurement of hydrogen permeation in polymeric materials. *International Journal of Hydrogen Energy*, 25(11):1129–1136, 2005.
- [48] B. Flaconnèche et al. Permeability, diffusion and solubility of gases in polyethylene, polyamide 11 and poly(vinylidene fluoride). *Oil & Gas Science and Technology*, 56(3):261–278, 2001.
- [49] R. Borg and G. Dienes. *An Introduction to Solid State Diffusion*. Academic Press, Inc., San Diego, 1988.
- [50] A. Cerezo. Diffusion. Department of Materials University of Oxford, 2005.
- [51] H. Wipf. Diffusion of hydrogen in metals. In Alefeld and Völkl [68], pages 51–91.
- [52] G. Young Jr. and J. Scully. The diffusion and trapping of hydrogen in high purity aluminum. *Acta Metallurgica*, 48(18):6337–6349, 1998.
- [53] Y. Sohn. Diffusion in solids, 2005. Lecture notes at the University of Central Florida.
- [54] J. Adams and W. Wolfer. On the diffusion mechanisms of helium in nickel. *Journal of Nuclear Materials*, 158:25–29, 1988.
- [55] P. Shewmon. *Diffusion in solids*. Minerals, Metals & Materials Society, 2nd edition, 1989.
- [56] J. Crank. *The Mathematics of Diffusion*. Clarendon Press, Oxford, 1970.
- [57] M. Glicksman and A. Lupulescu. Kinetics, 2004. Lecture notes at the Rensselaer Polytechnic Institute Troy.
- [58] A. Brass and A. Chanfreau. Accelerated diffusion of hydrogen along grain boundaries in nickel. *Acta Materialica*, 44(9):3823–3831, 1996.
- [59] W. Shmayda et al. Effects of textures on hydrogen diffusion in nickel. In T. J. Collins, editor, *LLE Review*, volume 91, pages 125–129. University of Rochester, Laboratory for Laser Energetics, 2002.
- [60] K. Hauffe. *Anorganische und Allgemeine Chemie in Einzeldarstellungen Band 2: Reaktionen in und an festen Stoffen*. Springer, 1955.
- [61] J. Agren. Diffusion at phase boundaries. In *Marie Curie Summer School - Knowledge-Based Materials*. 2004.
- [62] L. G. Harrison. Influence of dislocations on diffusion kinetics in solids with particular reference to the alkali halides. *Transactions of the Faraday Society*, 57:1191–1199, 1961.

- 
- [63] I. Kaur et al. *Fundamentals of grain and interphase boundary diffusion*. John Wiley and Sons, 3rd edition, 1995.
- [64] J. Hwang and R. Balluffi. Measurement of grain-boundary diffusion at low temperatures by the surface accumulation method — I. method and analysis. *Journal of Applied Physics*, 50(3):1339–1348, 1979.
- [65] M. J. Danielson. Use of the devanathan-stachurski cell to measure hydrogen permeation in aluminum alloys. *Corrosion Science*, 44(4):829–840, 2002.
- [66] Y. Yamada-Takamura et al. Hydrogen permeation barrier performance characterization of vapor deposited amorphous aluminum oxide films using coloration of tungsten oxide. *Surface and Coatings Technology*, 153(2-3):114–118, 2002.
- [67] J. Völkl and G. Alefeld. *Diffusion in Solids, Recent Developments*. Academic Press, 1975.
- [68] G. Alefeld et al. *Hydrogen in metals I – Basic properties*. Topics in Applied Physics Vol. 28. Springer, 1978.
- [69] B. Flaconnèche et al. Transport properties of gases in polymers: Experimental methods. *Oil & Gas Science and Technology*, 56(3):245–259, 2001.
- [70] W. Umrath, editor. *Grundlagen der Vakuumtechnik*. Leybold Vakuum, 1997.
- [71] N. Marquardt. Introduction to the principles of vacuum physics. In S. Turner, editor, *Proceedings of Vacuum Technology*. CERN Accelerator School, 1999.
- [72] Pfeiffer Vacuum GmbH. *Arbeiten mit Turbopumpen*, 2003. Manual PT 0053 PD.
- [73] K. Yamakawa et al. Hydrogen permeability measurement through Pd, Ni and Fe membranes. *Journal of Alloys and Compounds*, 321(1):17–23, 2001.
- [74] K. Yamakawa et al. Hydrogen permeation through Pd/Fe and Pd/Ni multilayer systems. *Journal of Alloys and Compounds*, 393(1-2):5–10, 2005.
- [75] P. Andrew and A. Haasz. Effect of thin copper and palladium films on hydrogen permeation through iron. *Journal of the Less-Common Metals*, 173(1-2):732–739, 1991.
- [76] R. Ash et al. Diffusion in heterogeneous media: properties of a laminated slab. *British Journal of Applied Physics*, 14:854–862, 1963.
- [77] W. Prins and J. Hermans. Theory of permeation through metal coated polymer films. *Journal of Physical Chemistry*, 63(5):716–720, 1959.
- [78] K. Vasko. *Schichtsysteme für Verpackungsfolien mit hohen Barriereigenschaften*. Ph.D. thesis, Technische Universität München, 2006.

- 
- [79] G. Rossi and M. Nulman. Effect of local flaws in polymeric permeation reducing barriers. *Journal of Applied Physics*, 74(9):5471–5475, 1993.
- [80] P. Mercea et al. Permeation of gases through poly(ethylene terephthalate) membranes metallized with palladium. *Journal of Membrane Science*, 35(3):291–300, 1988.
- [81] P. Mercea et al. Permeation of gases through metallized polymer membranes. *Journal of Membrane Science*, 24(3):297–307, 1985.
- [82] G. Czeremuszkin et al. A simple model of oxygen permeation through defects in transparent coatings. In *42th Annual Technical Conference Proceedings, Society of Vacuum Coaters*. 1999.
- [83] E. Jamieson and A. H. Windle. Structure and oxygen-barrier properties of metallized polymer film. *Journal of Material Science*, 18(1):64–80, 1983.
- [84] T. Beu. Gas transport through metallized polymer membranes. *Materials Chemistry and Physics*, 26:309–322, 1990.
- [85] M. Yanaka et al. How cracks in  $\text{SiO}_x$ -coated polyester films affect gas permeation. *Thin Solid Films*, 397(1-2):176–185, 2001.
- [86] R. Goetz et al. Final report of the X-33 liquid hydrogen tank test investigation team. Technical report, NASA, 2000.
- [87] B. W. Grimsley et al. Hybrid composites for  $\text{LH}_2$  fuel tank structure. Technical report, NASA Langley Research Center, Hampton Virginia Polytechnic Institute and State University, NASA Marshall Space Flight Center, Huntsville, 2001.
- [88] J. Humpenöder. *Gaspermeation von Faserverbunden mit Polymermatrices*. Ph.D. thesis, Forschungszentrum Karlsruhe, Institut für Materialforschung, 1997.
- [89] P. Molyneux. "Transition-site" model for the permeation of gases and vapors through compact films of polymers. *Journal of Applied Polymer Science*, 79(6):981–1024, 2001.
- [90] S. Paul. Permeation data, 2004.
- [91] Plastics Design Library Staff. *Permeability and Other Film Properties of Plastics and Elastomers*. William Andrew Publishing/Plastics Design Library, 1995.
- [92] H. Saechtling and W. Zebrowski. *Kunststoff-Taschenbuch*. Hanser, 24th edition, 1989.
- [93] Goodfellow. Materialinformationen LDPE. URL [http://www.goodfellow.com/csp/active/gfMaterialInfo.csp?text=\\*P\&MATID=ET31\&material=1](http://www.goodfellow.com/csp/active/gfMaterialInfo.csp?text=*P\&MATID=ET31\&material=1), 2005.

- 
- [94] Goodfellow. Materialinformationen PP. URL [http://www.goodfellow.com/csp/active/gfMaterialInfo.csp?text=\\*P\&MATID=PP30\&material=1](http://www.goodfellow.com/csp/active/gfMaterialInfo.csp?text=*P\&MATID=PP30\&material=1), 2005.
- [95] Goodfellow. Materialinformationen PVC. URL [http://www.goodfellow.com/csp/active/gfMaterialInfo.csp?text=\\*P\&MATID=FV33\&material=1](http://www.goodfellow.com/csp/active/gfMaterialInfo.csp?text=*P\&MATID=FV33\&material=1), 2005.
- [96] J. F. O'Hanlon. *A User's Guide to Vacuum Technology*. Wiley-Interscience, 2nd edition, 1989.
- [97] B. McCool and Y. Lin. Nanostructured thin palladium-silver membranes: Effects of grain size on gas permeation properties. *Journal of Material Science*, 36(13):3221–3227, 2001.
- [98] R. Collins and J. Turnbull. Degassing and permeation of gases in tube materials. In D. Slater, editor, *Advances in Electron Tube Techniques, Proceedings of the Fifth National Conference*, pages 186–190. 1960.
- [99] S. Black. An update on composite tanks for cryogenics. *High-Performance Composites*, 2005.
- [100] Microcosm, Inc. Successful qualification of full-scale, all-composite cryogenic LOX tank opens the way to low-cost, responsive launch-on-demand. URL [http://www.smad.com/42\\_inch\\_tank\\_pressrelease.pdf](http://www.smad.com/42_inch_tank_pressrelease.pdf), 2006.
- [101] V. P. McConnell. DC-XA spacecraft to fly first composite liquid hydrogen fuel tank. *High-performance Composites*, March/April:80–82, 1996.
- [102] D. C. Freeman Jr. et al. Reusable launch vehicle technology program. *Acta Astronautica*, 41(11):777–790, 1997.
- [103] XCOR Aerospace. Cyro compatible fluoropolymer composite material. URL [http://www.xcor.com/products/cryo\\_compatible\\_composites.html](http://www.xcor.com/products/cryo_compatible_composites.html), 2006.
- [104] T. Shimoda et al. Study of CFRP application to the cryogenic propellant tank of reusable launch vehicle. In *42nd AIAA/ASME/ASCE/AHS/ASC Structures, Structural Dynamics, and Materials Conference, Seattle*. 2001.
- [105] W.-D. Ebeling. Insulation design and analysis report for the aluminum-lithium specimen. Interim Report FTS-RIBRE-TN-0001, Daimler-Benz Aerospace, 1996.
- [106] D. Dosio. FESTIP structures technology — summary final report. Technical Report FTS-ALS-FIR-5000-0017, Alenia Aerospazio, 1997.
- [107] V. Diaz et al. Tank construction design selection report. Technical Report FSS-TN-CAS-0002, CASA, 1996.
- [108] J. Antonenko and W.-D. Ebeling. FESTIP - technologies in heat management. Technical Report FTS-RIBR-RP-003, Daimler-Benz Aerospace, 1997.

- [109] netcomposites. NASA complete testing of prototype composite cryogenic fuel tank. URL <http://www.net-composites.com/news.asp?2390>, 2004.
- [110] ILK Dresden. Leistungen des ILK Dresden: Kryostate. URL <http://www.ilkdresden.de/de/leistungen/kaelte/kryostate.htm>, 2001.
- [111] W.-B. Klemmt et al. Wirbelstromprüfung an Flugzeugstrukturen mit SQUID's. In *DGLR Jahrestagung in Bremen, Deutscher Luft- und Raumfahrtkongress*. 1998.
- [112] G. Hartwig. Faserverbund-Eigenschaften zum Bau eines LH<sub>2</sub>-Leichtbau-Tanks. Technical report, 2004.
- [113] Digitale Bibliothek. *Wikipedia 2005/2006*, chapter X-33, pages 905505–905506. Directmedia Publishing GmbH, 2005.
- [114] B. McKinney. Northrop Grumman, NASA successfully test composite hydrogen fuel tank for reusable launch vehicles. Technical report, Northrop Grumman, 2003.
- [115] B. McKinney. Northrop Grumman, NASA complete testing of prototype composite cryogenic fuel tank. Technical report, Northrop Grumman, 2004.
- [116] J. Völkl and G. Alefeld. Diffusion of hydrogen in metals. In H. Wipf, editor, *Hydrogen in Metals III – Properties and Applications*, pages 321 – 348. Springer, 1997.
- [117] K. Jousten. Thermal outgassing. In S. Turner, editor, *Proceedings of Vacuum Technology*. CERN Accelerator School, 1999.
- [118] N. Schindler et al. Some investigations on the effective short time outgassing depth of metals. *Journal of Vacuum Science & Technology A*, 16(6):3569–3577, 1998.
- [119] J. de Segovia. Physics of outgassing. In S. Turner, editor, *Proceedings of Vacuum Technology*. CERN Accelerator School, 1999.
- [120] J. Compton et al. Some measurements of outgassing properties and far-infrared reflectivities of two optical blacks. *Journal of Physics D: Applied Physics*, 7(18):2501–2510, 1974.
- [121] C. Gould and J. Schuchman. Vacuum behavior of various materials. In *IEEE Transactions on Nuclear Science*. 1967.
- [122] G. Arnaud et al. Tesla HF couplers: outgassing of copper plated AISI 304L samples. Technical report, Laboratoire de l'Accélérateur Linéaire, Université de Paris-Sud, 2002.
- [123] D. Desiderio. Outgassing measurements on a selected set of non-metallic materials. Technical report, European Large Scale Facility - Aerospace & Space Materials Technology Test House, 2003.

- 
- [124] R. Rampini et al. Outgassing kinetics testing of spacecraft materials. *Materialwissenschaft und Werkstofftechnik*, 34(4):359–364, 2003.
- [125] Standard test method for total mass loss and collected volatile condensable materials from outgassing in a vacuum environment, 1993. Norm ASTM E 595-93.
- [126] R. Calder and G. Lewin. Reduction of stainless-steel outgassing in ultra-high vacuum. *British Journal of Applied Physics*, 18(10):1459–1472, 1967.
- [127] K. Kishiyama et al. Measurement of ultra low outgassing rates for NLC UHV vacuum chambers. In *Proceedings of the Particle Accelerator Conference, Chicago*. 2001.
- [128] D. Santeler. Estimating the gas partial pressure due to diffusive outgassing. *Journal of Vacuum Science & Technology A*, 10(4):1879–1983, 1992.
- [129] H. Dylla et al. Correlation of outgassing of stainless steel and aluminum with various surface treatments. *Journal of Vacuum Science & Technology A*, 11(5):2623–2636, 1993.
- [130] N. Kanani. *Galvanotechnik - Grundlagen, Verfahren, Praxis*. Hanser, 2000.
- [131] G. Altenmüller et al. *VDI-Lexikon Werkstofftechnik*. VDI-Verlag, 1993.
- [132] P. Crimmann. *Grenzflächenmodifizierung und -analyse im Polypropylen-Kupfer-Verbund*. Ph.D. thesis, Martin-Luther-Universität Halle-Wittenberg, 2003.
- [133] K. Bobzin et al. PVD low temperature deposition processes for machine parts for integration of tribological functions within the surface. *Materialwissenschaft und Werkstofftechnik*, 35(10/11):843–850, 2004.
- [134] C. Chiang et al. Deposition and permeation properties of SiN<sub>x</sub>/parylene multilayers on polymeric substrates. *Surface and Coatings Technology*, 200(20-21):5843–5848, 2006.
- [135] M. Minatoa and H. Iwamoto. Vacuum characteristics of sprayed metal films. *Journal of Vacuum Science & Technology A*, 19(4):1662–1665, 2001.
- [136] Gemeinschaft Thermisches Spritzen e.V. Was ist Thermisches Spritzen? URL <http://www.gts-ev.de/ts-info.htm>, 2005.
- [137] J. Vlcek et al. Industrial application of cold spray coatings in the aircraft and space industry. *Galvanotechnik*, 96(3):684–699, 2005.
- [138] R. Song et al. Effects of laser surface remelting on hydrogen permeation resistance of thermally-sprayed pure aluminum coatings. *Surface and Coatings Technology*, 130(1):20–23, 2000.
- [139] Verbal communication with Henning Beuscher, AIMT, 2006.

- [140] Lacke und Anstrichstoffe – Gitterschnittprüfung, 1994. Norm DIN EN ISO 2409.
- [141] G. Dick and R. Suchentrunk. Zukunftstechnologie aprotische Aluminiumabscheidung - Rückblick und Perspektiven. *Galvanotechnik*, 95(6):1362–1368, 2004.
- [142] J. Karthaus. *Galvanische Abscheidung von Metallen aus nichtwässrigen Elektrolyten für die Mikrosystemtechnik*. Ph.D. thesis, Universität Karlsruhe, 2000.
- [143] A. Holleman and N. Wiberg. *Lehrbuch der anorganischen Chemie*. Walter de Gruyter, 1995.
- [144] R. C. Lasky. Tin pest: A forgotten issue in lead-free soldering? In *SMTA International*. Dartmouth College, 2004.
- [145] J. Feuerlein. Coating of CFRP laminates tank 2. Technical Report TM-W-ET-05-0236, Contraves Space AG, 2006.
- [146] M. Weber. Comparison flatwise tensile tests. Technical report, Contraves Space AG, 2006.
- [147] G. B. Thorwarth. *Herstellung und Eigenschaften amorpher Kohlenstoffschichten in der Plasma-Immersionen-Ionenimplantation*. Ph.D. thesis, University of Augsburg, 2005.
- [148] Pfeiffer Vacuum GmbH. Quality inspection certificate of calibrated leak CT408, 2004.
- [149] P. J. Mohr and B. N. Taylor. CODATA recommended values of the fundamental physical constants: 2002. *Reviews of Modern Physics*, 77(1):1–107, 2005.
- [150] J. Humpenöder. Gas permeation of fibre reinforced plactics. *Cryogenics*, 38(1):143–147, 1998.
- [151] DWD. Ausgabe der Klimadaten: Tageswerte. URL [http://www.dwd.de/de/FundE/Klima/KLIS/daten/online/nat/ausgabe\\_tageswerte.htm](http://www.dwd.de/de/FundE/Klima/KLIS/daten/online/nat/ausgabe_tageswerte.htm), 2006.
- [152] Verbal communication with Stefan Glöde, Lüberg Elektronik GmbH, 2007.
- [153] G. Firpo and A. Pozzo. Easy method enhancing the sensitivity of a helium mass-spectrometer leak detector. *Journal of Vacuum Science & Technology A*, 22(2):328–331, 2004.
- [154] Verbal communication with Jens Feuerlein, Oerlikon Space, 2007.
- [155] REB Research and Consulting. The permeability of hydrogen in aluminum, copper, iron, gold, kovar, niobium, palladium, platinum, silver, tantalum, titanium, and vanadium. URL <http://www.rebresearch.com/H2perm2.htm>, 1996.



- 
- [156] E. Clark. Tritium release estimate from CLWR – tritium extraction facility waste overpack. Technical report, Westinghouse Savannah River Company, 2001.
- [157] P. S. Korinko et al. Process development of aluminide coatings for hydrogen isotope permeation resistance. In *Conference Proceedings: Tritium 2001 at Tsukaba*. Westinghouse Savannah River Company, 2001.
- [158] E. Serra et al. Hydrogen permeation measurements on alumina. *Journal of the American Ceramic Society*, 88(1):15, 2005.
- [159] S. Steward. Review of hydrogen isotope permeability through materials. Technical report, Lawrence Livermore National Laboratory, 1983.
- [160] W. Song et al. A study of hydrogen permeation in aluminum alloy treated by various oxidation processes. *Journal of Nuclear Materials*, 246(2-3):139–143, 1997.
- [161] K. Verghese et al. Hydrogen permeation through non-metallic solids. *Journal of Nuclear Materials*, 85-86:1161–1164, 1979.
- [162] D. R. Harding et al. Thoughts on target fabrication issues for IFE. Technical report, OMEGA, 2004.
- [163] D. Begeal. Hydrogen and deuterium permeation in copper alloys, copper-gold brazing alloys, gold... *Journal of Vacuum Science & Technology A*, 15(3):1146–1154, 1978.
- [164] J. Gorman and W. Nardella. Hydrogen permeation through metals. *Vacuum*, 12(1):19–24, 1962.
- [165] B. Howard et al. Hydrogen permeability of palladium-copper alloy composite membranes over a wide range of temperatures and pressures. In *14th National Hydrogen Association Meeting, Washington DC*. 2003.
- [166] H. Wipf. Solubility and diffusion of hydrogen in pure metals and alloys. *Physica Scripta*, T94(1):43–51, 2001.
- [167] W. Robertson. Hydrogen permeation, diffusion and solution in nickel. *Zeitschrift für Metallkunde*, 64(6):436–443, 1973.
- [168] P. Andrew and A. Haasz. Hydrogen permeation through copper-coated palladium. *Journal of Applied Physics*, 70(7):3600–3604, 1991.
- [169] M. Ciocco et al. High-pressure, high-temperature hydrogen permeability measurements of supported thin-film palladium membranes. In *Pittsburgh Coal Conference, Pittsburgh PA*. 2003.
- [170] B. D. Morreale et al. Evaluation of high-pressure, high-temperature inorganic hydrogen membranes. In C. Padro and F. Lau, editors, *Advances in Hydrogen Energy*, pages 93–110. Kluwer Academic/Plenum Publishers; New York, 2000.

- 
- [171] A. Aiello et al. Hydrogen isotopes permeation through fusion oriented materials. In K. Watanabe et al., editors, *International Tritium Workshop on Tritium-Material Interactions - Contamination and Decontamination, Toyama, Japan*. 2001.
- [172] E. Van Deventer and V. A. Maroni. Hydrogen permeation characteristics of some austenitic and nickel-base alloys. *Journal of Nuclear Materials*, 92:103–111, 1980.
- [173] D. Rudd and J. Vetrano. Permeability of metals and enameled metals to hydrogen. Inc. report naa-sr 6109, North American Aviation, 1961.
- [174] E. Van Deventer et al. Hydrogen permeation characteristics of aluminum coated and aluminum-modified steels. *Journal of Nuclear Materials*, 88:168–173, 1980.
- [175] S. Hara et al. Hydrogen permeation through palladium-coated amorphous Zr-M-Ni (M = Ti, Hf) alloy membranes. In *International congress on membranes and membrane processes, Toulouse*, volume 144, pages 115–120. 2002.
- [176] D. Wang et al. Hydrogen permeation measurements of partially internally oxidized Pd-Al alloys in the presence and absence of CO (U). Technical report, Chemistry Department, University of Vermont, Burlington, 2003.
- [177] C. Nishimura et al. Hydrogen permeation and transmission electron microscope observations of V-Al alloys. *Journal of Alloys and Compounds*, 356-357:295–299, 2003.
- [178] W. Rogers et al. Diffusion coefficient, solubility and permeability for helium in glass. *Journal of Applied Physics*, 25(7):868–875, 1954.
- [179] Goodfellow. Materialinformationen FEP. URL <http://www.goodfellow.com/csp/active/gfMaterialInfo.csp?MATID=FP34&material=1>, 2005.
- [180] Goodfellow. Materialinformationen HDPE. URL <http://www.goodfellow.com/csp/active/static/a/et32.html>, 2005.
- [181] Goodfellow. Materialinformationen PBT. URL [http://www.goodfellow.com/csp/active/gfMaterialInfo.csp?text=\\*P\&MATID=ES34&material=1](http://www.goodfellow.com/csp/active/gfMaterialInfo.csp?text=*P\&MATID=ES34&material=1), 2005.
- [182] Goodfellow. Materialinformationen PC. URL [http://www.goodfellow.com/csp/active/gfMaterialInfo.csp?text=\\*P\&MATID=CT30&material=1](http://www.goodfellow.com/csp/active/gfMaterialInfo.csp?text=*P\&MATID=CT30&material=1), 2005.
- [183] Goodfellow. Materialinformationen PET, PETP. URL <http://www.azom.com/details.asp?ArticleID=2047>, 2005.
- [184] Goodfellow. Materialinformationen PI. URL [http://www.goodfellow.com/csp/active/gfMaterialInfo.csp?text=\\*P\&MATID=IM30&material=1](http://www.goodfellow.com/csp/active/gfMaterialInfo.csp?text=*P\&MATID=IM30&material=1), 2005.
- [185] Goodfellow. Materialinformationen PS. URL [http://www.goodfellow.com/csp/active/gfMaterialInfo.csp?text=\\*P\&MATID=ST31&material=1](http://www.goodfellow.com/csp/active/gfMaterialInfo.csp?text=*P\&MATID=ST31&material=1), 2005.

- 
- [186] Goodfellow. Materialinformationen PTFE. URL [http://www.goodfellow.com/csp/active/gfMaterialInfo.csp?text=\\*P\&MATID=FP30\&material=1](http://www.goodfellow.com/csp/active/gfMaterialInfo.csp?text=*P\&MATID=FP30\&material=1), 2005.
- [187] Goodfellow. Materialinformationen PVDF. URL [http://www.goodfellow.com/csp/active/gfMaterialInfo.csp?text=\\*P\&MATID=FV30\&material=1](http://www.goodfellow.com/csp/active/gfMaterialInfo.csp?text=*P\&MATID=FV30\&material=1), 2005.
- [188] Goodfellow. Materialinformationen PVF. URL [http://www.goodfellow.com/csp/active/gfMaterialInfo.csp?text=\\*P\&MATID=FV33\&material=1](http://www.goodfellow.com/csp/active/gfMaterialInfo.csp?text=*P\&MATID=FV33\&material=1), 2005.
- [189] Goodfellow. Materialinformationen UPVF. URL [http://www.goodfellow.com/csp/active/gfMaterialInfo.csp?text=\\*P\&MATID=CV31\&material=1](http://www.goodfellow.com/csp/active/gfMaterialInfo.csp?text=*P\&MATID=CV31\&material=1), 2005.
- [190] Goodfellow. Materialinformationen UPVC. URL <http://www.goodfellow.com/csp/active/gfMaterialInfo.csp?MATID=CV31\&material=1>, 2005.
- [191] Kawasaki Heavy Industries. Presentation of hydrogen activities, 2004. Presentation at BMW, München.
- [192] B. Sankar and P. Ifju. Fiber reinforced composites for hydrogen storage systems. Technical report, University of Florida, 2004.
- [193] Goodfellow. Materialinformationen Silikon-Elastomer MQ/VNQ/PMQ/PVMQ. URL <http://www.goodfellow.com/csp/active/gfMaterialInfo.csp?MATID=SI30\&material=1>, 2005.
- [194] Y. Yang et al. An improved throughput method for the measurement of outgassing rates of materials. *Vacuum*, 46(12):1371–1376, 1995.
- [195] A. Chambers et al. *Basic vacuum technology*. Institute of Physics Publishing, Bristol, 1995.
- [196] V. Nemanic and J. Setina. A study of thermal treatment procedures to reduce hydrogen outgassing rate in thin wall stainless steel cells. *Vacuum*, 53(1):277–280, 1999.
- [197] S. Ichimura et al. Measurement of outgassing characteristics from a vacuum chamber fabricated for pressure calibration in UHV/XHV region. *Vacuum*, 53(1):277–280, 1999.
- [198] L. Eriksson. Thermal outgassing rate for various beam line materials. 1999. Presentation.
- [199] K. Odaka and S. Ueda. Dependence of outgassing rate on surface oxide layer thickness in type 304 stainless steel before and after surface oxidation in air. *Vacuum*, 47(6-8):689–692, 1996.
- [200] J. Chen and Y. Liu. Thermal outgassing from stainless steel vacuum chambers. *Chinese Journal of Physics*, 24(1):29–36, 1986.

- 
- [201] M. Saitoh et al. Influence of vacuum gauges on outgassing rate measurements. *Journal of Vacuum Science & Technology A*, 11(5):2816–2821, 1993.
- [202] L. Yin et al. The vacuum chamber for the SSRF storage ring. In *Proceedings of the Second Asian Particle Accelerator Conference, Beijing, China*. 2001.
- [203] H. Halama and J. Herrera. Thermal desorption of gases from aluminum alloy Al 6061, their rates and activation energies. *Journal of Vacuum Science & Technology A*, 13(1):463–466, 1976.
- [204] F. Watanabe et al. In situ deoxidization/oxidization of a copper surface: A new concept for attaining ultralow outgassing rates from a vacuum wall. *Journal of Vacuum Science & Technology A*, 13(1):147–150, 1995.
- [205] D. Dykes and D. Higgins. Possible cavity construction techniques for the diamond storage ring. Technical report, Daresbury Laboratory, Warrington, UK, 1995.
- [206] F. Watanabe et al. Attaining an ultralow outgassing rate of  $10\text{E-}12\text{ Pam}^3\text{s}^{-1}\text{m}^{-2}$  from an oxygen-free high conductivity copper chamber with beryllium-copper-alloy flanges. *Journal of Vacuum Science & Technology A*, 13(5):2587–2591, 1995.
- [207] P. He et al. Outgassing and surface properties of tin coated SNS ring vacuum chambers. In *Particle Accelerator Conference*. 2003.
- [208] S. S. Rosenblum. Vacuum outgassing rates of plastics and composites for electrical insulators. *Journal of Vacuum Science & Technology A*, 4(1):107–110, 1986.
- [209] R. Barton and R. Govier. A mass spectrometric study of the outgassing of some elastomers and plastics. *Journal of Vacuum Science & Technology A*, 2(3):113–122, 1965.
- [210] V. Nguyen-Tuong. Vacuum outgassing of artificial dielectric ceramics. *Journal of Vacuum Science & Technology A*, 12(4):1719–1721, 1994.

# Danksagung

Diese Arbeit ist als Industriepromotion bei der BMW Forschung und Technik GmbH im Rahmen des EU-Projektes *StorHy* entstanden. Unzählige Arbeiten sind durchgeführt worden, die ohne die Hilfe vieler Personen nicht möglich gewesen wären. Diesen Menschen gilt mein herzlicher Dank.

Ein großer Dank geht an meinen Doktorvater, Prof. Dr. Siegfried R. Horn, der mir diese Dissertation ermöglicht und mir in regelmäßigen Gesprächsrunden oder spontan zustande gekommenen Diskussionen viele wichtige Informationen und Ratschläge gegeben hat. Neben der wissenschaftlichen zeige ich mich für Ihre organisatorische und materielle Unterstützung erkenntlich. Prof. Dr. Ferdinand Haider danke ich für die Übernahme der Zeitgutachtens. Bedanken möchte ich mich weiterhin bei Prof. Dr. Kunibert G. Siebert für erweiterte Einblicke in die Welt der numerischen Simulation.

Großartige praktische Unterstützung bekam ich von Johannes Höchtl, Alexandre Santos Abreu und Dorothea Nieberl v. a. beim Aufbau und Inbetriebnahme der beiden Permeationsmessenanlagen. Fabian Wrobel und Dr. Matthias Klemm haben durch ihre zahlreichen, z. T. an Wochenenden durchgeführten, REM-Aufnahmen viel Elektronenlicht ins Materialdunkel gebracht. Susanne Denzer, Sabine Bessel und Danuta Trojak haben durch ihre vielfältigen Hilfen zum Gelingen der Arbeit beigetragen. Euch allen gebührt meine Anerkennung und Dankbarkeit. Dem Lehrstuhl EP 6 möchte dafür danken, dass ich die Möglichkeit hatte, Eure Kameras und Mikroskope zu benutzen. Götz Thorwart gebührt großer Dank für die applizierten DLC Schichten. Nicht zu vergessen sind die zahlreichen Arbeiten der Feinmechanischen Werkstatt. Stellvertretend möchte ich Herrn Armin Jaehner dafür danken.

Ich möchte mich recht herzlich bei Michael Zenner für die BMW-seitige Betreuung der Arbeit bedanken. Du hast dich in vielerlei Hinsicht für meine Belange eingesetzt und mir so viele Möglichkeiten eröffnet. Ein großer Dank gilt Michael Bauer für die vielen Diskussionen, Beratungen in CAE- und CFK-Fragen, das Erstellen von technischen Zeichnungen und dem Beschaffen von CFK-Platten. Dem restlichen TIS Team bin ich für das angenehme Arbeitsklima verbunden. Ferner möchte ich mich bei den Kollegen von EG-52 für Informationen zur normgerechten Materialprüfung und für das Wasserstrahlschneiden bedanken.

Den Kollegen vom *StorHy*-Projekt möchte ich für die sehr produktive Zusammenarbeit danken. Eure kritischen Fragen und Hinweise in den regelmäßigen Treffen haben mich neben den wissenschaftlichen auch die anwendungsbezogenen Aspekte nicht vergessen lassen. Insbesondere gilt mein Dank Oerlikon Space AG, und hier stellvertretend Jens Feuerlein, für die Zurverfügungstellung der vielen CFK-Platten und die sonstige enge Zusammenarbeit. Vielen Dank auch an Uli Burger, der für mich die CAD-Zeichnungen des StorHy-Tanks anfertigte.

Ein Großteil dieser Promotion umfasste das Finden von geeigneten Beschichtungen. Die

dabei geleistete Arbeit der beteiligten Firmen war bemerkenswert. Mein erster Dank geht an Klaus Waldhardt, Dr. Hartmut Sauer und Henning Beuscher von der AIMT Holding GmbH für die vielen investierten Stunden. Ein großer Dank geht an Stefan Glöde, Walter Stabla und Ronald Flieger von der Fa. Lüberg Elektronik GmbH & Co. Rothfischer KG für die sehr gute Zusammenarbeit. Unvergessen wird mir das Beschichten des *Tank 2* mit einer “Nachtruhe” von 2<sup>00</sup> bis 4<sup>00</sup> Uhr bleiben. Weiterhin möchte ich Herrn Härtel von Aluminal Oberflächentechnik GmbH & Co. KG, Herrn Leistner von Leistner GmbH und Herrn Klotzek von OMT GmbH für ihre Beschichtungen danken.

Mein besondere Dank geht an meine Familie und Freunde, ohne die ich nicht zu dem geworden wäre, der ich bin. Es war mir sehr wichtig zu wissen, dass es Euch gibt. Als letztes und am meisten möchte ich mich bei meiner Freundin bedanken. Marilyn, du hast nicht nur meine Arbeit akribisch korrekturgelesen, sondern mir in den letzten drei Jahren viel Geduld und Liebe entgegengebracht.

# Lebenslauf

## Persönliche Daten

Daniel Schultheiß  
geboren am 05.10.1977 in Potsdam

## Ausbildung

- 09.1984 – 08.1991     Polytechnische Oberschule Geltow
- 09.1991 – 06.1997     Ernst-Haeckel-Gymnasium, Werder/Havel
- 1998 – 2003             Diplomstudium Luft- und Raumfahrttechnik, Universität Stuttgart
- Schwerpunkte: Statik und Dynamik, Raumfahrtsysteme
  - Studienarbeit: *Aktualisierung und Erweiterung einer datenbankbasierten Methodik zur Massenabschätzung von Raumtransportsystemen*
  - Diplomarbeit: *Gravity Compensation of Deployable Solar Arrays for Small Spacecraft*, University of Cambridge
- 2004 – 2007             Dissertation, Universität Augsburg

## Berufstätigkeit

- 02.2004 – 03.2004     Wissenschaftlicher Mitarbeiter, Universität Augsburg
- 04.2004 – 03.2007     Doktorand, BMW AG, München
- seit 04.2007            Spezialist Entwicklung, BMW AG, München

Augsburg, den 15.04.2007

